École doctorale "C2MP" ED 606

Sciences et Technologies

Thèse

pour l'obtention du titre de

Docteur de l'Université de Lorraine

présentée par

Guillaume URBANCZYK

Interaction of High-Power waves with the plasma periphery of WEST & EAST tokamaks

---

Thèse soutenue publiquement le 29 Novembre 2019 à Nancy devant le jury composé de:

Prof. Etienne GRAVIER	Président du jury – ULorraine
Dr. Annika EKEDAHL	Rapporteur – CEA
Prof. Xinjun ZHANG	Rapporteur – ASIPP Chine
Prof. Kristel CROMBE	Examinatrice – UGent/ERM
Prof. Stéphane HEURAUX	Directeur de thèse – ULorraine
Dr Laurent COLAS	Co-directeur de thèse – CEA
Dr. Philippe JACQUET	Invité – CCFE Culham

ABSTRACT

Ion Cyclotron Resonance Heating (ICRH) in the H minority scheme can allow thermal ions to absorb up to half of the injected power. Meanwhile, ICRH heating can prevent heavy impurity accumulation similarly to broad ECRH [Sertoli 2017]. In order to benefit from ICRH in the core, waves must be coupled to the plasma from antennas whose location at the edge is subject to a trade-off between (1) efficient coupling and (2) impurity generation. This thesis presents mostly experimental observations made on these two aspects in EAST and WEST superconducting medium size tokamaks, on L-mode scenarios combining Lower Hybrid Current Drive from two launchers and D[H] minority heating by ICRH antennas. All ICRH antennas have been able to couple more than 1MW per antenna, with indications of efficient wave absorption. The heating efficiency changes consistently with the total power injected. However in some cases without low-Z materials coating (Li, B), heating effect may only last several hundred milliseconds (time-scale for impurity transport up to core plasma) after powering ICRH.

Lower Hybrid (LH) power helps improving ICRH coupling. Experiments reveal that fueling from the mid-plane not only helps to couple waves from nearby antennas like in other devices, but also has an impact on the scrape-off layer (SOL) density in regions that are not magnetically connected to the valves. Localized mid-plane nozzle valves allow in EAST better coupling compared to poloidally distributed valves. Core density control requirements for long-pulse operation, in particular in L-mode regime, however limit the amount of gas that can be injected. If injected from radially retracted points, gas can spread and help reducing sputtering yield on active antenna limiters by a combination of four effects: (a) reduce thermal effects by cooling down the SOL (b) improve coupling and therefore reduce the overall near-field amplitudes for a given RF power, (c) increase the electron mobility in the SOL and thus mitigate the excitation of parallel components of the electric field and (d) dilute impurities which are the main contributors to sputtering.

During ICRH, impurities can contaminate the plasma to a level detrimental for the operation, *e.g.* 100% of ICRH power radiated in many L-mode discharges in WEST and H-mode discharges in EAST. Tungsten (W) production measured by extreme ultraviolet spectroscopy increases significantly when an ICRH antenna

magnetically connected to W surfaces is powered, compared to a reference phase without ICRH. On some components such as antenna side limiters, the rise is larger than with a similar LH, NBI or ECRH power. The relative contribution of each object and physical process (RF-sheaths, fast ion ripple losses) to core contamination yet remains poorly known. Comparing antenna limiters with W-coating *vs* low-Z materials helped quantifying the role of these components. The core W content, in presence of divertor sources only, is correlated with the total injected power, either from ICRH or LH. Since 2018 the LH guard limiter tiles were W-coated. Their contribution to the core W content appears more important than divertor sources, particularly when the magnetically connected ICRH antenna is powered. Two-strap ICRH antennas magnetically connected to W components at the mid-plane already compromise high performance operations.

In addition to low-*Z* materials in regions magnetically connected to antennas, using arrays of more than two straps toroidally would allow near-field's cancelation and RF-sheaths reduction. Other concepts (active limiters, TWAs) have been proposed but remain to be tested.

Key Words: Ion Cyclotron Resonance Heating (ICRH), Scrape-Off Layer (SOL), Radiofrequency (RF) Sheath, Wave coupling, Local gas injection, Impurity

Contents

1. Introduction

Nuclear fusion is a reaction in which two or more atomic nuclei are combined to form one or more different atomic nuclei and subatomic particles (neutrons or protons). The difference in mass between the reactants and products is manifested as either the release or absorption of energy. This difference in mass arises due to the difference in atomic "binding energy" between the atomic nuclei before and after the reaction. Fusion is the process that powers active or "main sequence" stars like the sun (Fig.1.1a), or high magnitude stars like the crab nebula (Fig.1.1b). Nowadays telescopes enable to observe various kinds of objects where gigantesque amount of matter can naturally meet together under tremendous gravitational forces. Surely the example we know the best is our sun (Fig.1.1a) and this is why we try to imitate it for creating a new, clean, sustainable and safe source of energy, the nuclear fusion.

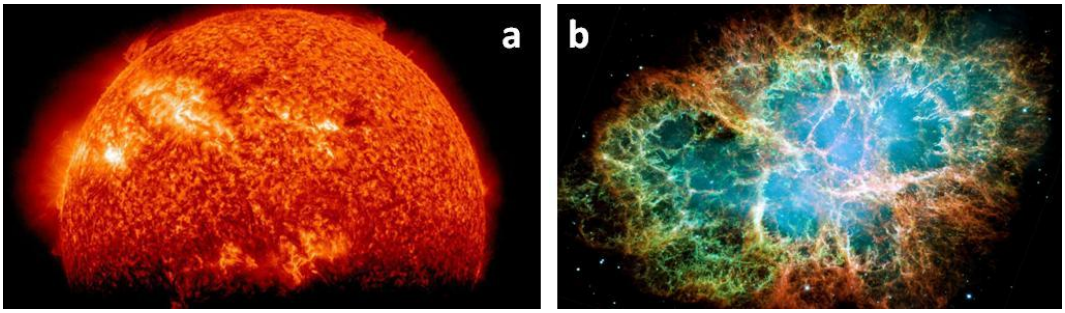

Figure 1.1: Pictures of (a) our sun and (b) of the Crab Nebula (supernova)

1.1 Fusion in plasma devices

1.1.1 What is a plasma ?

The Plasma is one of the fourth fundamental states of matter, and is basically an ionized gas (Fig.1.2). It can be composed more specifically of ions, atoms which have some of their orbital electrons removed, and free electrons. Plasma can be generated either by heating or subjecting a neutral gas to a strong electromagnetic field to the point where an ionized gaseous substance becomes increasingly electrically conductive, like in a neon light tube when the gas is ionized (2000°C) by the

difference of potential between the anode and the cathode when you switch on an interrupter. This type of plasma considered “cold” can then be contained inside a glass tube to create light. Cols plasmas are also used a lot in the industry to replace vacuum, treat surfaces and wastes, etching at high precision … However these plasmas are far from the conditions required for fusion.

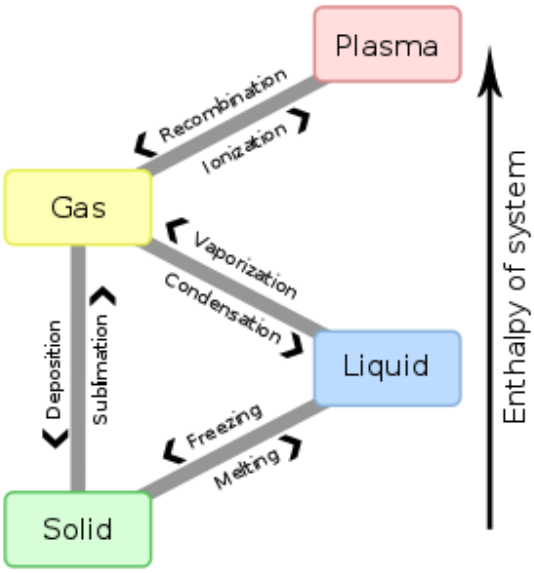

Figure 1.2: Four states of matter and transitions between them

1.1.2 Fusion for energy

Most likely nuclear fusion reaction to be used one day on nuclear fusion reactors based on reactivity (Fig.1.3) is also the one that happen at the edge of the sun between deuterium and tritium [G. Van Oost 2008]:

$$ {}_{1}^{2}D + {}_{1}^{3}T \rightarrow {}_{2}^{4}H_{e}(3.56MeV) + {}_{0}^{1}n(14.03MeV) \qquad (1.1) $$

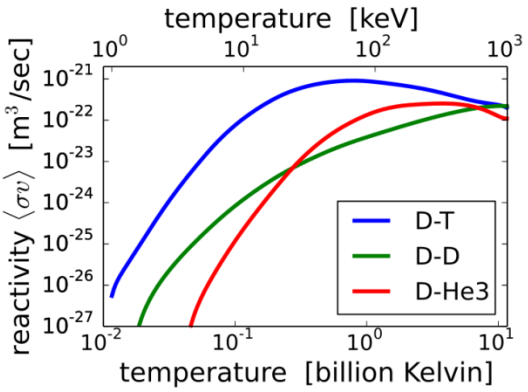

Figure 1.3: Fusion reaction rate as a function of temperature for three different reactions. The DT rate peaks at a lower temperature (about 70 keV, or 800 million kelvin) and at a higher value than other reactions commonly considered for fusion energy. (https://en.wikipedia.org/wiki/Nuclear_fusion)

As can be seen on the eq.1.1, deuterium and tritium have to fuse together, but as they both have the same charge once ionized in a plasma, this is not about to happen easily. Both ions basically have to get close enough so that the weak interaction force becomes stronger than the Columbian repulsion and they can fuse together. Once this happens, products of the reaction are a helium nuclei and a neutron with a lot of energy (14MeV vs 4.8MeV on average for fission reactions) that can be collected by a coolant to produce electricity exactly as it has been done in nuclear fission for decades. Notice also that unlike fission, this reaction does not produce any long life radioactive element but only requires to manage tritium and materials activation under large particle fluxes which is nothing compared to products of a fission reaction, the so-called long life nuclear waste with high radiation level. This is probably one of the main advantages of the fusion, with the abundance of resources (D, T) and its remarkable safety.

Let's now explain how we manage in practice to bring nucleus close enough to fuse together. Intuitively one can feel that bringing two magnets with the same polarity together takes energy, similarly bringing two ions with the same charge together takes energy. In plasmas, this energy can be seen as the temperature of the plasma, equivalent to the average kinetic energy carried by particles. Based on the plasma density that can be done in current devices and the efficiency by which particles are confined, temperature should be above 10keV which is more than 100 million degrees in order to start having the reaction happening (which is increasing

the D-T reaction cross-section as shown in Fig.1.3). A more accurate criterion taking three key parameters into account for fusion ignition can be derived from the energy balance of the reaction; this is the *Lawson criterion* [J.D. Lawson 1957]:

$$n.\tau_e.T_i > 3.10^{21} keV/s \quad (1.2)$$

With n the density, T_i the ions temperature and τ_e the energy confinement time which is the characteristic time by which the plasma loses its energy (heat). To understand this notion, an analogy can be made between the plasma and a house heated at 25°C while the temperature outside is only of 0°. An infinite confinement time would mean that the heater can be switched off and that the temperature in the house will never change, which is of course never the case because of heat diffusion. Now since the energy inside the house is proportional to its volume whereas the speed at which the energy flows out is only proportional to its surface, one understands why a bigger house will stay warm longer than a small one. For the same reason that building larger house allows keeping energy inside longer, building larger devices should also allow keeping the energy longer, and therefore more easily stay in regimes suitable for fusion reactions by maximizing the so-called confinement time.

The next objective is to maximize the triple factor in eq.1.2, either by increasing plasmas density (by injecting more gas), temperature (by heating the plasma), or their product (by increasing the magnetic field). Devices are highly constrained by operational and engineering limitations (materials, heat loads, magnetic field coils …) that in practice prevent from fulfilling what physics tells us to do (increase further the triple factor in eq.1.2). Physics limits the density for instance due to magneto hydrodynamic, engineering limits affect heating systems and the intensity of magnetic field that can be done, while interaction between plasma and material limits the damages that the device can sustain.

1.1.3 Fusion devices

Several concepts and devices can be used to make nuclear fusion reaction on earth:

- The *inertial confinement* uses lasers to shoot high density pellets of fuel [Pfalzner 2006], however this approach only allows about one shot lasting several nanoseconds per day because aligning another pellet takes time. This

approach is mostly used for military purpose.

- The *Z-machine* consists in suddenly discharging electricity stocked in pools (capacitors) through grills that are brought together by strong induced electric fields, compressing the fuel pellet in between, from about 2mm down to 0.16mm in 7ns (https://fr.wikipedia.org/wiki/Z_machine). This approach is mostly used to generate X-rays by Sandia laboratories in the US.
- *Stellarators* are plasma device that rely primarily on very complex external magnets to confine the plasma and not relying on current drive to induce an extra poloidal field to close the magnetic field lines like in tokamaks (https://en.wikipedia.org/wiki/Stellarator) [D.A Hartmann 2008].

Tokamaks were invented by Russians more than sixty years ago – ***to***roïdalnaïa ***ka***mera s ***ma***gnitnymi ***k***atushkami – to confine a plasma in a toroidal chamber with magnetic coils. Tokamak is the concept that got most of the attention since the sixties

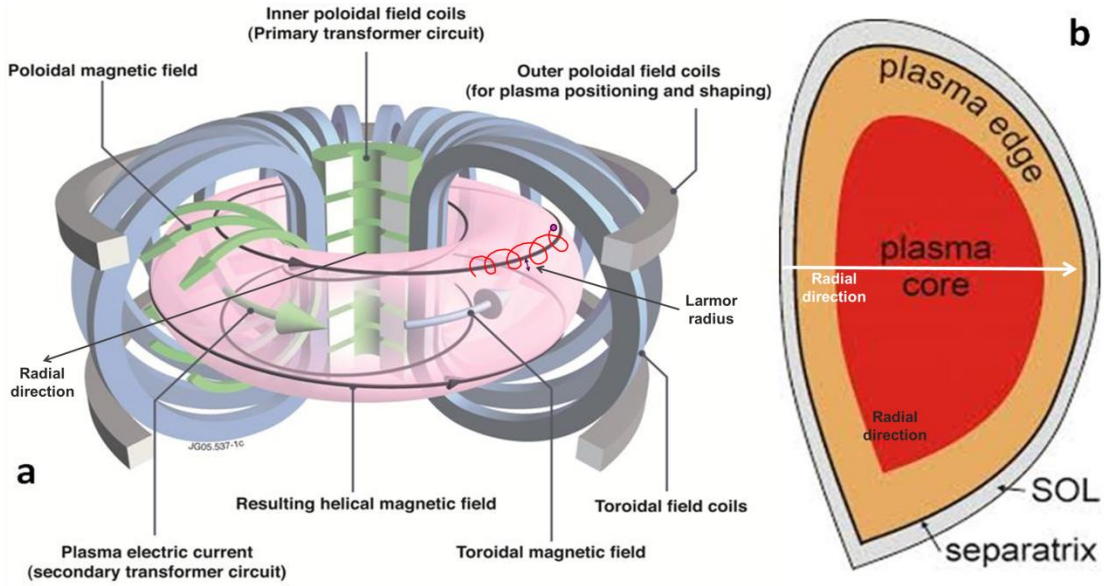

Figure 1.4: (a) 3D Schematic view of a Tokomak (courtesy by EUROfusion [FusionWiki]) and (b) 2D Poloidal cut of the plasma showing the core (hottest part), the edge (colder) the separatrix corresponding to the last closed surface and out of it the Scrape-Off Layer (SOL)

The figure 1.4 shows the key elements of a tokamak. As a charged particle plunged into a magnetic field turns around it like represented by the red line in Fig.1.4a, we

can say that the particle is well confined within one Larmor radius if magnetic field lines are correctly closed, and there is the first challenge. Initially, toroidal field coils – that give to the tokamak its torus shape – produce a toroidal magnetic field. The problem is that this toroidal magnetic field is not homogeneous; it is inversely proportional to the radius, so decreases as we move from the center to the edge. This means that a particle turning around a field line will experience a stronger field – and so a stronger curvature – on one side than the other, giving rise to a ∇B drift that deviate its trajectory vertically (for instance ions downwards and electrons upwards). To counter this effect, the inner poloidal field coils combined with the current flowing through the plasma induce another poloidal magnetic field, which added to the toroidal one, results in a total helical magnetic field lines wound on closed magnetic surfaces. With this configuration the curvature drift alternatively pushes the trajectories towards the outer and inner magnetic surfaces. Finally outer poloidal coils are added all around the structure for controlling the shape and position of the plasma according to the scenario. In a toroidal fusion power reactor, the magnetic fields confining the plasma are formed in a helical shape, winding around the interior of the reactor. The safety factor, labeled q or q(r), is the ratio of the times a particular magnetic field line travels around a toroidal confinement area's "long way" (toroidally) to the "short way" (poloidally):

$$q = \frac{R.B_p}{r.B_t} = \frac{d\phi}{d\theta} \tag{1.3}$$

With R large radius, r a given radial location, B_p and B_t respectively the poloidal and the toroidal magnetic field components. For instance when q=2, it means that particles make two poloidal loop when doing a toroidal one. If q increases, it means particles travel faster and faster in the poloidal direction compared to the toroidal direction, and follow trajectories with higher and higher pitch-angle compared to the toroidal direction. Since the plasma is only weakly confined along the field lines, it is almost homogeneous along magnetic surfaces, which allows assuming that any parameter radial profiles is quite homogeneous along magnetic field lines, and almost torodially. The term "safety" refers to the resulting stability of the plasma; plasmas that rotate around the torus poloidally about the same number of times as toroidally are inherently less susceptible to certain instabilities. The term is most commonly used when referring to tokamak devices. Although the same considerations apply in

stellarators, by convention the inverse value is used, the rotational transform, or i. Despite of great effort in all devices and equivalently fruitful discoveries resulting from each field of application, new methods of construction which have increased the quality and power of the magnetic fields improving stellarators performance, the tokamak remains the most promising concept for fusion energy, since best performance of other devices so far still remain much lower than these achieved in tokamaks (about three orders of magnitude difference in terms of Lawson criteria between stellarators and tokamaks (eq.1.2)).

1.2 Plasma heating and current drive systems in tokamaks

At the beginning of the discharge in a tokamak, the gas is first injected, cold, then rapidly ionized as density grows and collisions increase. Once there are positively charged ions and negatively charged electrons moving on opposite direction of the torus, a current appears. Due to Coulomb collisions, plasma has a small electric resistance, and this enables to heat it using Joule effect. Unlike most physics states, as plasma temperature T rises, collisional frequency and plasma resistivity decrease as $1/T^{3/2}$. This particularity of a plasma puts a limit to the use of Joule effect whose efficiency decreases until it saturates once the plasma has reached temperatures of about few tens of millions degrees, still not enough for fusion reactions to take place (150 million degrees). Surely the current could still rise to compensate resistance decrease ($P_\Omega=R.I_p^2$ with P_Ω the ohmic power and I_p the plasma current) but here again, too strong current might leads to the brutal apparition of Magneto-Hydro-Dynamic (MHD) instabilities in the plasma often leading to a disruption (loss of plasma control). To prevent such event, the edge safety factor ($q(r=0.95xR)=q_{95}$) should for instance be kept above some critical value ($q_{95}>2$).

Other solutions presented in the following parts are needed [Y. Kazakov 2015]. One solution is to accelerate particles and send them into the plasma where they can collide with others and share their kinetic energy; this is the Neutral Beam Injection (NBI) detailed in the next subsection.

Other plasma heating methods rely on high-power electromagnetic waves [R. Koch 2015]. Plane wave is a physical quantity whose value, at any moment, is constant over any plane that is perpendicular to a fixed direction in space. Efficient heating

occurs when the wave frequency ($\omega=2\pi.f$) resonates with the particle gyrofrequency ($\omega_s = n.\Omega_s + k_{//}.v_{//}$) with $v_{//}$ the parallel speed of a particle specie s in transverse gyration at frequency Ω_s. Phase resonance between plane wave oscillating as $\exp(-i\omega+i\mathbf{k}.\mathbf{r})$ with **k** the so called wave vector. Once accelerated, the resonant particles, if properly confined, subsequently transfer their energy and momentum to the bulk via collisions. The nature of the resonant particles and the value of *n* determine different ranges of frequencies summarized on Fig.1.5 and detailed in the next subsections. An analogy can be made between plasma and food heating with waves: in the same way waves in a tokamak resonate with charged particles, waves in a microwave oven excite water molecules based on their momentum. Note that wave frequency in a microwave oven is exactly the one of lower hybrid (GHz), only the power launched in a tokamak by a typical lower hybrid grill (100kW) is typically 2 to 3 orders of magnitudes above what is used to warm up food in microwaves (1kW).

Alpha heating is another solution a little bit more futuristic which requires to build tokamak big enough so that the helium nucleus emitted from the fusion reaction travels through a bigger volume of plasma, consequently losing more energy, so that at some point the plasma ignition conditions are fulfilled and its temperature remains stable without additional external energy; this is what DEMO (DEMOntration power station) wishes to achieve [DEMO]. First ITER (International Thermonuclear Experimental Reactor) should produce by fusion 10 times the power injected in the device to heat the plasma [ITER] (which is still remains smaller than the total amount of electricity necessary to power each system!). Significant heating of the burning plasma is expected from alphas (He product cf. eq.1.1).

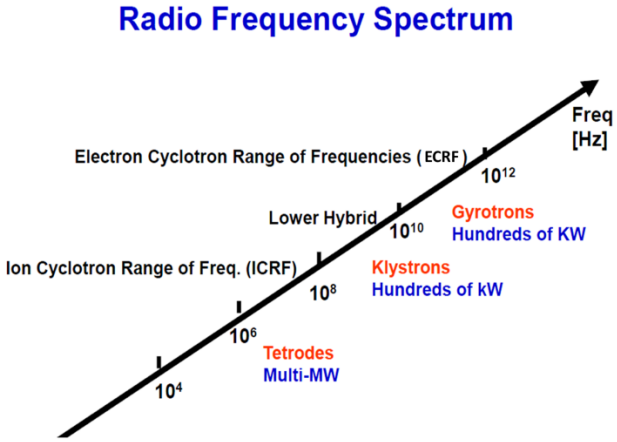

Figure 1.5: Frequency spectrum with the three waves heating systems, and their respective power source name (in red) and the power usually available on one single

source (in blue)

Beyond heating the plasma to increase its temperature, it is also necessary as mentioned in the previous section to drive current trough the plasma in order to close the magnetic field lines and improve particles confinement. Current can be inductively driven by applying a voltage to the central solenoid (near the internal poloidal field coil in Fig.1.4) but the voltage resource stocked in capacitors before each discharge is limited and not sufficient to sustain current drive for long periods of time. Non-inductive current drive is then necessary to allow long discharges in steady state. Despite all auxiliary heating system are capable under certain conditions to drive current, lower hybrid frequency waves described in section 1.2.3 are the most efficient for this purpose.

1.2.1 Neutral Beam Injection – NBI

This technique consists in accelerating an ion beam with an electric field until hundreds of keV on nowadays tokamaks and until about 1MeV on ITER. This represents high energies that can be deposited through collisions in the plasma according a well-known direction (the one of the beam) [R. Koch 2008]. For now, world highest fusion power was achieved on JET tokamak (16MW) by injecting 22MW of NBI together with 3MW of ICRF (Ion Cyclotron Range of Frequency waves). NBI biggest challenge comes from the high energy beam neutralization before it is sent into the plasma. This neutralizing step is essential since as the objective of the tokamak is to confine charged particles, reciprocally none is supposed to enter it, so the beam must be neutralized before being injected. The difficulty of this step comes from the fact that as ion energy increases, it becomes much harder to neutralize (Fig.1.6). On ITER for instance, the size of the machine implies to inject beams at much higher energy than what is used on nowadays machines, so that it will penetrate deeper and be absorbed in the core. Otherwise, the beam decay length being proportional to its energy, if this last one is not high enough relatively to tokamak dimensions, most power would be deposited in the plasma edge, which is not suitable. From neutralization point of view, Fig.1.6 clearly shows that positive ions are not a good option for ITER, so it is planned to use negative ions which are easier to neutralize at high energies. Finally the charged beam that was not neutralized is diverted by a strong magnetic field and lost onto sacrificial materials that will be subject to further activation challenges.

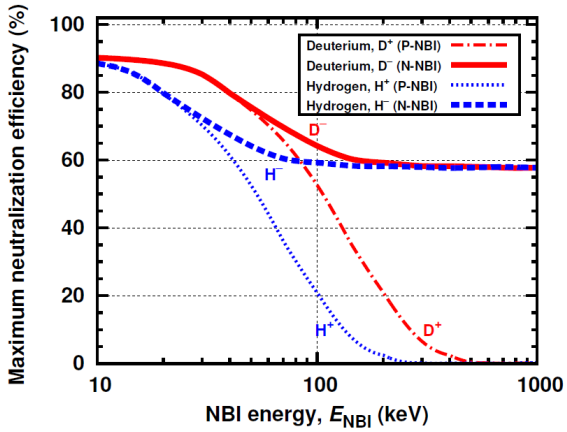

Figure 1.6: Maximum neutralization frequency for deuterium and hydrogen ions as a function of beam energy [R. Koch 2008].

1.2.2 Electron Cyclotron Resonance Heating – ECRH

The Electron Cyclotron Resonant Heating consists in sending a wave in the electron cyclotron frequency range – defined as (Ω_{ce}=e.B_0/m_e Є 100→200GHz) with e the elementary charge, B_0 the magnetic field and m_e the electron mass – which the electromagnetic field will accelerate electrons that rotate around magnetic field lines at the same frequency [Westerhof 2008]. First thing to notice is because the magnetic field is inversely proportional to the radius r, so does particles gyrofrequency, which can be rewritten such as $\Omega_{ce}(r) = \alpha.e/m_e.r$. This means that the position of the resonance can be controlled either by adapting the magnetic field or using gyrotrons with different frequencies. Moreover, the higher the frequency, the smaller the wavelength in vacuum the antenna ($\Delta L \simeq \lambda = c/f$), which is another advantage of ECRH antennas which can be small since the wave propagates in similar fashion as an optical beam. The wave can even be conveniently reflected on mirrors, allowing selecting different incidence angles and playing with this obliquity to drive current. As it is written on Fig.1.5, a gyrotron is used to generate such high frequency waves and can deliver several MW power. Since ECRF wave freely propagates in vacuum, there is not difficulty to couple them to the plasma unlike waves in lower hybrid or ion cyclotron range of frequencies. With such power that can be conveniently sent and absorbed in very precise locations, ECRH is a very efficient system not only for heating plasma or driving current, but its numerous assets are also very useful to control plasma [Stober 2012] during the start-up phase, and even treat MHD

instabilities such as:

- Sawteeth modulations [A. Mück 2005]; quasi-periodic relaxation that is commonly observed in the core plasma near q=1 surfaces and causes a sudden drop in the temperature and density in the center of the plasma.
- Neoclassical Tearing Modes [F. Felici 2011]; a metastable mode and formation of a "seed island" triggered by a sufficiently large deformation of the bootstrap current and which can grow and lead to degraded confinement or ultimately disruption.

  The bootstrap current is a Neoclassical toroidal current produced in the presence of a pressure gradient, associated with the existence of trapped (banana) particles in toroidal magnetic confinement systems. These trapped particles must be able to complete their (banana) orbits, so a requirement for the existence of the bootstrap current is $\nu_{ei} < \nu_b$ (the collision frequency is less than the banana bounce frequency). The difference in particle density on banana orbits crossing a given radial position r then leads to a net toroidal current at r. The bootstrap current is estimated (roughly) as [Miyamoto 2005]

$$j_b \approx -\sqrt{\frac{a}{R}}.\frac{1}{B_p}\frac{dp}{dr} \qquad (1.4)$$

Here, a/R is the inverse aspect ratio, B_p the poloidal magnetic field, and p the pressure. More precise estimates can be made by simulating particle orbits. Finally by depositing power at the center, ECRH can also prevent impurity accumulation in the core [Sertoli 2017]. For these reasons, ECRH could for instance be used in WEST to cure core contamination by impurity, while it is envisaged as the first heating system to be implemented on ITER, with 24 gyrotrons of 1MW.

1.2.3 Lower Hybrid Current Drive – LHCD

Lower Hybrid frequencies ($\omega_{LH} = [(\Omega_{ci}.\Omega_{ce})^{-1} + \omega_{pi}^{-2}]^{-1/2} \sim$ few GHz) are in between electron and ion cyclotron frequencies with ω_{pi} the ion plasma frequency. They are generated by klystrons capable of delivering several kW each. Several klystrons are added in parallel to generate high power LH waves, separated on different wave guides until the grill where they enter the plasma [Ignat D.W. 1981]. Those waves are evanescent under relatively high densities ($\sim 7.10^{17} m^{-3}$), which makes their coupling quite difficult since grills cannot be positioned that close to the plasma

where they would suffer from excessive heat loads. Gas puffing is used on several devices to locally increase densities in front of grills [Ekedahl 2009], and keep them far enough from the plasma. Thanks to their large parallel electric field, LH waves also have the interesting property of – Landau – damping very efficiently at high parallel phase velocities to the electron thermal speed ($v_{||} \geq 2.5 v_{te} = 2.5(T_e/m_e)^{1/2}$). They are consequently able to drive current in the plasma periphery where electrons temperature is lower (off-axis), allowing good control of plasma current profile. Nevertheless the current that LH waves can drive non-inductively is not sufficient to sustain all the plasma current with acceptable recycled power. The idea is then to use it mainly for shaping current profiles, building internal transport barriers and access attractive steady-state operations with high bootstrap current. ITER should enable to reach more than70% of bootstrap current, with high β_N (=Thermal pressure/Magnetic Presure~3) and good confinement [ITER]. The magnetic pressure is an energy density associated with a magnetic field. Any magnetic field has an associated magnetic pressure contained by the boundary conditions on the field. It is identical to any other physical pressure except that it is carried by the magnetic field rather than (in the case of a gas) by the kinetic energy of gas molecules. A gradient in field strength causes a force due to the magnetic pressure gradient called the magnetic pressure force.

1.3 Ion Cyclotron Resonance Heating system - ICRH

ICRH such as ECRH consists in sending waves in the plasma which going through damping will convert its electromagnetic energy into ions kinetic energy. Ions being much heavier than electrons though, their gyrofrequency is much lower ($\Omega_{ci}=q_i.B_0/m_i$). *Tetrodes* are capable of producing waves in this range of frequencies (10→100MHz) [Dumortier 2015]. Once generated, waves are conducted into *coaxial lines* towards the tokamak, where they will be coupled to the plasma by *antennas*. Note that their wavelength is like the tokamak size, of the order of several meters ($\Delta L \simeq \lambda = c/f$), making both their transport and coupling to the plasma – detailed in the following part – very tricky problems since we cannot imagine antennas that would be as big as the tokamak itself. As can be seen on Fig.1.7 below, if the antenna is not well matched with the plasma (which must be optimized with the *matching system*), the wave is not well coupled, therefore reflected back in direction of the generators, which could induce severe damages on the tetrodes. A *stub tuner* can also

be used like in EAST, in order to adapt antenna impedance with the one of the plasma, and to prevent the reflected power to reach and damage the generators by reflecting most of it back towards the antenna. Otherwise the *service stub* which is a transmission line of length λ/4 connected to a load, with λ the ICRF wavelength, like in WEST. These safety systems are essential, thus those multi-reflections give rise to a standing wave with very high voltages, which if overcome a critical value may threshold arcing, damaging the system. We will now detail the key steps of ICRH process, namely waves coupling and absorption in the plasma.

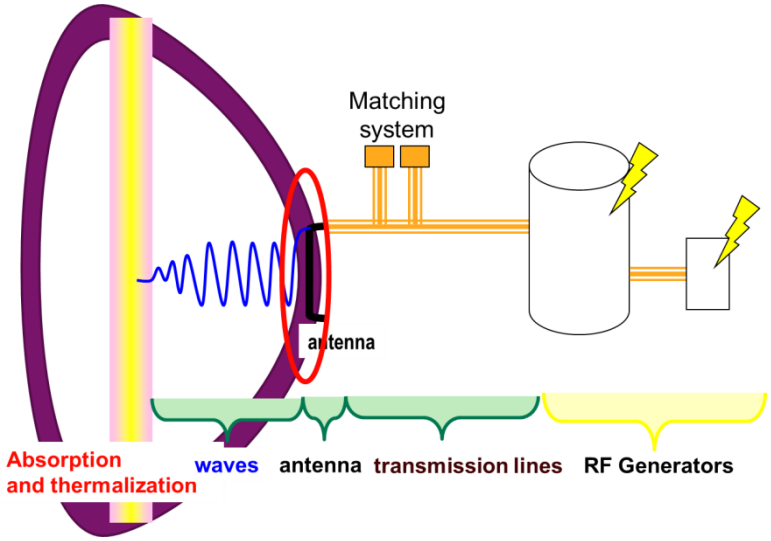

Figure 1.7: Illustration of a typical RF system with waves emitted by generators and carried by transmission lines up to antennas radiating under plasma, and wave propagate up to a resonance layer were they can be absorbed by charged particles

1.3.1 Waves Coupling

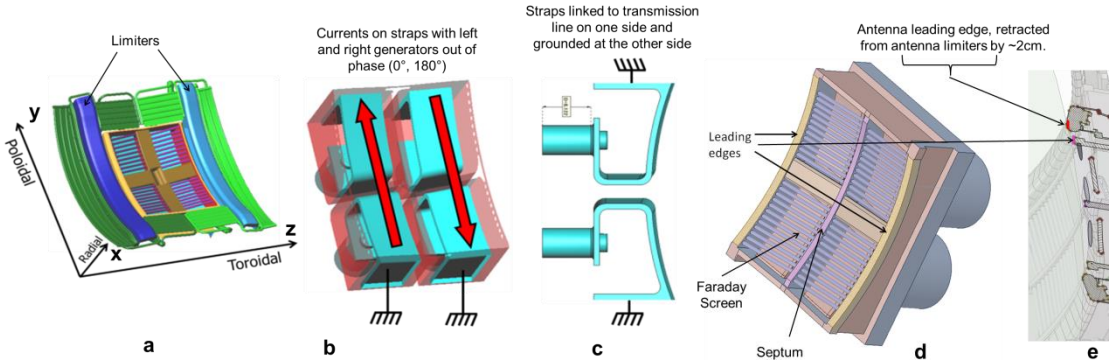

Figure 1.8: Example of ICRF antenna geometry (WEST-like) with the straps (c), the Faraday screen, the septum (d) and the limiters (a) with a poloidal cut of all

components (e). Key geometric dimensions are defined. Currents are represented on the straps of the antenna (b) and represent a case of most used dipole phasing (0, π).

ICRF waves are excited by *current straps* in the antenna (Fig.1.8c). Those are typically about 50cm high (L_{strap}) for 10cm large (δ_{strap}) and are positioned almost perpendicularly to the total magnetic field [Dumortier 2015] (Fig.1.8a). The distance between the straps also plays an important role for the wave spectrum excited (Fig.1.9). Current J_{ant} flows in the strap according to the poloidal direction and consequently excites mainly the poloidal electric field (Fig.1.8b) parallel to waves trajectories over a gyroperiod. This can also be seen as a voltage V_0 proportional to the current J_{ant} and applied from the transmission line on one side of the straps, and grounded on the other side (Fig.1.8c). The ICRF wave is a plane wave that can be characterized by its frequency ω close to Ω_{ci}, its refractive index n, its amplitude and phase (between two straps). Those are usually condensed in the form of a triplet ($\boldsymbol{k}$, E, B) composed of the wave vector ($\boldsymbol{k}$=n.ω/c) and both electromagnetic field components. From those parameters can be deduced its propagation properties and this will be done in the next chapter. We will see that if the plasma parameters are favorable, the wave can propagate normally until the plasma core where it can be damped to ions thermal velocity, else it may either vanish or be reflected. The *coupling resistance* R_c (Ω/m) is an indicator of the efficiency of this process [Louche & Koch 2015]. It can be estimated from voltage and current probes measurements in transmission lines (U, I), and φ the phase difference between voltage and current signals measured by a phase detector. The coupling resistance can then be calculated as follow:

$$R_C = \left(|U|/|I|\right).\exp(i\phi) \tag{1.5}$$

The bigger the coupling resistance, the more power P_t can be transferred to the plasma as can be seen on the following formula:

$$P_t = R_C.L_{Strap}.J_{ant}^2/2 \tag{1.6}$$

In practice, the key parameters to play on to optimize the coupling efficiency are the wave vector ($\boldsymbol{k}_{||}$=$n_{||}$ω/c) and the phase between straps. For instance in the case of a four straps antenna we can represent the normalized coupling resistance - proportional to the power spectrum P_t – in function of the wave vector for different phases. It can

be seen on Fig.1.9, that the highest values of $\boldsymbol{k}_{||}$ are obtained for the *dipole phasing* (0, π) corresponding to the case in Fig.18b and the blue curve in Fig.1.9. Nevertheless its corresponding maximum values on the spectrum are relatively low compared to other phases, which will make its coupling harder. Note also that its spectrum is symmetrical so it can be used to heat the plasma. We will see on the next part that the bigger wave vector is, the better the absorption. Others phasing such as (0, π/2, π, 3π/2) or (0, -π/2, -π, -3π/2) lead to non-symmetrical spectrums, meaning the power is deposited asymmetrically in the plasma, which can be used to drive current. M*onopole phasing* (0, 0, 0, 0) was not represented on the left graph since its low $\boldsymbol{k}_{||}$ modes (also called coaxial modes) are an order of magnitude above others phases – as can be seen on the right graph – so that information would be hard to extract from the graph.

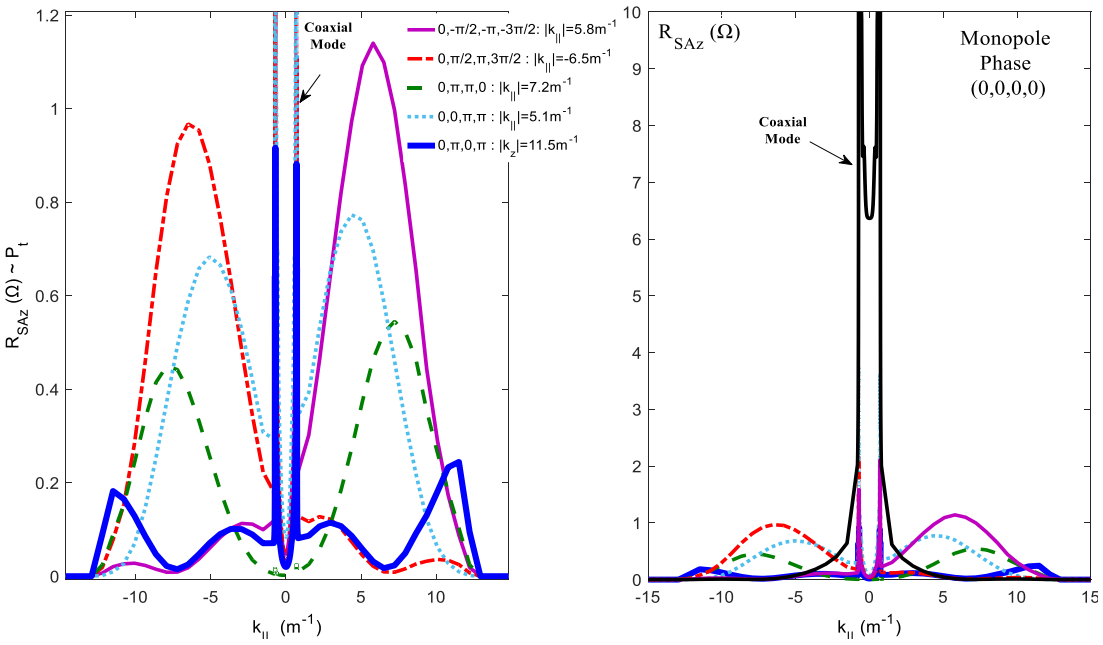

Figure 1.9: Power spectrum in function of the parallel wave vector for different phases of an EAST-like 4-strap antenna. Monopole phasing case is represented separately as its coaxial modes (black peaks) grow high compared to other phases.

We will see in the next chapter that the reason why ICRF waves are so hard to couple is because like LH waves, to propagate normally they need to reach a minimal density (~10^{18}m^{-3}) bellow which they are evanescent. From this assumption we can already imagine a very simple model represented on Fig.1.10, on which an electric field E_0 excites a wave (E_i, k_v) with k_v the wave vector components in the directions

perpendicular to the magnetic field (parallel direction close to the toroidal direction in Fig.1.8a) in the evanescent region of width δ_{ev}, so a part of the wave manages to tunnel through this layer and reach the region where it can propagate (E_t, k_p) while another one is reflected back (E_r, k_v). In a Cartesian frame (x,y,z) like in Fig.1.8a, all RF quantities are assumed to oscillate as $\exp(-i\omega_0 t+ik_z z)$, where ω_0 is the wave pulsation, z is the direction of the confinement magnetic field in a flattened tokamak and $\boldsymbol{k}_z$ is the characteristic parallel wavevector. Wave propagation is investigated along direction x, representative of the radial direction in our slab approximation, i.e. plane wave amplitudes vary with x only. For the sake of simplicity the RF electric field **E** is assumed purely transverse to z, with a polarization along direction (x,y). This situation is representative of the Fast magnetosonic wave in a tokamak environment when the poloidal wave vector is null ($\boldsymbol{k}_y$=0). Space is divided into two separate zones. The RF wave is assumed evanescent in the region x<0, i.e. we postulate that the complex RF electric field amplitude E_y transverse to x can be described by the equation

$$\partial_{xx}^2 E_y - k_v^2(k_z)E_y(x) = 0 \quad ; \quad x<0 \tag{1.7}$$

Where $k_v^2(k_z)$ is implicitly assumed real positive. Similarly the RF wave is propagative in the region x>0 and obeys the equation

$$\partial_{xx}^2 E_y + k_p^2(k_z)E_y(x) = 0 \quad ; \quad x>0 \tag{1.8}$$

With $k_p^2(k_z)$ assumed real positive.

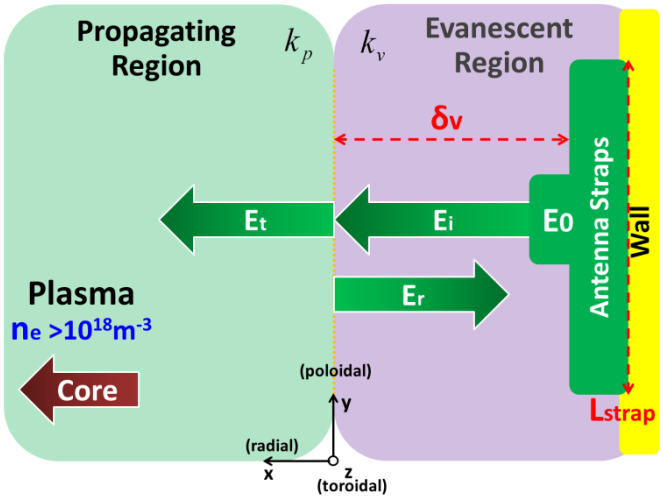

Figure 1.10: Illustration of a simple model
of wave propagation in the plasma periphery

Power carried by each wave can be assessed by the pointing vector representing the directional energy flux (the energy transfer per unit area per unit time) of an electromagnetic field and defined as $P_x = \mathrm{Re}(E \times H^*)_x = \mathrm{Re}(E_y \times B_z^*)/\mu_0$. Then writing the power conservation at the interface between both domains, we get:

$$P_t = P_i - P_r = \frac{E_0 E_0^*}{\mu_0 \omega} . \frac{4k_p \left|k_v^2\right|}{\left|k_p^2\right| + \left|k_v^2\right|} \exp(-2\left|k_v\right|\delta_v) \propto \exp(-2\left|k_v\right|\delta_v) \qquad (1.9)$$

By analogy with eq.1.5 we can write:

$$R_C = \left(2 / L_{Strap} J_{ant}^2\right).P_t \propto \exp(-2\left|k_v\right|\delta_v) \qquad (1.10)$$

From this last relation, it appears clear that the coupling resistance decreases exponentially both with the evanescent length and the wave vector module.

1.3.2 Waves Absorption

Once the wave reaches the region where the density is high enough, it starts propagating normally until reaching positions where it can resonate and damp its electromagnetic power on surrounding ions. ICRH tends to create high-energy tails in the distribution function of the heated particles. For heating at the *n*-th cyclotron harmonic, the diffusion coefficient is of the form:

$$D \propto \left|J_{n-1}E_+ + J_{n+1}E_-\right|^2 \approx \left|J_{n-1}\frac{k_\perp v_\perp}{\omega_s}\right|^2 \left|E_+\right|^2 \qquad (1.11)$$

where E+ and E- are, respectively, the left-hand and right hand components of the electric field:

$$E_+ = (E_x + iE_y)/2\,; \quad E_- = (E_x - iE_y)/2 \qquad (1.12)$$

Ions *absorb* the energy of the wave. Various scenarios can rely on many different mechanisms of absorption [Louche & Koch 2015] [Kazakov 2015] :

- ***Fundamental resonance*** ($\omega_0=\Omega_{ci}$): Wave electric field rotates at the same frequency as surrounding ions which are consequently accelerated.

$$D_0 \propto K\left|E_+\right|^2 \qquad \text{with K a constant} \tag{1.13}$$

This kinetic energy is then redistributed to other ions through collision process and the bulk plasma heats up. Besides, notice that this technique cannot be used in case of single ion species plasma since the wave electric field rotates in the opposite side as the ion gyromotion, so that no energy can be transferred. This is the *screening effect* and can be understood by writing the wave polarization as a function of plasma particles gyrofrequency:

$$\left|\frac{E_+}{E_-}\right| \approx \left|\frac{\omega_0 - \Omega_{ci}}{\omega_0 + \Omega_{ci}}\right| \approx \left|\frac{N\Omega_{ci} - \Omega_{ci}}{N\Omega_{ci} + \Omega_{ci}}\right| \tag{1.14}$$

One understands that in a plasma with only one ion species i, at the ion cyclotron resonance, heating the fundamental N=1 does not work because the resonant wave component is absent (left-hand polarized component of the wave E_+ vanishes). This will be rigorously demonstrated in the next chapter. For this reason fundamental can be used only on *multiple species plasmas*, and lead to the so called *ion-ion hybrid* (or Buchsbaum) *resonance*.

- ***Harmonics resonance*** (ω_0=N.Ω_{ci} with N an integer higher than 1) consists in sending waves at frequency multiple of the fundamental. Absorption occurs when the wave reaches a region where its frequency is a multiple of ions gyrofrequency. One advantage is that it can be used to heat a single species plasma since the polarization of a harmonic wave in the direction of ion rotation is not null (no screening effect). Yet, another problem at constant polarization is that over its gyromotion, ion is equally accelerated and decelerated, so that on average, no energy is transferred. This problem is overcome by sending waves with inhomogeneous electric field, so that the acceleration phase can be made stronger than the deceleration one. This method can be used with relatively good efficiency for low values of N, thus it can be shown expressing the quasi-linear diffusion coefficient of the N^{th} harmonic that it decreases exponentially with N [Koch 2015]:

$$D_N \propto \left|\frac{k_\perp v_\perp}{\omega_s}\right|^{2(N-1)} \left|E_+\right|^2 \tag{1.15}$$

Pay special attention on the distinction between wave screening effect at the fundamental on a single ion specie plasma and balance between acceleration

and deceleration over a gyroperiod. Both mechanisms are totally different, so that playing on the inhomogeneous character of the electric field would never allow heating single ion specie plasma at the fundamental.

- ***Minority Heating*** consists in having a plasma composed of several ions species with one in significantly smaller amount (<10%). The fact of having several species brings up another key phenomenon for ICRF called *ion-ion hybrid resonance*. Moreover, dynamic being dictated by the majority specie, waves sent with frequency corresponding to the minority specie fundamental (Ω_{ci}) are not screened anymore (eq.1.14). Damping now occurs in the zone between each specie resonance surface. The minority ions receive the energy from the wave and spread it to others species by collisions. In practice ${}_1^1H$ is often used as minority with ${}_1^2D$ in majority. The *three-ion scheme* also consists in heating the fundamental of a minority whose resonance location falls in the ion-ion hybrid resonance range of both others majority species [Kazakov 2017], where the amplitude of the left-handed polarization can reach very high values.

- ***Majority Heating*** consists in heating the majority specie (>90%). This one also dictates the dynamic of the plasma, so that sending waves at the fundamental is not appropriate since large amount would be screened as mentioned previously. In this scenario, better efficiency is reached by sending waves at a harmonic of the majority specie gyrofrequency (eq.1.15). To further maximize the absorption, it can also be useful to create a population of fast ions, either by accelerating them with ICRH which can take some time, or inject them with NBI [Lerche 2019].

- ***Landau Damping*** is a non-collisional mechanism belonging to the kinetic theory of plasma waves, which means the condition of resonance does not only depend on the wave vector $\boldsymbol{k}$ and frequency ω but also on the particle speed v; it can be written $v = \omega/\boldsymbol{k}$. In the kinetic theory, particles energy distribution function is considered, so that a certain number of particles slower than the wave will feel acceleration while faster ones are to the contrary decelerated. The efficiency of this process is consequently based on a population of particles slower than faster ones. This is not the case of ions. But

electrons which are almost always maxwellian, can benefit from this process, mainly used by LHCD to drive off-axis currents where electrons are slower.

- ***Transit Time Magnetic Pumping*** is conceptually the same as Landau damping except that the energy transfer is not based on the electric field of the wave but on it magnetic component. It can also be seen as a Doppler shift.

- ***Mode conversion*** is the process by which a given wave spectrum (Fig.1.9) changes. Modes can be characterized by the excitation of particular values $\boldsymbol{k}_{\parallel}$, however, if the wave front meets discontinuities in the plasma, either surfaces with strong variations in the magnetic equilibrium or in densities, plane waves can be scattered and give rise to the excitation of others $\boldsymbol{k}_{\parallel}$ modes which propagation properties and absorption mechanisms can be very different and used in some scenarios.

Note that one can now imagine many heating scenarios combining those mechanisms. This constitutes a field of research particularly important for future devices, on which a single frequency could for instance at the same time heat the fundamental of the minority specie and a harmonic of the majority (ex: He^3-T, H-D, and three ions species [Lerche 2019]).
Several others interrogations might emerge from this brief introduction, but they will not be treated in further details since it would take us too far out of the scope of this thesis.

To evaluate the quality of the absorption, we talk about *single pass absorption*. It represents the percentage of power that can be absorbed when the wave crosses the bulk once (Fig.A4). Different scenarios lead to different absorption efficiencies, the optimal case being full single pass absorption, so that there would be a minimal number of reflections of the wave against the right cutoff at the edge ($R=n_{//}^2$), and consequently a minimum of power losses in the periphery and on Plasma Facing Components (PFCs).

1.4 Plasma Edge Sheaths

Sheaths constitute one of the biggest challenges in plasma periphery since they arise as magnetic field lines intercepted any Plasma Facing Component (PFC)

[Chabert 1969]. Simply because of mass difference ($m_e << m_i$), electrons accumulate faster than ions on PFC surface, forming a negatively biased layer that repulses electrons and attracts ions (an illustration of the process available on Fig.2.1). This can result in the formation of a positively biased layer in front of PFC surface, essentially populated by ions and only few Debye lengths thick (few millimeters);

$$\lambda_{De} = \sqrt{\frac{\varepsilon_0 k_B T_e}{n_e e^2}} \qquad (1.16)$$

with ε_0 the vacuum permittivity, k_B the Boltzmann constant, T_e and n_e respectively the electron temperature and density, typically few eV and about $10^{18} m^{-3}$ in a tokamak edge plasma. The separation of charges over this short layer naturally results in a big drop of the potential of the plasma with respect to the ground; the one also enables to equilibrate charged particles fluxes, by stopping electrons with too small energy and accelerating ions towards the wall, so that *ambipolarity* (quasi-neutrality) is preserved. Nevertheless, such equilibrium is reached at the cost of an increase of ions energy while flying across the sheath electric field. Over these accelerations, their sputtering yield increases, and beyond some critical value, ions become dangerous projectiles. The sputtering yield Y_{eff} of a given ion on a given material is the efficiency by which an ion with a given impact energy on a surface made of a given material can sputter an atom out of the solid structure. This can be simply be written as $Y_{eff} = \Gamma_{in} / \Gamma_{out}$ with Γ_{in} the incident ion flux on the material and Γ_{out} the outer flux of atoms sputtered from the material. This will be further explained in the next chapters. Ions collide with heavy metal atoms, and over long periods, slowly modify PFC structure by displacing atoms, creating interstices, clusters and dislocations. Those effects not only have microscopic consequences on material properties – melting point, conductivity, mechanical strength – but they might also lead to void swellings which is a macroscopic dilatation of the material, and this could be faithful to a machine designed for economical purpose. Another critical and more immediate consequence of sheaths is if an atom is directly kicked-out from the structure. In this case, a high-Z atom (as tungsten and molybdenum which are favorite candidates to build vacuum vessels) is released into the plasma. As it moves from the edge deeper in the plasma, temperatures rise, and so do collisions frequencies. The atom will then be several times ionized, so that it ends up in the core sometimes after having been through more than twenty ionization states. Those are the so called *high-Z impurities* [Dux 2007], they badly decrease plasma performance by radiating energy that will not contribute

to fusion reactions.

Moreover, we will see in the next chapter that ICRH also plays an important role in the problematic of sheaths. Because the coupling of the wave is never perfect, a parasitic mode is excited, giving rise to a wave (called *slow wave*) with a high electric field component parallel to magnetic field lines (green arrow on Fig.2.1). The electric field of this wave will contribute to increase even more the electric field already existing across the thermal sheath. The process by which ICRF waves enhance sheath electric fields is the *RF-rectification* [Colas 2007] which theoretical aspects are addressed in the next chapter. At this point it is of prime importance for this thesis to have in mind that ICRH can play an important role in impurities production, which has been extensively studied experimentally and confirmed by simulations.

1.5 Thesis outline

This thesis takes place among other experiments involving ICRF to heat tokamak plasmas, either aiming at maximizing ICRF coupling efficiency or related to the characterization of RF sheath influence on the impurity production. The work is presented according these two topics which were studied experimentally in both EAST and WEST tokamaks and benchmarked with complementary simulations. One difficulty of this topic comes from the fact that despite peoples' experience, most of us keep expecting ICRH to behave somehow gently in some regime allowing simultaneously to optimize wave coupling and mitigate impurity production. These aspects are however matter of trade-off governed by undutiful combination of non-linear processes, making any conclusion actually pretty sensitive to a wide set of parameters which cannot systematically be checked and are therefore often wrongly assumed to have negligible influence. Another aspect is that ICRF life becomes easier as the machines get larger. Big difficulty of nowadays tokamaks is that they are either small with respect to ICRF wavelength and energy deposition, either not designed in order to optimize scenarios with ICRF, which numerous requirements are not particularly challenging technologically but require very high level of anticipation and communication between RF physicists and engineers who do not always speak the same language and whose short term goals often appear hard to conciliate. Making bigger devices like JET, ITER or CFETR will improve the confinement of particles and energy, and allow benefiting from more favorable regimes than what can

be done in medium size tokamaks like EAST and WEST. In this work we will try our best to fix as many parameters as we can and explore different regimes and scenarios to hopefully extract information on optimal settings, relevant for more than only one tokamak, and try to extrapolate them up to future devices.

- **Chapter 2** introduces key approximations to allow simplifying the model and use Maxwell's equations, to assess ICRF wave properties. Thermal then RF sheath theories are then presented before explaining how it plays a key role for impurity production. It is finally shown how theory can be used in codes to simulate phenomena which ideally have been observed experimentally or which could be measured if the appropriate diagnostics were available.
- **Chapter 3** summarizes the experimental context of the thesis
- **Chapter 4** presents the experimental setup composed of EAST and WEST tokamaks, each having its peculiarities, but both having two ICRF and LH antennas and many diagnostics in common. Each tokamak is described along three axes comporting a general description, a more detailed description of the ICRF system and finally of the fueling methods. Details are finally given on Langmuir probes and spectrometers which have been extensively used in both devices.
- **Chapter 5** first recalls some methods to optimize ICRF coupling such as minimizing the distance strap-cutoff layer, increasing the plasma density, increasing wave frequency, and the influence of different local gas injections in both devices in scenarios with additional LH power. By injecting gas locally, it is shown that LH power can help increasing ICRF coupling most likely by increasing density at the edge. Finally it is found that injection at the mid-plane is the best fueling option to improve waves coupling.
- **Chapter 6** localizes and characterizes impurity sources related to ICRH. Different approaches are used in both tokamaks which are equipped with different materials and diagnostic; while WEST is a full-tungsten environment with visible spectroscopy allowing local and accurate characterization of impurity sources, EAST has plenty of materials differently connected to ICRF antennas but can only use UV spectroscopy to measure impurity in the core and extract relatively local information on where an interaction most likely took place.

- **Annex** contain further elements that are more or less important for the understanding of the thesis depending on lectors knowledge. Since the thesis will mostly focus on experiments, simulation results and brief descriptions of the codes can be found in the Annex. Overviews of several discharges used in the thesis are also provided. Finally, we provide elements in favor of a possible analogy between infrared and spectroscopic observations in RF environment, I hope these preliminary observation will inspire dedicated experiment to rigorously enlighten this idea.

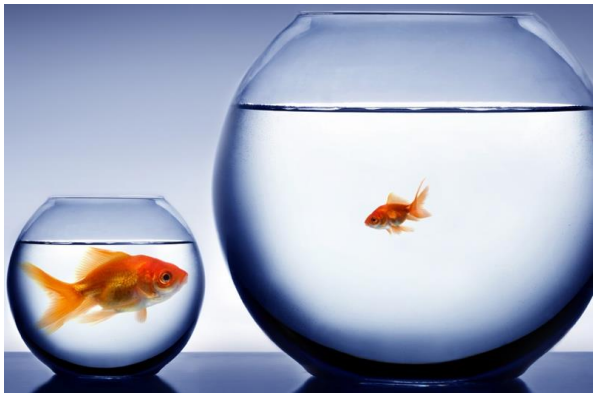

Life becomes easier as the machine get larger

2. Theory of ICRF waves and interaction with plasma

To help the lector visualize the plasma structure on the zone of interest for this thesis, the sketch in Fig.2.1 below was drawn. Physical process by which Slow Wave (SW) leads to the formation of a Radio-Frequency (RF) sheath, across which potential drops, enhancing ions sputtering yield and impurities release, is represented on this figure and will be extensively discussed in this chapter. Equations describing waves' propagation in plasma (which an excellent overview can be found in [Louche & Koch 2015] and references therein) and RF sheaths processes [Chabert 1969] will be successively addressed bellow and solved in particular cases of interest.

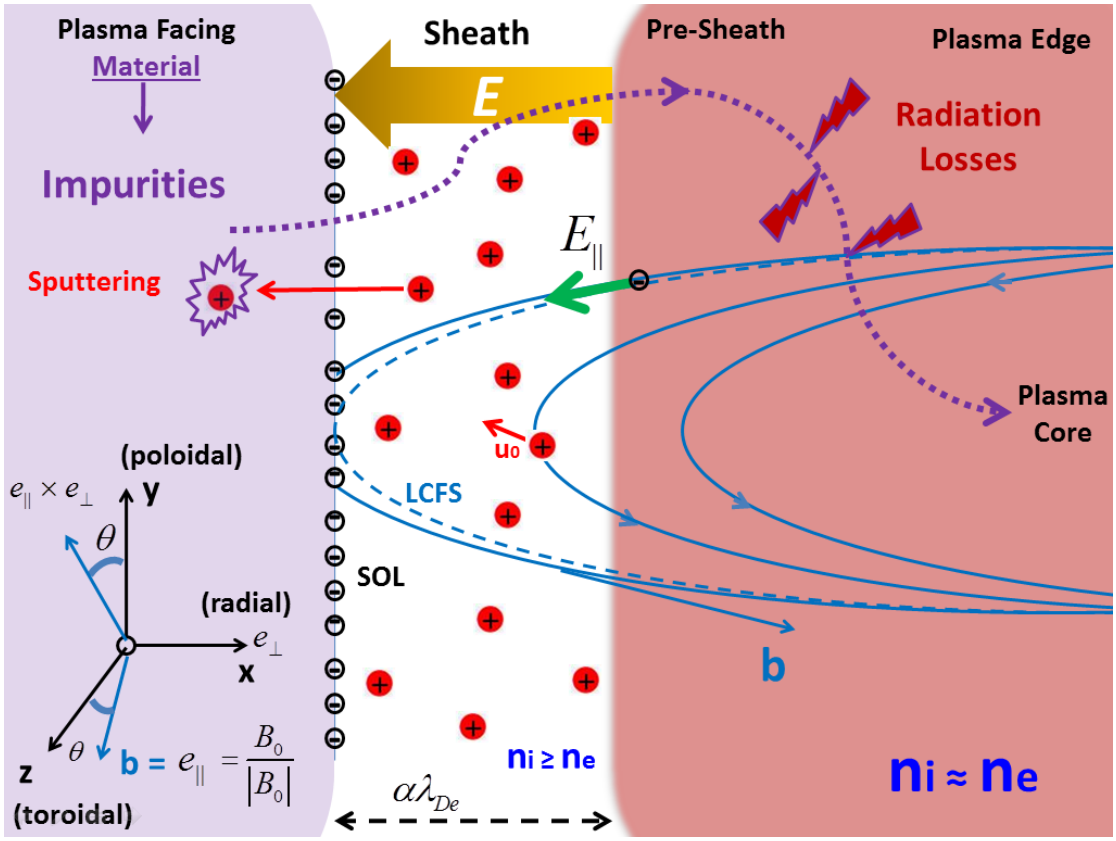

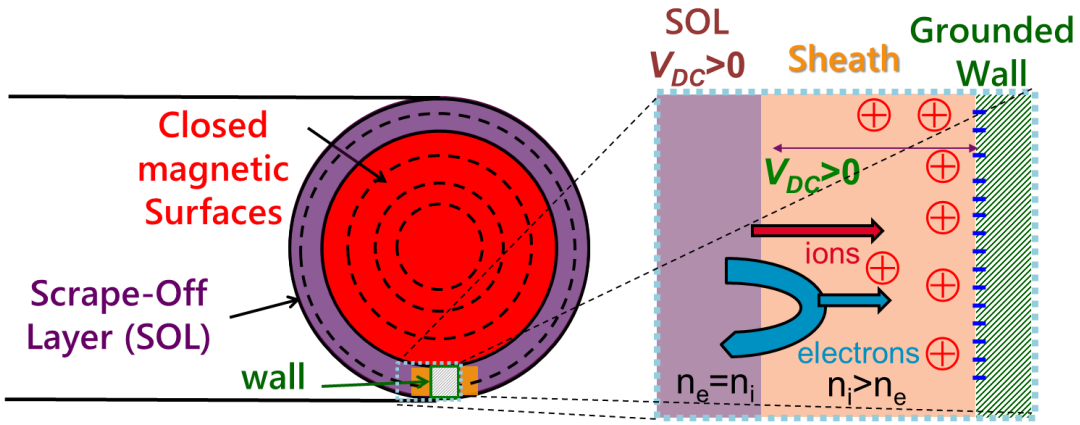

Figure 2.1: Tokamak plasma border illustration;
Conducting metal object is on the left (purple zone), RF sheath plasma is the center white part which width is a few Debye lengths(λ_{De}), and the plasma bulk is on the right side (pink zone)

Since this thesis investigates the influence of high-power waves on tokamaks periphery, the understanding of how waves propagate in the plasma and how they interact with plasma facing components (PFCs) is of prime interest. On the Fig.2.1, we see that confining magnetic field lines (represented in blue) are mostly closed, but a few of them are opened and reach material surface. It exist a Last Closed Magnetic Surface (LCFS) represented by the dashed blue line, which represents the frontier between the well-confined plasma bulk and what is called the Scrape-Off Layer (SOL), region where all magnetic field lines are opened and intercept a PFC. Ion Cyclotron Range of Frequencies (ICRF) antennas are typically inside the SOL, such that limiters intercept many magnetic flux tubes. Maximizing the coupling efficiency of ICRF waves to the plasma consequently implies to deal with this SOL region. Several designs using different kinds of materials have been tried, thus in spite of all efforts to solve problems in the SOL, it seems that they merely can be minimized, trading-off between good coupling efficiency and robustness of the structure exposed to SOL plasma.

ICRF waves are mostly Fast Waves (FW) with a radial electric field ($E_{\perp}$) that propagate until the core where they can give their energy to particles undergoing damping process. Thus some ICRF waves are also parasitically launched with an electric field component parallel to the magnetic field lines ($E_{\parallel}$), those are known as Slow Waves (SWs). Notice that another referential (blue) was introduced to the

bottom left of the Fig.2.1. This one takes into account the fact that the magnetic field is tilted of an angle θ compared to the toroidal direction. When such SWs propagate in the SOL, they locally create strong electric fields along magnetic field lines – as represented by the green arrow on the Fig.2.1 – to which charged particles react. Nevertheless electrons being much lighter than ions ($m_e << m_i$), they react faster and accumulate on the surface of PFC. Ions are then attracted in order to balance fluxes ambipolarity, which basically means to keep the plasma macroscopically neutral. We consequently end up with lots of negative charges on one side and a cloud of positive charges on the other side, which results in a strong potential drop across a region only large of few Debye lengths (order of millimeter), called the *Sheath*. This leads to a strong electric field (E_{RF}) represented by the big orange arrow on the Fig.2.1, the one contributes to strongly accelerate ions, increasing their sputtering yield, which has consequences on impurities production.

2.1 Approximations

Let's remind that if the lector feels confused about any notation used below, he (she) is welcome to take a look back to Fig.2.1 into which most important actors of the key processes we are about to discuss are represented and their meaning explained right after. Now in front of such a complicated state as the plasma, we need to make numerous approximation in order to perform calculations in simplified – though not always simple – cases. Each approximation is preliminary introduced and justified bellow:

1) Fully ionized plasma → Free charges (neutrals neglected)
2) Cold plasma → Effects of first order perturbed kinetic pressure are negligible when compared to perturbed magnetic forces such that everything happens as if $T_e \approx T_i \approx 0$ eV.
3) Collisionless plasma → Thermal dissipation by binary collision neglected
4) Charge ambipolarity → Quasi-neutrality: $n_0 \approx n_{e^-} \approx n_{ions}$
5) ICRF wave monochromatic ($\partial / \partial t \xrightarrow{Fourier} -i\omega$) and planar ($\nabla \xrightarrow{Fourier} ik$), ω and k being respectively the *wave pulsation* (ω=2πf) and the *wave vector*.
6) Electrons follow a Maxwellian distribution

7) Fluid immobile in the absence of wave → $v_s = \delta v_s$ (small fluid perturbation caused by the wave),
v_s being the speed of species s; in fully ionized plasma s can either be an ion i or an electron e

8) No static electric field in the plasma → $E = \delta E$

9) Total magnetic field is the superposition of confining and wave magnetic fields → $B = B_0 + \delta B$
Note that terms with δ correspond to very small perturbation (ex: $\delta B << B_0$)

10) No current source → $j_{ext} = 0$ (wave is studied as coming from infinity, no antenna considered)

It is worth listing all approximations to really take conscience of how many simplifications we made to bring expressions into a mathematically appreciable state. This gives a small idea of how complex is the plasma and how complicated it may become – not even thinking about taking everything into consideration – but only if we went further in the plasma core where already several approximation do not hold anymore.

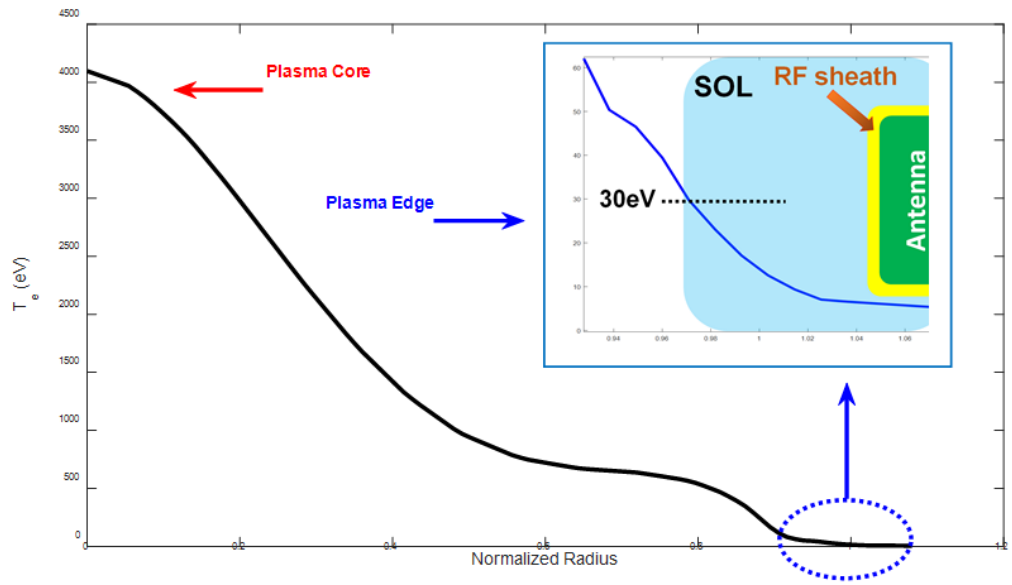

Figure 2.2: Typical temperature profile of a plasma in EAST (Shot n°62946 with 2.6MW LH, 1MW ICRF and 400kW ECRF) showing that we can reasonably make a cold plasma approximation at the edge

2.2 ICRF waves in the plasma

In order to visualize from the beginning the philosophy of the calculations we are going to do now, the Fig.2.3 represents the mains blocks and the coherence between them that will guide us all along.

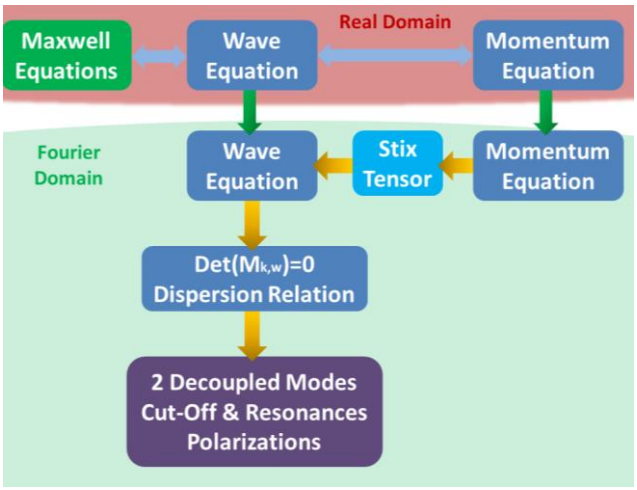

Figure 2.3: Illustration of the following ICRF waves theory calculations

2.2.1 Dispersion Relation

Now we just have to follow the scheme on Fig.2.3, making the appropriate simplifications quoted in section 2.1, and using coordinates systems established on Fig.2.1. We start by writing respectively the *Faraday and Ampere Maxwell's equations*:

$$\nabla \times E = -\frac{\partial B}{\partial t} \tag{2.0}$$

$$\nabla \times B = \mu_0 J + \frac{1}{c^2}\frac{\partial E}{\partial t} \tag{2.1}$$

Where c is the speed of light. We then take the rotational of the eq. 2.0 and commutate time partial derivative with rotational and substituting the rotational of the magnetic field by eq. 2.1, we get the *wave equation*:

$$\nabla \times \nabla \times E + \frac{1}{c^2}.\frac{\partial^2 E}{\partial t^2} = -\mu_0 \frac{\partial}{\partial t}(J + J_{ext}) \tag{2.2}$$

According to the 10th approximation $J_{ext}=0$. Then doing the transformation into

Fourier space according to the 5th approximation, and apply the perturbation method according 8th approximation we get:

$$k \times k \times \delta E + \frac{\omega^2}{c^2}.\delta E = i\omega\mu_0 J \tag{2.3}$$

Since J is a function of δE, it is actually non-linear. *Ohm's law* already provides a linear relation between J and δE:

$$J = \bar{\bar{\sigma}}.\delta E \tag{2.4}$$

$\bar{\bar{\sigma}}$ is the *linear conductivity tensor*. We can now rewrite eq. 3.3 only in function of the electric field by substituting J using Ohm's law and use $\varepsilon_0.\mu_0 = 1/c^2$:

$$\begin{aligned} k \times k \times \delta E + \frac{\omega^2}{c^2}\left(1 + \frac{i}{\omega.\varepsilon_0}\bar{\bar{\sigma}}\right)\delta E = 0 \\ k \times k \times \delta E + \frac{\omega^2}{c^2}.\bar{\bar{\varepsilon}}.\delta E = 0 \end{aligned} \tag{2.5}$$

The term in parenthesis was casted into one single tensor $\bar{\bar{\varepsilon}}$ which divided by the vacuum permittivity becomes the *cold dielectric tensor* also known as *Stix tensor*. Now we need to find a way to express the linear conductivity tensor, and we will proceed by analogy between the eq. 2.4 and another relation we have to write. Let's start with the *current definition*:

$$J = \sum_s J_s = \sum_s n_s q_s v_s \tag{2.6}$$

According to the 1st hypothesis, s can either be an ion or an electron. Moreover according to the 4th approximation of quasi-neutrality, $n_0 = n_{e-} = n_{ions} = \sum_s n_s$. The charge q_s can either be +e or –e respectively for ions or electrons (e being the elementary charge e ≈ 1,6.10^{-19}C). Most work has to be done on v_s. This is time to use the 2nd hypothesis and start considering the plasma as a fluid following the momentum equation, the one will enable us to express v_s as a function of δE:

$$n_s m_s \left(\frac{\partial v_s}{\partial t} + (v_s.\nabla).v_s\right) = n_s q_s \left(E + v_s \times B\right) - \nabla\bar{\bar{P}}_s \tag{2.7}$$

Now we can make simplifications according to previous approximations; the 2nd cold approximation provides $\nabla\bar{\bar{P}}_s = 0$, then with the 7th approximation the term

$(v_s.\nabla).v_s$ being of second order in δv_s, can be neglected in front of others first order terms. Finally, doing the transformation into Fourier space we get:

$$-i\omega\delta v_s = \frac{q_s}{m_s}\delta E + \frac{q_s}{m_s}\delta v_s \times B_0 \qquad (2.8)$$

Vector b = $B_0 / |B_0|$ was defined on Fig.2.1, and it will be our reference in the following part of the calculation. We will use an arbitrary referential (x',y',b) such that:

$$\delta v_s = \begin{pmatrix} v_{x'} \\ v_{y'} \\ v_b \end{pmatrix} \quad , \quad \delta E = \begin{pmatrix} E_{x'} \\ E_{y'} \\ E_b \end{pmatrix} \quad \text{and} \quad B_0 = \begin{pmatrix} 0 \\ 0 \\ B_0 \end{pmatrix}$$

Projecting the equation 2.8 on each direction of this basis leads to:

$$\begin{cases} -i\omega v_{x'} - (q_s B_0 / m_s) v_{y'} = (q_s / m_s) E_{x'} & (2.9) \\ -i\omega v_{y'} + (q_s B_0 / m_s) v_{x'} = (q_s / m_s) E_{y'} & (2.10) \\ -i\omega v_b = (q_s / m_s) E_b & (2.11) \end{cases}$$

Introducing the *cyclotron frequency* $\Omega_{cs} = q_s B_0 / m_s$ ($= 1.6\times10^{-19}\times3.7/1.66\times10^{-27} = 350MHz$ for *WEST*), and re-arranging the system by doing linear combinations of the first and second lines, respectively (2.9)+*i*(2.10) and (2.9)-*i*(2.10) we get:

$$\begin{cases} -i(v_{x'} + iv_{y'}).(\omega - \Omega_{cs}) = (q_s / m_s)(E_{x'} + iE_{y'}) & (2.12) \\ -i(v_{x'} - iv_{y'}).(\omega + \Omega_{cs}) = (q_s / m_s)(E_{x'} - iE_{y'}) & (2.13) \\ -i\omega v_b = (q_s / m_s) E_b & (2.14) \end{cases}$$

Equations 2.12 and 2.13 are now written in such a form that suggests introducing rotating vectors, respectively for velocity and electric field:

$$v_{\pm} = (v_{x'} \pm iv_{y'}) / \sqrt{2}$$

$$E_{\pm} = (E_{x'} \pm iE_{y'}) / \sqrt{2}$$

Now we can write eq.2.12 and 2.13 in the rotating basis and get the expression:

$$v_{\pm} = i\frac{q_s}{m_s}\frac{E_{\pm}}{\omega \mp \Omega_{cs}} \tag{2.15}$$

Now substituting this expression of the speed into the current definition (equation 2.6), we finally get the current expressed in function of E field in the rotating basis (e_+,e_-,b):

$$j_{\pm} = i\sum_s \frac{n_s q_s^2}{m_s}\frac{E_{\pm}}{\omega \mp \Omega_{cs}} \tag{2.16}$$

$$j_b = i\sum_s \frac{n_s q_s^2}{m_s}\frac{E_b}{\omega} \tag{2.17}$$

Now we can make an analogy with Ohm's law (eq.2.5) and identify the terms of the tensor $\bar{\bar{\sigma}}$. We also introduce the *plasma frequency* $\omega_{ps}^2 = q_s^2 n_s / \varepsilon_0 m_s$:

$$\bar{\bar{\sigma}} = i\varepsilon_0 \sum_s \omega_{ps}^2 \begin{pmatrix} 1/\omega - \Omega_{cs} & 0 & 0 \\ 0 & 1/\omega + \Omega_{cs} & 0 \\ 0 & 0 & 1/\omega \end{pmatrix} \tag{2.18}$$

Note that in a single ion species plasma the cyclotron frequency reduces to $\Omega_{cs} = \Omega_{ci}$ and the ratio of the positively to the negatively rotating components of the electric field converges to zero as the wave frequency converges to the ion cyclotron frequency $\left|E_+ / E_-\right| \approx \left|\omega - \Omega_{ci} / \omega + \Omega_{ci}\right| \xrightarrow{\omega \to \Omega_{ci}} 0$. This explains why ICRF technique cannot be used to heat single ion species plasmas, since its electric field only rotates on the negative side (also called left side, opposite to positive ions rotation) when approaching resonance so that no energy can be transferred (imagine a watch on a table and its reflection on a vertical mirror, clock hands turn at the exact same frequency and in opposite direction as their image); this is the *screening effect* that was mentioned in part 1.3.2.

From relation 2.6 we can write the *Stix tensor in* this *rotating basis*:

$$\bar{\bar{\varepsilon}} = \varepsilon_0 \begin{pmatrix} \varepsilon_L & 0 & 0 \\ 0 & \varepsilon_R & 0 \\ 0 & 0 & \varepsilon_{\parallel} \end{pmatrix} \tag{2.19}$$

With

$$\varepsilon_L = 1 - \sum_s \frac{\omega_{ps}^2}{\omega(\omega - \Omega_{cs})} \tag{2.20}$$

$$\varepsilon_R = 1 - \sum_s \frac{\omega_{ps}^2}{\omega(\omega + \Omega_{cs})} \tag{2.21}$$

$$\varepsilon_{\parallel} = 1 - \sum_s \frac{\omega_{ps}^2}{\omega^2} \tag{2.22}$$

Going back to the blue basis $(e_\perp, e_{\parallel} \times e_\perp, e_{\parallel})$ with $e_{\parallel} = b$ on Fig.2.1, we finally get the form:

$$\bar{\bar{\varepsilon}} = \varepsilon_0 \begin{pmatrix} \varepsilon_\perp & -i\varepsilon_X & 0 \\ i\varepsilon_X & \varepsilon_\perp & 0 \\ 0 & 0 & \varepsilon_{\parallel} \end{pmatrix} \tag{2.23}$$

with

$$\varepsilon_\perp = \frac{\varepsilon_R + \varepsilon_L}{2} = 1 - \sum_s \frac{\omega_{ps}^2}{\omega^2 - \Omega_{cs}^2} \tag{2.24}$$

$$\varepsilon_X = \frac{\varepsilon_R - \varepsilon_L}{2} = \sum_s \frac{\omega_{ps}^2}{\omega} \cdot \frac{\Omega_{cs}}{\omega^2 - \Omega_{cs}^2} \tag{2.25}$$

Note that because of the 3rd approximation about collisionless plasma, Stix tensor does not depend of the wave vector ***k***. Now we can rewrite eq.2.6 using Stix tensor in the basis $(e_\perp, e_{\parallel} \times e_\perp, e_{\parallel})$, with $n = kc/\omega = n_\perp . e_\perp + n_{\parallel} . e_{\parallel}$:

$$n \times n \times E + \bar{\bar{\varepsilon}} . E = \bar{\bar{K}} . E = \begin{pmatrix} \varepsilon_\perp - n_{\parallel}^2 & -i\varepsilon_x & n_\perp n_{\parallel} \\ i\varepsilon_x & \varepsilon_\perp - n^2 & 0 \\ n_\perp n_{\parallel} & 0 & \varepsilon_{\parallel} - n_\perp^2 \end{pmatrix} \begin{pmatrix} E_\perp \\ E_X \\ E_{\parallel} \end{pmatrix} = 0 \tag{2.26}$$

This equation admits solutions only if $\det(\bar{\bar{K}}) = 0$, which leads to the *dispersion relation*:

$$\varepsilon_\perp n_\perp^4 - \left[(\varepsilon_\perp + \varepsilon_{\parallel})(\varepsilon_\perp - n_{\parallel}^2) - \varepsilon_X^2 \right] n_\perp^2 + \varepsilon_{\parallel} \left[(\varepsilon_\perp - n_{\parallel}^2)^2 - \varepsilon_X^2 \right] = 0 \tag{2.27}$$

2.2.2 Fast and Slow waves

The dispersion relation fourth order in $n_\perp$, but it can also be seen as a second order equation in $n_\perp^2$. This leads to two modes that are decoupled because of the 3rd approximation of collisionless plasma, but taking thermal effects into account would lead to a more complicated coupled result. Notice that this truly is a dispersion relation since the pulsation ω of the wave is hidden in each component of the Stix tensor. Now solving this equation of second order far from the coupling region ($\varepsilon_\perp \neq n_\parallel^2$) leads to the two following solutions both obeying the ordering $|\varepsilon_X|, |\varepsilon_\perp|, |n_\parallel^2| << |\varepsilon_\parallel|$:

Fast Waves mode; $$n_{\perp FW}^2 = \frac{(n_\parallel^2 - \varepsilon_R)(n_\parallel^2 - \varepsilon_L)}{\varepsilon_\perp - n_\parallel^2} \qquad \text{with} \left|n_{\perp FW}^2\right| << |\varepsilon_\parallel| \qquad (2.28)$$

Slow Waves mode; $$n_{\perp SW}^2 = \varepsilon_\parallel (1 - \frac{n_\parallel^2}{\varepsilon_\perp}) \qquad \text{with} \left|n_{\perp SW}^2\right| \approx |\varepsilon_\parallel|$$

(2.29)

Group and phase velocities of each mode can be calculated respectively with the formulas:

$$v_G = \frac{\partial \omega}{\partial k} \qquad (2.30)$$

$$v_\varphi = \frac{\omega}{k} = \frac{c}{n} \qquad (2.31)$$

Combining the orderings of equations 2.28 and 2.29 we get $n_{\perp FW} << n_{\perp SW}$, then using eq.2.31 we find that $v_{\varphi SW} << v_{\varphi FW}$. This explains why a mode is said to be "Slow" compared to the other so called "Fast" wave. From those expressions, resonances and cut-offs for each type of wave can be determined and are summarized in the following table with their corresponding densities expressions in case of single species plasma:

	Resonances	Cut-Offs
Fast Waves	$n_{\parallel}^2 = \varepsilon_{\perp}$ Alfvén Resonance	$n_{\parallel}^2 = \varepsilon_R, \varepsilon_L$ $N_{CR/CF} = \frac{\varepsilon_0}{e^2}\left(\frac{1}{m_i}.\frac{1}{\omega(\omega \pm \Omega_i)} + \frac{1}{m_e}.\frac{1}{\omega(\omega \pm \Omega_e)}\right)^{-1}(n_{\parallel}^2 - 1)$
Slow Waves	$\varepsilon_{\perp} = 0$ LH Resonance	$n_{\parallel}^2 = \varepsilon_{\perp}$ and $\varepsilon_{\parallel} = 0$ $N_{C-SW} = \frac{\varepsilon_0 m_e}{e^2}\left(\frac{\omega - \Omega_i}{\omega + \Omega_i}.\frac{\omega - \Omega_e}{\omega + \Omega_e}\right)\left(\frac{\omega - \Omega_i}{\omega + \Omega_i} + \frac{\omega - \Omega_e}{\omega + \Omega_e}\frac{m_e}{m_i}\right)^{-1}(1 - n_{\parallel}^2)$

Table 2.1: Fast and Slow waves' resonances and cut-off conditions with corresponding densities noted N to distinguish from wave numbers n.

A cut-off is a layer where the perpendicular wave number is null ($n_{\perp}^2 = 0$), meaning conditions are not favorable for the wave to propagate. When reaching such surface, the largest part of wave power is reflected while a little part is transmitted towards an evanescent region – characterized by an imaginary wave number ($n_{\perp}^2 < 0$) – where the wave vanishes. Using the ordering equality, the SWs number can for instance be approximated by $n_{\perp SW} \approx \sqrt{\varepsilon_{\parallel}} \approx i\omega_{pe}/\omega$ leading to a SW evanescent length of $l_{SW} = 1/|k_{\perp SW}| = c/\omega|n_{\perp SW}| \approx c/\omega_{pe}$, typically less than a centimeter. The SW cut-off density is also very low (~4.10^{16}m^{-3} in EAST and ~$9.2.10^{16}$m^{-3} in WEST, cf. Annex 11), which explains why it only plays a role at the plasma edge. The FW to the contrary propagates above higher densities (10^{19}m^{-3} in EAST and ~5.10^{18}m^{-3} in WEST for dipole phasing (180°), cf. Annex 11), so once it is launched by an antenna from the edge, it first has to tunnel through a thin evanescent layer (~4cm cf. Fig 5.15 for EAST and Fig.A.21 in WEST) before reaching higher density plasma favorable for its propagation. Note this cutoff density decreases as going from dipole (180°) to monopole (0°) phasing due to the excitation of lower $\boldsymbol{k}_{\parallel}$ as shown in eq.1.5 and 1.10 (9.10^{17}m^{-3} in EAST and ~5.10^{17}m^{-3} in WEST for phasing less than 60°, cf. Annex 11). In practice, such areas can be localized in the plasma by measuring density profile and finding which position corresponds to a cut-off density. The figure 2.4 below shows the behavior of each wave (evanescent of propagative) according to its radial position and the magnitude of the corresponding density; note that there are several orders of magnitude difference between the antenna position (~10^{17}m^{-3}) and the plasma core

($\sim 10^{19} m^{-3}$).

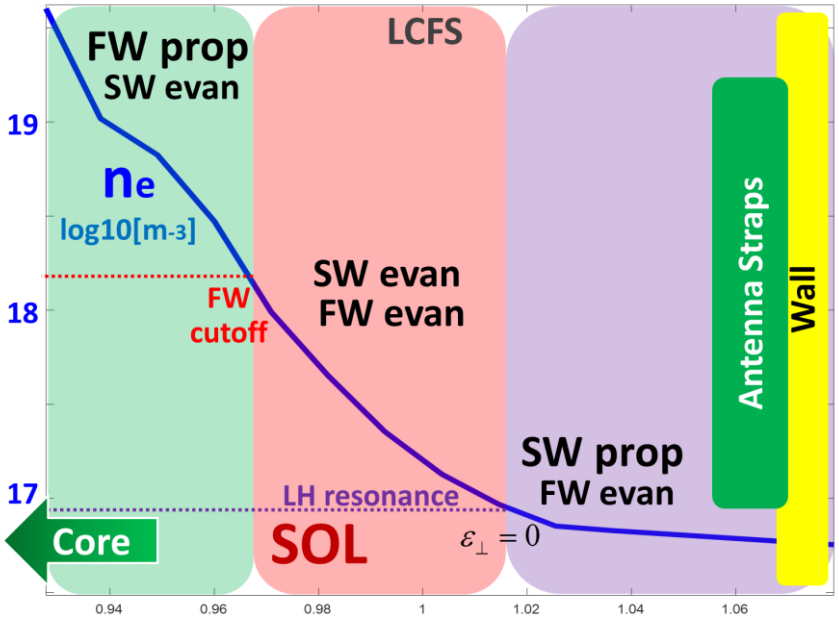

Figure 2.4: Slow and Fast waves propagation behavior in the plasma border according to its normalized radial position and roughly corresponding density magnitudes (example of EAST-like density profile in blue).

Once the wave propagates, it mostly goes towards higher densities until it reaches another area where its refractive index grows infinitely ($n_\perp^2 \xrightarrow{Resonance} \infty$), this is the resonance. This time the wave is no longer reflected but absorbed by the plasma. The magnetic field which is actually a function of the radial position, reaches in this region such a value that the cyclotron frequency ω_0 equals the wave frequency Ω_{cs} ($\omega_0 = \Omega_{cs}(r_{res}) = q_s B_0(r_{res}) / m_s$). The wave undergoes a damping process by which it gives some of its energy to the surrounding charged particles [Louche & Koch 2015].

In the case of the FW mode of interest for ICRH heating, the resonance occurs when $n_\parallel^2 = \varepsilon_\perp$. Considering the simplified case of a purely perpendicular propagation of the wave ($n_\parallel^2 = 0$) and writing the expression of $\varepsilon_\perp$ (equation 2.24) in the case of two ions species plasma, leads to:

$$\varepsilon_\perp = 1 - \frac{\omega_{pe}^2}{\omega_0{}^2 - \Omega_{ce}^2} - \frac{\omega_{p1}^2}{\omega_0{}^2 - \Omega_{c1}^2} - \frac{\omega_{p2}^2}{\omega_0{}^2 - \Omega_{c2}^2} = 0 \qquad (2.32)$$

For $\Omega_{c1} \leq \omega_0 \leq \Omega_{c2}$, the two first terms can be neglected in front of the two last

terms, so that the solution of the equation 2.32 in ω is:

$$\omega_{i-iH}^2 = \frac{\omega_{p1}^2\Omega_{c2}^2 + \omega_{p2}^2\Omega_{c1}^2}{\omega_{p1}^2 + \omega_{p2}^2} \tag{2.33}$$

This is the expression of the *ion-ion hybrid* (or Bushsbaum) *resonance* mentioned in part 1.2.3. Notice also that equation 2.33 written in the case of single ion specie plasma would not admit any solution after ordering, which is consistent with the *screening effect* mentioned in section 1.3.2.

Respectively, cut-off and resonance concepts have be put in correlation with coupling and heating efficiency or wave absorption, introduced in the previous chapter (1.2). While improving the coupling may consist in minimizing the width of the evanescent layer, optimizing absorption results in a good control – appropriate amount at the appropriate radial position – of targeted ions.

We can finally determine the *polarization* of those waves, which gives an indication on how the wave electric field oscillates – amplitude and frequency – in different directions. From
equation 2.26, we can make appropriate simplifications according to each mode orderings:

- **Fast Waves**; $\left|E_{\|}/E_{\perp}\right| = \left|n_{\|}n_{\perp}/\varepsilon_{\|}\right| << 1$ so $\left|E_X\right|, \left|E_{\perp}\right| >> \left|E_{\|}\right|$ the relation simplifies into $\begin{pmatrix} \varepsilon_{\perp} - n_{\|}^2 & -i\varepsilon_X \\ i\varepsilon_X & \varepsilon_{\perp} - n^2 \end{pmatrix}\begin{pmatrix} E_{\perp} \\ E_X \end{pmatrix} = \begin{pmatrix} 0 \\ 0 \end{pmatrix}$ from which we deduce the:

$$FW\ polarization \qquad \frac{E_X}{E_{\perp}} = i\frac{\varepsilon_X}{\varepsilon_{\perp} - n_{\|}^2} \tag{2.34}$$

- **Slow Waves**; $\left|E_{\perp}/E_X\right| = \left|-in_{\perp}^2/\varepsilon_{\perp}\right| >> 1$ so $\left|E_{\perp}\right|, \left|E_{\|}\right| >> \left|E_X\right|$ the relation simplifies into $\begin{pmatrix} \varepsilon_{\perp} - n_{\|}^2 & n_{\perp}n_{\|} \\ n_{\perp}n_{\|} & \varepsilon_{\|} - n_{\perp}^2 \end{pmatrix}\begin{pmatrix} E_{\perp} \\ E_{\|} \end{pmatrix} = \begin{pmatrix} 0 \\ 0 \end{pmatrix}$ from which we deduce the:

$$SW\ polarization \qquad \frac{E_{\perp}}{E_{\|}} = \frac{n_{\|}n_{\perp}}{n_{\|}^2 - \varepsilon_{\perp}} \tag{2.35}$$

2.3 Debye Sheath

The Debye sheath (also electrostatic sheath) is a layer in a plasma which has a greater density of positive ions, and hence an overall excess positive charge, that balances an opposite negative charge on the surface of a material with which it is in contact. In this part, no wave is considered, we will only explain sheath due to the fact that the electrons usually have a temperature on the order of magnitude or greater than that of the ions and are much lighter. Consequently, they are faster than the ions by at least a factor of $\sqrt{m_i / m_e}$. We will then according to the Fig.2.1 consider the negatively charged surface of the PFC, separated from the quasi-neutral plasma by the ions populated sheath. Writing Poisson's equation at the interface sheath-plasma leads to a characteristic length for a sheath's width, corresponding to the distance after which particles in the plasma do not feel the influence of an electric field (effect screened), this is the so called Debye length:

$$\lambda_{De} = \sqrt{\varepsilon_0 k_B T_e / n_e e^2} \tag{2.36}$$

In the plasma edge where temperatures are typically or the order of several tens of electron-volt and densities vary around 10^{18}m^{-3}, this Debye length is of millimeter order. The sheath width in a point (z, y) of a wall (z and y being respectively the toroidal and poloidal directions according to Fig.2.1) can then be estimated in function of the potential drop normal to the surface at this point ΔV(x, z) with the *2D Child Langmuir Law*:

$$\delta(z, y) = \lambda_{De} \left(\frac{e.\Delta V(z, y)}{k_B T_e} \right)^{3/4} \tag{2.37}$$

This length can be compared with the particles mean free path in the SOL of the meter order, which makes the 3rd collisionless approximation still valid inside the sheath. Looking closely at the sheath-plasma interface and with what was just said, the attractive effect of the negatively biased layer is screened from ions in the main plasma, it consequently can be intuited that the first force that they will feel approaching the sheath is repulsive, due to the closer and positively biased ion cloud. For this reason, when the energy of the ions exceeds the famous Bohm speed u_B, ions induce a constant potential drop across the sheath [Stangeby 2000]. This lead can be

calculated by writing the energy conservation at the sheath-plasma interface, and it leads to the *Bohm sheath criterion*:

$$u_0 \geq u_B = \sqrt{k_B \left(T_e + \gamma T_i\right) / m_i} \tag{2.38}$$

u_0 being the speed an ion coming from the plasma, the one much be above the Bohm speed u_B to enable it penetrating into the sheath. k_B is the Boltzmann's constant, m_i the ion mass, T_e and T_i the electrons and ion temperatures. γ is a constant that can take different values above unity according to the model used.

The positive charge density [coulombs m^{-2}], integrated through the sheath thickness, almost equals the negative charge density existing on the solid surface. Thus the rest of the region upstream of the sheath—the essentially neutral plasma itself—is almost completely shielded from the electric field due to the space charge density in the sheath. The shielding is not perfect, however, and a small electric field $E \approx kT_e/2eL$, penetrates throughout the length of the plasma where the particle source exists. This is called the *pre-sheath* electric field and it acts on the ions in the SOL to help move them toward the target. In this region, because the PFC is several Debye lengths far from the plasma, its negatively biased surface does not have any influence on electrons outside the sheath. In the sake of ambipolarity, electrons and ion fluxes towards the wall must be the same, while a net energy is transfer occurs from electrons to ions inside the sheath (Fig.A28), accelerating ions above Bohm speed towards the wall and repulsing electrons away. On Fig.2.1, the term "Pre-Sheath" was written to keep its existence at mind, but was not materialized since its width is much larger than the sheath itself.

We can now evaluate the potential drop through a floating sheath (insulated from the ground) by writing the equality of electrons and ions fluxes at the sheath entrance, which gives:

$$\phi_f{}^{plasma} = \frac{k_B T_e}{2e} . \ln\left(2\pi \frac{m_e}{m_i}\left(1 + \frac{T_i}{T_e}\right)\right) \tag{2.39}$$

ϕ_f is the *floating potential of the plasma,* corresponding to the difference between the potential of the plasma and the floating potential of a probe ($\phi_f{}^{plasma} = \phi_p - \phi_f$), meaning no net current can be driven by an insulated probe. This is to be split with the floating potential measured by Langmuir probes (ϕ_f). This type of probe will be

further detailed in the next chapter. It is just worth to mention another key parameter that can be measured with such probe, it is the *saturation current*:

$$I_{sat}^{+} = e.n_i.u_B / 2 \tag{2.40}$$

We can then write the expression of the current–voltage relation of the net current I that would arrive on a probe biased at a potential V, and plunged into a plasma. It is often called I-V *characteristic* and its typical trend is represented on the figure bellow:

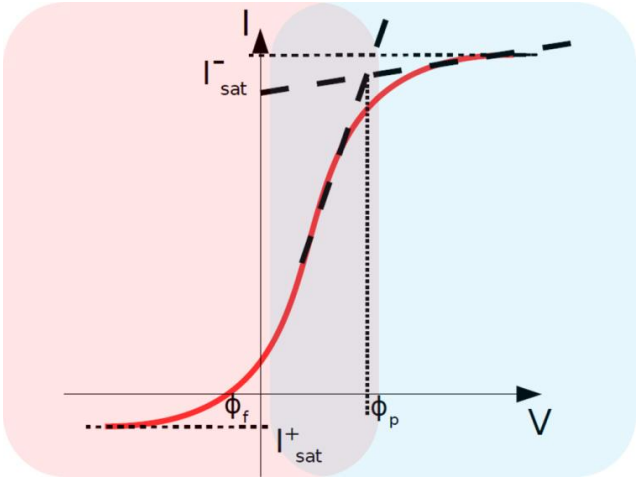

Figure 2.5: Theoretical I-V characteristic of a probe biased at potential V. ϕ_f corresponds to the floating potential, ϕ_p to the real plasma potential, I^+_{sat} and I^-_{sat} respectively the ion and electron saturation currents.

$$I = I_{sat}^{+}\left(1-\exp\left(\frac{e}{k_B T_e}\left(\phi_f - V\right)\right)\right) \tag{2.41}$$

When sheath principle was introduced both in section 1.4 and at the beginning of this chapter, it has been explained that sheath forms when a magnetic field line intercepts a PFC, however the magnetic field is absent from every formulas in this part. Its value is here assumed to have negligible influence on the dynamic of the process (however it can have [Chodura 1982], [Stangeby 2012]), besides its direction determines the *criterion for sheath formation*:

$$\sin\alpha_{in} > \sqrt{m_e / m_i} \tag{2.42}$$

With α_{in} the incident angle between the magnetic field line and the PFC surface. This means that in an ideal case of objects with perfectly smooth geometries, magnetic field lines incidence would be too small for any sheath to form. Yet, notice that m_e is much smaller than m_i so that this incidence angle must be very small. For

example, to prevent sheath from forming in deuterium plasma, the incidence of magnetic lines on PFC should be smaller than 1° which of course is too small to be achieved in practice in all PFCs of a tokamak.

We should now keep in mind that thermal sheath always forms on top of PFCs that intercept magnetic field lines, but on top of it, ICRF waves also play their part. Most of the electric field component parallel to magnetic field lines being carried by the slow mode, their presence in the edge (even evanescent) can enhance the process, leading to even stronger acceleration of ions towards PFCs. We will now talk about this contribution from ICRF, which relies on substantially different mechanism as the one just described.

2.4 ICRF-induced RF Sheath and DC Rectification

We just showed the principle by which thermal effects may lead to the formation of a sheath, thus this sheath rapidly reached equilibrium of fluxes, with a continuous potential drop that we will now write V_{DC}. We now take the ICRF wave into account to see how it plays a role at the edge. The Fig.2.6 bellow provides an illustration of the whole rectification process with the key equations we are about to write.

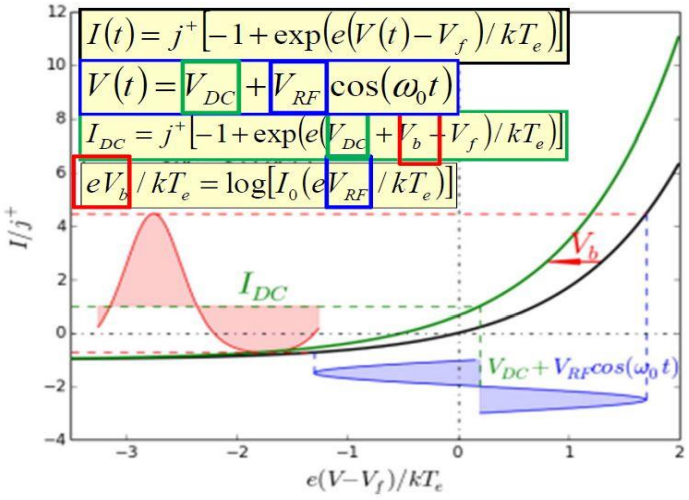

Figure 2.6: Illustration of the RF→DC rectification and key equations of the process Courtesy by L. Colas.

We assume a wave sent at a frequency ω_0 with amplitude V_{RF}. The total instantaneous sheath potential can then be written as the sum of both contributions:

$$\tilde{V}(t) = V_{DC} + V_{RF}\cos(\omega_0.t) \tag{2.43}$$

And this expression can be injected into the equation 2.41 providing the corresponding theoretical current that would flow onto any object plunged in the sheath:

$$\tilde{I}(t) = I_{sat}^{+}\left(1-\exp\left(\frac{e}{k_B T_e}\left(\phi_f - \tilde{V}(t)\right)\right)\right) \tag{2.44}$$

Note that ϕ_f still corresponds to the floating potential that was expressed in equation (2.39) only taking thermal effects into account; this will be a key point of the next chapter devoted to probes. Note also that a cosine in hidden inside $\tilde{V}(t)$, so taking the exponential of such term introduces a non-linearity in the expression, and that, is playing a trick we are about to discuss. It is important at this point to clarify some ordering notions concerning the RF sheath; let recall the fact that the magnetic field is decreasing inversely to the radius as we move towards the edge, so in our present case, we are clearly in the region of the plasma with the weakest magnetic field and consequently the smaller ion cyclotron frequency. The RF wave thus is already propagating with a much larger frequency ($\omega_0 >> \omega_{pi}$ in SOL low density plasma), so that ions in the sheath cannot react to the immediate wave field but only to its average over a wave period ($T_0=2\pi/\omega_0$). Besides, electrons being much lighter and faster will be sensible to the immediate wave oscillations. Moreover, instantaneous phenomena described by the two previous equations are way beyond time resolution capacity of measuring tools currently used with electrostatic probes (few MHz). This hints us to go look for average expression over a wave period that will be fully relevant for all species, eventually leading to relevant information. Let's then take the *average over T_0* of the current expression 2.44:

$$\begin{aligned}
\left\langle\tilde{I}(t)\right\rangle &= I_{sat}^{+}\left\langle 1-\exp\left(\frac{e}{k_B T_e}\left(\phi_f - V_{DC} - V_{RF}\cos(\omega_0.t)\right)\right)\right\rangle \\
\left\langle\tilde{I}(t)\right\rangle &= I_{sat}^{+}\left[1-\exp\left(\frac{e}{k_B T_e}\left(\phi_f - V_{DC}\right)\right)\frac{1}{T_0}\int_{t}^{t+T_0}\exp\left(\frac{eV_{RF}}{k_B T_e}\cos(\omega_0.t)\right)dt\right]
\end{aligned} \tag{2.45}$$

In the integral over a period of the exponential of a cosine we recognize the form of the zero order *Bessel function* defined as:

$$I_0(X) = \frac{1}{\pi}\int_0^{\pi}\exp\left(X.\cos(T)\right)dT \tag{2.46}$$

The expression 2.45 can then be rewritten as:

$$\left\langle \tilde{I}(t) \right\rangle = \bar{I} = I_{sat}^{+} \left[1 - \exp\left(\frac{e}{k_B T_e} \left(\phi_f - V_{DC} \right) \right) I_0 \left(\frac{eV_{RF}}{k_B T_e} \right) \right] \qquad (2.47)$$

And we can now make the Bessel term enter inside the exponential as a new term which origin is the RF sheath non-linearity. This new term can be seen as a *biasing voltage* V_b:

$$V_b = \frac{k_B T_e}{e} I_0 \left(\frac{eV_{RF}}{k_B T_e} \right) \qquad (2.48)$$

So that we get

$$\bar{I} = I_{sat}^{+} \left[1 - \exp\left(\frac{e}{k_B T_e} \left(\phi_f - V_{DC} + V_b \right) \right) \right] \qquad (2.49)$$

We finally notice that even if the wave oscillating voltage cancels over an RF period, the current induced does not. The fact that electrons react to the instantaneous field and ions do not, creates instantaneous substantial currents, which over an RF period result in a *DC rectification* of the voltage. In a simplified picture, a magnetic flux tube connects a point of a normal PFC on one side, to another point of another PFC where the potential is rectified by RF sheath on its other side, the difference of potential between both points then gives rise to the circulation of DC current along the field line. These effects can be both experimentally observed [Van Nieuwenhove 1990] and simulated among which can be quoted avaloids [Antar 2001], blobs [Krasheninnikov 2001], E×B density convections or convective cells [Bécoulet 2002]. Note also in the expression 2.48 that the biasing voltage induced by the rectification process increases with the maximum voltage V_{TL} of the wave in the transmission line, which is linked to its power P_{ICRF} (see equation 2.50, with Z_0 the impedance of the coaxial lines, defined as the ratio of the amplitudes of voltage and current of a single wave propagating along the line, typically 50Ω in EAST and 30Ω in WEST). At this point, the role that ICRH power will play on the edge can already be intuited.

$$P_{ICRF} = (V_{TL} / 2)^2 / Z_0 \qquad (2.50)$$

2.5 Impurities production

In this section, we will explain why SWs (which electric field has a strong component parallel to the magnetic field) are the first candidate responsible for enhancing RF sheaths on PFCs, by transporting strong localized RF voltages to RF sheaths. SWs can be created in two ways; they can be parasitically launched directly from ICRF antennas when the alignment between current straps with the magnetic field is not perfect, or either be the result of fast waves rectification when reflecting on a PFC (cf. Fig.4.2 in [Ochoukov 2013]). When the FW reaches a PFC surface, low density makes its propagation difficult, but it does not vanish. The FW to SW rectification process then consists in exciting the SW mode. This intensity of this phenomenon depends of both the intensity of the FW coming and its incidence angle with the PFC. An illustration of the mechanism is provided in Fig.2.7 bellow.

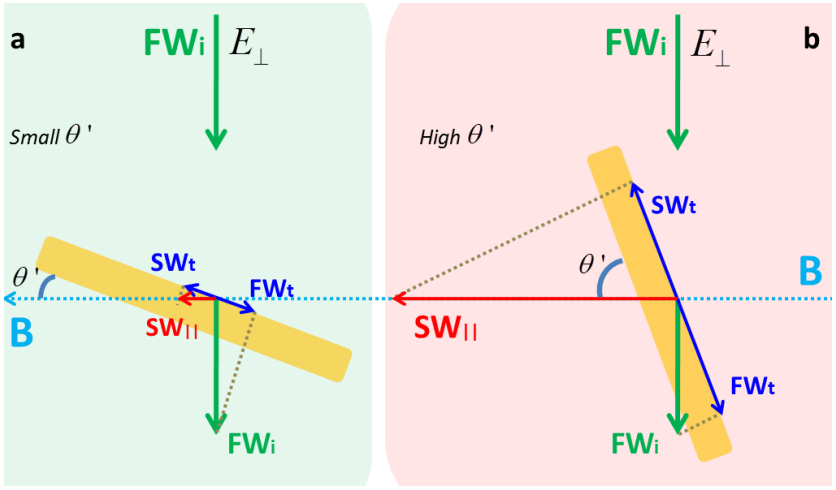

Figure 2.7: Demonstration of the effect of the angle between a PFC and the magnetic field (a) for B-field almost tangent to the surface and (b) for almost normal incidence

The efficiency of the rectification can be evaluated by calculating the intensity of the SW created, which is the electric field component parallel to the background magnetic field:

$$\left|E_{\parallel}\right| \propto \left|E_{FW,i}\right| . \left(\left|n_{\perp}\right|_{FW,i} - \left|n_{\perp}\right|_{FW,r} \right) B_{\perp} B_t \qquad (2.51)$$

Where $|E_{FW,i}|$ is the incident FW electric field value, $|n_\perp|_{FW,i}$ and $|n_\perp|_{FW,r}$ are the perpendicular index of refraction of the incident and reflected FW respectively, B_t the toroidal magnetic field and $B_\perp$ is the component of the magnetic field perpendicular to the surface. While the perpendicular component is usually negligible for most PFCs designed to get a razing incidence like the divertor ($\theta' \leq 10° \rightarrow B \approx B_t$), it can be high for instance on limiters sides where magnetic field lines incidence can be almost normal, causing larger excitation of SW (Fig.2.7b) and RF sheath. This expression is valid in the case of a fast wave propagating in vacuum and coupling to an electrostatic slow wave [Myra & D'Ippolito 2008 PoP], a case that is characteristic of fast waves propagating in the low density plasmas in the shadow of the limiters. Once SWs are created, their parallel electric field represents a danger for the edge. It nevertheless requires some conditions for enhancing RF sheath that may lead to deleterious effects. After showing that SWs propagate as Resonance Cones nearly parallel to the magnetic field lines [Myra & D'Ippolito 2008 PRL] (with the source located at the point of the cone from which SW is emitted), Myra & D'Ippolito calculated for different RF powers, the quantity of voltage V_0 carried by resonance cones that is penetrating the sheath. The result of this calculation is represented on Fig.2.8.a [Myra & D'Ippolito 2010]. By doing so, they showed that this quantity remains benign under relatively low energies, but may become problematic if the parameter Λ_0 reaches the order unity.

$$\Lambda_0 = -\frac{\lambda_{De}\varepsilon_{\|}}{\delta_{strap}}\left|\frac{\alpha e V_0}{T_e}\right|^{3/4} \qquad (2.52)$$

$\varepsilon_{\|}$ being the component of the dielectric tensor parallel to the magnetic field defined in the relation 2.22, α a correction coefficient of order unity, and δ_{strap} was introduced at the beginning of the part 1.2.2 on coupling and corresponds to the toroidal width of current straps, which is of same order as resonance cones parallel scale length that really matters in eq.2.52. Simplifications can even be made from the simulation results on Fig.2.8.a. It appears on the left part of the graph that for $\Lambda_0 << 1$ that the ratio of sheath and RF voltages is null, so that the voltage carried in the sheath by the wave is very small. On the right part of the graph to the contrary ($\Lambda_0 \geq 1$), the voltage induced across the sheath by the wave grows exponentially. Making further numerical approximations – $\lambda_{De} \approx n_e^{-1/2}$, $\varepsilon_{\|} = 1 - (\omega_{pe}/\omega)^2 \approx -(\omega_{pe}/\omega)^2$, $\omega_{pe} \approx n_e^{1/2}$ and

$V_0 \approx P_{ICRF}^{1/2}$ according to eq. 2.48 – another expression of the factor Λ_0, more convenient to test experimentally can be found [Ochoukov 2014]:

$$\Lambda_0 \propto \sqrt{n_e}.P_{ICRF}^{3/8} \tag{2.51}$$

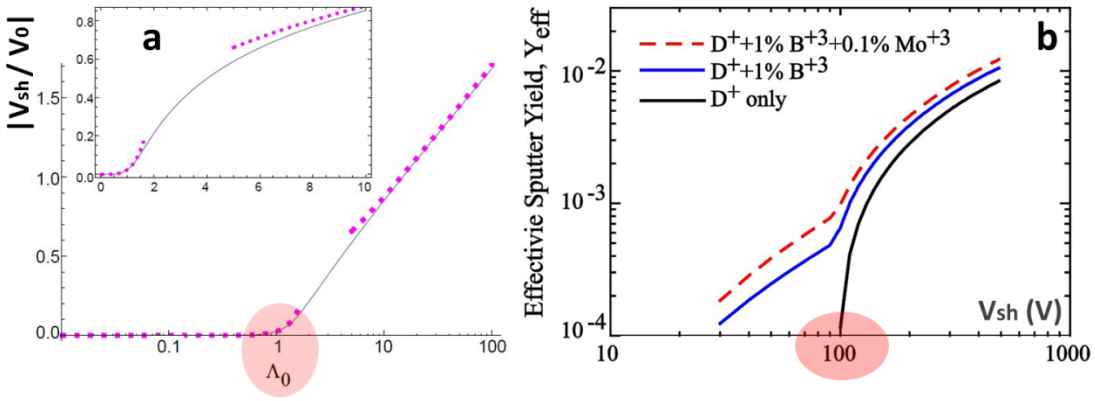

Figure 2.8: (a) Sheath voltage V_{sh} as a fraction of the voltage V_0 carried by SWs inside resonance cone vs a log scaled sheath parameter Λ_0, which unity is like a critical value above which SW voltage is fully transmitted to the sheath [Myra & D'Ippolito 2010] (b) Effective sputtering yields vs sheath voltage V_{sh} [Wukitch 2009], showing for three different plasma compositions, similar increase as sheath potential overcomes 100V

Putting both graphs in correlation on the same figure, it appears from Fig.2.8a that sheath potential enhancement starts at a very precise point defined by the parameter Λ_0, with unity as threshold value. From Fig.2.8b, the link between the sheath potential and ions sputtering yield is represented, showing another kind of threshold-like potential value (100V) above which even for different plasma compositions, sputtering yields increase dramatically, and as explained on the introduction of sheath given in section 1.4, strong sputtering yields may result in significant increase of impurities production. Fig.2.9 shows how the sputtering of tungsten evolves as a function of different ions species energy of impact. These curves were computed with equations available in section 3.3.1 of [Stangeby 2000] and show that the sputtering increases with incident ions mass and energy. For species lighter than He such as D and H, the sputtering reaches a maximum around 2keV and slightly decreases at higher energies. Note again that in the red region representing typical range of energies gained while crossing RF sheaths, sputtering yield evolves with a highly non-linear fashion as illustrated in Fig.2.8.

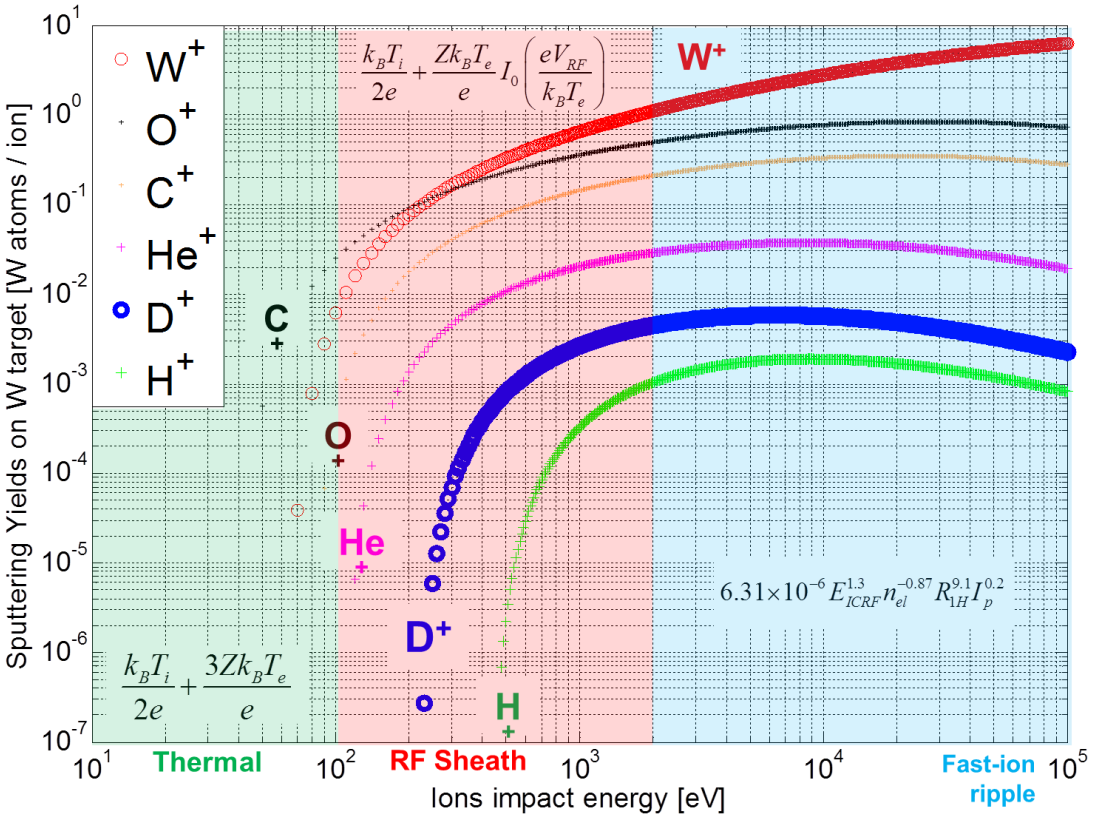

Figure 2.9: Effective sputtering yields of different ions on a tungsten target as a function of their impact energy. Typical ranges of impact energies of ions with charge Z are respectively represented in green when the ion only crosses a thermal sheath, in red when ICRH is applied and ion crosses an RF sheath (eq. 2.48), and in blue when it is characterized as fast ion. Details on the fast ion ripple losses* scaling law can be found under [Basiuk 2004] with E_{ICRF} the ICRF energy injected and lost in ion ripple estimated with calorimetry and R_{1H} the major radius of the IC resonance layer.

* The toroidal field coils in Tore Supra and WEST are supra-conducting, and their number is restricted to 18. As a result, the ripple corresponding to the curvature of the field lines between coils is fairly large (about 7% at the plasma boundary). Fast ion ripple losses therefore correspond to the loss of ions resulting from a local and periodic decrease of the magnetic pressure between coils.

3. ICRF experiments in tokamaks

From the beginning of ICRF, two main challenges occurring in plasma edge emerged – namely wave coupling and impurity sources enhancement – and have been motivating dedicated experiments in many devices over the past 50 years. ICRH was one of the first heating methods and is still going strong despite numerous hurdles it encountered and overcame. Another strong point in favor of ICRH is that life should become easier as the machines will get larger and power will increase; ions absorbing ICRF wave energy can collide fast enough with others ions and thermalize before leaving the plasma. This can further be of great interest for instance to prevent impurity from accumulating in the plasma core, which was typically only observed in JET (Fig.3.1) which is the largest device with high level of ICRF power so far [Lerche 2016].

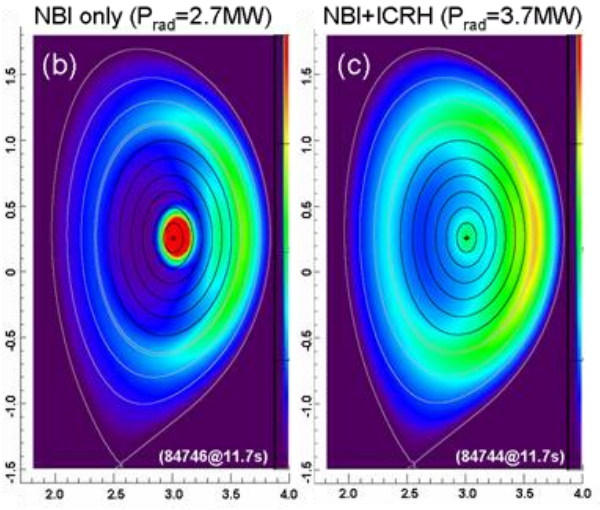

Figure 3.1: Example of core impurity screening
with H minority ICRH in D plasmas in JET [Lerche 2016]

3.1 ICRF wave Coupling

At the beginning of ICRF with first applications made in the sixties and notable advances on TM-1-VCh tokamak [Vdovin 1973], it was not yet clear how ICRF wave

coupling to plasmas should be optimized. It later became a matter of interest when trying to maximize the amount of power radiated in the plasma. In 1990 in DIII-D [Mayberry 1990], experiments were made, aiming at studying the coupling of fast waves, and first step understanding of wave coupling correlation with plasma density profile in front of the antenna were made. Later in 2004, others experiments in many others devices complemented what was hinted first in DIII-D. ICRF loading studies took place in JET [Bilato 2004] and confirmed that plasma-antenna distance is by far the most important parameter for the coupling optimization. Due to high densities in Alcator C-Mod plasmas though [Parisot 2004] despite this distance actually always appeared to be minimized, beyond this cut-off layer position, further dependences where observed in the confined region with the edge density profile shape. These second order effects were later on very well explained in [Messian & Weynants 2011]. Studies in Tore Supra [Clairet 2004] also documented ICRF coupling dependence on edge density profile and confirmed the relevance of the distance between the RF density cut-off and the antenna strap (Fig.3.2). Since Tore Supra was a limiter machine, it was also shown that the recycling regimes and connection length between plasma edge limiting elements are important and can dramatically influence the density in the SOL due to the so called convective cells. Convective cells and E×B density convections affecting RF waves coupling were studied in Tore Supra [Bécoulet 2002] and other machines like JET [Kirov 2009] and EAST [Kong 2013]. Beyond simplified 1D picture of wave coupling, the reality is much more complex since the antenna mouth is a 2D curved surface that in principle should perfectly match with the plasma curvature in order to preserve similar coupling efficiency in each point of the antenna mouth. This requires very accurate control of the plasma shape which can be challenging, especially in some experiments requiring changing the shape or position of the plasma (ex: X-point or vertical positions scans). Different coupling efficiency in different regions can then induce mutual coupling between the straps and perturb the matching of the whole antenna. This could for instance explain coupling improvement lately observed in WEST while passing from lower to upper single null configuration. In order to maximize ICRF coupling, we will show that the plasma density should first be increased, followed by the waves frequency but this is usually constrained either by the scenario or the coils engineering limits. There are besides other tools that can be used to improve ICRF performances like local gas injection to increase density locally at the edge and shorten waves' evanescence

length. Local gas injection was first used in ASDEX Upgrade [Bobkov 2015], then in JET and DIII-D [Jacquet 2016], EAST [Urbanczyk 2019 NF] and WEST [Urbanczyk 2019 RFPPC] which results will be shown in chapter 5.

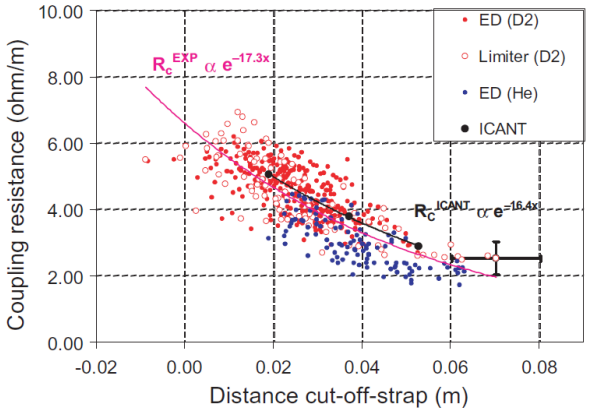

Figure 3.2: Relation between the RF coupling efficiency and the antenna–plasma distance for a collection of 40 discharges performed with a central magnetic field of $B_0 = 3$ T and for an ICRH frequency of $F_{ICRH} = 48$ MHz. Best-fit of the expected exponential decay of the coupling resistance (corrected from the resistive loss of the antennae) brings a maximum wavenumber coupling at $<\boldsymbol{k_x}>^{exp} \sim 8.65 m^{-1}$. Experimental results are in close agreement with absolute value ($<\boldsymbol{k_x}>^{ICANT} \sim 8.2 m^{-1}$) computed with the ICANT code. [Clairet 2004]

Phasing between straps can also be changed to excite different spectra (Fig.1.9) with lower $\boldsymbol{k}_{\parallel}$ that help improving wave coupling (eq.1.10) [J.H.Zhang 2017], [Bobkov 2017 PPCF], [Lerche 2009 AIP], but this often comes at the cost of stronger RF sheath excitation.

3.2 Experimental characterization of RF sheath effects

On several machines, experiments with ICRF raised numerous difficulties and challenges already in the 60^{ies}. First formalisms of RF sheath formation were established at in 1962 [Butler & Kino 1963] outside the fusion community, in the context of plasma RF discharges. Soon were observed in JET first traces of Scrape-Off Layer parameters modification by ICRF (ex: electron temperature and density profiles, floating potentials …) and production of impurities [Bures 1988]

[Jacquinot 1991]. RF sheath rectification effect was then formulated in 1989 [Perkins 1989] and its effect evidenced on TEXTOR by measuring DC currents extending all around the vessel and reconnecting on metal objects [Van Nieuwenhove 1990]. RF sheath voltages were estimated with triple probes on Phraedrus-T, enabling to explain ICRF-induced impurities production by an increased sputtering yield of ions accelerated by large sheath potential values [Tanaka 1996]. Impurities enhancement observation on Alcator C-Mod were attributed to ICRF slow wave mode, which parallel – to B – electric field creates a radiofrequency sheath on plasma facing materials [Wukitch 2004]. Special attention was then given to closely connected objects where sheath effects are stronger, new designs started being tested for antennas [Thomas 1996]. Amongst most important steps of improvements can be quoted surface coating with low-Z material like beryllium in JET [Bures 1992] to mitigate radiation losses, insulating Faraday screen of Phradeus-T [Sorensen 1996], tilted antenna in Alcator C-Mod [Garrett 2012] to respectively maximize the excitation of fast mode (perpendicular component of the electric field) and minimize parasitic slow mode excitation (parallel component), boron coating and 3-strap antenna in ASDEX Upgrade [Bobkov 2013] to compensate image currents induced on passive antenna components like limiters.

Some thematic were grouped under ITPA priority tasks defined by ITER organization to methodically tackle various problems. Among them, the IOS 5.1 task is devoted to the study of near and far fields-induced RF rectifications and is the package to which most of this thesis experimental results belong. Near field concern effects resulting from direct excitation of the slow wave near the antenna (generally evanescent elsewhere), which effect can be transported along magnetic flux tubes and also affect connected regions. Far field refer to sheath excitation resulting from a poor absorption of the fast wave and power deposition in the edge. These notions will be further detailed in the last chapter. One of the main protocols basically consists in using an edge diagnostic to provide information on the SOL parameters radial profile and scan safety factor values (q_{95}) values to magnetically connect to different poloidal heights of ICRF launchers. Combining data over a whole range of q_{95} values allows generating 2D maps of SOL measured parameters around ICRF antennas (Fig. 3.3). Such maps have been drawn for instance with Gas Puff Imaging (Fig. 3.3a and b) around both ICRF antennas of Alcator C-Mod [Cziegler 2012]. Fig.3.3c, d [Colas 2007] and e [Kubic 2013] are 2D – radial and poloidal – maps of respectively currents,

temperatures and potentials in front of ICRF antenna of Tore Supra which visible (f) and infrared (g) pictures shown. Note the correlation between the antenna hot regions visible on the infrared picture taken during antenna active phase and corresponding SOL parameters. Langmuir reciprocating probe was used to measure both ion fluxes and temperatures [Colas 2007] while a reciprocating Retarded Field Analyzer (RFA) was used to estimate potentials [Kubic 2013]. Similarly, graph h gives a schematic view of the protocol of experiments on ASDEX U which result is the RFA potential 2D map (i) [Colas 2014]. The last graph j shows poloidal potential distributions from JET in two cases of radial locations respectively connected (red curve) and not connected (green curve) to powered ICRF antenna limiters.

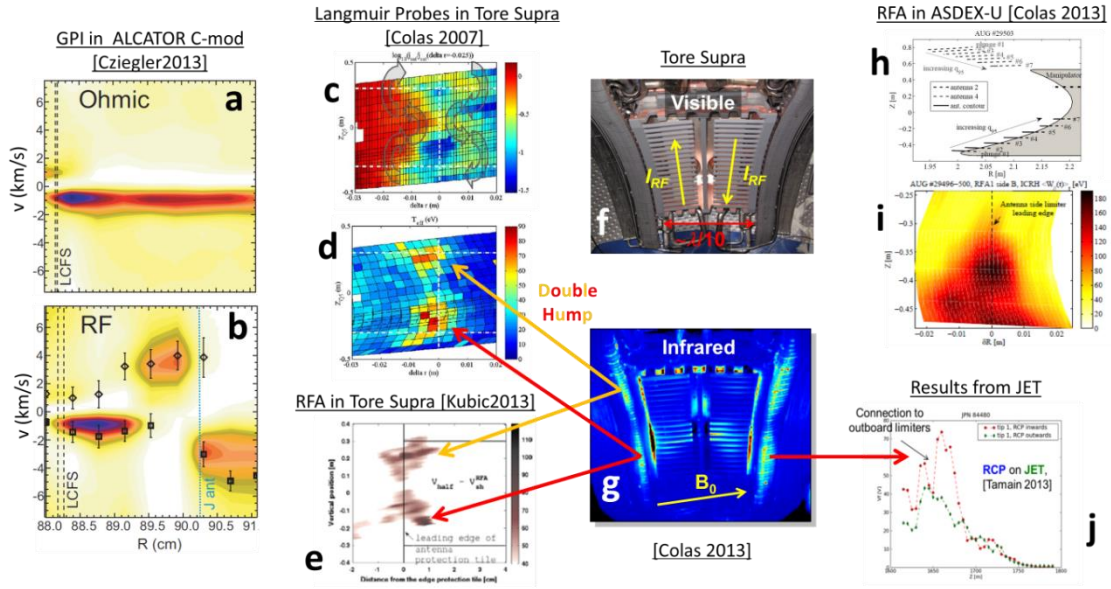

Figure 3.3: Overview 2D SOL mapping experimental results on different tokamaks with different diagnostics; GPI on Alcator C-mod, Langmuir (c, d, j) and RFA (e, i) reciprocating probes on Tore Supra, ASDEX Upgrade and JET. Pictures f and g also provide visible and infrared views of ICRF antenna of Tore Supra, and scheme h illustrates the experimental protocol on ASDEX Upgrade.

Several techniques such as Langmuir (section 4.3.1), emissive and ion sensitive probes (which a very nice overview can be found under [Ochoukov 2013]) were also used to study ICRF waves' influence on SOL plasma density, temperature and potential rectification were extensively explored and compared in Alcator C-Mod [Ochoukov 2014] and LAPD [Martin 2017]. Langmuir probes happen to be the most

practical technique which is why we will only use this one in the present thesis. Innovative experiments to characterize differently the effects caused by ICRF on different machines and with different diagnostics [Kostic 2018] will also be useful to deepen our understanding. Beyond those near-field studies, ICRF waves' are also capable of inducing RF sheath formation in sometimes rather unexpected locations, it can therefore be necessary to localize impurity sources others than antennas immediate neighboring, which motivated dedicated experiments in several devices like Alcator C-Mod [Lipshultz 2001], ASDEX.U [Dux 2009], JET [Colas 2018], EAST [Urbanczyk 2018] and WEST [Urbanczyk 2019 RFPPC] presented in the last chapter. In general, dominant impurity sources are located first near the outer strike point of divertors and on antenna limiters. Once in the core region, it is however challenging to determine the origin of an impurity, such that in JET where the origin of tungsten during ICRH is not yet understood. The best overview of ICRF-related plasma surface interaction experiments is provided by [Bobkov 2019].

3.3 Trade-off relation between RF sheath excitation and coupling resistance increase

As briefly mentioned in the beginning of the thesis outline (section 1.5), improving wave coupling efficiency – at fixed $\boldsymbol{k}_{\parallel}$ requiring minimizing the distance from the strap to the cutoff layer and therefore increasing the density at the edge – often comes with an increase of plasma surface interactions due to the increase of particle influx on the materials as will be shown in the last chapter. The goal is then to find an optimal regime balancing both effects; namely coupling enough power to the plasma in order to have some influence on its energy and temperature in the core, and simultaneously be careful not to increase plasma surface interactions beyond a level that could be unacceptable, regarding both plasma facing components lifetime and core contamination by impurities, leading to radiation losses. ICRF wave coupling efficiency and impurity production are then entangled by trade-off relying on several non-linear processes coupled together:

- *Sheath potential* rectification explained in section 2.4 and which a simplified expression can be derived:

$$V_{sh} = \phi_f - V_{DC} + \frac{k_B T_e}{e} I_0\left(\frac{eV_{RF}}{k_B T_e}\right) \qquad (3.1)$$

with I_0 the Bessel function of order zero.

- *Sputtering yield* evolution with ions energy of impact, highly non-linear in the energy range where RF sheath is typically the dominant mechanism as shown the red region in Fig. 2.9 [Stangeby 2000].

In addition, *data measured* by available diagnostics detailed in section 4.2 and physical quantities used in theoretical expressions are also linked though non-linear fashion. For instance the electron temperature extracted from I-V curves fitting (eq. 2.39), or particle fluxes either deduced from probes ion saturation current (eq. 4.18) or from visible spectroscopes sampling the light emitted by neutral atoms and relying on the so-called S/XB coefficients (cf. figure and equation 4.19 and Annex 3).

Dealing with these coupled non-linear processes is the main difficulty of this thesis, and one of the main reason why extrapolating results from a given scenario to another one, and even worse from one device to another is hardly straightforward.

In spite of all those efforts to design an antenna that would be simultaneously capable of coupling power efficiently, having it well-absorbed and mitigating plasma-material interactions, an optimal solution remains to be found, and new concepts to be tested [Ragona & Messiaen 2016].

4. Experimental setup

During this thesis, experiments both related to ICRF wave coupling (section 3.1 and chapter 5) and impurity sources characterization (section 3.2 and chapter 6) were done both in EAST and WEST which are the only two medium size superconducting tokamaks equipped with two ICRF antennas and two LH launchers. Heating scenarios were therefore relatively similar in both devices, with most diagnostics in commons, and some which are only available in one device. Data collected during similar experiments in each machine are sometimes complementary and by doing analogies and comparisons between both tokamaks, extract more relevant information. As far as this thesis is concerned, there are still differences in both machines likely to explain different experimental behaviors. A difference which may matter for wave coupling studies is for instance the poor pumping capacity of WEST compared to EAST, limiting the amount of gas that can be injected locally by keeping control of the plasma density. Of interest for impurity sources studies is the very different machine conditioning with daily lithium coating and many different materials in EAST against full tungsten environment in WEST with very occasional boronization.

4.1 EAST

4.1.1 General description

EAST (Experimental Advanced Superconducting Tokamak) is a superconducting device equipped with two divertors allowing lower, double and upper single null (USN) configurations. It main goals are to fulfill high power long pulse discharges in steady state, trying to fully maximize both bootstrap and non-inductively driven currents, with thermal equilibrium reached on the water cooled ITER-like W monoblock divertor. Its heating capacities combine all existing types of auxiliary heating systems (Fig.1.11); two neutral beam injectors (4+4MW), an electron cyclotron frequency antenna with two gyrotrons of 1MW each capable of delivering roughly 500kW, two lower hybrid (LH) launchers with 4 and 6MW each capable of coupling up to 2 and 3 MW, and two ion cyclotron frequency antennas with 6MW each and capable of coupling up to 2MW. In 2017, EAST was able to achieve a

discharge longer than 100s in high confinement mode (H-mode), proving it capability to manage several aspects that only emerge beyond a minute such as for instance:

- plasma density control despite strong outgassing from all plasma facing components due to the repetition of ELMs inducing high heat loads
- impurity accumulation (especially tungsten) that may lead to an increase in radiation and disruption [X.Zong 2018]. Note lithium power was injected around 70s to help mitigating impurity accumulation and make it through 100s [G.Z.Zuo 2013]
- constant power coupling from LH and ICRH despite sharp H-mode pedestal inducing a broadening of evanescence layers and coupling difficulties
- instabilities and MHD events …

The next objective is to inject over 10MW total power, which task is hard to fulfill due to the large number of systems that are simultaneously pushed towards their respective operational limits.

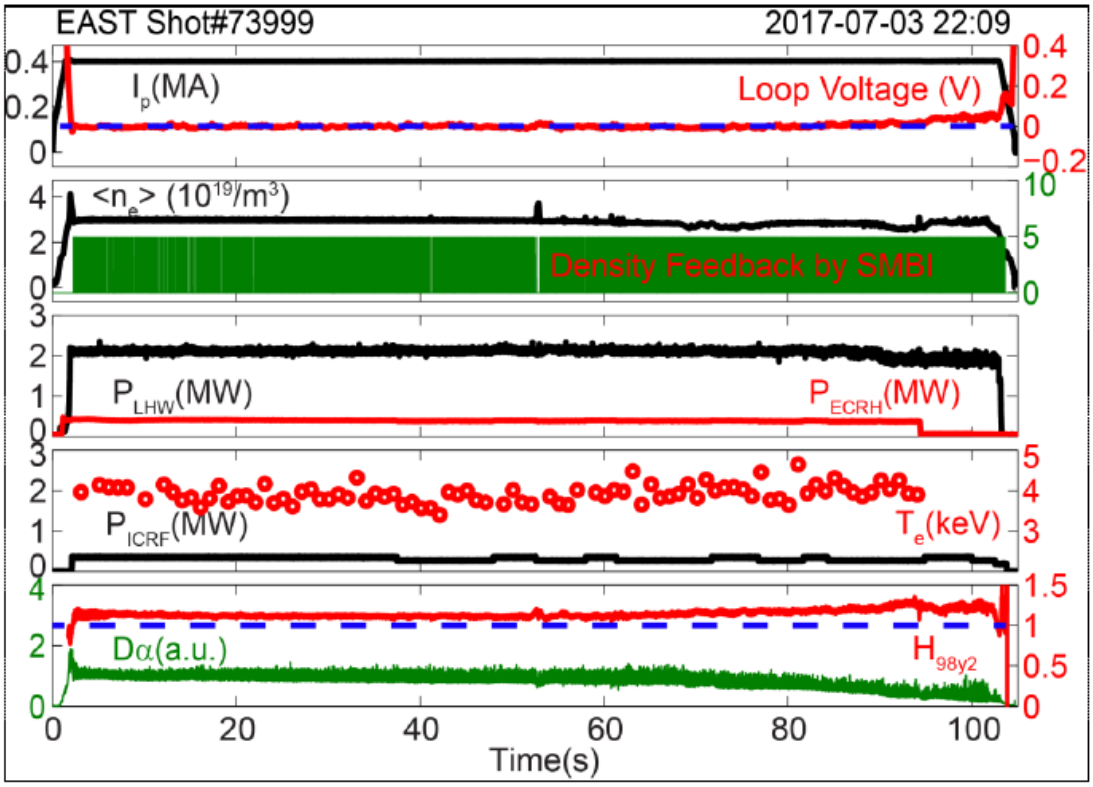

Figure 4.1: EAST discharge in H-mode over 100s.

I_p=400kA, $<n_e>$=3.$10^{19}$$m^{-3}$, Te_0=4keV, P_{RF}=3MW, H_{98}=1.1, USN

Because the lower divertor was still in carbon before 2020, our studies mostly use the upper tungsten divertor, operating in USN configuration. The typical plasma parameters were as follows: toroidal magnetic field Bt≈2.3T, plasma current Ip=500kA (q_{95}=5) during the 2016 session and Ip=400kA (q_{95}=6) during the 2017 session, major radius R_{out}≈1.85m, minor radius a≈0.44m, triangularity δ≈0.3-0.6 and elongation κ≈1.65. Auxiliary heating systems mostly used for experiments discussed in this thesis are the two Lower Hybrid Current Drive (LHCD) grills respectively located in E-port (4.6 GHz and 1.79<$n_{\|}$< 2.26) and N-port (2.45 GHz and 1.85< $n_{\|}$ <2.6) [M.H Li 2016], and the two ICRF antennas located in B-port (31.5 MHz) and I-port (35 MHz) (see Fig.4.2 and 4.3). In 2011 however, frequency of both ICRF antennas was only 27MHz [X.J.Zhang 2011], but these older cases will not be discussed in this thesis.

As shown on Fig.4.2a, a fast X-mode reflectometer in J-port provides electron density profiles [S.Zhang 2014]. As it is mostly used to measure core densities, specific effort was made to refine the edge region where gas is injected, which will be further detailed in the next chapter. The mid-plane reciprocating Langmuir probe was used to measure the radial profiles of the SOL parameters in J-port (T_e, n_e, V_f) [W.Zhang 2010] while Helium Beam Emission Spectroscopy (He-BES) in A-port [Schmitz 2008] allows determining the SOL density and temperature profiles from different spectral line ratios. Helium is puffed from the A-port in the direction of the B-port and optic fibers are aligned on the toroidal plane and oriented towards the B-port with an angle of roughly 45° incidence with respect to the magnetic field lines, measuring parameters right in front of the antenna. Since this diagnostic needs to puff pretty large quantities of helium (~10^{18}e/s), it cannot always be used to study B-port ICRF antenna coupling since its measure may itself have an influence on its coupling. During local gas injection experiments though (chapter 5), the amount of deuterium which was continuously puffed during those discharges (10^{20}e/s) being way above what the diagnostic needs to perform its measurements, we assume that is had negligible influence on the B-port ICRF wave coupling.

Langmuir probes were also fixed at different poloidal positions from the mid-plane to the top left corner of the antenna (Fig.4.12). The protective head design was optimized to mitigate sensitivity to the RF sheath by constraining the plasma to be sampled by lateral holes whose inner surface is approximately parallel to the

magnetic field lines, preventing large sheath expansion [Urbanczyk 2017]. Despite those design efforts to reduce sensitivity to the RF sheath, ongoing-upgrades are still needed to improve the probe's data in the presence of ICRH, which will be discussed in section 4.3.3.

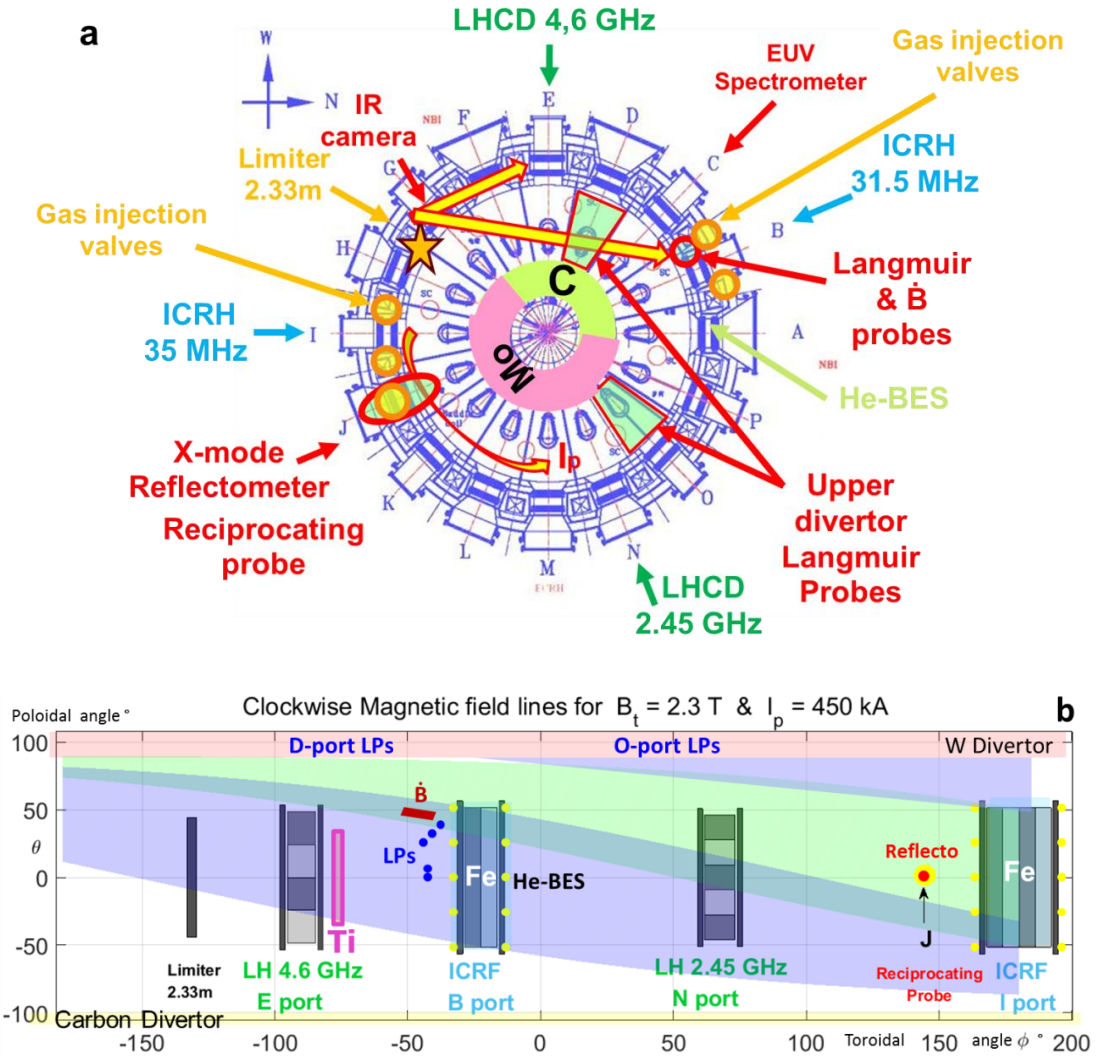

Figure 4.2: (a) Top view of EAST, with toroidal positions of heating systems and diagnostics used in the study, and two third of high field side wall in Mo and the other third in graphite (b) Toroidal-Poloidal (ϕ-Θ) 2D map showing magnetic connections between objects for a case (#75127) with q_{95}=5.6 in between 2016 and 2017 experiments: Fixed and reciprocating Langmuir probes are indicated by blue and red dots, while gas puff valves are represented by yellow dots

4.1.2 ICRF system in EAST

The B-port antenna excites a spectrum of plane waves peaked typically at $\boldsymbol{k}_{\parallel}\approx 12.5\ m^{-1}$ for which the R cutoff density is $n_{CO}\approx 6.3.10^{18} m^{-3}$. The I-port antenna typical parallel wavevector is $\boldsymbol{k}_{\parallel}\approx 13.6\ m^{-1}$ with a cutoff density of $n_{CO}\approx 9.10^{18} m^{-3}$. In order to optimize the ICRF heating efficiency, B-port is always operated in dipole phasing due to its geometry (Fig. 4.3). I-port antenna is however generally powered with 60° phasing ($\boldsymbol{k}_{\parallel}\approx 3\ m^{-1}$), allowing better coupling efficiency and sometimes better wave absorption as predicted by TOMCAT code (71% single pass absorption vs 55% in dipole). Both antennas were setup to heat hydrogen minority (7%) in deuterium plasmas. At the RF frequency of the waves launched by the I-port antenna the fundamental H cyclotron resonance layer was located in the plasma center. In 2017 the operating frequency for the B-port antenna was changed from 34 down to 31.5 MHz and the fundamental H cyclotron resonance was slightly shifted off-axis.

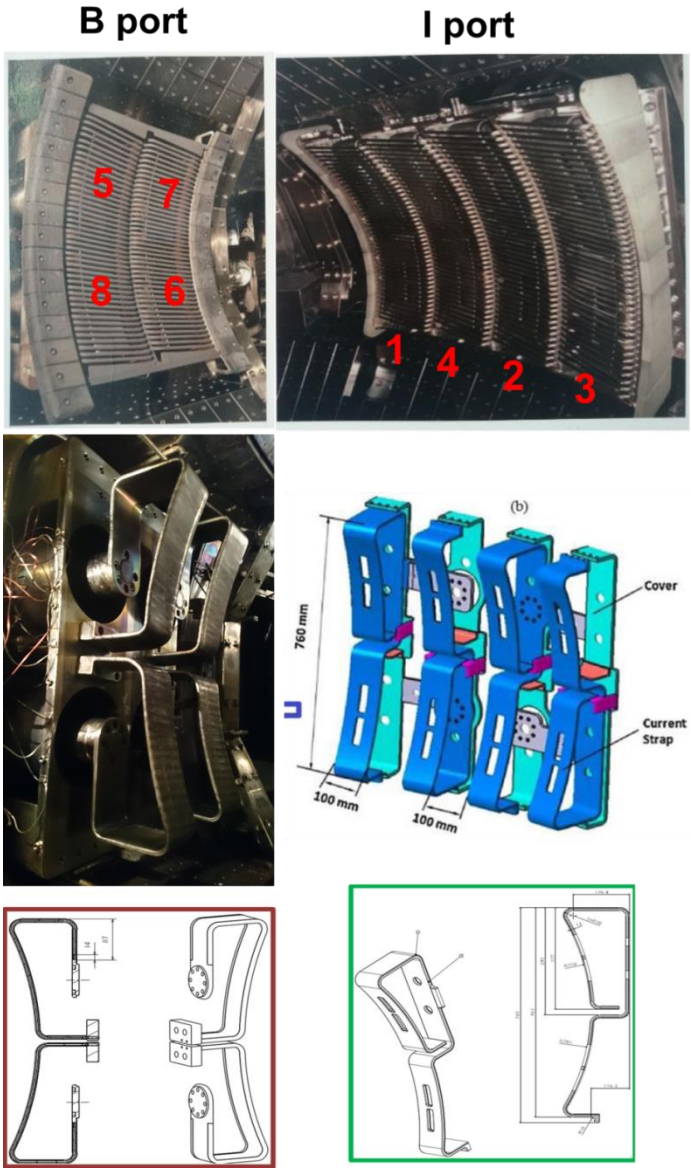

Figure 4.3: EAST B and I ports ICRF antennas pictures and straps design

The EAST ICRF antenna loading can be estimated by two different methods respectively based on voltage/current probes [J.H.Wang 2017] and voltage probe arrays [J.H Zhang 2017]. In this study we will use the second technique which often gives more accurate results due to lower sensitivity to LH-induced perturbation [J.H.Wang 2018]; for each shot, the maximum voltage Vmax is measured with voltage probe arrays in different points of each transmission lines of characteristic impedance Z_0 as shown on Fig.4.4 – respectively near the stub tuner and the antenna –. For coupling resistances calculation, we will preferentially use data of the probes that are close to the antennas. The transmitted power P_{trans} was measured by the directional

coupler in front of each transmitter. A weakness of these assessments is that they neglect losses in the transmission lines so that P_{trans} is equivalent to the power radiated by the antenna. Coupling resistances are finally calculated for each line as follows $R_c=2\ P_{trans}\ Z_0^2/V_{max}^2$ with error smaller than 5%. In chapter 5, it will be shown that only coupling resistances of one line per antenna were represented as the others followed similar trends and values. Our poor knowledge of power losses in the transmission lines prevents us from accurately quantifying the absorption efficiency of the waves. We will therefore rather talk about ICRF system "heating efficiency" defined as the ratio of plasma energy increase per generator power, regardless of any losses over the whole system.

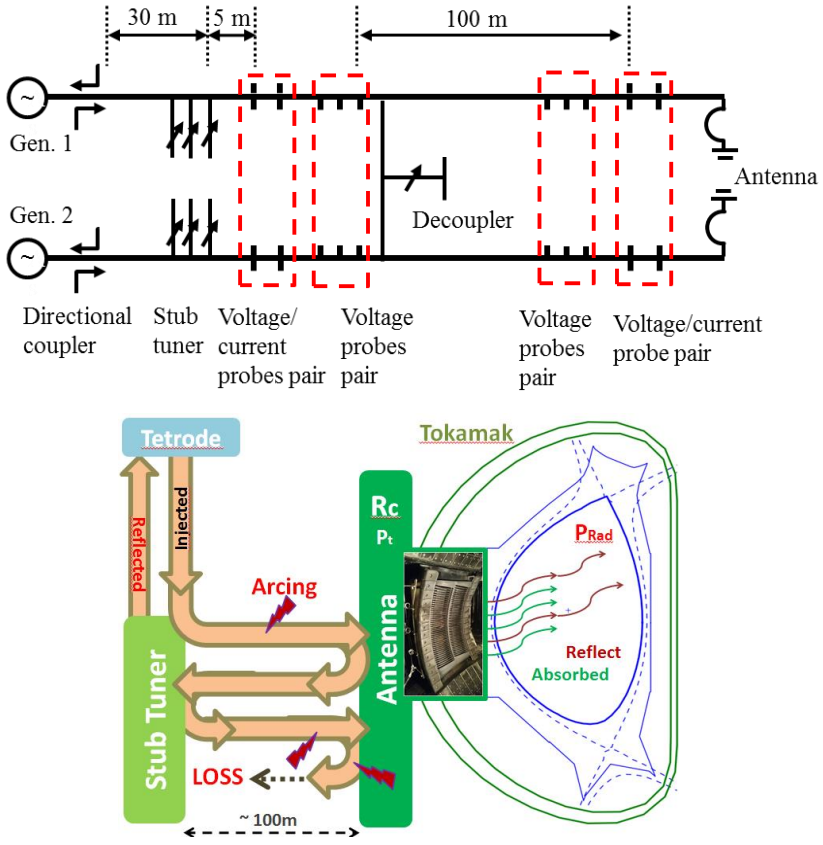

Figure 4.4: (a) Schematic diagrams of two (of eight) EAST-ICRF transmission networks. The distance between two sets of probe pairs is about 2.2 m. Courtesy [J.H.Wang 2018]

(b) Illustration of power flow in an EAST-like ICRF circuit.

4.1.3 Fueling and pumping in EAST

The routine fueling system at EAST is based on a group of valves located at the

mid-plane just above the J-port and around E-port 4.6GHz LH antenna, which control relies on piezoelectric valves [Q.P.Yuan 2009]. A Supersonic Molecular Beam Injector (SMBI) [X.W.Zheng 2013] is also used routinely for feedback control of the density as it only takes small quantities of gas to achieve good control, typically 9.10^{21} particles per second at constant pressure of about 1.5 bar. SMBI pulse typically last for 10ms and allow efficient fueling of plasma with maximal deposition around pedestal region. This is a key asset particularly for long pulse operation when density control becomes of prime importance due to increased outgassing. Local deuterium puffing was first used to improve LH wave coupling in H-mode when the density drops at the edge [E.H.Kong 2013]. After successful results on the lower hybrid system, the technique has been applied to improve ICRF wave coupling which is in general, difficult in EAST. Independently from routine fueling valves, deuterium can now be puffed locally on each LH grill and ICRF antenna through distributed piezo-valves (Fig.4.2b & 3c), and from the J-port through a single nozzle located at R=2.5m on the mid-plane (Fig.4.2b & 3d), also equipped with a piezo valve. Injecting more gas is beneficial for wave coupling; this is a consensus shared among the RF community. For the development of scenarios, the question is whether coupling can be improved while minimally disturbing the rest of the plasma, in particular without degrading the pedestal in H-mode. In the studies presented in chapter 5, we will not try to mitigate the influence that gas puffing may have on H-mode pedestals, but choose to focus on its influence on the edge in absence of ELMs. Mostly to simplify the analysis of the edge diagnostics data, but also because EAST ICRF system [J.H.Wang 2017] does not have very strong load resilience, operations in H-mode are not appropriate to the present study which is performed in L-mode.

4.2 WEST

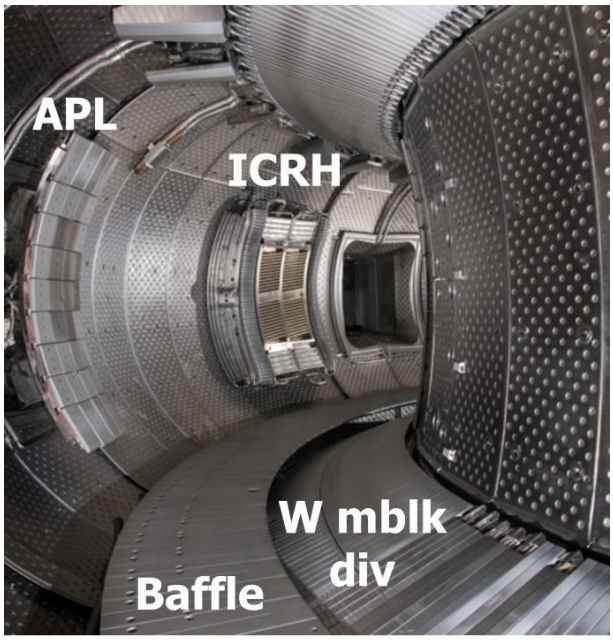

Figure 4.5: Picture of WEST inner vessel with on the left the Antenna Protection Limiter which can be moved during a discharge, the Q2 ICRH antenna, the baffle, top and bottom divertors with 12 ITER-like tungsten monoblocks plasma facing units

4.2.1 General description

WEST is an almost full tungsten (W) Environment in Steady State Tokamak [Bucalossi 2014] mostly operating in lower single null configuration with typical parameters B_o=3.7T at R_o=2.5m, a=0.5m and $I_p \approx$ 500kA. Its main goal is to validate tungsten monoblocks Plasma Facing Units design for ITER with up to 20MW/m² [Pitts 2013] provided by two LH and three ICRF antennas [Ekedahl 2015]. The LHCD system is composed of two antennas powering respectively 4 MW for the Full Active Multijunction (FAM) launcher [Bibet 1995] and 3 MW for the Passive Active Multijunction (PAM) launcher [Guilhem 2011]. The $n_{//}$ spectra are adjustable for $n_{//0}$ = 2 ± 0.3 for the FAM and for $n_{//0}$ = 1.7 ± 0.3 for the PAM. The ICRH system is the main heating system, expected to deliver once fully commissioned 9 MW for 30s, 6 MW for 60s and 3 MW for up to 1000s.

Amongst preferential diagnostics used in the thesis, WEST is equipped with an X-mode reflectometer with frequency bands respectively swept in ranges of 50-110GHz for SOL and pedestal regions and 75-110GHz for core plasma, to measure

electron density profiles starting at $n_{emin} \approx 10^{16} m^{-3}$ up to $n_{emax} \approx 4.10^{19} m^{-3}$ with 1µs time resolution. Many probes are also fixed in various regions of the vessel and will be presented further in the next section.

Two VUV-XUV spectroscopes allow measuring metal impurities in core plasma. One of them I used for safety and real time feedback control (SURVIE) while the other one (SIR) instead has a lower time resolution but higher spectral resolution and is mostly used for physics. On top of those core diagnostics, visible spectroscopy (360-420nm) was also implemented with 240 lines of sight (LOS) pointed towards each limiter and divertor [Meyer 2016]. These spectrometers will be further discussed in section 4.3. A Bremsstrahlung spectrometer with 12 poloidally spread LOS also provides a measure of Z_{eff}.

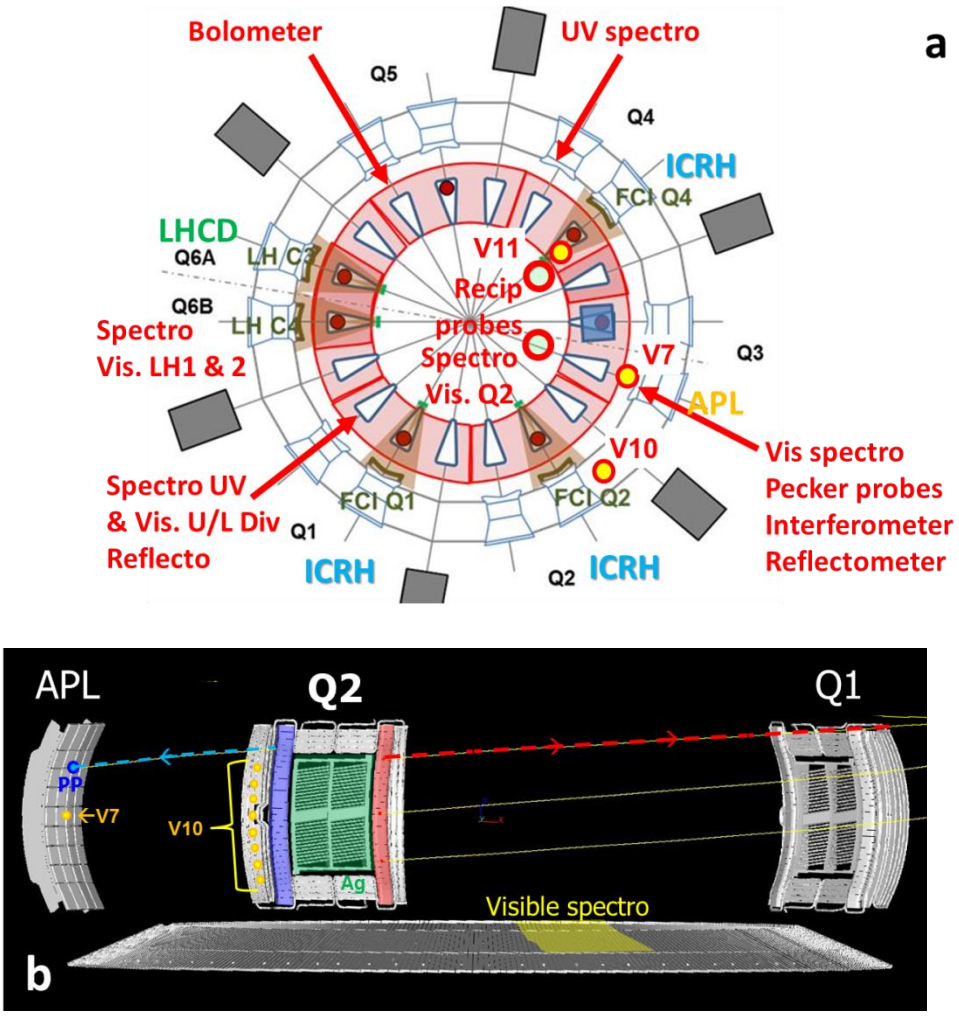

Figure 4.6: (a) Top view of WEST, with toroidal positions of heating systems and diagnostics used in the study (b) Toroidal-Poloidal (ϕ-Θ) 2D map showing magnetic

connections between objects for a case with B_T=3.7T and I_p=500kA : Reciprocating pecker probe on the Antenna Protection Limiter (APL) is indicated by a blue dot, while gas puff valves are represented by yellow dots

4.2.2 ICRF system in WEST

Each antenna has four straps, silver coated Faraday screen and CFC limiters coated with a 100µm layer of tungsten (Fig.4.7). Pairs of straps at similar toroidal location are fed by a tetrode (two per antenna) which power is split thanks to the so-called conjugate T-bridge (Fig.4.8) allowing good load resilience of the system [Helou 2015]. A capacitor is connected in series to each strap of same index (i.e. Si) and the capacitance Ci can be changed in real time, to allow adapting the matching to plasma's fluctuation [Helou 2019]. The ICRF system operates in between 48 and 57MHz in order to heat H minority nearby the center on different scenarios [Bourdelle 2015]. All antennas (LH and ICRH) are actively cooled for long pulse operation and gas can also be locally injected to increase density at the edge and facilitate waves coupling to the plasma [Jacquet 2016].

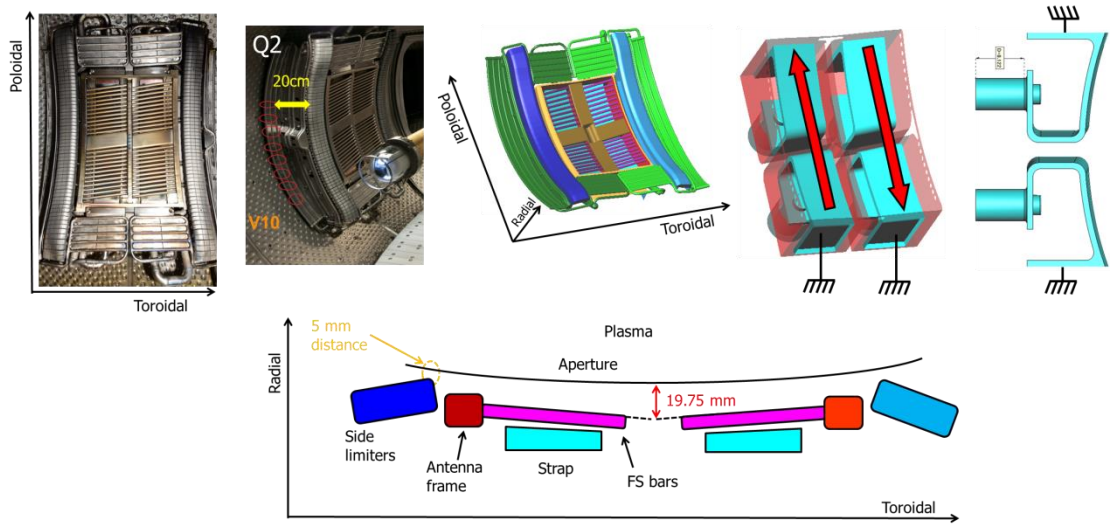

Figure 4.7: WEST ICRF antenna design.

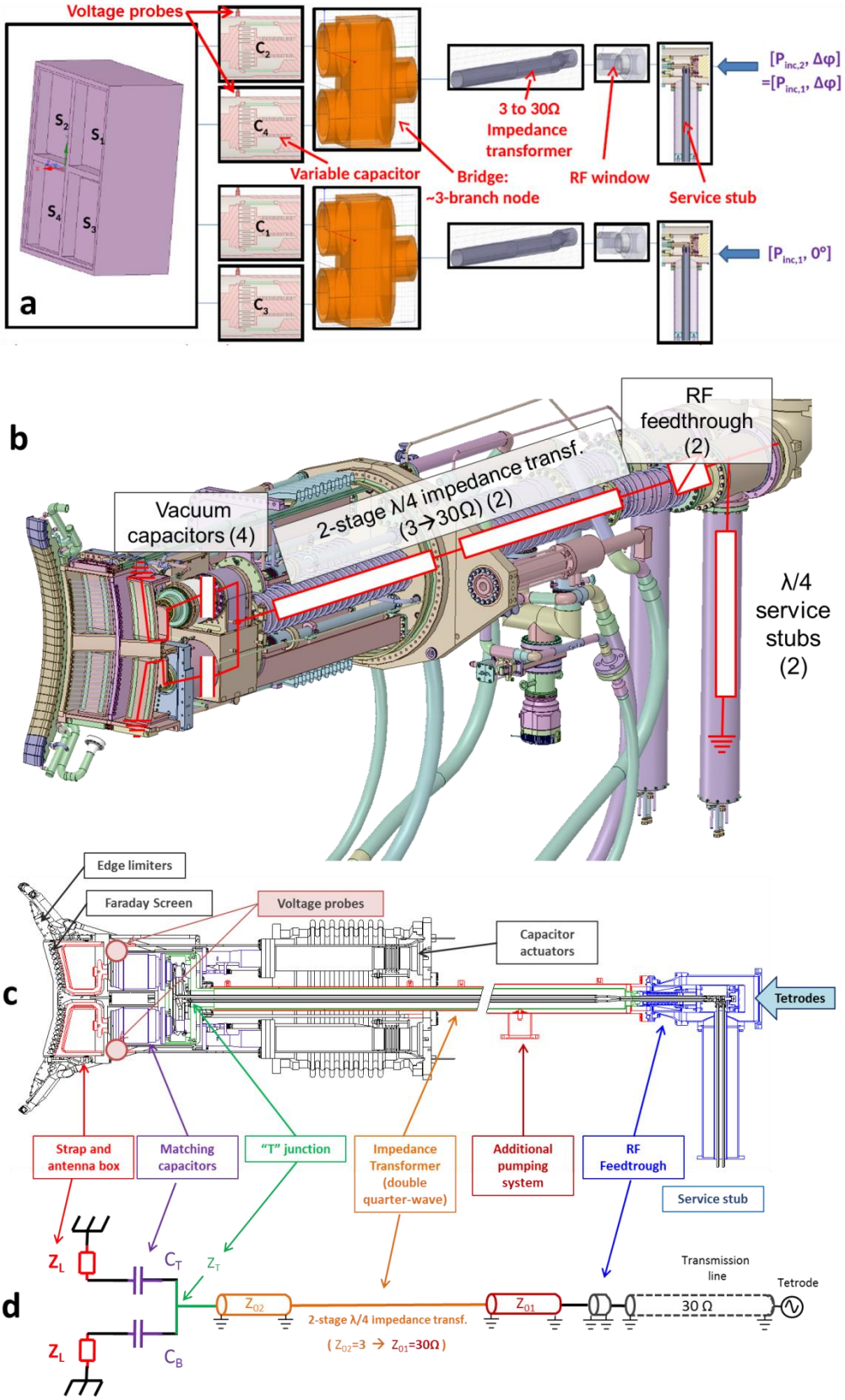

Figure 4.8: (a) Exploded, (b) 3D and (c) projected views of the WEST ICRF network with all key components and (d) analogy with an electric circuit

4.2.3 Fueling and pumping in WEST

Like in EAST, WEST plasmas are composed of a majority of deuterium (or helium during He campaign) with a minority of hydrogen and impurities. D_2 can therefore be injected through the main line represented in blue in Fig. 4.9a. This line allows injecting gas most often from the top valve (V11) and nearby any limiter at the low field side depending on the scenario, either form a single point located at the mid-plane (V7 on APL) or poloidally distributed along the object's poloidal height (cf second picture in Fig.4.7 with V10 nearby Q2 antenna) (Fig.4.9b). These valves can in principle be used to increase the density mostly locally around the antenna and improve its coupling. In WEST however, the amount of gas that can be injected is limited due to low pumping efficiency. The total capability of the nominal divertor pumping system should at term rise up to $22 m^3/s$ spread through 10 pumping ducts, however during the C3 campaign when experiments were done, only 5 ducts were available, limiting the pumping to 11 m^3/s. So far, injecting above 5.10^{20} e/s would result in a fast increase of the plasma density, incompatible with steady state operation. These aspects will be further discussed in the next chapter [Urbanczyk 2019]. Four other valves are distributed along the torus respectively nearby inner and outer targets of the upper and lower divertors, but these can only be used in steady state long pulses due to long time response and slow effect on plasma density.

Two other sets of valves are used to inject impurities and hydrogen. These are typically used for wall conditioning with boron (deuteriated diborane) or glows, impurity seeding applications, and also to tune the H concentration at its optimal value for maximizing ICRH absorption. These piezo-electric valves only open above some threshold voltage and are therefore not made for injecting tiny quantities of gas (less than 10% of the quantities of deuterium injected), which is why the hydrogen concentration until 2019 was often too low (<3%). From 2019, a bottle with a mix of 90% D_2 and 10% H_2, is used on the main line to allow reaching higher H concentration and hopefully improve ICRF heating efficiency.

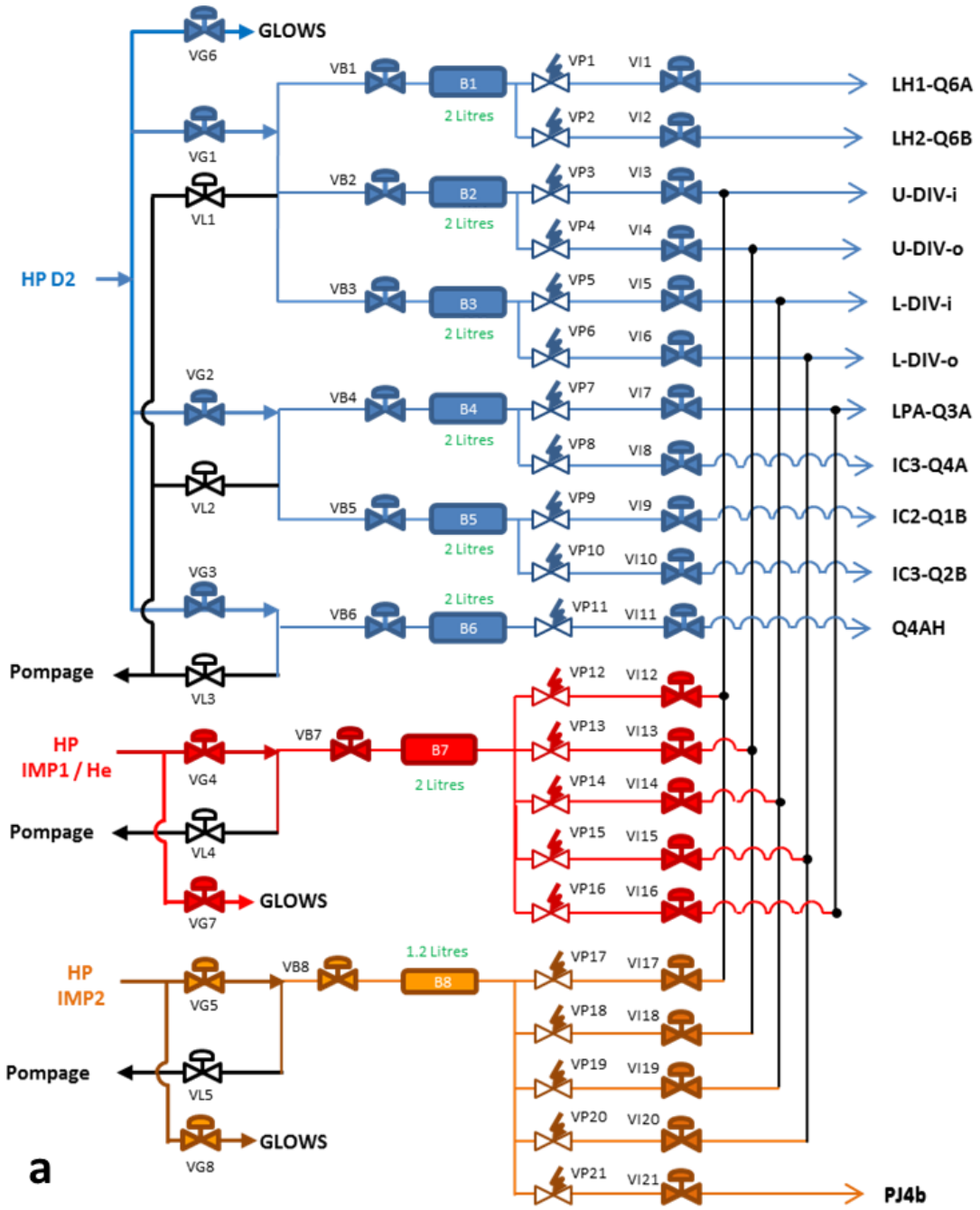

Figure 4.9: (a) Matrix of WEST gas fueling system

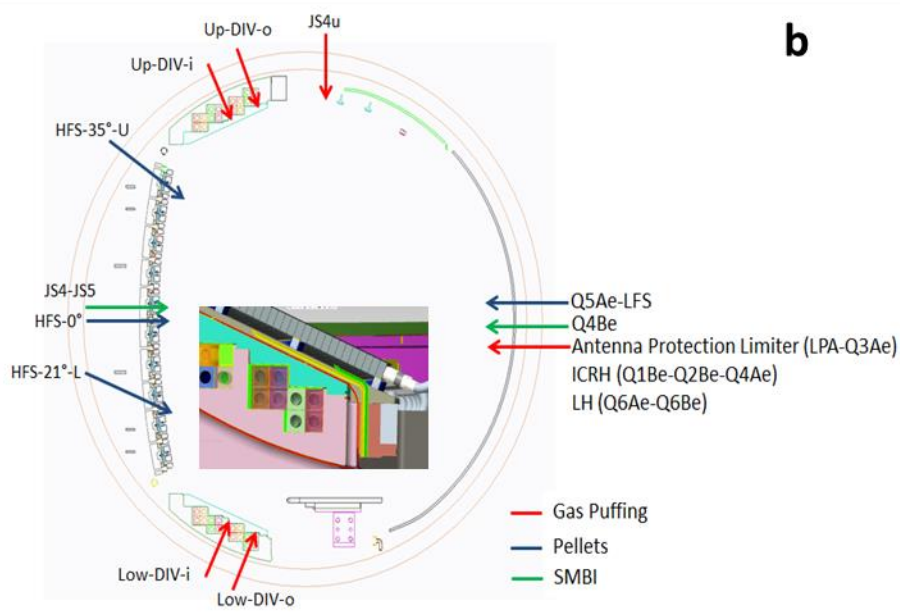

Figure 4.9: (b) Valves location on a poloidal cut view

4.3 Key diagnostics used in both devices

Many diagnostics were used in both devices such as the bolometry for the radiated power, the interferometry for line-integrated density, the reflectometry for density profiles [S.Zhang 2014], the ECE for temperature profiles, voltage probes for RF power, magnetic probes for plasma energy … and spectroscopy to characterize impurities in the plasma. Ultraviolet (UV) spectroscopy, also present in both tokamaks, was extensively used and will therefore be detailed in section 4.3.2.1. Only in WEST was used visible spectroscopy lines of sight pointed toward limiters of ICRF antennas and others limiters partially connected to them to locally characterize impurity sources (section 4.3.2.2). Langmuir probes were also used in both devices with different design, different electronics and in different locations. Theory of I-V curve characteristics is first explained. Triple probes designed, built and implemented in EAST for the thesis are then presented. And WEST double probes method is then briefly described.

When analyzing either visible spectroscopy or Langmuir probes data, the notion of *magnetic connection* will play an important role like in experiments summarized in Fig.3.3. The idea to have in mind being that particles follow magnetic flux tubes, and that when an effect is measured on a surface facing the SOL plasma, it most likely

propagates along the magnetic field line starting from the surface on one side, and reaching another surface elsewhere in the vessel. We will therefore pay specific attention to the magnetic connections between diagnostics and ICRF antennas, which allows characterizing RF sheath influence from various locations.

4.3.1 Langmuir Probes

Langmuir probes constitute one of the older diagnostic having been used for a century to measure plasma parameter simply by inserting in it a piece like of metal like those represented on Fig.4.10. They are cheap, easy to manufacture, to install and to use. They provide data with high temporal and spatial resolutions that allow calculations of plasma potential φ_p, electrons temperature T_e and density n_e. They consequently constitute a very useful tool for the study of plasmas with relatively cold temperatures that materials can sustain, which is the case of the Scrape-Off Layer (SOL) plasmas in tokamaks. Yet, Langmuir probes sensitivity to several phenomena specific to tokamak plasmas leads to couples of drawbacks that will be discussed in this section.

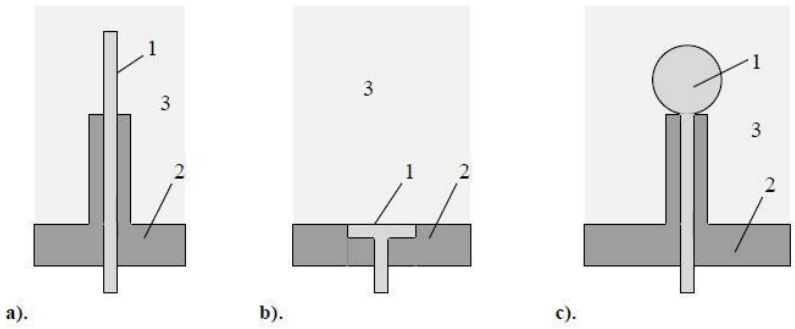

Figure 4.10: Different Langmuir tips geometries

4.3.1.1 Langmuir Probes theory – I-V curve

Most classic Langmuir probes consist in applying a voltage to a piece of metal plunged inside the plasma. Then the metal collects a small current from the plasma, measured across a voltage divider which resistance value can be adapted to the magnitude of currents measured. The voltage applied is then swiped, so that a

current-voltage characteristic – I-V curve – can be drawn such as the one on Fig.2.5, from which can be extracted the three parameters of interest. Yet, Langmuir probes biggest drawback arises at this point, where slightly abusive physical approximations are necessary for the mathematical treatment of I-V curves.

We have seen in the third and fourth parts of the previous chapter that sheaths form on surfaces of any material plunged in the plasma, locally changing plasma properties and consequently probe collection conditions. This phenomenon further depends on probe geometry (Fig.4.10) and plasma characteristics. In practice, classical theory is used even if it may leads to more or less wrong results, depending on the following conditions:

1) Plasma isotropic over a larger scale than particles mean free path
2) Probe dimension much larger than sheath width (order of Debye length)
3) Collisionless sheath (sheath width much smaller than particles mean free path)
4) Particles gyroradius larger than probe dimension (weakly magnetized plasma)

→ Same effective collection surfaces for ions and electrons

In case of very thin tips (smaller than ions Larmor radius), ions effective collection area corresponds to the whole probe surface whereas electrons follow too closely magnetic lines and are only collected on the probe projection surface projection according to background magnetic field direction

5) Secondary electron emission neglected
6) Current collected by the probe can be neglected in front of plasma current
7) Quasi-neutral plasma at probe's proximity
8) Electrons energy follows a Maxwellian distribution
9) Clean probe surface (impurities neglected)
10) Cold probe (tips temperature bellow 500°C)

With those conditions respected, we can start extracting information from the I-V curve. Respectively three values can be identified on the curve for Fig.2.5 to calculate the three physical parameters of interest:

- *Floating potential* φ_f (or V_f) corresponds to the point with a null current. Any non-polarized and insulated metal object plunged into the plasma is not collecting any net current, it is floating. Its potential adjusts on the so

called floating potential to preserve particles fluxes ambipolarity. Usually, as soon as it is plunged in the plasma, a sheath forms on its surface and it starts collecting more electrons than ions, so that its potential drops to negative values to equilibrate fluxes. This explains why we often expect the floating potential to be negative. Notice that what the probe collects depends on the surrounding plasma, which is itself quasi but not neutral ($\varphi_p \neq 0$). This means equilibrium can still be reached with floating potential values smaller than the plasma potential but not necessarily negative.

- *Electrons saturation current* J^-_{sat} (or V_p) corresponds to the regime when the probe potential is above plasma potential, so that it mainly collects electrons leading to positive and large current values.
- *Ions saturation current* J^+_{sat} (or I_s) is reached when the biased voltage is significantly lower than plasma potential, so that the probe mainly collects ions leading to negative and small current values

Once those three parameters are identified, an expression must be found to link them to the plasma potential, electron temperature and density. Let then use the 8th approximation and mathematically express the fact that electrons follow a Maxwellian distribution:

$$f(v_e) = n_e \sqrt{\frac{m_e}{2\pi k_B T_e}} \exp\left(-\frac{m_e v_e^2}{2k_B T_e}\right) \tag{4.1}$$

We then write the definition of the current received by the probe at potential V:

$$j = e \int_{-\infty}^{+\infty} \int_{-\infty}^{+\infty} \int_{v_{\min}}^{+\infty} v_z . f(v_x, v_y, v_z) . dv_x dv_y dv_z \tag{4.2}$$

With $v_{\min} = \sqrt{2e(\phi_p - V)/m_e}$. After calculation of the integrals and multiplying both side of the equation by the probe collection area A we obtain the electrons current collected by the probe:

$$\begin{cases} J_e(V > \phi_p) = J^-_{sat} \\ J_e(V \leq \phi_p) = J^-_{sat} \exp\left(\dfrac{-e(\phi_p - V)}{k_B T_e}\right) \end{cases} \tag{4.3}$$

With

$$J^-_{sat} = e.n_e v^e_{th} A/4 \tag{4.4}$$

With $v_{th}^{e} = \sqrt{8k_B T_e / \pi m_e}$ the electron thermal speed. This expression corresponds to the right part of the Fig.2.5 materialized in blue, where probe current is dominated by electrons because its potential is too high. As it decreases, blue zone meats with red zone, they merge and create a purple zone of transition. Probe electrons collection decreases exponentially while it reciprocally starts collecting more and more ions. Same expression consequently works in the red zone for ions:

$$\begin{cases} J_i(V \geq \phi_p) = -J_{sat}^{+} \exp\left(\dfrac{e(\phi_p - V)}{k_B T_i}\right) \\ J_i(V > \phi_p) = -J_{sat}^{+} \end{cases} \tag{4.5}$$

With $J_{sat}^{+} = e.n_i v_{th}^{i} A/4$ and $v_{th}^{i} = \sqrt{8k_B T_i / \pi m_i}$ the ion thermal speed. Note we already met this expression in equation 2.41. Note also that the expression of the ion saturation current given in equation 2.40 is different than the one above. This is because if the temperature of electrons is significantly higher the one of ions – which is sometimes but not always the case in a sheath – the dynamic is no longer determined by ion thermal speed but by Bohm speed so that the ion saturation current takes the form of:

$$J_{sat}^{+} = 0,6.A.n_e \sqrt{k_B T_e / m_i} \tag{4.6}$$

From eq. 3.3 taken in the middle zone of Fig.2.5, it is now possible express the temperature in function of the electron saturation current gradient such as:

$$k_B T_e = e / \left| \frac{d \ln(J_e)}{dV} \right|_{V \leq \phi_p} \tag{4.7}$$

From equation 4.5 we then get the expression of the electron density:

$$n_e = J_{sat}^{+} / 0.6A\sqrt{k_B T_e / m_i} \tag{4.8}$$

Finally, *plasma potential* φ_p is the potential of the plasma with respect to the ground. In practice it corresponds to the potential of the space around the probe. It is not the same in the whole plasma and especially not in the SOL where sheaths can induce significant modifications and electric fields as we have seen in the previous chapter. This potential is defined as the inflexion point of the I-V curve and can be expressed as follow:

$$\phi_p = \phi_f + \frac{k_B T_e}{e} \ln\left(\frac{J_{sat}^{-}}{J_{sat}^{+}}\right) \tag{4.9}$$

4.3.1.2 Triple Probes

As we just saw, only three points of the curve (floating potential, ion and electron saturation currents) are really needed to calculate the three parameters of interest. Moreover, drawing the whole I-V curve sets the diagnostic time resolution limits; since voltage cannot be swept too fast else particles do not have enough time to respond. Instead, another method illustrated on Fig.3.2 consists in using three tips. One is floating ($V_f \sim \varphi_f$), and the two others biased positively ($V_p \sim J^-_{sat}$) and negatively, respectively measuring the electron and ion ($I_s \sim J^+_{sat}$) saturation currents.

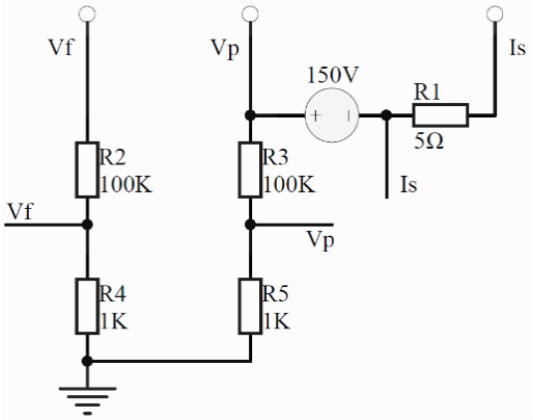

Figure 4.11: Electronic circuit of triple Langmuir probes used on EAST

From those three signals, the same parameters as before can be calculated directly:

- Electron Temperature: $T_e = (V_p - V_f)/\ln 2$ (4.10)
- Electron Density: $n_e = I_s/(eA\sqrt{2T_e/m_i})$ (4.11)
- Plasma Potential: $\phi_p = V_f + \alpha_{cold} T_e/e \approx V_f + 2.8T_e/e$ (4.12)

Those formulas are written on the form used in practice for computing the three parameters. At first approximation, this seems like a good option; the electronic circuit is very simple and cheap, three formulas above are easy to compute and time resolution is no longer limited by voltage sweeping, so it can be pushed until

acquisition card limits enabling to observe smaller time scale fluctuations and used for instance for MHD studies. Yet spatial resolution is reduced since the three calculated parameters are no longer based on one tip measurements but on three, so that calculations lead to average values in the space between the tips, of the fairly small order of centimeter. A more serious problem concerns formula 4.12 which coefficient α_{cold} corresponds to a cold probe with:

$$\alpha_{cold} = \ln(J_{sat}^{-} / J_{sat}^{+}) \approx \ln(\sqrt{\pi m_i / m_e}) \overset{D}{=} 2.8 \tag{4.13}$$

Yet, as plasma parameters change – power injected, shape, gap-out, discharge duration, density, temperature – plasma-materials interaction can become very serious. This is especially true for reciprocating Langmuir probes that can enter deep inside the plasma and be subject to very strong heat loads. In those cases, tips heat up, so that the 10th cold probe condition is violated and eq.4.12 should not be used. If temperature keeps increasing further, tips might start emitting electrons and the 5th approximation would be violated too, since secondary electron emission cannot be neglected anymore. This can happen when plunging too deep inside the plasma, for instance around the Last Closed Flux Surface (LCFS). In such case, α_{cold} should be replaced by the hot version:

$$\alpha_{hot} = \ln\left(\frac{J_{sat}^{-}}{J_{sat}^{+} + J_{emitted}}\right) \approx 1 \tag{4.14}$$

With $J_{emitted}$ the emitted current. This explains why plasma potential tends to be overestimated by Langmuir probes. Another problem concerns the 9th approximation of clean probe. In many tokamaks indeed, it is current to use different kinds of coating to prevent high-Z impurities from being sputtered into the plasma. Before starting the experiments, a low-Z material such as silicium, boron or lithium can be sprayed on all PFCs so that instead of dealing with heavy impurities that have bad consequences on radiation losses, light impurities are sputtered, ionized only few times and have little impact on the discharge. In EAST specifically, lithium has become a daily step before experiments start. Every morning, lithium is sprayed on the whole vacuum vessel volume, including fixed probes. This abusive used of lithium coating is consequently one more factor that influences probes measurements. Yet on top of those drawbacks, the worst one concerns the influence of ICRF-induced RF-DC rectification discussed in section 2.4. Looking back at both equation 2.49 and Fig.2.9, we see that the influence of RF waves is to bias the surface to a DC potential. I-V characteristics

translate horizontally so that we cannot know if the fluctuations observed on measured signals are real or a consequence of the rectification. In addition, as we saw on eq. 2.48, the effect gets worst as RF power is increased. Furthermore, applying Poisson's equation in a sheath and solving it with appropriate conditions, RF sheath thickness can be expressed from *Child Langmuir Law* :

$$\delta_{sheath} \propto \lambda_{De} \left| \frac{\phi_p - V_{tip}}{T_e} \right|^{3/4} \tag{4.15}$$

From this expression, thickness of the sheath around the tip appears to increases when its voltage decreases towards the ion saturation regime. Because collection surface increases with the sheath, so that saturations is never reached on ion branches of the I-V characteristic. As a consequence, each single tip I-V characteristic expression cannot be formulated. This represents a big problem for triple probe technique which is not even drawing the I-V curve but only taking a guess on the three points positions. The estimation of the reliability of Langmuir probe measurements under RF environment constitutes one of the biggest challenges of this diagnostic. It is still possible to evaluate if the effective collecting area of the probe is dominated by its geometry of by the sheath, by calculating the ratio of the current collected without sheath $I(V_{tip}=\varphi_p)$ to the sheath expended current $I(V_{tip}=-150V)$. Note that sheath width expressed in equation 3.15 is indeed minimal when a tip is biased at the plasma potential. In practice however, since voltages are fixed in the triple probe configuration, the currents with and without sheath can fairly be approximated by the ion and electron saturation currents; $I(V_{tip}=-150V) \approx J^+_{sat}$ and $I(V_{tip}=\varphi_p) \approx J^-_{sat}$. The ration of equations 4.4 to 4.6 finally provides a convenient form to validate the relevance of experimental results:

$$\frac{J^-_{sat}}{J^+_{sat}} = \frac{1}{0.6}\sqrt{\frac{m_i}{2\pi m_e}} \tag{4.16}$$

If the experimentally calculated left member of the equation is close to the right member predicted by theory, then it can be said of the data that they are relevant, otherwise the formulas 4.10, 4.11 and 4.12 may lead to results with unacceptable errors.

4.3.1.3 Implementation in EAST

At the beginning of the thesis the lack of diagnostics in the edge and surrounding of ICRF antennas required to develop some diagnostics myself, including their design, fabrication, installation in the vessel, wiring, installation of acquisition system, and development of tools to treat and analyze the data. I started by designing a reciprocating probe head combining an emissive wire with a triple probe which was inserted in one of the ports, unfortunately the wire burned too rapidly and the probe could not often be used not to perturb the discharges. I therefore designed other triple probes which were fixed in arrays nearby ICRF antenna and in magnetically connected regions (Fig.4.12). A protective head was this time added to improve both the reliability and the sustainability of the probe. To mitigate sensitivity to the RF sheath, the principle is to constrain the plasma to be sampled by lateral holes whose inner surface is approximately parallel to the magnetic field lines, preventing large sheath expansion. Despite those design efforts to reduce sensitivity to the RF sheath, ongoing-upgrades are still needed to improve the probe's data in the presence of ICRH.

Finally, the Langmuir probes were fixed on B-port antenna's left limiter and are seen on Fig.4.12. Two probes on the mid-plane and three to the top where the strongest RF sheath rectifications and heat loads are expected from previous studies (see [Colas 2007] and [Bobkov 2010] and references therein). Note that every Langmuir probe is actually a triple probe, capable of high temporal resolution sampling at the expense of often stronger sensitivity in RF environments due to sheath rectification. Special effort was consequently put into optimizing the design of the three probes fixed to the top of the antenna. Inspired by tunnel probes [Gunn 2016] we added protective head that constrains the tips to sample the plasma from lateral holes, the area of which is less sensitive to sheath expansion than if the tip were entirely exposed to the plasma (Fig.4.12 a & b) [Urbanczyk 2017]. Furthermore, such a design offers the advantages of being much more robust as tips do not get eroded as fast as when directly exposed to the plasma, and the data reliability is also improved as only a small part of the tip is exposed, greatly diminishing global heat loads and expected to prevent occurrence of secondary electron emission. Despite those design efforts to reduce sensitivity to the RF sheath, ongoing-upgrades are still needed to improve the probe's data in the presence of ICRH. In addition, eight B-dot probes

were fixed to a corner of the B-port antenna (Fig.4.12c), four of them having an aperture aligned with the magnetic field lines and the others having apertures perpendicular to the field lines, each type measuring fast and slow wave amplitudes, respectively [Ochoukov 2017].

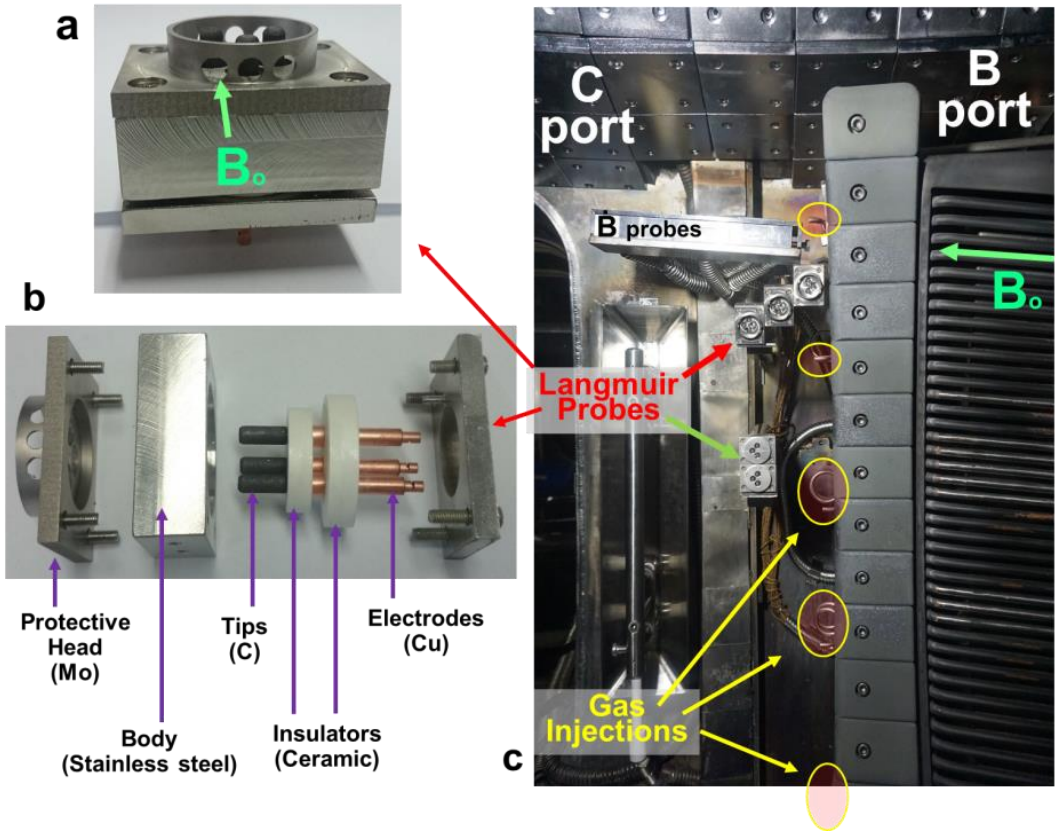

Figure 4.12. (a) View of the Langmuir probe mounted emphasized by lateral holes to collect plasma (b) Exploded view of the same probe with each piece of material detailed (c) Picture in EAST between C and B ports showing antenna lateral gas injectors, Langmuir and B-dot probes fixed in 2017

4.3.1.4 Double probes in WEST

In WEST, all the probes were already developed and installed by Jamie GUUN and Jean-Yves PASCAL, I only learnt how to pilot the pecker probes and analyze the data. Double probes technique consists in using two tips polarized with a single power source (KEPCO 200V-1A) which voltage is swept. Alternatively voltage increases on one probe while it decreases on the other one. This double probe configuration

constitutes a natural protection against overheating due to excessive electron current collection which often occurs on the positively biased tip of triple probes. Moreover, strongest asset of double probes concerns RF sheath problem mentioned previously. When probe voltage goes towards ion saturation regime, sheath expands so that saturation cannot be reached and I-V curve expression cannot be formulated. With double probes however (Fig.4.13), one probe can be set as reference, and its voltage with respect to the ground (V_1) can be measured across a high resistance voltage divider so that almost no current flows into this part of the circuit. Voltage source being measured in the same way, the voltage of the second tip is simply the sum of both ($V_2= V_1+V$). The key point is that the same current flows through each tip with opposite signs, so that each tip half of I-V curve can be drawn against each other's to form a full I-V curve passing through the origin; respectively
$I_1=-I(V_1)$ for the first tip and $I_2=I(V_2)$ for the second with $I_1= -I_2$. Everything happens as if the whole system is floating. The RF→DC rectification voltage expressed in equation 2.48 is now measured by the reference probe, so that any sheath rectification automatically rectifies I-V curves axis position.

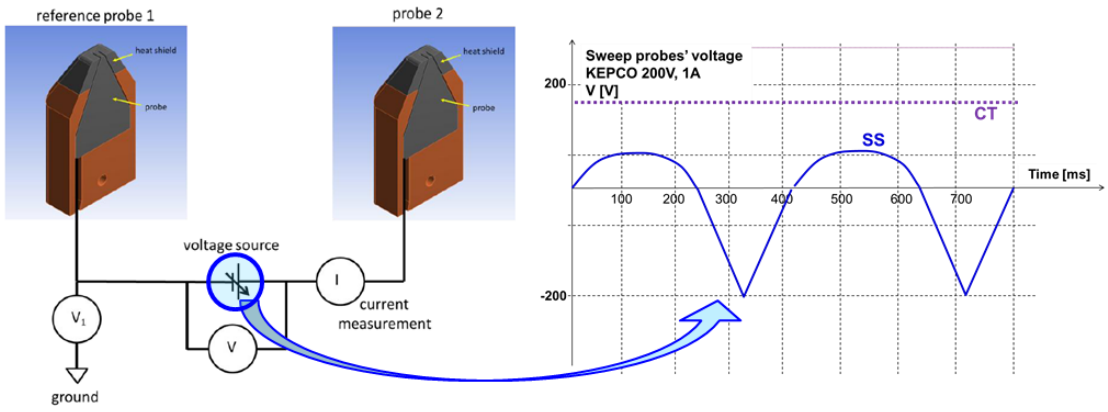

Figure 4.13: Double probes wiring method used in WEST and probe voltage signal (Courtesy of J. Gunn from ITER report on Langmuir and mousetrap probes)

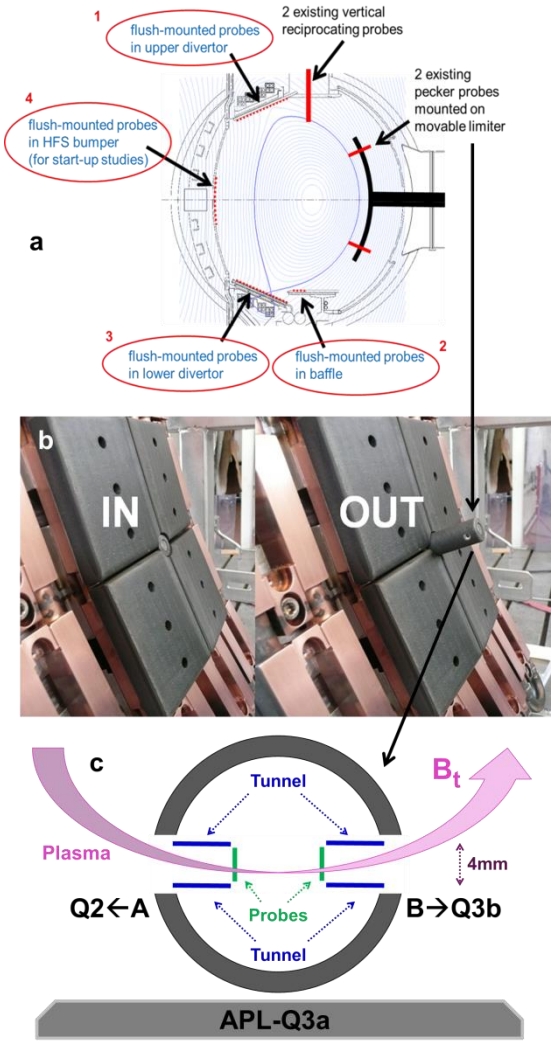

Figure 4.14: Probes in WEST vessel and cartoon of pecker tunnel probes on APL

Langmuir probes can be found in many different locations in WEST, summarized in Fig. 4.14 and all mounted with the similar electronics presented in Fig 4.13. Reciprocating tunnel probes [Gunn & Pascal 2011] are symmetrically installed 25cm on top and to the bottom of the mid-plane on the APL (Fig.4.14). Only the top one was represented in Fig. 4.6b because it sampled most of the data presented in the thesis. Tunnel and plate voltages are swept between -200 and 50 volts, allowing also both floating potential and ion saturation current measurements. As the probe magnetically connects to the top of the Q2 ICRH antennas, it is used to measure potential rectification nearby Q2 antenna limiter when powering it. This will be further discussed in the following chapters and can also be used to benchmark several assumptions made in sections 2.1 and 4.3.1.1. Ion saturation current is often used to

estimate the local electron density, but it can also be used to estimate ions flux as follow:

$$I_{sat} = \sum_{Z} Z.\Gamma_{Z\parallel} \geq \Gamma_{D^+\parallel} \tag{4.17}$$

I_{sat} includes all ions and not only deuterium, but we will make the assumption that I_{sat} is only due to D^+ ions parallel flux. This is fairly true for relatively clean plasmas, and becomes less acceptable as the impurity content increases.

$$\Gamma_{D^+\parallel} = \frac{I_{sat}}{e.S_{aperture}} \approx 1,1324.10^{-24}.I_{sat}\left[ions/m^2/s\right] \tag{4.18}$$

Under some assumptions, this equation therefore allows to asses ions fluxes with probes. We will show further in section 4.3.2.2 that these fluxes can also be assessed by visible spectroscopy.

4.3.2 Spectroscopy

Spectroscopes are used to study the interaction between matter and electromagnetic radiation. It has therefore a wide range of applications such as chemistry, medicine, up to astronomy and physics. The most common type of spectroscope is an eye, capable of observing radiations emitted in the so-called visible wavelength range roughly going from 380 up 780nm. In plasmas, ions emit radiations of different wavelengths depending on their nature and ionization state. The spectrum radiated by a given plasma therefore depends on its composition and temperature. An atom sputtered from a Plasma Facing Component (PFC) of any composition (Li, C, Fe, Cu, Ag, Mo, W), is therefore released in a plasma with a majority of deuterium and is seen as an impurity since it basically cannot contribute to fusion reactions which is the main goal (Fig. 4.15). Nearby the surface (edge), plasma is relatively cold and only neutrals excitation and smallest ionization states can be observed with visible spectroscopes. As impurities penetrate deeper in the plasma core, temperature increase and impurities are ionized many times and can be observed with Ultraviolet (UV) spectroscopes. It is therefore useful to have both types of spectroscopes in order to characterize impurity sources with a visible spectroscope and study their influence on plasma core contamination with an UV spectroscope.

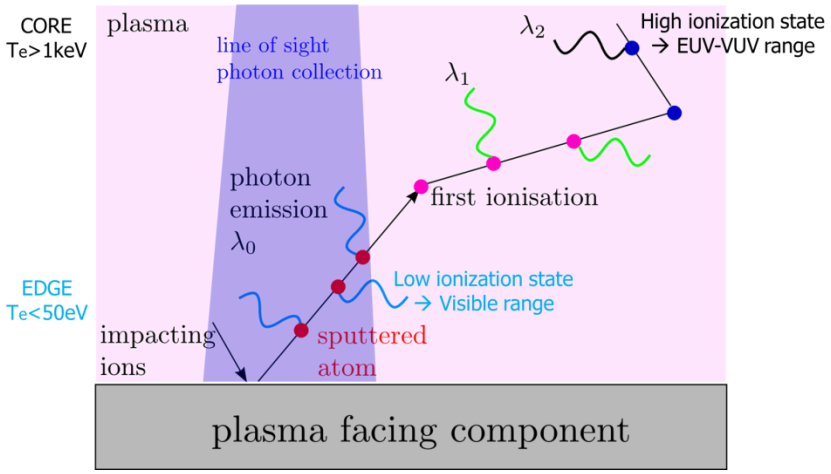

Figure 4.15. Illustration of atom sputtering and successive ionizations in plasma with increasing temperature

4.3.2.1 Ultraviolet spectroscopy

In EAST, the brightness of various high-Z impurity lines (20Å to 150Å) are monitored with a flat-field extreme ultraviolet (EUV) spectrometer [L. Zhang 2015]. Spectra emitted by the plasma are reflected with 87° incidence on a concave holographic grating focal-plane and collected by a CCD camera of 26.6×6.6mm² with 1024×255 pixels. Wavelength resolution can be optimized down to 0.22-0.3Å defined as full width at half maximum. The spectrometer is measuring W continuum (noted W for W-UTA, which is an average of all spectral lines from W^{27+} up to W^{45+}) and a series of lines brightness which those of most interest for discussions in the last chapter are summarized in Fig.4.16.

Ions	λ (Å)	E_i~Te (keV)	ρ
Ti^{17+}	144.76	1.2	< 0.7
Mo^{31+}	127.87	1.8	< 0.5
Fe^{22+}	132.91	1.9	< 0.6
W-UTA=$W^{24+\rightarrow 45+}$	45→70	0.5	< 0.85

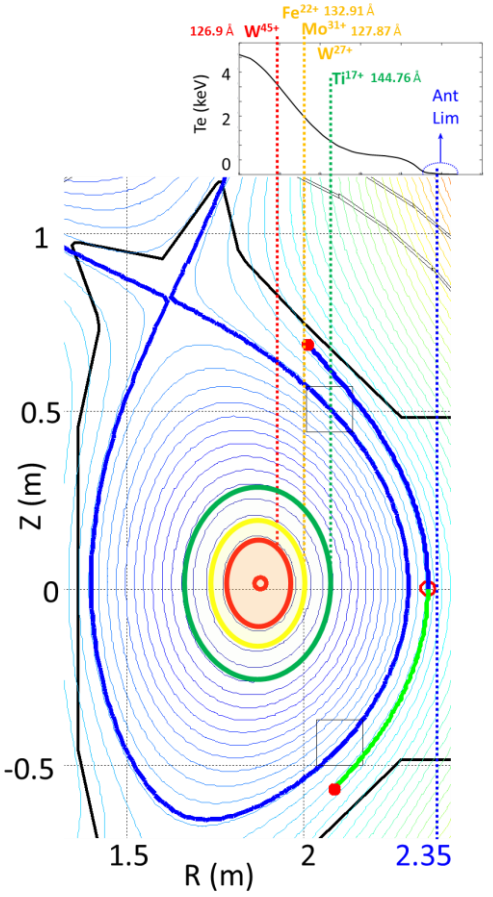

Figure 4.16: Spectral lines observed by EAST EUV spectrometer in the present study with the corresponding emitted wavelength λ, temperature T_e to maximize given ionization states and normalized radius ρ at which ionization roughly occurs in typical EAST plasmas.

In WEST, two VUV-XUV spectroscopes allow measuring metal impurities in core plasma, with wavelengths respectively ranging from 0.5 to 70nm and 22 to 30nm. While the one has a lower spectral resolution but is resolved in real time to serve as safety system in case of critical plasma surface interaction events (SURVIE), the other has lower time resolution but is more versatile with better spectral resolution allowing more accurate physics studies (SIR), we will therefore mostly use the latter one [Scwhob 1987].

The SIR wavelength domain is 15-350 Å with its 600 g/mm grating (standard set-up) and 30-700 Å with its 300 g/mm grating. The grating can be selected between pulses.

The spectrometer is equipped with two identical detectors. Between pulses, the central wavelength of each detector can be selected by moving them along the Rowland circle. The wavelength interval viewed by a single detector (with the 600 g/mm grating) varies from 25 Å at the short-wavelength end to 65 Å at the long-wavelength end of the range. Thanks to the mechanical accuracy of the design and manufacturing, the instrument function width (which can be taken as the resolution) is 0.25 Å throughout the wavelength domain. The typical time resolution is 30ms. The shortest data acquisition period is 15ms. The SIR can also oscillate to have its line of sight scanning the lower half of the plasma. For this purpose the spectrometer is mounted on a movable cradle equipped with a hydraulic jack. The fastest frequency is 0.5 Hz. This allows measuring a radial profile in 1s. The wavelength calibration has been performed by a careful and systematic analysis of the spectra in various plasma conditions. It benefits from a wavelength calibration valid over the entire wavelength domain within 0.2 Å. For any given position of a detector, there is a specific calibration allowing reaching an accuracy of 0.05 Å. It is absolutely calibrated in brightness. The calibration is performed every few years with the help of an ultrasoft-X ray source of the Manson type equipped with a 100% efficiency proportional gas counter.

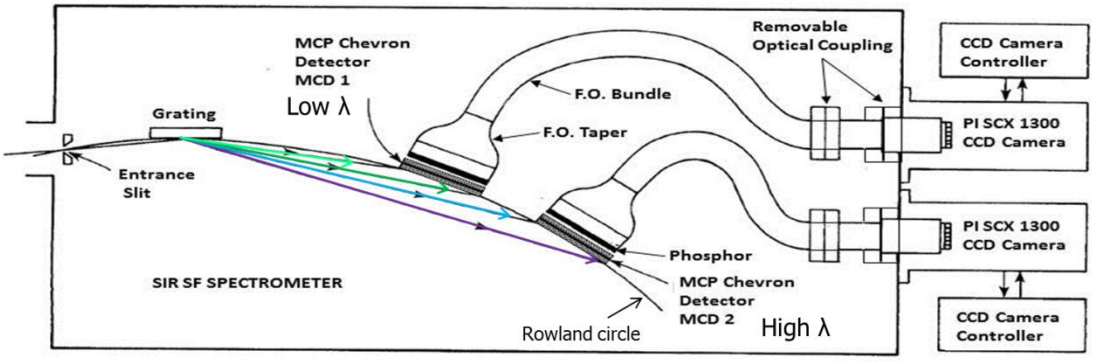

Figure 4.17. Scheme of the SIR spectroscope

4.3.2.2 Visible spectroscopy

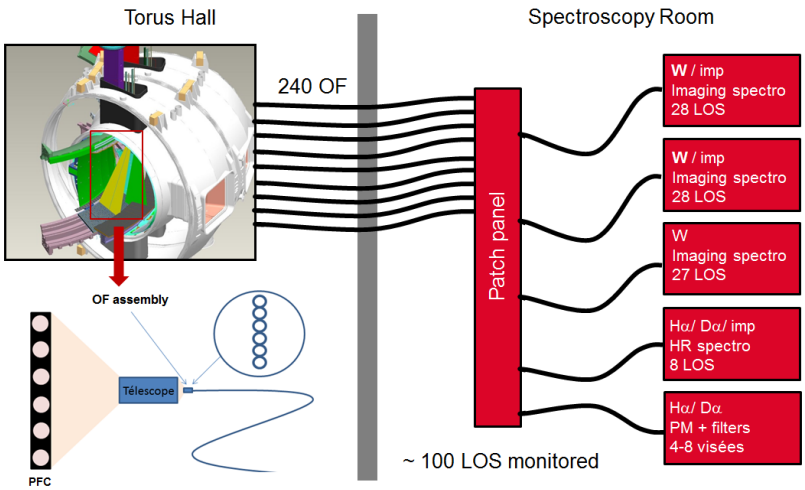

Figure 4.18: Schematic view of WEST visible spectroscopy system

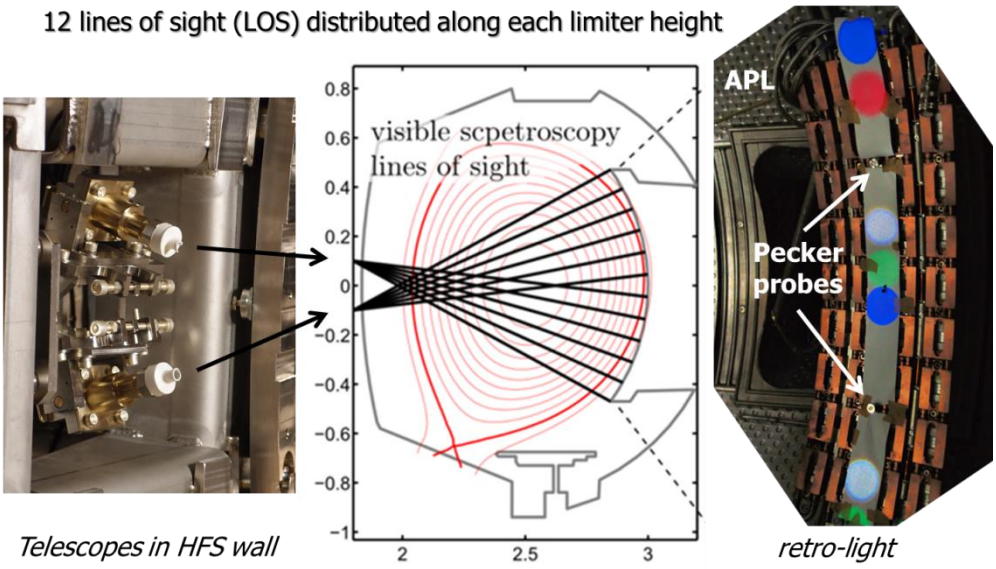

Figure 4.19: Pictures of the telescopes embedded in the High Field Side (HFS) wall with Lines Of Sight (LOS) looking along the Antenna Protection Limiter (APL) poloidal height with about 9cm special resolution

WEST visible spectroscopy (Fig. 4.18 and 4.19) is composed of 240 lines of sights looking at different objects such as divertor (10mm spatial resolution) baffle and most antennas protection limiters (86mm spatial resolution or 12 LOS along

poloidal height of each limiter) [Meyer 2016]. Two spectrometers with spectral resolution of 1Å however only allow monitoring 28 LOS each, such that only 56 LOS can simultaneously be used, hence the importance of optimizing monitored lines depending on what scenario require. All LOS are relatively calibrated, while only one line serves as reference and is absolutely calibrated (Photons/m².s.sr) to allow quantitative studies. First impurity sources where characterized during the first WEST experimental campaign [Meyer 2018].

W outflux is the result of particles influx on tungsten materials respectively pondered by their sputtering yields:

$$\Gamma_W = \Gamma_D.Y_D + \Gamma_{Low-Z}.Y_{Low-Z} + \Gamma_W.Y_W \tag{4.17}$$

We define the effective sputtering yield Y_{eff} as follow:

$$\frac{\Gamma_W}{\Gamma_D} = Y_D + \frac{\Gamma_{Low-Z}}{\Gamma_D}.Y_{Low-Z} + \frac{\Gamma_W}{\Gamma_D}.Y_W = Y_{Eff} \tag{4.18}$$

The effective sputtering yield therefore strongly depends on plasma composition and can increase dramatically in presence of impurities as shown in Fig. 2.9. This parameter is of great interest for this thesis because it allows characterizing the influence of RF sheath due to ICRH on impurity production precisely by enhancing ions sputtering yield. In order to estimate it experimentally, we will mostly focus on measurements of DI_δ (δ from Balmer series 410.1nm) and WI (400.9nm) lines brightness, respectively emitted by neutral deuterium and tungsten among the different species observable in the spectrum (360-420nm wavelength range). On an absolutely calibrated object, it is therefore possible to get fair estimations of the effective sputtering yields by taking the ratio of both lines and multiply it by the S/XB coefficients ratio characterizing the dependence of the number of ionization events per photon [Brezinsek 2017 and 2011], allowing to convert photon fluxes into particle fluxes as follow:

$$Y_{Eff} = \frac{\Gamma_W}{\Gamma_D} = \frac{WI}{DI_\delta}.\frac{S/XB_{WI}(T_e)}{S/XB_{DI}(T_e)} \approx \frac{WI}{DI_\delta}.\frac{1}{100} \tag{4.19}$$

S/XB coefficients dependence on electron temperature can be found in the literature and ADAS database and were plotted in Fig. 4.20 for the two species of interest.

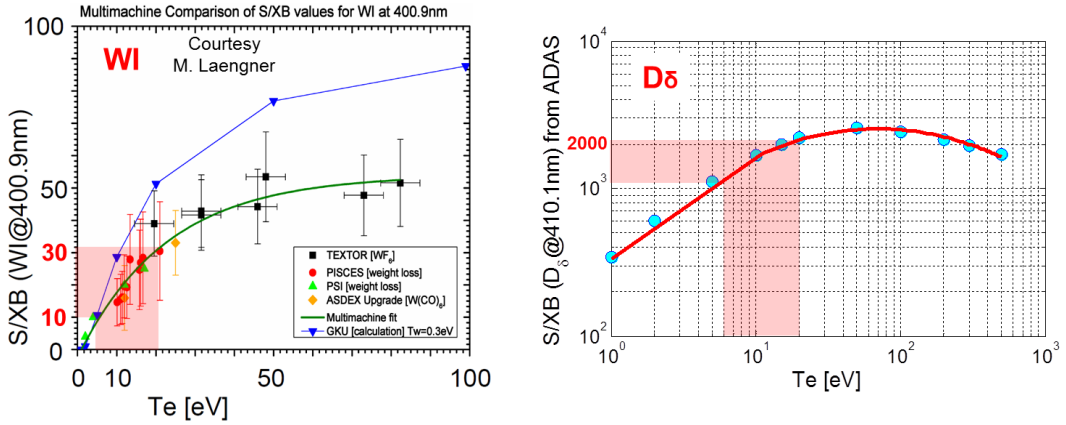

Figure 4.20: S/XB coefficients estimations for neutral tungsten [Brezinsek 2017] and deuterium δ line. Red regions correspond to Te~15eV typical of WEST plasma SOL.

In order to estimate these coefficients, it is now necessary to estimate electron temperatures in WEST typical SOL plasmas. Data from any probe represented in Fig. 4.14 can here be used [Gunn & Pascal 2011]. During a discharge (53679) when different quantities of gas were injected from the valve #7 located on the middle of the APL (Fig. 4.6), all probes were simultaneously used providing measurements of Te in the SOL in different locations and fueling conditions. Results from APL pecker and top reciprocating probes are represented in Fig. 4.21. Divertor probes data were also consistent with these data; by default we will therefore determine S/XB coefficients for SOL temperatures of about 15eV, respectively $S/XB_{DI\delta}\approx2000$ and $S/XB_{WI}\approx20$. S/XB coefficients for different species of Balmer series and their ratio with tungsten are plotted in annex 1. Note these S/XB coefficients only take into account atomic physics, while non negligible amount of impurities may be related to molecules. While molecules can account for up to 50% of impurity productions in a non-metallic environment [Escarguel 2002], they hopefully can only account for 20% at most in tungsten environment like WEST (Fig.A11). Despite SOL electron temperatures are usually rather constant in any scenarios [Kočan 2009], ions temperatures can however change significantly in particular in presence of ICRH due to RF sheaths. Retarded Field Analyzer (RFA) [Kočan 2008] [Kubic 2013] could then be used to directly measure ions temperatures and get more accurate estimations of sputtering yield. Note that this is in practice very challenging and to be meaningful would at least require having the RFA magnetically connected to the region observed by visible spectroscopy LOSs.

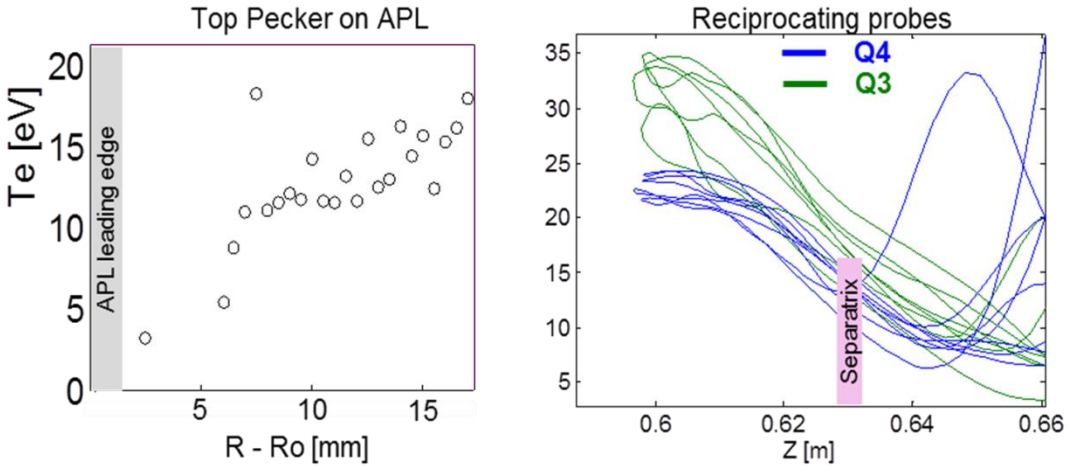

Figure 4.21: SOL temperature measured by different Langmuir probes in WEST (#53679)

In EAST, only 16 lines of sight cover both the inner and the outer targets of the upper divertor at 150Hz sampling rate. This diagnostic will not be very much used in the following discussions.

5. ICRF coupling optimization with local gas puff

In view of improving ICRF wave coupling in EAST and WEST necessary to fulfill high-power discharges, several series of experiments in L-mode were devoted to the use of local gas injection as a tool to increase density in front of the antennas. During the first session in EAST, the quantity of deuterium simultaneously puffed from five different poloidal positions on each side of one ICRF antenna was gradually increased. Steady gas puffing on this antenna (~8.10^{20}e/s) increased antenna coupling resistance by 100%, but puffing more gas did not provoke any further improvement. In WEST, increasing the quantity of gas injected from 1 to 8.10^{20}e/s generally slightly helped increasing consistently the coupling efficiency. In both machines however, plasma central electron density was not kept constant when using local puff but kept increasing during the discharges. In WEST this can be explained by the poor pumping capacity (11m^3/s, cf. section 4.2.1). In EAST however cryogenic pumps allow better pumping. Therefore a second session was done in 2017, during which the global density was well-controlled and remained constant, the distance between the separatrix and the first wall was also increased by 2cm allowing, the gas to spread better, and puffing more gas this time lead to better wave coupling. The same amount of gas was then puffed from three different locations including a single nozzle valve located at the mid-plane and valves distributed poloidally in different points along ICRF antennas' height. In EAST Injection made entirely from mid-plane location led to the best results with the highest coupling simultaneously achieved for both antennas and smallest heat loads on the divertor target (below 1MW/m^2). In WEST so far, no significant improvement was observed with local injection compared to routine fueling from valve at the top of the vessel in agreement with experiments in Tore Supra and TEXTOR [Van Wiessener 2011]. This can be explained by the facts that unlike in others devices (Table 5.3), not only very tiny quantities of gas were injected (due to low pumping capacity), but the ICRF wave cut-off layer is not in the SOL but in the confined region. It is therefore understandable that small quantities of gas did not have much influence on the cut-off position. However we found that increasing the LH power can help increasing density in the SOL more than in the core (Fig.5.6a) and therefore the coupling efficiency of ICRF antennas. Extensive analysis of the

edge diagnostics in each device also made it possible to observe an electron density increase and a temperature decrease likely caused by the ionization of neutrals in the SOL. Heat loads on the EAST divertor target were also slightly mitigated by gas injection, which is favorable from the perspective of long pulse scenario development. As far as wave coupling efficiency is concerned, most experimental trends were also successfully reproduced by antenna modelling with the RAPLICASOL Finite Element Code (Annex 1.2) with experimental density profiles from reflectometry as the main input.

Shots	Fueling Scheme	Local Injection (1e20 e/s)	Ip kA	ne $10^{19}m^{-3}$	Config	ICRF I port MW	ICRF B port MW	LHCD 2,45GHz MW	LHCD 4,6GHz MW
2016 session									
69942	Routine	0	500	2.9	USN	0.840	0.800	0.500	1
69938	Small B	7.9	500	4.4	USN	0.830	0.800	0.500	1
69939	Medium B	9.1	500	4.4	USN	0.830	0.800	0.500	1
69940	Big B	11.9	500	4.4	USN	0.830	0.800	0.500	1
2017 session									
75205	Routine	0	400	2	USN	0	0	0	0
75214	Routine	0	400	3	USN	0.6	0.6	0	0.5
75206	I-port	9.1	400	3	USN	0.6	0.6	0	0.5
75207	J-port	9.1	400	3.4	USN	0.6	0.6	0	0.5
75194	Small B	7.9	400	3	USN	0.6	0.6	0	0.5
75198	Medium B	9.1	400	3.4	USN	0.6	0.6	0	0.5

Table 5.1. Shot list of gas puff experiments in EAST

Shots	Valve Number	Fueling Scheme	Local Injection (1e20 e/s)	Ip kA	ne $10^{19}m^{-3}$	Config	ICRF Q1 MW	ICRF Q2 MW	ICRF Q4 MW	LHCD Q6a MW	LHCD Q6b MW
53677	V10	Polo. Distrib Q2	1 -> 8	500	2.8 -> 3.3	LSN	0.2	0.2	0.2	1.7	0.25
53679	V7	Mid-plane nozzle APL	1 -> 8	500	2.8 -> 3.3	LSN	0.2	0.2	0.2	1.7	0.25
53680	V9	Polo. Distrib Q1	1 -> 8	500	2.8 -> 3.3	LSN	0.2	0.2	0.2	1.7	0.25
53683	V11	Top valve Q4a	1 -> 8	500	2.8 -> 3.3	LSN	0.2	0.2	0.2	1.7	0.25
54532	V11	Top valve Q4a	1 -> 20	700	6 -> 8	LSN	0.6	0	0	0.7	0.2
54533	V2	Polo. Distrib LH1	1 -> 20	700	6 -> 8	LSN	0.8	0	0.7	0.4	0.2
54534	V1	Polo. Distrib LH2	1 -> 20	700	6 -> 8	LSN	0	0	0.7	0.45	0.45
54536	V9	Polo. Distrib Q1	1 -> 20	700	6 -> 8	LSN	0.8	0	0.7	0.4	0.4

Table 5.2. Shot list of gas puff experiments in WEST

Parameters	JET	ASDEX-U	EAST	WEST
f_{ICRH} [MHz]	42	30 - 36,5	34 - 35	48 - 57
$k_{\parallel}$ [m^{-1}] (π phas)	6,6	8	14	9
$n_{e,cut\text{-}off}$ [$10^{18} m^{-3}$]	2	5 -- 4	9 -- 6	9
Cut-Off position	SOL	SOL	SOL	**Confined reg°**
B_T [T] / I_p [MA]	2,7 / 2,5	2 /0.8 - 2.5 /0.8	2,5 / 0,5	3,7 / 0,5
P additionnal	NBI	NBI	LH	LH
Confinement	**H - mode**	**H - mode**	**L - mode**	**L - mode**
Local Gas flow [e/s]	0,5 - 2 x 10^{22}	0,5 - 1 x 10^{22}	8 - 11 x 10^{20}	**1 - 8 x 10^{20}**
Best Solution	Mid-plane	Mid-plane	Mid-plane	-
Effect	Local	Local	Global	-

Table 5.3. Tokamaks and ICRF heating system parameters

5.1 Experimental method

In order to develop tools to increase antenna coupling, and also investigate the side effects that local gas injection may have on the SOL, ICRF performance and heat loads, series of experiments were done in EAST and WEST. Unlike in JET [Jacquet 2016] and ASDEX Upgrade [W.Zhang 2016], we chose to work in L-mode to avoid the difficult interpretation of the edge diagnostics in H-mode (Table 5.3). The first experimental session in EAST took place in 2016 (Fig.5.1a). Deuterium was only puffed from the B-port (Fig.5.12c) in different quantities. No particular effort was made to keep the central electron density constant: as additional gas was locally puffed on top of the routine plasma fueling (kept constant), a large increase of the density was obtained, resulting first in antenna arcing and ultimately prompt disruptions. In 2016, three similar shots during ICRF power modulations between 0.5 and 1 MW were done. Both antennas were alternatively activated (Fig.5.1a). A shot (#69942) was done using the routine fueling valves, while in others shots, gas was additionally puffed around the B-port all along three discharges at respective rates of 7.9 10^{20}e/s (#69938), 9.1 10^{20}e/s (#69939) and 11.4 10^{20}e/s (#69940). The fact that no further improvement was observed when increasing the quantity of gas puffed (Fig.5.3b) was believed to be related to a too short outer gap, and it was consequently

increased during a later session.

The second session took place in 2017 (Fig.5.1b) during which the density was well-controlled and kept constant throughout the experiment (Fig.5.1f) simply by reducing the gas injected by the main fueling valve. The outer gap was also increased to make the effect of the local gas puffing more obvious (Fig.5.2). This time, gas was not only puffed around the B-port (#75194 & #75198) but also around the I-port (#75206) - the injection system of which has the same design as that of B-port - and from J-port (#75207) through a single valve at the mid-plane. The same quantity of gas (9.1 10^{20}e/s) was puffed from each port. Shot #75214 serves as the reference discharge without other local injection but with routine fueling valves in operation.

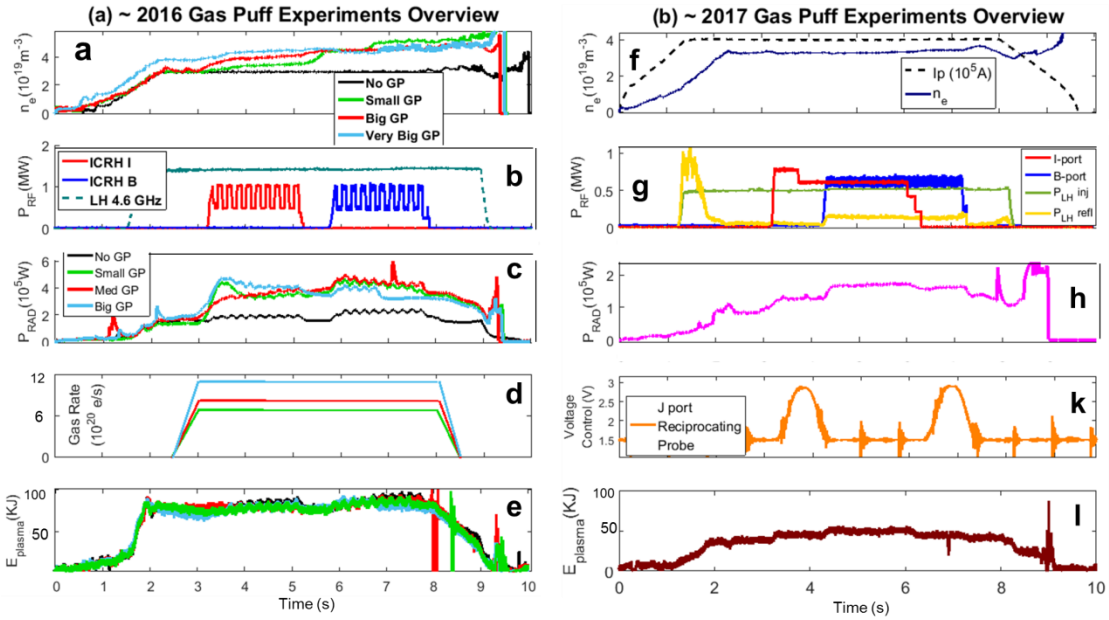

Figure 5.1: Overview of plasma parameters evolution during 2016 (left panel) and 2017 (right panel) gas puff experiments. For the 2016 session: (a) central electron density (de-convoluted from interferometry data) for different gas rates, (b) RF powers, (c) bulk radiated power (from bolometer), (d) gas injection rates which were the same in 2017 and (e) plasma stored energy. For the 2017 session: (f) central electron density and plasma current, (g) ICRH and LH powers, (h) plasma radiated power from bolometry, (i) probe reciprocations and (j) plasma energy from diamagnetic loops. Only one curve is plotted when the signal associated did not change much for different pulses. Cf detailed shot list in Table 4.1.

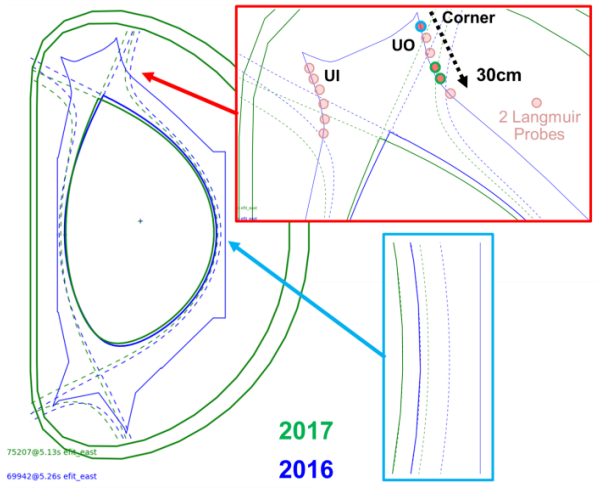

Figure 5.2: EFIT reconstruction of plasma equilibria during 2016 (blue) and 2017 (green) gas puff experiments. Both equilibria are superimposed and zoomed-in areas of interest have been added. Matrices of red circles on the upper divertor represent pairs of Langmuir probes. Upper outer probes circled by blue and green roughly correspond to 2017 plasmas strike point positions.

In WEST as well, different quantities of gas were injected from different valves gradually from 1 up to 8.10^{20}e/s (Table 5.2). Poor pumping capacities did not allow keeping the density constant along the feed-forward scan, and it increased linearly from 2.8 up to $3.3.10^{19}m^{-3}$, making more difficult to disentangle edge from core effects (Fig.5.3). Pecker probe on the upper part of the APL were used to sample SOL density profiles (Fig.5.3f) at two different times corresponding to two different levels of injection from the valve V10 which is magnetically connected to the probe (Fig. 4.6b).

For convenience on all figures and discussions, local gas puffing is simply referred to as gas puffing, especially in EAST, when talking about the “no puff” case, one should understand that no gas was locally puffed from any of the locations discussed all along, but deuterium was of course injected from both the routine fueling valve and the SMBI (1 to 5% of plasma global fueling with short and strong injections spread along the discharge with often most intense use during the ramp-up phase).

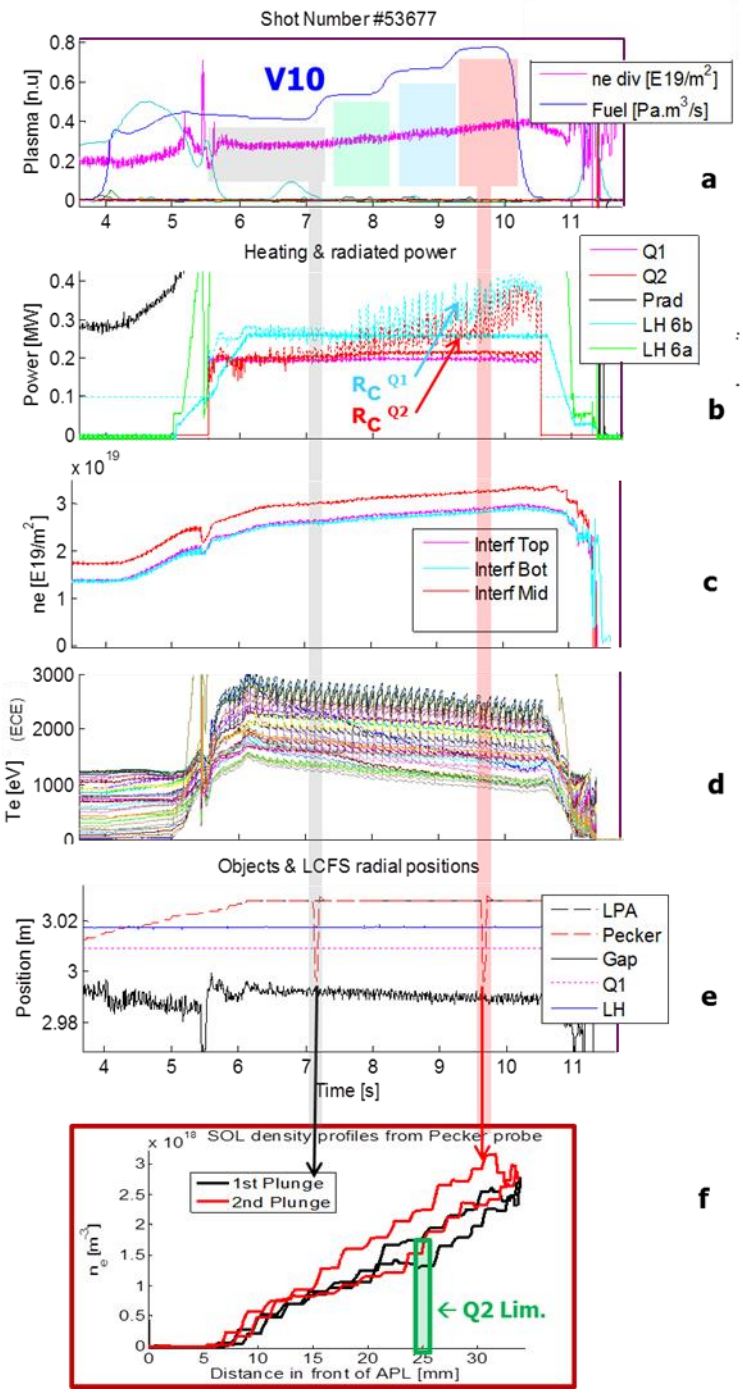

Figure 5.3: Time traces of a typical shot (53677) of the local gas injection experiments in WEST with (a) the level of injection from valve V10 and the divertor density, (b) the LH and ICRH power with coupling resistances of each antennas in dashed lines, (c) the line-integrated density from the interferometer, (d) the electron temperature from ECE, (e) the position of the separatrix and limiters with Pecker probe on the upper part of the APL plunging twice and (f) the density profiles measured.

5.2 Experimental results

The best way to increase the loading is to put the antenna closer to the plasma, but this is limited by heat loads and impurity issues. The second most efficient way is to increase the overall plasma density but this is in practice limited by Greenwald's value over which plasma can disrupt. The third most efficient way is to increase wave frequency [Helou 2019], but this is in practice also dictated by the scenario. We also found that increasing the LH power can help increasing density in the SOL more than in the core Fig.5.6a and therefore the coupling efficiency of ICRF antennas. It is known that as more power is injected, more goes in the SOL and contributes to ionizing neutrals and increasing the SOL electrons density [Kocân 2009], but other synergistic mechanisms may also contribute to the beneficial effect of LHCD to the ICRF coupling observed experimentally. Finally, another way to improve ICRF loading is to fuel the plasma using valves in the vicinity of ICRF antennas, thus aiming to locally increase the SOL density without impacting too much the central plasma density, which can be challenging if the pumping efficiency of the machine is not high enough.

5.2.1 Effect of gas injection on ICRF antennas loading

In JET, DIIID [Jacquet 2016] and ASDEX Upgrade [W.Zhang 2016], experiments were done in H-mode and best coupling improvements at given gas rate were obtained by injecting gas at the mid-plane nearby ICRF antennas and the effect was relatively local toroidally (Table 5.3 and Fig.5.4).

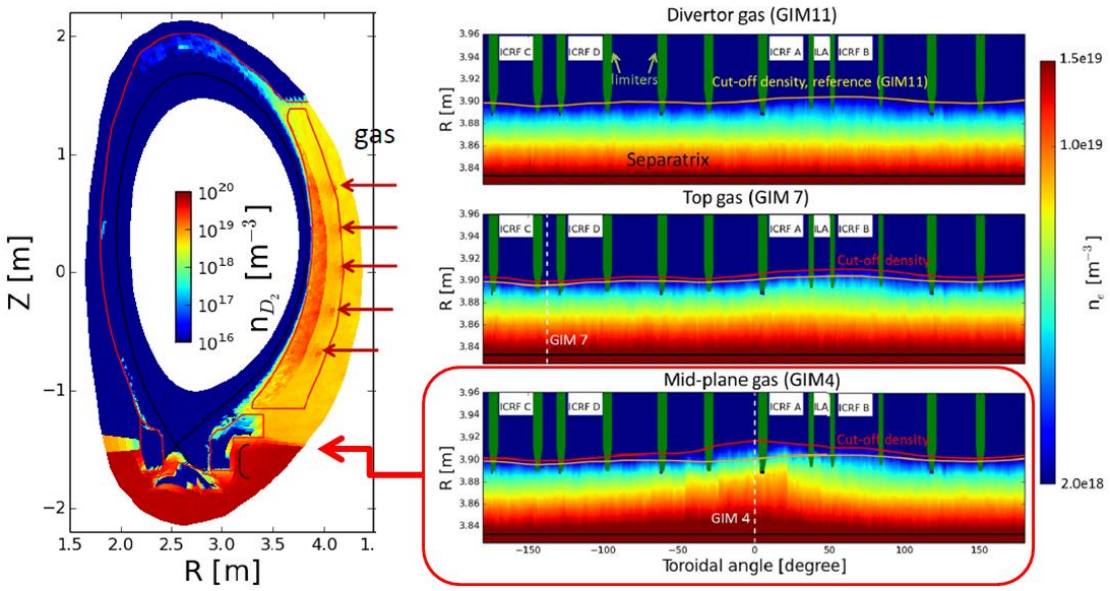

Figure 5.4: On the left, poloidal cross-sections of the neutral density (n_{D2} for molecular) for mid-plane gas puffing. The poloidal cross-section is taken at the toroidal position where the mid-plane valve (GIM4) is located.
On the right, toroidal cross-sections of the electron density in the outer mid-plane for the divertor, top and mid-plane gas puff cases. The yellow solid line is the position of cut-off density for divertor gas puffing and reported in the second and third subfigures as reference line. The red solid-line is the position of cut-off density for top or mid-plane gas puffing. These are EMC3-Eirene simulations for JET cases which further details can be found under [W.Zhang 2017].

In EAST, the B-port antenna (31.5MHz) usually has smaller coupling resistances than I-port antenna (35MHz) which is also twice bigger, therefore already in 2015 (when both antenna operated at 27MHz), local gas injection was used in priority on B-port antenna and results shown in Fig.4.12c. In WEST as well, for a given position radial position of both ICRF antennas, Q2 always happened to have a smaller coupling than Q1, and V10 was also used more often than others local valves. In spite of low level of gas injected at that time, it already lead to encouraging coupling improvements shown in Fig.5.5a for EAST [J.H.Zhang 2017] and in Fig 5.6b for WEST with coupling resistances defined like in [Helou 2015] as

$$R_c = \frac{2P_t}{I_s^2} \tag{5.1}$$

With

$$I_s = \frac{1}{2}\sum |I_i|^2 \tag{5.2}$$

where P_t is the power radiated by the antenna and I_i the currents exciting the straps array. In WEST, currents I_i are in practice deduced from voltage V_i, measured by voltage probes located at the input of the straps and close to each capacitor (cf Fig.4.8), from the approximate relation $|I_i|=|V_i|/|X|$, with X the reactance of the strap (since $Re(Z)=|R|<<|X|= Im(Z)$). This reactance is specific to the front face of the antenna but is relatively independent of the coupling conditions. In the case of the WEST antennas, the strap reactance X has been fitted to vacuum coupling case as function of the RF frequency ν only as $X=0.0001\nu^3-0.0078\nu^2+0.72\nu-3.17$ [Helou PhD p.132-133]. The transmitted power P_t is measured by bidirectional couplers, measuring both injected (P_{in}) and reflected power (P_r). In WEST these couplers are located before antennas inputs and at the generator plant. Power measurements performed at the antenna side allow expressing the transmitted power independently of the transmission line losses occurring between the plant and the antennas. ($P_t \approx P_{in}-P_r$). In EAST however, these couplers are close to the stub tuner and far from the antenna, such that losses in transmission lines in principle should not be neglected. In first approximation these losses can be taken into account by adding a coefficient $\alpha<1$ (ex: $\alpha=0.5$ means 50% losses in transmission lines) such that $P_t \approx \alpha.P_{in} - P_r/\alpha$. Since we however have no clear idea of the value α should get, we will neglect losses in transmission lines and acknowledge that the power will generally be overestimated. Only in section 6.3.2.1 we will try to estimate absorption efficiency which will require making a slightly more realistic assumption on this coefficient. Transmitted power can then be expressed as follow:

$$P_t = \frac{1}{2}R_e\left(V \times I^*\right) = \frac{1}{2}R_e\left(Z.I.I^*\right) = \frac{|I|^2}{2}R_e\left(Z\right) \tag{5.3}$$

With such definition we get

$$R_c\left(i\right) = R_e\left(Z_i\right) = R_i \tag{5.4}$$

In 2016, similar experiment was done in EAST and larger quantities of gas were injected. Surprisingly no further improvement was observed when increasing the quantity of gas puffed from 8.8 10^{20}e/s up to 11.4 10^{20}e/s (Fig. 5.4b and Fig. 5.9a). Actually, when too much gas was puffed (11.4 10^{20}e/s (#69940) and more than 2 10^{21}e/s injected in total), arcing was observed in the B-port antenna, suggesting that

part of the neutral gas is ionized inside the antenna box. A similar effect was observed in ASDEX when too much gas was injected close to the ICRF antenna side-limiters [Bobkov 2015].

After a certain amount of local gas is injected (Fig.5.4b), the saturation of the coupling improvement observed on the EAST B-port antenna is believed to be related to the port-B gas injection system design. The valves are poloidally distributed and are too close to the antenna limiters and to the separatrix, so that neutrals get ionized very quickly (before having time to spread poloidally and toroidally) and the electrons are transported away from the antenna structure, especially near the top and bottom of the gas injection array.

Similarly in WEST, valve V7 located at the center of the APL (Fig.4.6) is often too close from the plasma, preventing the gas to spread before being ionized, which can lead to such a local increase of density and D^+ influx on surrounding materials that it may behave like an impurity source as observed during C2 campaign with visible spectroscopy [Meyer 2018]. As detailed under the dedicated section 4.3.2.2, visible spectroscopy lines of sight are among other objects covering the APL poloidal height. The time evolution of the intensity of certain lines on the spectrum sampled by different lines of sight can then be compared, as for instance plotted in Fig.5.7a, the neutral tungsten (WI) and nitrogen (NI) for two adjacent lines of sight looking at the APL, respectively one above the mid-plane (LOS#5) and one at the mid-plane (LOS#6) were valve V7 is located. Whatever the species, it appears that the line pointed towards the valve V7 reacts very consistently with the gas injection rate in black. It is also possible to visualize this effect differently (Fig.5.7b), by plotting poloidal profiles of the WI averaged between 5s and 6s (gas on) and 7s to 8s (gas off), with gas injected from V7. The profile gets picked at the center when the gas is injected from V7, meaning that a source of impurity appears around the valve. This is likely due to the fact that this limiter was too close from the plasma, such that gas was directly injected from a region where T_e is already pretty high, preventing the gas to diffuse before being ionized right at the limiter surface.

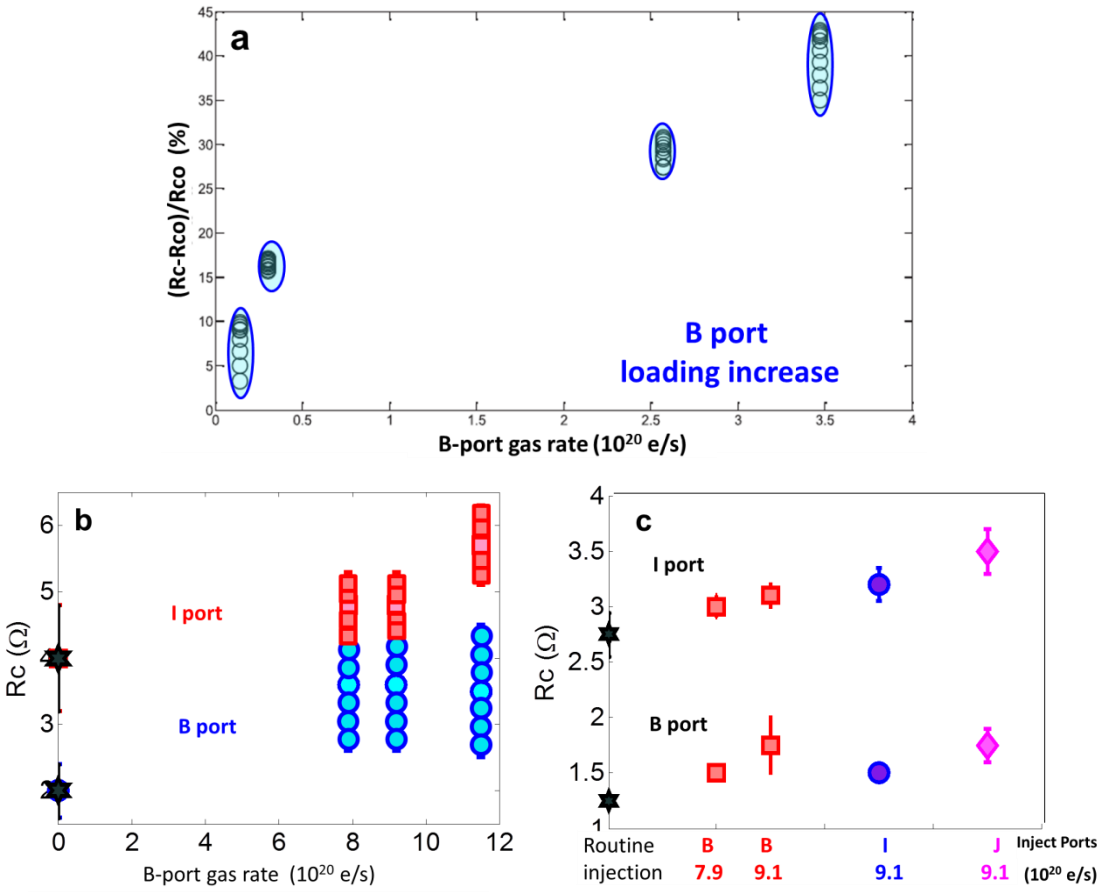

Figure 5.5. ICRF coupling resistance evolutions during the gas puffing experiments of (a) 2015 : The third graph shows relative variation of the B-port antenna coupling resistance as a function of the rate of the injected gas in B port. Rc_0 denotes the coupling resistance without the gas injection. (b) 2016 : respectively routine puffing (#69942), 7.9 10^{20}e/s (#69938), 9.1 10^{20}e/s (#69939) and 11.4 10^{20}e/s (#69940) (loading variations are due to power modulations) (c) 2017 : routine injection (no puff) (#75214), puff on I-port (#75206), puff on J-port (#75207) and puffing on B-port at two different rates (#75194 & #75198).

Loading resistance of the EAST I-port antenna is also enhanced by puffing gas from the B-port (Fig.5.4b and Fig.5.9a), whose top injection nozzles are magnetically connected to the I-port antenna (see Fig.4.2b). In addition, when too much gas is injected, neutrals may diffuse farther than usual in all directions, and get ionized over a larger area, therefore affecting more field lines, extending magnetic connections' range potentially up to all objects around the torus. One could also claim that this is

actually the result of a global increase of the density as shown on the top graph of Fig.4.1a (central electron density) and could explain the further coupling enhancement observed on the I-port antenna when 12.10^{20} e/s are injected from the B-port valves. The results from the 2017 experiment also support this claim.

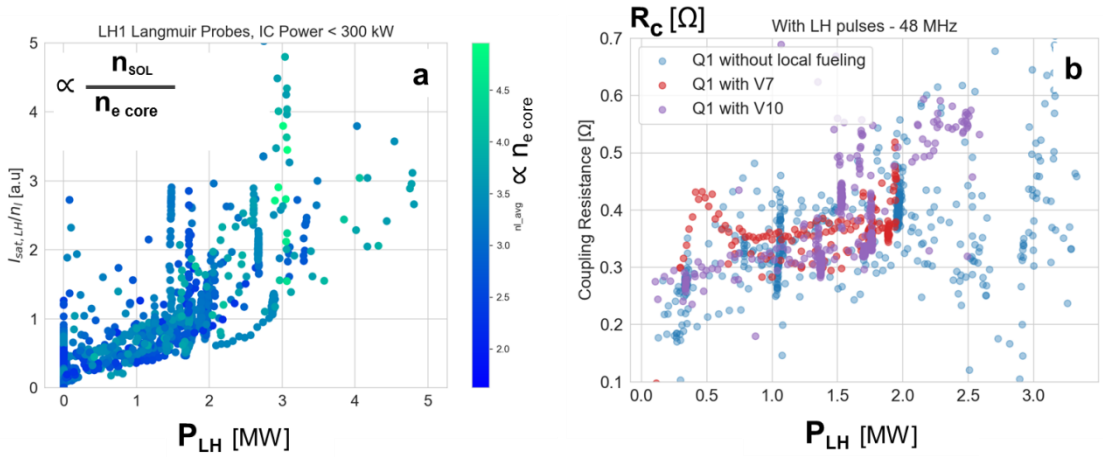

Figure 5.6: (a) Ratio of ion saturation current measured by Langmuir probes fixed on LH launchers corners (proxy of SOL density) over the linearly integrated density from interferometry (proxy of core density) and (b) Q1 ICRF antenna loading plotted against LH power for WEST C3b campaign shots and different valves (Fig. 4.6).

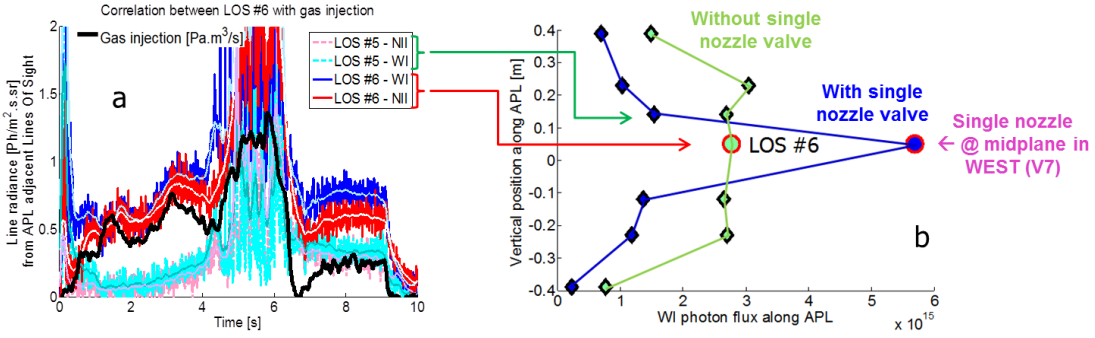

Figure 5.7: (a) Time evolution of neutral tungsten (WI) and nitrogen (NI) for two adjacent lines of sight looking at the APL, respectively one above the mid-plane (LOS#5) and one at the mid-plane (LOS#6) were valve V7 is located, and V7 gas injection rate in black. (b) Poloidal profiles of the WI averaged between 5s and 6s (gas on) and 7s to 8s (gas off), with gas injected from V7.

In 2017 in EAST and 2018 in WEST, gas was puffed in similar amounts from different locations around the torus detailed under sections 4.1.3 and 4.2.3 (~9.1 10^{20}e/s constant in EAST and four steps in feed forward from 1 up to 8.10^{20}e/s in

WEST (Fig.5.3a)). In WEST however since only half of the pumping capacity was available, these level of injection already lead to constant increase of the core density making difficult to disentangle edge from core effects. During another session in 2019, different valves were used in feedback instead with steps requests on core density from 5 up to $7.10^{19}m^{-2}$. The different injection points in each devices are as follow:

- Around ICRF antennas of each device, through injection arrays poloidally distributed along antenna limiters, and also around LH launchers in WEST
- From single nozzle valves located at the mid-plane, retracted by 20cm with respect to the antenna limiters in EAST J-port, and V7 fixed on APL in WEST
- From top valve in WEST (V11).

In order in EAST to minimize the problem of premature gas ionization and convection away from the antenna, the outer gap was increased by 2cm so that unlike in the 2016 experiment (Fig.5.2) the distance between the antenna straps and the cutoff layer would not reach a minimum as soon as a small quantity of gas was injected. As a consequence, different gas puffing rates from the B-port had indeed distinct influences on the wave coupling of the local antenna (Fig.5.5c and Fig.5.11).

In WEST though, poloidally distributed valves are radially retracted about 7cm behind the antenna leading edge, a priori sufficiently to let the gas diffuse before being ionized. This design allowed observing an improvement of the coupling consistent with the increasing injection rate (Fig.5.3, Fig.5.8 and Fig.5.9). It is however not straightforward that this correlation is meaningful since the plasma density also keeps increasing consistently with the antenna loading.

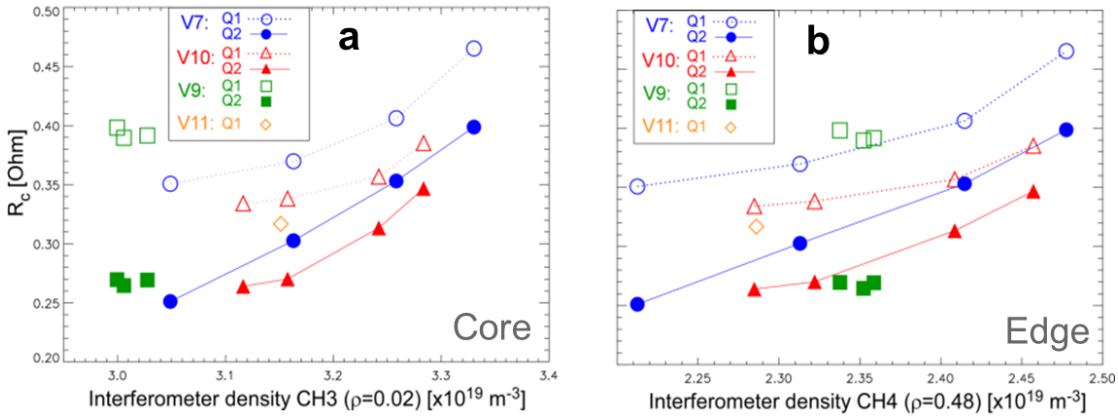

Figure 5.8: WEST Q1 and Q2 antenna loading evolution for different gas

injection rate and valves (Table.5.2), as a function of two different interferometry lines respectively looking through (a) the whole plasma (CH3) and (b) the edge (CH4)

In other EAST cases, gas was puffed in I and J ports in the same proportions as in the so-called "big puff" case in the B-port (~9.1 10^{20}e/s). We first see that both antennas loadings always increase when using main chamber gas injection from any point compared to routine fueling (Fig.5.5c and Fig.5.9b). As expected, local gas injection from the B-port has a stronger effect on the B-port antenna loading and puffing from the I-port has a stronger impact on the I-port antenna loading but, as in 2016, cross-effects are also seen, particularly on the coupling resistance of the I-port antenna which is partially magnetically connected to the upper part of the B-port injection array. The effect of I-port puffing on the B-port antenna loading is weaker but visible, being roughly equivalent to the low gas puff level of local B-port injection (Fig.5.5c and Fig.5.9b).

In the last case, gas was puffed from the single nozzle valve located at mid-plane and radially retracted as compared to the B and I ports injection systems that distribute gas near each antenna protection and in five different poloidal points from the bottom to the top of the antennas (Fig.4.12c). Puffing on the J-port was the most successful, as coupling for both antennas simultaneously reached their highest levels. The effect is stronger for the I-port antenna, which is located much closer to the J-port valve injection point. Surprisingly, even the B-port antenna which is at the farthest possible location away from the valve experienced a coupling improvement to level similar to that of when the same amount of gas was directly puffed around the antenna itself. The fact that best coupling conditions are obtained with mid-plane valve is in agreement with previous experiments [Jacquet 2016], [Bobkov 2015], [Lerche 2015], [Pinsker 2011] and simulations [W.Zhang 2016], [W.Zhang 2017] which show that best coupling efficiencies are achieved by puffing gas directly at the mid-plane instead of puffing it closer to the divertor, but the toroidal extension of the mid-plane gas injection enhancement observed in EAST is larger than what was observed in ASDEX [Jacquet 2016], [Bobkov 2015] and in JET [Lerche 2015], which showed a gradual decrease in the coupling enhancement with the toroidal distance between the antennas and the mid-plane injection point (Table 5.3).

In WEST however, no significant improvement was observed with local injection compared to the injection at the top of the vessel (Fig.5.9). This can be explained by the facts that unlike in others devices, not only very tiny quantities of

gas were injected (due to low pumping capacity), but the ICRF wave cut-off layer is not in the SOL but in the confined region (Table 5.3). It is therefore understandable that small quantities of gas did not have much influence on the cut-off position. Another important point is that valves located at the mid-plane are only a good solution if they are radially retracted enough to let neutral gas diffuse before being ionized (~20cm behind antenna limiters), like in ASDEX, JET or EAST. Putting the valves too close to the plasma – like V7 in WEST APL – has shown its potential drawbacks (Fig.5.7).

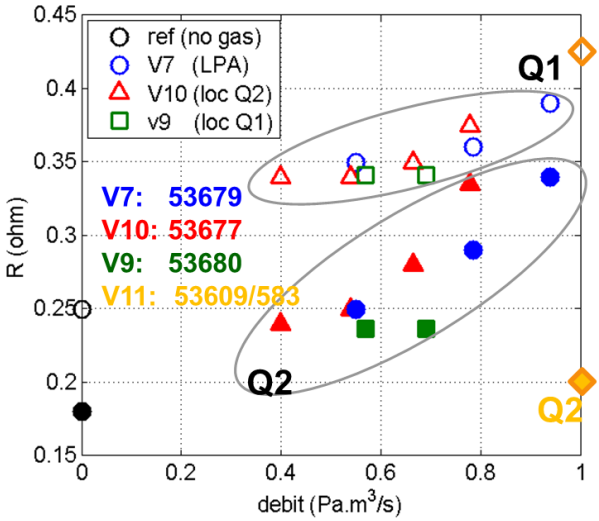

Figure 5.9: WEST Q1 and Q2 antennas loading evolution with gas rate for different injection valves

As mentioned, in general mid-plane injection mainly helps increasing density around the toroidal location of the valve. The fact that mid-plane injection simultaneously improves coupling of both antennas and that it has a similar effect as local gas injection (in particular for the B-port antenna) is a peculiarity of EAST that is not yet well-understood. We are in particular not able to say if this effect is homogeneous toroidally or only the fruit of fortunate connections between antennas and the region were the injected neutrals are ionized. A possible explanation could be related to a large neutral diffusion from the valve to the SOL. For EAST L-mode plasmas with SOL temperatures and densities respectively ranging as 10~70eV and 10^{18}-10^{19}m-3, neutrals ionization mean free path are estimated to be of the order of 3~11cm. Since J-port injection is radially retracted of 20cm with respect to the antenna limiters, the spreading of the neutral gas poloidally and toroidally is expected

to be larger with respect to the injection at the antenna limiters. A similar case can be found in ASDEX Upgrade where neutrals typically diffuse inside a cone with a 90° angle from the valve, and their ionization starts at about 2eV with a rate increasing with Te. This type of injection typically results in a cosine-like distribution of neutrals relatively to the injection point as shown in Fig.4.2 of [W.Zhang 2016]. For a given quantity of gas injected, higher density values are therefore expected in front of a single nozzle valve (like in J-port) compared to homogeneously distributed valves (like in I and B ports). A qualitative illustration of this effect is provided in the Fig.5.10.

With poloidally distributed valves, gas ionized in front of top and bottom injection points follows magnetic flux tubes that are weakly connected to the antenna's front face. Part of the gas likely does not help increasing much the density in front of antennas, but might increase density more uniformly in both poloidal and toroidal directions with a smaller maximum [W.Zhang 2016], [W.Zhang 2017]. This could explain why larger injections from distributed valves are necessary to reach similar coupling as with a single mid-plane valve.

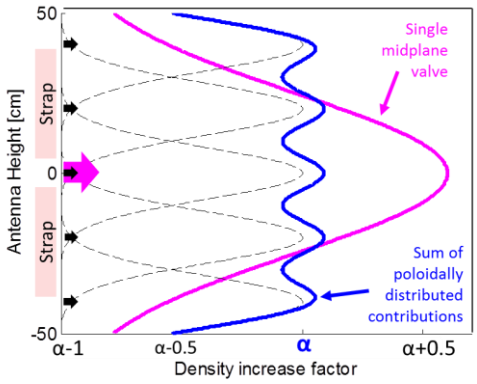

Figure 5.10: Comparison of single mid-plane vs poloidally distributed valves contribution to local density increase for same injection rate

In Fig.5.10, each black arrow corresponds to injection points 3cm behind antenna limiter edge (Fig.4.12c) such that neutrals are almost immediately ionized and do not diffuse much considering the relatively low valve pressure injecting gas at subsonic levels. The J-port nozzle valve is about 20cm behind the antenna leading edge (represented in Fig.5.8 as the large magenta arrow). Therefore neutrals can diffuse more before getting ionized. In most neutral transport codes [W.Zhang 2016], [W.Zhang 2017], As can also be seen in simulations of neutrals diffusive transport

from a fueling valve up to the SOL made with DEGAS 2 code [Stoler 2010], the further we look radially away from an injection point, the more spread is the density increase. For a given quantity of gas injected, we define the density increase factor α as the ratio of the maximal density obtained at the antenna aperture (R=Rant) with poloidally distributed valves, against the same quantity with routine fueling:

$$\alpha = \frac{\max_{R=Rant}(n_e)_{polo\_distrib\_valve}}{\max_{R=Rant}(n_e)_{routine\_fueling}} \quad (5.1)$$

α=1 would for instance mean that the maximal density obtained with poloidally distributed valves is equivalent to this obtained with routine fueling scheme. α=2 would mean that maximal density reachable with distributed valves can be twice larger than what routine fueling would lead to. Fig.5.10 shows that density at the mid-plane would typically increase more with the mid-plane valve rather than with poloidally distributed injections with the same gas rate. At the corners however density increase could be higher with distributed valves, which is typically important for LH launchers whose wavelength is short and waveguides small and covering whole antenna's height. Though these regions are basically out of interest for the coupling of ICRF waves as their wavelength is much longer then LH and current straps are closer to the mid-plane. This approach strictly stands for neutrals diffusion from the valve and does not take into account ionized particles transport. We acknowledge this explanation is rather speculative and not only lacks of physical ingredients such as recycling, but mostly of experimental proofs. Note this explanation can justify that J-port valve has a bigger impact on I-port loading than its own distributed valves. It can however hardly be used to discuss J-port valve impact on B-port antenna loading, not only since there is no apparent magnetic connection, but also because of possible toroidal attenuation of density as seen in ASDEX [Bobkov 2015] and JET [Lerche 2015] due to poloidal and/or radial spreading.

Note also that coupling resistances were all significantly higher during 2016 (Fig.5.3b) than 2017 (Fig.5.3c) experiments. This is partly due to the increased outer gap settings used in 2017 but it could also be related to the fact that higher LH power levels were applied during the first session (Fig.5.2), which may facilitate the neutral gas ionization in the SOL as observed in WEST (Fig.5.6a). More dedicated experiments are necessary to understand the role that LH power may have on the SOL ionization processes and on the ICRH coupling enhancement. The toroidal repartition

of LH launchers and ICRH antennas (Fig.4.2 and 4.6) could also explain the homogeneous effect observed with all the valves in WEST and with the J-port mid-plane injection in EAST. The next section uses several diagnostics data to provide local evidences of gas puffing influence on SOL parameters.

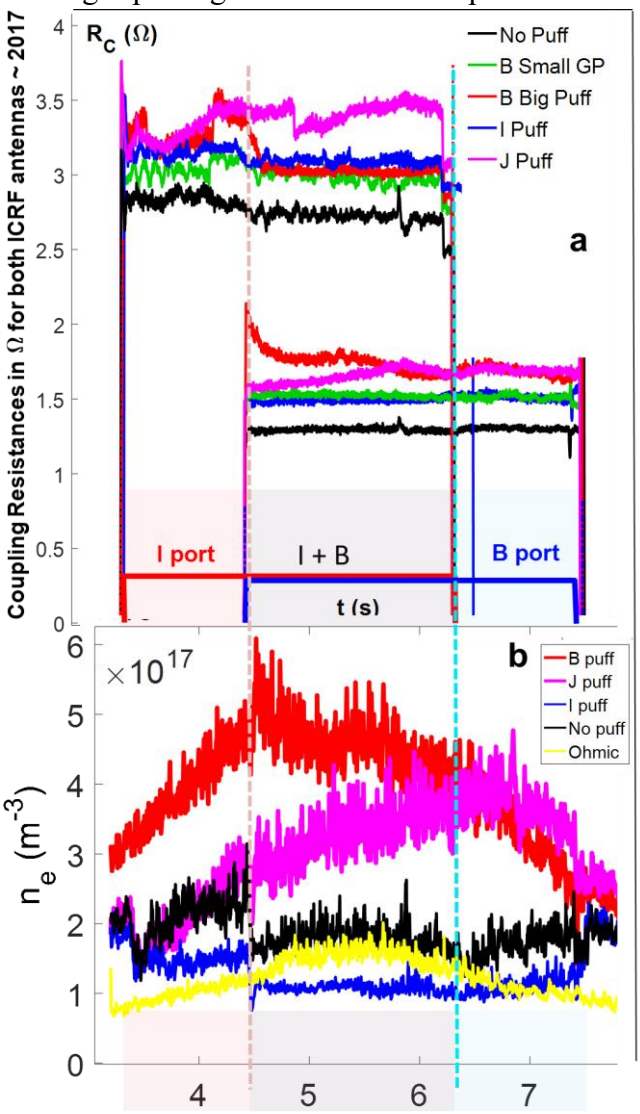

Figure 5.11: Time traces of (a) ICRF coupling resistances of each antenna and (b) average SOL densities measured by the three Langmuir probes fixed at the B-port antenna top left corner (Fig.4.12) during 2017 experiments.
Cf detailed shot list in Table 5.1.

5.2.2 Effect of gas injection on SOL parameters

In this section, we discuss side effects induced in the SOL parameters when injecting gas around the ICRF antennas from different locations. We will comment

results from WEST and focus on EAST 2017 experiments during which a complementary set of specific edge diagnostics were used in several locations to provide an overview as comprehensive as possible.

We will start by analyzing the B-port region in EAST, using the Langmuir and B-dot probes shown on Fig.4.12 together with He-BES (Helium beam) profiles, before looking at the J-port reciprocating probe and reflectometer profiles. ICRF system "heating performance" is also assessed by only looking at plasma energy (W_{ENG}) improvement when powering ICRH (Fig.5.10) $\Delta W_{ENG}/P_{ICRH}$. Note this method can give somehow strange results since power losses in transmission lines are neglected while they should not, and the plasma energy content levels (Fig.5.1j) are different before and after the phase with ICRH.

In WEST we will look at visible spectroscopy and probes data (Fig 4.14) from Pecker on APL, simple probes at corners of each LH launcher and embedded in divertor targets and RFA on top of the machine.

To give a slightly more global picture of SOL parameters change in EAST, data from the three top Langmuir probes shown in Fig.4.12 were averaged (Fig.5.12 (a, b, c)). Despite efforts made on probes design, their inherent sensitivity to RF sheaths justified benchmarking these data with these of He-BES (Helium-Beam spectroscopy) (Fig.5.13). Colored areas have been added on each graph to materialize time periods with different RF heating cases. Both diagnostics observed the global increase in density averaged over 50ms (Fig.5.10b and Fig.5.13) and decrease in temperature (Fig.5.12a) caused by gas puffing. Only in the case of puffing on the I-port was the Langmuir probe density value anomalously small, which is believed to be a local effect as antenna coupling improved compared to the case without gas puffing (Fig.5.5c).

In the case of gas puffed on the B-port, the gas valve and probes proximity could explain particularly high values of the density locally. The density still reaches its peak as the B-port antenna is turned-on and then keeps decreasing, in good agreement with coupling resistances on Fig.5.5 b & c and Fig.5.11. This is believed to be the consequence of the B-port-induced near fields at the origin of E×B density convection away from the antenna [Messian & Weynants 2011], [Urbanczyk 2017]. In the case of gas puffed on the J-port though, as the valve is very far and not magnetically connected to the B-port, high density values are representative of a global increase. Heat loads seem strongly correlated with density variations. From the B-dot probes

Fast (FW) and Slow wave (SW) amplitudes measurements can reveal interesting elements, yet analysis can be complex. We will then proceed by order of difficulty, starting at the time period with only the I-port antenna is active. In this case, FW and SW amplitudes are likely the result of far-field-induced perturbations as probes are far and screened from I-port antenna. While nothing is observed when the gas is puffed away from the probes, a large decrease in both FW and SW amplitudes is observed when gas is puffed from the B-port, either suggesting that probe apertures were obstructed by neutral gas, or that puffing gas could locally mitigate far-fields. Reproducibility on several shots is consistent, yet more probes will be fixed in order to assess to what extent such effects may be true. Having only the B-port antenna active is slightly more complex as not only should the launched wave near-field but also the unabsorbed wave-induced far-field be taken into account in the analysis. As coupling improves, one may expect smaller amplitudes of the RF near fields for given RF field amplitude in the plasma core. But as the heating efficiency is low (Fig.5.10f), more power is expected to reflect back and induce far-fields in the probe region, which could explain higher field amplitudes with gas puffing. Such a mechanism is particularly consistent with the fact that while only the B-port is active, SW amplitudes tend to increase as heating efficiencies decrease. In the specific case of gas puffed on the B-port though, notice that both FW and SW fields are higher, which contrary to the case when only the I-port antenna was active. This is believed to be due to near-fields enhanced propagation by high neutral density from the antenna to the probes. The last case with both antennas active at the same time is too complex and won't be discussed here. From these results, it can be said that gas locally puffed on the B-port had a strong influence on the surrounding SOL parameters with density increasing (Fig.4.5c and 4.7b), temperature decreasing (blue series in Fig.4.5b and 4.6a), and apparent reduction of far-fields. In the case of gas puffed on the J-port mid-plane – far away and magnetically disconnected – similar effects on density and temperature profiles were observed.

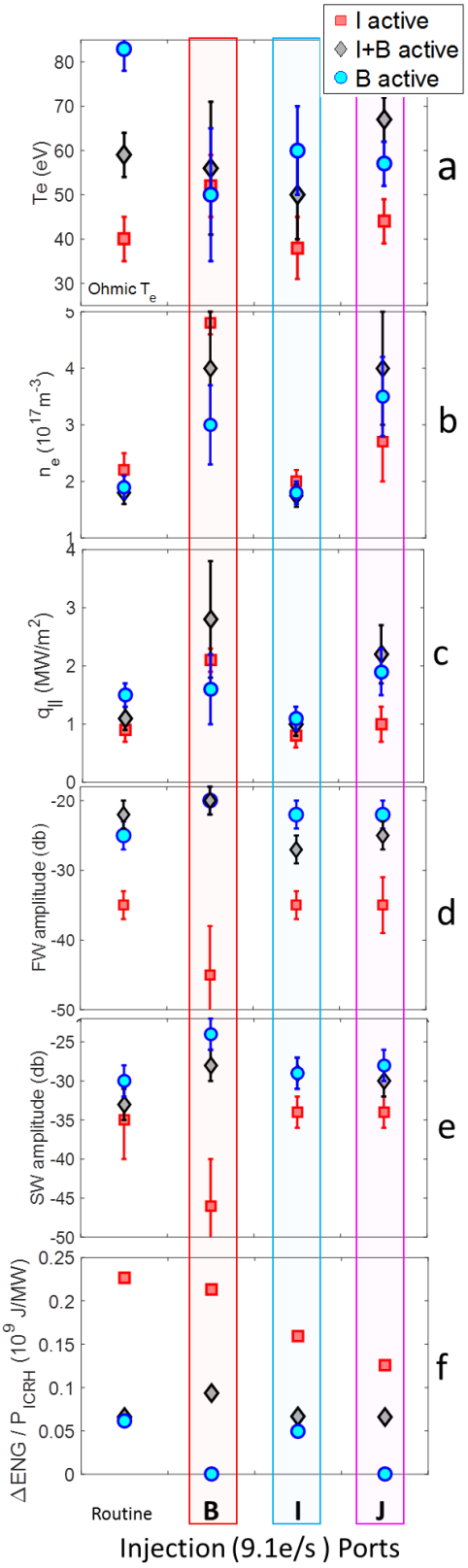

Figure 5.12: The B-port Langmuir and B-dot probes data evolution during the 2017 gas puff experiments: Electron temperature (a), density (b), parallel heat fluxes (c), ICRF Fast (d) and Slow (e) wave amplitudes and ICRF heating efficiency (f). Signals

of the three triple probes at the top of the antenna shown on Fig.4.12 were averaged to give a more global and reliable picture of local gas puffing influence on their region. Cf detailed shot list in Table 4.1.

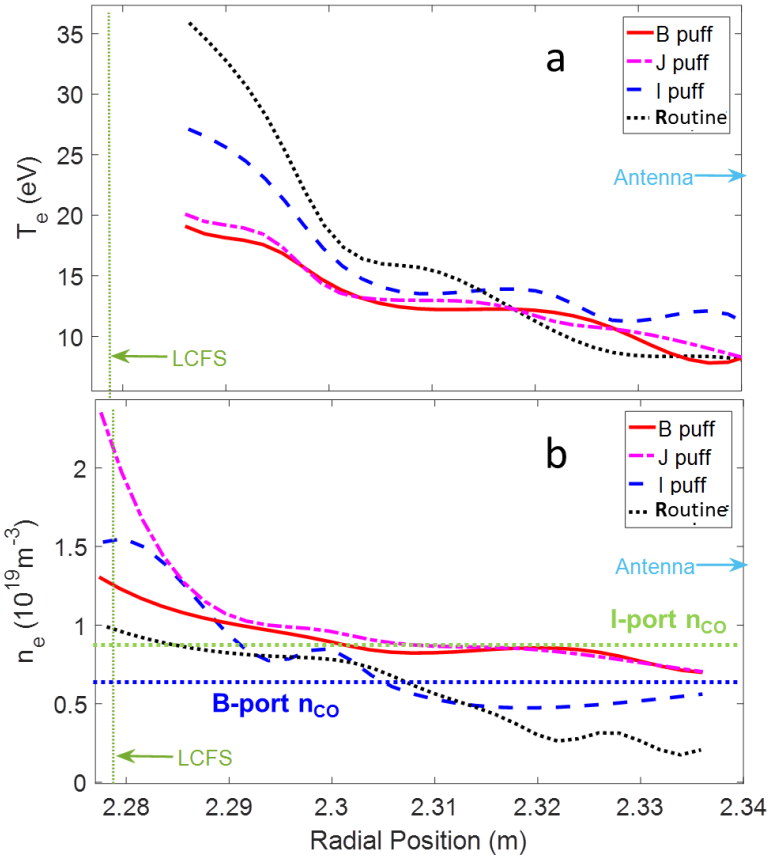

Figure 5.13: Electron temperature (a) and density (b) profiles from the A-port He-BES during the 2017 gas puffing experiments at 7 seconds (when only the B-port antenna was active) for the four different fueling schemes. Cf detailed shot list in Table 4.1.

In WEST, the electron temperature in the SOL represented in Fig.4.20b and measured by RFA reciprocating probes at the top of the device (Fig.4.6a) remains pretty stable despite the injection rate increases. Most likely this could be because the probes were not magnetically connected to the injection points (V10). On the other side, the density measured by simple probes embedded in LH launchers corners (Fig.5.6a), pecker probe (Fig.5.14) and interferometry (Fig.5.3c and Fig.5.8) increases consistently with the gas injection. It is however challenging to make sure that this is an effect specific to the edge while the global density keeps increasing along the discharge.

To try disentangling edge from core effects, the ratio of the density measured by Langmuir probes against the line-integrated density was for instance plotted against the LH power in Fig.5.6a, showing that the density increases faster in the edge than in the core, also consistent with probes data (Fig.5.14) Note however that the ICRF cutoff layer position – which matters the most for coupling studies – is different from the one of Langmuir probes. Ideally, one should rather use reflectometry data, but these did not allow observing significant displacement of the cutoff along local injections.

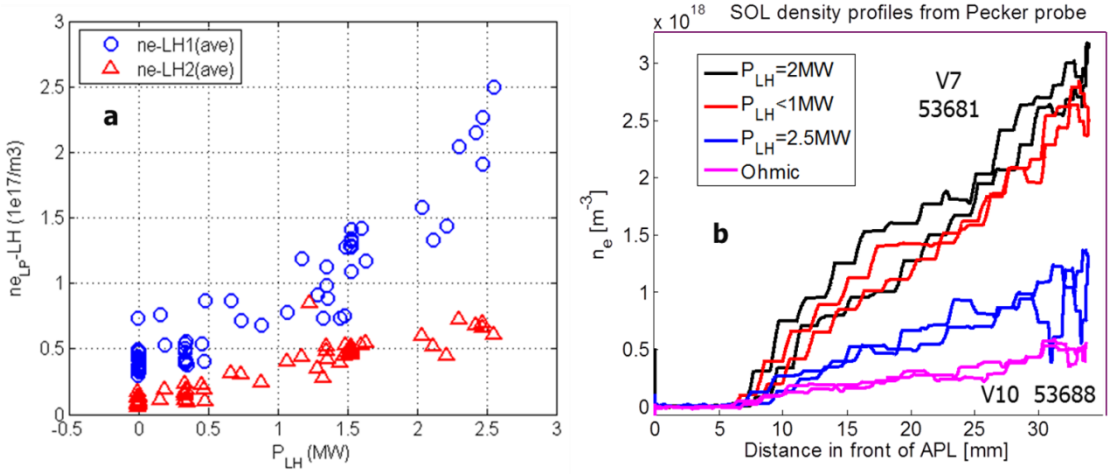

Figure 5.14: Electron density (a) from Langmuir probes embedded on LH launchers and (b) profiles from upper Pecker probe on WEST APL for different LH power.

In EAST however, reflectometry allowed to observe more significant displacements of the cut-off layer. We now propose to take a closer look at the J-port region by analyzing the reflectometer and reciprocating probe profiles. Reflectometer profiles averaged over 50ms for gas puffed from the B and J ports were plotted together with reference profiles of a typical shot with density feedback controlled by SMBI and without gas locally injected on the antenna (Fig.4.8). The benefit of gas puffing over routine fueling clearly appears by increasing edge densities and significantly shortening the evanescence layer of the wave down by 2cm with the J-port mid-plane injection. According to He beam spectroscopy located near B-port, there is no difference in the cut-off position between B-port injection and J-port injection (Fig.4.7b). The cutoff positions are also similar for “routine” and “I-port” fueling consistent with B-port antenna loading (Fig.4.3c). Besides, according to the reflectometer located in J-port, the gas injection throughout J-port shortens the evanescence layer by 2cm compared to the B-port injection (Fig.5.15), consistent with

I-port antenna loading (Fig.5.5c and Fig.5.11) [Messian & Weynants 2011]. Considering that part of the gas puffed around the B-port might not contribute to an increase in density profile at the mid-plane and that the distance between the B-port and the reflectometer is rather large, could together explain why profiles during gas puffing on the B-port flatten a bit but do not improve as significantly as when gas was injected from the J-port mid-plane. Notice Helium beam density values are of roughly similar order of magnitudes, yet He-BES profiles are rather flat in the SOL.

The reciprocating probe was inserted twice per shot as can be seen on graph k of Fig.5.1b. Moreover, as instances of gas puffed on the B-port were identical to those of routine puffing, they were not represented not to overload Fig.5.16. Surprisingly in most cases no significant density increases were observed on the reciprocating probes due to gas puffing unlike the much more visible observation on the reflectometer profiles (Fig.5.15). Known from precedent studies [Urbanczyk 2017], [Bécoulet 2002], [Kirov 2009], strong local density convections due to local E×B drifts affect this region when the I-port antenna is active, higher potential gradients and consequently lower densities are measured when the I-port antenna is powered. Higher densities and lower potentials on the contrary are registered when the B-port antenna is powered, as it is far and magnetically disconnected from the probe (Fig.4.12b). This suggests that a non-negligible part of the gas that is puffed is pumped-out and does not contribute to increasing the density in front of the antenna. In particular, note this edge density pump-out effect is much stronger when gas is puffed along I-port antenna height from ten points (blue curves) instead of from a single mid-plane valve (pink curves). Despite the lack of strong experimental proof, we would like to stress that this observation might also be the result of stronger potentials and therefore density convections at the antenna corners rather than at the mid-plane [Bobkov 2010]. So far based on the SOL parameters modification in presently discussed cases, the mid-plane injection is advantageous for increasing the density in front of the ICRF antennas.

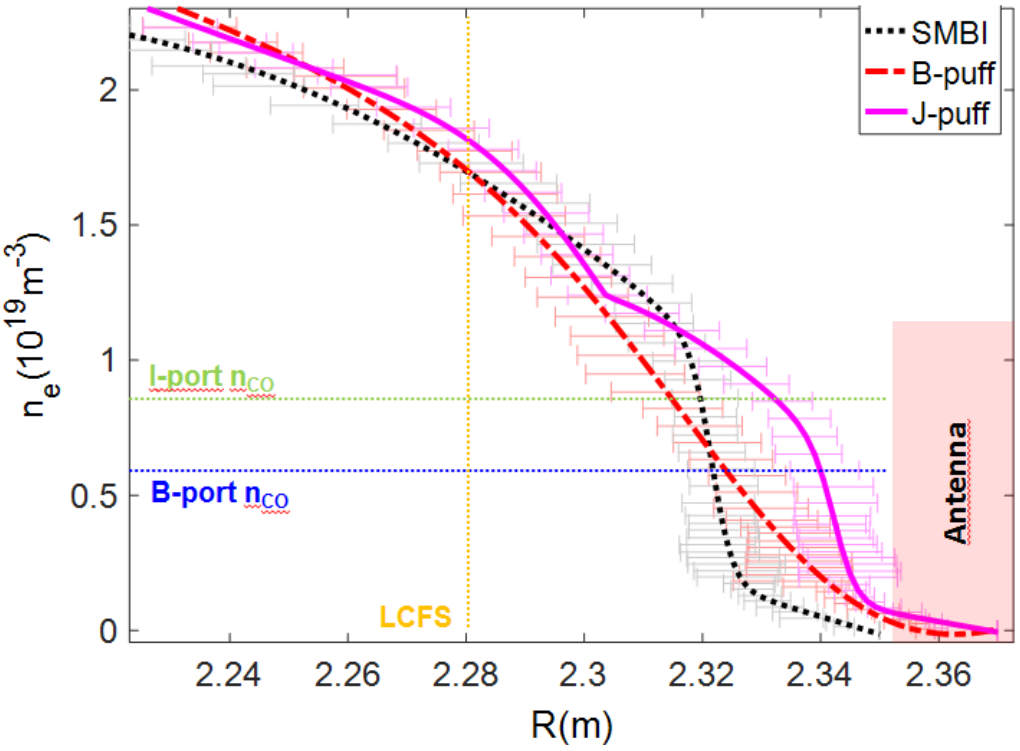

Figure 5.15: Density profiles from the J-port reflectometer in three different cases with the SMBI corresponding to the classic or routine case, and when gas was puffed from B and J ports. Cutoff densities of each antenna are also indicated to show the benefit of gas puff for shortening the evanescence layer.

Cf detailed shot list in Table 5.1.

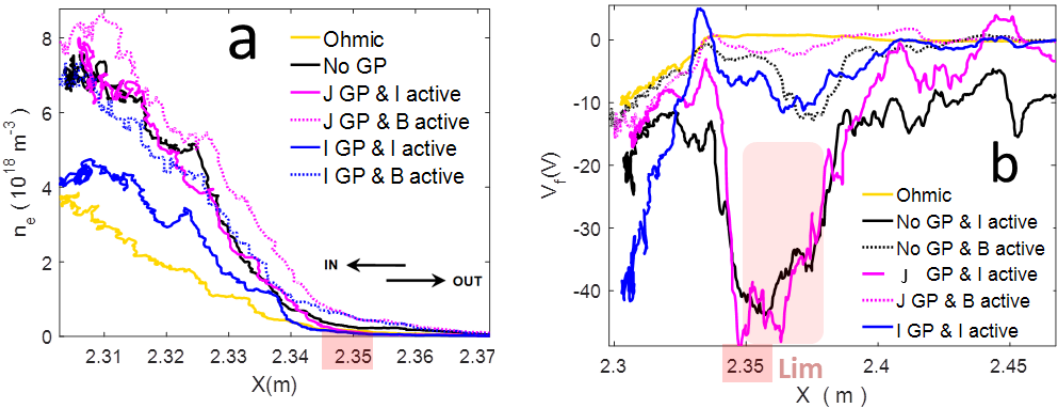

Figure 5.16: Electrons density (a) and floating potential (b) profiles from the J-port reciprocating Langmuir probe during the 2017 gas puff experiments. The ICRF antenna limiters position (2.35m) is indicated in red. Cf detailed shot list in Table 5.1.

5.2.3. Gas injection influence on impurity sources in WEST

In Fig.5.8 and 5.9, we observe that Q1 antenna systematically has a higher coupling (~30%) than Q2 antenna. This was partially explained (10%) by the fact that Q2 antenna was mounted with a toroidal asymmetry, such that the right side limiter was 4mm closer than the left one. This radial gap between both limiters was actually predicted from the beginning thanks to visible spectroscopy data which were systematically smaller on the left than on the right limiter (Fig.5.17).

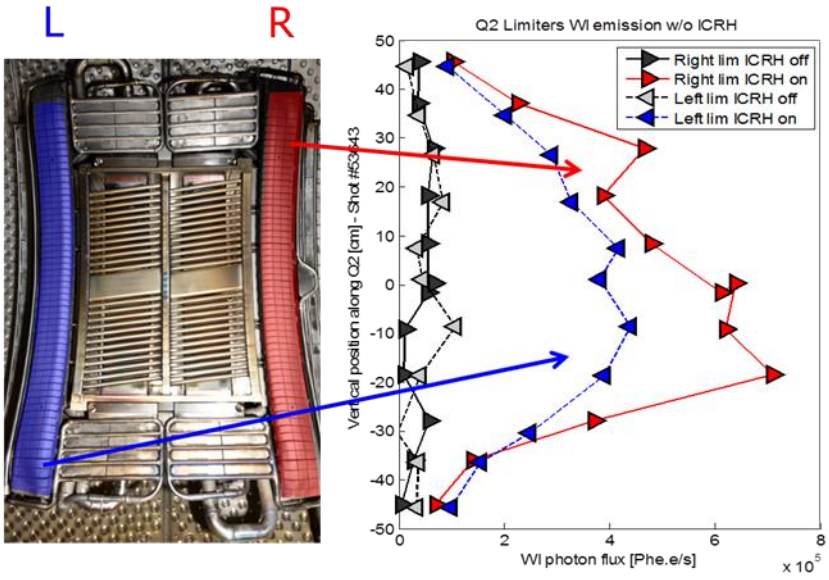

Figure 5.17: WI poloidal profiles along WEST Q2 antenna limiters.

In WEST, visible spectroscopy can also be used as a proxy like in Fig.5.7b to characterize the influence of injections on local particle fluxes such as poloidal profiles of DI and WI. Looking at Q2 right limiter (Fig. 5.18), it appears that the deuterium influx on the surface increases consistently with the D_2 injection rate for both valves. Poloidal profiles of the effective sputtering yield estimated based on assumptions detailed in section 4.3.2.2 (eq. 4.19), follow patterns consistent with local temperature decrease in surfaces magnetically connected to the valves. The effect is particularly visible when the gas is injected from 8 points poloidally distributed along Q2 antenna's height. The effective sputtering yield decreases significantly in regions materialized by blue arrows in Fig.5.18a roughly corresponding to antenna corners in comparison with case of injection from V7 (red stars linked with magenta dotted lines). This observation could be the combination of three effects;

- the local cooling effect due to the gas on the right limiter, which connection

length is very short (7cm)

- the global improvement of the coupling in particular near the corners usually victim of higher fields caused by RF sheath excitation
- the improvement of electron mobility in the SOL resulting from gas density increase [Palkina 1971], and balance of the dominant parallel transport with poloidally homogeneous sources of gas

The profiles of tungsten (WI) however do not change much for different valves and levels of injection, revealing that impurity production changes little in the injection rate explored.

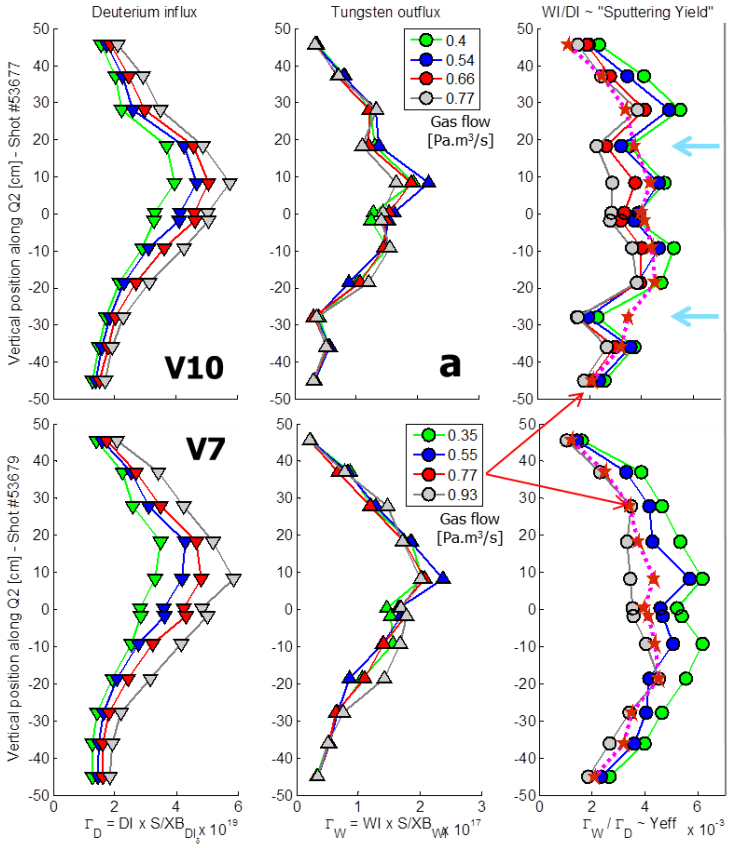

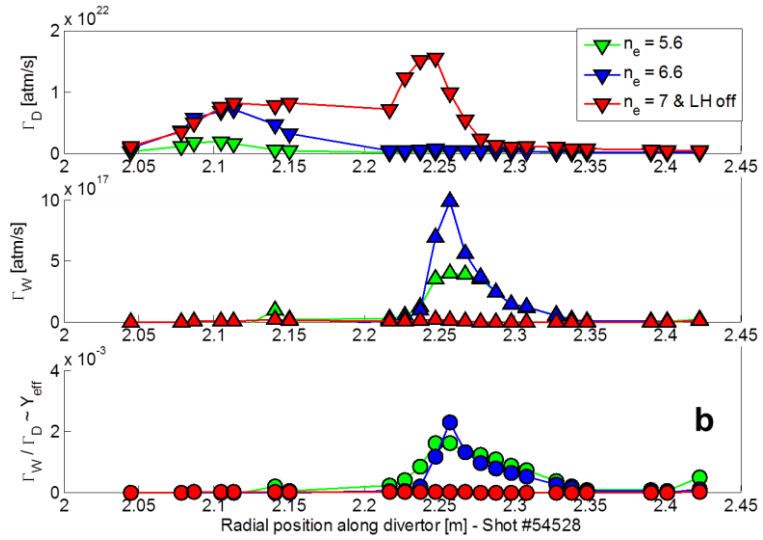

Figure 5.18: Deuterium and tungsten fluxes estimated from DI and WI calibrated data (Ph/m²/s/sr) poloidal profiles along (a) WEST Q2 antenna right limiter and (b) divertor targets, with S/XB coefficients determined in section 4.3.2.2. Different profiles are superposed in (a) for different fueling rate on V10 and V7 and different core densities in (b). An effective sputtering yield is estimated from the ratio of both species fluxes (eq. 4.19)

In the divertor region, no particular behavior was observed during the first session with feedback fueling. However during the 2019 session with feedback fueling and high density requests, for densities above $6.5.10^{19}m^{-2}$, deuterium flux on the divertor target kept increasing up to strong temperature decrease at the target from 15eV down to 3eV measured by embedded Langmuir probes and resulting in a strong decrease of tungsten sources as seen in Fig.5.18b. An overview of the discharge with divertor probe signals is provided in Annex 4.

5.2.4. Gas injection influence on divertor heat loads in EAST

In order to get a wider picture of the influence of local gas injection on the SOL, the last aspect to be discussed concerns the divertor region. As the experiments we have done were all in USN (Upper Single Null) configuration, we will focus on the upper tungsten divertor outer targets in two different toroidal regions monitored by triple Langmuir probes arrays. So far we have seen on Fig.4.6 that despite the cooling effects of the neutral gas on the SOL, density increase may lead to stronger heat loads on the antenna limiter, with $q_{//} \approx \gamma\, j_{sat}\, T_e$ and γ assumed to be 1. The last question to be

answered is if this density increase also has similar influence on the divertor region which could compromise the use of local gas injection for long pulse operations and scenarios with high heat fluxes. It was shown for the 2016 experiments that the ICRH-induced negative floating potentials can be greatly mitigated on most upper divertor probes with local gas injection, whereas ion fluxes, on the contrary, increase [Perkins 2017]. As was mentioned in the previous section, Langmuir probes are sensitive to RF sheath expansion which can make data interpretation more complex in cases with high RF power. In 2017, the same probe arrays (Ports D and O) on the Upper Outer (UO) divertor target – as represented on Fig.5.2 – were used to estimate heat fluxes (Fig. 5.19). Highest values were recorded around the D-port nearby the divertor corner by the top pair of probes indicated by blue circles on Fig.5.2. As shown in Fig. 5.19, gas injection generally helped reducing heat loads at the divertor target with best global mitigation (D and O ports simultaneously) under 1MW/m² achieved by injecting gas at the mid-plane (J-port puffing).

Note heat loads from each probe array have slightly different patterns that could possibly be attributed to toroidal asymmetries like these observed during ICRF operation in NSTX [Perkins 2012]. Since Langmuir probes are inherently sensitive to RF sheaths, different magnetic connections to ICRF antennas can lead to different results. Ideally this diagnostic should be benchmarked by another one insensitive to sheath rectification like IR camera; However this diagnostics data are not trustworthy due to the absence of calibration of the emissivity of EAST tungsten divertor monoblocks that are furthermore daily coated with lithium.

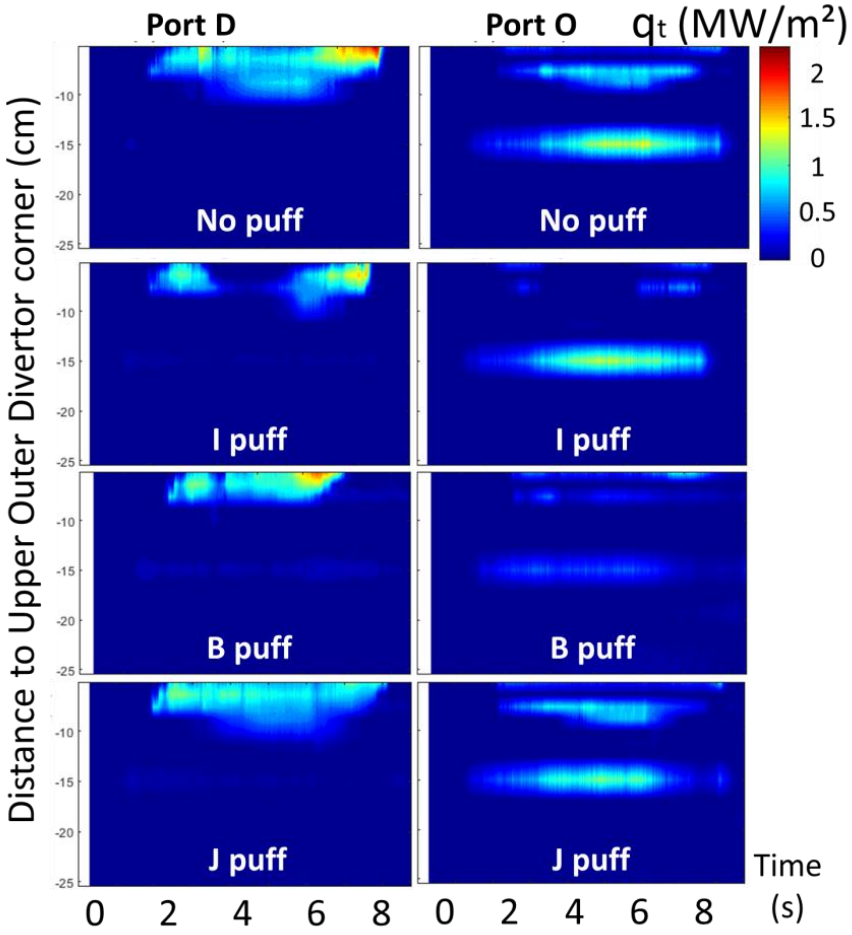

Figure 5.19: Upper Outer divertor target heat loads profiles from both D and O ports Langmuir probe [J.C.Xu 2016] arrays in each case of gas injection.
Cf detailed shot list in Table 4.1.

Summary of coupling experiments

In this section were presented ICRF coupling experiments in L-mode involving local gas injection in EAST and WEST. It is well known that to maximize waves coupling, the two most important parameters are the plasma global density and waves frequency. Once these two parameters are fixed, others parameter can help improving further ICRF waves coupling. Lower Hybrid (LH) power typically helped a lot improving ICRH coupling, likely due to fast electrons helping ionizing the neutral gas injected from magnetically connected valves. Experiments in EAST revealed that

fueling from the mid-plane not only helps to couple waves from nearby antennas like in other devices, but also has an impact on the scrape-off layer (SOL) density in regions that are not magnetically connected to the valves. Localized mid-plane nozzle valve (J-port) allow in EAST better coupling compared to poloidally distributed valves (B and I ports). However in WEST, no significant improvement was so far observed with local injection compared to routine fueling from valve at the top of the vessel. This can be explained by the facts that unlike in others devices (Table 5.3), not only the ICRF wave cut-off layer is not in the SOL but in the confined region, but also very tiny quantities of gas were injected due to low pumping capacity (such that small quantities of gas did not have much influence on the cut-off position). In addition, core density control requirements for long-pulse operation limit the amount of gas that can be injected, in particular in L-mode. Similar experiments should then be repeated with full pumping capacity and in H-mode.

In future experiments with ICRH in EAST, the study strongly suggests to fuel the plasma with single nozzle valve located at the mid-plane and radially retracted (J-port valve). In addition, keeping a significant LH power level is important to help ionizing the neutral gas injected nearby ICRH antennas.

If injected from radially retracted points, gas can spread and could probably help reducing sputtering yield on active antenna limiters by a combination of four effects: (a) reduce thermal effects by cooling down the SOL (b) improve coupling and therefore reduce the overall near-field amplitudes for a given RF power, (c) increase the electron mobility in the SOL and thus mitigate the excitation of parallel components of the electric field and (d) dilute impurities which are the main contributors to sputtering. Impurity aspects will finally be further addressed in the last section.

6. ICRH influence on impurity production

In view of future experiments on larger devices like ITER and the China Fusion Engineering Test Reactor (CFETR), WEST and EAST aim at long pulses operation at high power both to test the W-monoblocks technology for ITER and to learn how to make the control of the plasma compatible with steady state operations. Higher power demand nevertheless comes with challenges in terms of plasma surface interaction and impurity mitigation. Despite available methods for optimizing waves coupling detailed in the previous section, high power scenarios feasibility using the most of the ICRH power available at the generator depends a priori on where the impurities are produced, and on which physical mechanisms play a role in their production. ICRF plane waves can propagate under two eigenmodes with substantially different properties; the Slow Wave (SW) with non-negligible electric field component parallel to magnetic field and the Fast Wave (FW) which electric field component is perpendicular to magnetic field. SW parallel electric field is known [Urbanczyk 2018-19] [Bobkov 2017], [Meyer 2018], [L. Zhang 2015] for exciting RF sheath on PFCs in the SOL and induce deleterious Plasma Surface Interaction (PSI) effects and high-Z impurity production. In most tokamaks SOL plasma, the SW is evanescent such that it cannot propagate far from where it is excited. We will therefore refer to PSI observations related to direct excitation of the SW as near field effects. The FW must propagate up to the ion cyclotron resonance layer and heat core plasma. However, in scenarios with poor single-pass absorption, the RF fields are high throughout the machine (incl. the High Field Side (HFS)) and non-negligible amount of power can be carried by FW up to PFCs far away from the antenna. As FW reflects on Plasma Facing Components (PFCs) (actually an evanescent FW transmitted beyond a cut-off layer reflects on a PFC) part of the power is converted into SW and RF sheath are excited (Fig.2.7). We will then refer to PSI observation resulting from this type of mechanism as far field effects. ICRF can therefore have particularly deleterious effects near antennas where the strongest near-fields appear. To a smaller extent this can remain true further away, and sometimes even in non-magnetically connected regions due to far-field interactions [Urbanczyk 2017] as observed on many devices like Tore Supra [Colas 2007], [Kubic 2013], Alcator C-Mod [Ochoukov

2014], [Cziegler 2012] [Hong 2017], JET [Bobkov 2013], ASDEX Upgrade [Bobkov 2017] and LAPD [Martin 2017]. The ICRH wave absorption efficiency – estimated by comparing the break-in-slope technique with the ITER89-P scaling law in ref. [Y.Q.Yang 2017] – was found to be generally low (~35%). In this case, a significant part of unabsorbed power might well lead to far-field-induced interactions in unexpected locations, hence the need to localize and characterize impurity sources at least qualitatively [Dux 2009], [Lipshultz 2001], [Wukitch 2009]. We first discuss far-field effects on EAST high field side wall and WEST divertor target. Then we will present observations made on EAST divertor, mostly attributed to near field effects. Finally we will show examples of near field impacts on low field side PFCs either close or magnetically connected to active ICRF antennas.

Details on the effects influence on WEST operation are further discussed under [Colas 2019], while a very complete overview of this topic can be found under [Bobkov 2017 NME] and reference therein. Note experimental approaches are substantially different in all tokamaks (section 3.2); WEST has a full tungsten environment [Bourdelle 2015] equipped by numerous visible spectroscopy lines of sight [Meyer 2018] allowing relative comparison of impurity sources, whereas multiplicity of materials in EAST can be used to extract relatively local information on PSI with Extreme Ultraviolet (EUV) spectroscopy [L. Zhang 2015]. WEST visible spectroscopy data were absolutely calibrated only after C3 campaign such that not only qualitative but also quantitative studies were à posteriori possible. We also acknowledge that EUV spectroscopy is not the most appropriate diagnostic for impurity sources study, but as far as EAST is concerned, temperature and density profiles did not significantly change along EAST experiments, temperature effects on impurities brightness and transport are assumed negligible. The study uses the diversity of materials to extract, via Extreme UV (EUV) spectrometry in the plasma core, local information on dominant PSI process during ICRH. Intensities of EUV spectral lines characteristic of each material, normalized to line-integrated plasma density, exhibit different parametric dependencies over scans of ICRH and LH (Lower Hybrid) power and for different toroidal phasing between straps, strap power balance and magnetic configurations. This diversity of behavior is interpreted as the signature of different physical processes. Before 2017 only the upper divertor region contained tungsten (W). Large increase in core W content could be observed when moving from lower (LSN) to upper single null (USN) configurations. The W content was then

found to better correlate with the total injected power than the ICRH power, despite signs of RF-induced SOL biasing recorded locally by fixed divertor probes away from the strike points. Mo, covering part of the inner wall facing one ICRF antenna, was mainly sensitive to the ICRH power from this antenna, as well as to the phasing of its straps. Modelling suggests a possible interaction of the inner wall with residual ICRF waves crossing the plasma. Materials close and magnetically-connected to an active antenna show better correlation with ICRF antenna electrical tuning than those which are far away or not connected. This is in particular the case of W since 2018, when the limiter tiles of the LH launchers were changed. In these latter conditions, it is finally shown that, W sources at the mid-plane (equatorial plane) contribute to a significant fraction of the core contamination by tungsten (25% in ohmic regime, probably more during ICRH).

Shots	Ip	ne	Config	ICRF			LHCD				
				I port		B port	2,45GHz	4,6GHz	**P icrh**	**P lhcd**	**P tot**
				Phase	Power	Power	Power	Power			
69819	500	3	USN	**180**	0.840	0.800	0.500	1	1,64	1,5	3,14
69823	500	3	USN	**90**	0.830	0.800	0.500	1	1,63	1,5	3,13
69824	500	3	USN	**60**	0.830	0.800	0.500	1	1,63	1,5	3,13
69825	500	3	USN	**0**	0.830	0.800	0.500	1	1,63	1,5	3,13

Table 6.1. EAST shot list for I-port ICRF antenna phasing scan.

Power are written in MW, Phasing in degrees, I_p in kA, and n_e in $10^{19}m^{-3}$, B_t = - 2.25T.

Shots				ICRF power		LHCD power				
	Ip	ne	Config	I port	B port	2.45GHz	4.6GHz	**P icrh**	**P lhcd**	**P tot**
69671	500	3	USN	0.4	0.4	0,5	1	0,8	1,5	2,3
69672	500	3	USN	0.5	0.4	0,5	1,3	0,9	1,8	2,7
69673	500	3	USN	0.6	0.5	0,5	1,6	1,1	2,1	3,2
69675	500	3	USN	0.57	0.6	0,5	1,8	1,2	2,3	3,5
69677	500	3	USN	0.73	0.56	0,5	1,8	1,4	2,3	3,7
69678	500	3	USN	0.85	0.8	0,2	1,8	1,65	2	3,65
71128	450	2	USN	0,55	0	0	1	0,55	1	1,55
71130	450	2	USN	1	0	0	1	1	1	2
71135	450	2	USN	1,5	0	0	1	1,5	1	2,5
71136	450	2	USN	1,75	0	0	1	1,75	1	1,75

68552	400	3	USN	0.18	0.27	0.5	0.7	0.45	1.2	1.65
68553	400	3	USN	0.27	0.18	0.5	0.7	0.45	1.2	1.65
68554	400	3	USN	0.27	0.27	0.5	0.7	0.54	1.2	1.74
68555	400	3	USN	0.14	0.4	0.5	0.7	0.54	1.2	1.74
68556	400	3	USN	0.42	0.42	0.5	0.7	0.84	1.2	2.04

Red series	ICRF power per strap (unbalanced)							
Shots	I-port antenna strap number				B-port antenna strap number			
	#1	#2	#3	#4	#5	#6	#7	#8
68552	0	90	90	0	0	90	90	90
68553	90	90	90	0	0	90	0	90
68554	0	90	90	90	90	90	0	90
68555	0	0	140	0	0	140	140	120
68556	140	140	140	0	0	140	140	140

Table 6.2. EAST shot list for the study of impurity behavior with ICRF and total power written in MW, I_p in kA and n_e in $10^{19}m^{-3}$. In all these shots B_t = - 2.5T. In the blue series, LH power remained constant while it changed in the black series. Power balance on straps was changed in the red series (cf detailed table).

Shots				ICRF power	
	Ip	ne	H/H+D	Q1	Q2
53700	500	3	15	0.2	0.2
53701	500	3	7	0.2	0.2
53702	500	3	4	0.2	0.2
53703	500	3	3	0.2	0.2
53704	500	3	11	0.2	0.2
53705	500	3	11	0.2	0.2

Table 6.3. WEST shot list for the H concentration scan without LH

Shots				ICRF power			LHCD power				
	Ip	ne	Config	Q1	Q2	Q4	LHa	LHb	**P icrh**	**P lhcd**	**P tot**
53921	500	3->4	LSN	0	0.6	0	1	2	0.8	3	3.8
53923	500	3->4	LSN	0	0.8	0	1	2,5	0.8	3.5	4.3
53934	500	3->4	LSN	0	1	0	1.5	2.8	0.8	4.3	5.1
53971	500	3->4	LSN	0.2	0.2	0	1	0,5	0.8	1.5	2.3
54633	500	3->4	LSN	0.5	0	0.5	0	0	1	0	1
54657	500	3	LSN	0.4	0	0.5	0	0	0,9	0	0.9

Table 6.4. WEST shot list for the study of impurity behavior with ICRF and total power written in MW, I_p in kA and n_e in $10^{19}m^{-3}$.

6.1 Experimental conditions and protocols

Experiments in this section will mainly use the following parameters: toroidal magnetic field Bt=2.3T and USN configuration in EAST and Bt=3.7T and LSN configuration in WEST with plasma current of about 500kA. When not mentioned, all straps in a given ICRF antenna were fed with RF currents of comparable magnitude in dipole phasing (with 180° phase difference between RF-currents in toroidally-adjacent straps). It is important to mention that ICRH phases were not real-time controlled in EAST, which will be discussed in section 6.4. Lower Hybrid was almost always used both for heating the plasma and shaping current profiles to allow steady state operations. Only a couple of WEST discharges without LH and during which different H concentrations were explored (Table 6.3). Plasma isotopic ratio (H/H+D) rarely decreases below 5% in EAST, while in WEST it was on the contrary hard to increase the H concentration up to 7% for which ICRF absorption should be optimal according to TOMCAT modeling. To achieve better control of the H concentration, WEST decided to fuel the plasma with mixed bottle (90% D and 10% H) while EAST uses daily lithium coating before each session (~1 gram on average). Low-Z materials coating is also useful to keep impurities like oxygen and carbon down to acceptable levels in terms of radiated power. Clearly in WEST, the radiated power fraction is very high (sometimes over 100% in discharges with ICRH) which is why boron coating (boronization) was applied a couple of times to help commissioning systems, while EAST is simply not capable of doing any plasma without lithium coating. Low-Z materials coating can also have mitigating effects on high-Z impurity contamination like tungsten [H.Mao 2017], but sadly this effect does not last long enough to be compatible with long pulse high power operation since the thin layer (~1 μm) can be rapidly eroded (~1 min plasma) in particular where main impurity sources are observed [Dux 2009], [Lipshultz 2001], [Wukitch 2009], [Urbanczyk 2018-19].

In EAST, lines brightness measured by the EUV spectrometer presented in section 4.3.2.1 are systematically normalized by plasma density, and their parametric variations from pulse to pulse within the same experimental session are interpreted as a change in the sources of impurities rather than their transport. This assumption is fairly good for most species which radiate relatively close to the edge and easily

penetrate inside plasma. Note this can be questionable for W coming from the divertor region, as it is not only expected to be better screened but also its emissivity mainly comes from plasma center, and is therefore more sensitive to transport in both SOL and confined plasma. As far as edge turbulent transport is concerned, it has been shown in several devices that it usually does not change much in presence of ICRH [Wukitch 2014], [Bobkov 2017]. As for neoclassical transport, we acknowledge some changes may occur, yet as temperature and density profiles remained fairly similar along the experiments, this transport is not expected to significantly change our conclusions. More importantly, T_e in the core did not change much (<10% as shown in Fig.6.1f) and its profile remained relatively flat at the center without fast particles. The spectrometer was moreover measuring W continuum. These assumptions guarantee that W brightness measured by the EUV spectrometer was not significantly influenced by T_e changes. This assumption will be shortly benchmarked by neutral tungsten intensity (WI) measured in the upper divertor with visible spectroscopy.

In WEST on the contrary, EUV spectroscopy was not used as much as in EAST because temperature changed a lot along the discharges such that the SIR spectroscope (section 4.3.2.1) which was mostly used to look for instance at high ionization states of tungsten, happened to be very sensitive to temperature changes (cf. W^{45+} in Fig.6.3c & d). Fortunately, the 240 visible spectroscopy Lines Of Sight (LOS) allowed looking at almost all limiters, divertor targets, baffle and inner bumper, which is very useful for studying impurity sources (section 4.3.2.2), in particular since most of the materials in WEST are coated with tungsten, such that it is not possible to determine its origin only based on UV spectroscopy.

In EAST however, many different materials in the vessel (summarized in Fig.4.2b & Fig.4.16) can be observed with UV spectroscope and seen as footprints of PSI in a relatively precise locations; Iron is found on antenna Faraday screens (underneath a boron carbide coating), the upper divertor is made of tungsten (noted W for W-UTA designing tungsten continuum) and molybdenum (Mo) that covers half of the high field side wall ($-180° < \phi < 180°$ and $-90° < \Theta < 90°$ as indicated by pink regions in Fig. 4.2a). In addition, two titanium (Ti) passive plates were installed at one toroidal location of the outer mid-plane for the specific purpose of serving as impurity tracers ($\phi \sim -90°$ and $-30° < \Theta < 30°$). Ti was found appropriate mainly for three reasons; a spectral line can easily be distinguished with the UV spectroscope from those of others species present in EAST, it can be used as a permanent plasma facing

component without affecting the vacuum conditions and its cost is reasonably low. Table 6.5 summarizes materials position in the tokamak.

The blue area in Fig.4.2 shows that only the B-port ICRH antenna magnetically connects to the Ti plates while only the I-port antenna faces the Mo inner wall tiles. Such location was chosen to confirm the role of magnetic connections in RF sheaths formation [Kirov 2009] and ICRH-enhanced PSI.

In the following, the different spectral lines are monitored over scans of ICRH and LH power by several combinations of both antennas (Table 6.2), with several toroidal phasing between straps (Table 6.1).

Materials	Location
C	Limiters and Lower divertor
Fe	ICRH antennas Faraday screens
Ti	Between D and E port Mag. Connected to B-port
Mo	All walls except 130° of the high field side facing B-port
W	**Before 2018** : Only upper divertor
	After 2018 : Upper divertor and LH launchers limiters

Table 6.5: Summary of materials location in EAST

6.2 Links between ICRH and impurities production

The objective of the following series of shots is to give an idea of how different species behave with respect to different heating schemes and according to their position and magnetic connections with active ICRH antennas (in particular in EAST). Typical shots representative of most discharges used in this chapter are shown respectively for EAST (Fig.6.1) and WEST (Fig.6.2).

Cases only heated with LH are used to set reference levels for each impurity without ICRH (black curves in Fig.6.1 and grey and pink flat-tops in Fig.6.2). The influence of ICRF can then be compared to these references; red curves in Fig.6.1 representing a case when the B and I ports ICRH antennas were also powered successively in dipole phasing and with 5Hz modulations of power between 0.5 and

1MW and blue area in Fig.6.3 during which Q2 was powered up to 600kW. Note the electron temperature and density remained fairly constant along EAST discharges (Fig.6.1f) justifying that UV spectroscopy data can reasonably be interpreted as changes of impurity sources. On the contrary in WEST, large changes were observed with constant increase of the density along the discharge (Fig.6.2a) and brutal temperature changes (Fig.6.2d) to which typically highest ionized state of the tungsten (W^{45+} which ionization energy peaks at 2414eV) appeared to be very sensitive (Fig.6.2c). For the discharge 53923, W^{41+} which ionization rate peaks at 1994.8eV could therefore be a roughly better proxy of how tungsten content qualitatively varied along the discharge, but precise analysis would require much more advanced efforts and calibrated spectra which were not available.

Radiation power changes very consistently with the injected power (Fig.6.1g and 6.2b). In WEST though, radiated power is suspiciously insensitive to changes in the density and particularly sensitive to power on Q2 (Fig.6.2b). This is explained by the fact that the bolometer is also in Q2 port and its measures are perturbed by RF when Q2 is powered. This problem will be resolved as soon as possible for instance by adding a filter at the ICRF frequency in entry of bolometer acquisition system. In EAST, plasma energy content (Fig.6.1g) does not change much while injecting ICRH, suggesting either that ICRH power is not well coupled or not well absorbed. Typical L-mode steady D-alpha signal is also provided in Fig.6.1g.

In EAST, all metal impurity signals increase fairly similarly during the application of LH power, except Mo which appears particularly insensitive. It is worth mentioning that, seen from our EUV spectrometer [L.Zhang 2015], the Mo^{31+} line is hard to distinguish compared to other species, such that its temporal evolution can sometimes be difficult to interpret. When the ICRH antennas are activated, Fe from antennas Faraday Screens increase and correlate with power modulations (such as Ag in WEST). Ti plates magnetically connected to the B-port antenna also react when this antenna is activated. Fe coming from each ICRF antenna however react more with the B-port than with the I-port antenna, this can be explained by the fact that the B-port is twice smaller than the I-port, such that for a given amount of power coupled from each antenna in similar loading conditions, power densities and fields induced on the B-port will likely be much higher than on the I-port. Even though people may expect a compensation out of the fact that the area wetted in the I-port is larger, we have

shown in Fig.2.9 how non-linear both the RF sheath-induced potential rectification and effective sputtering yields can be, such that slight increase in the energy gained by ions across the sheath might result in disproportionally larger effect on impurity production.

Note Mo however showed opposite behavior with higher content observed when the I-port antenna was powered. Since Mo is symmetrically present all around the vessel's low field side, we believe it does not come from there, otherwise it should follow a similar trend as Fe. As represented on Fig.4.2 by the pinkish region, the I-port faces Mo high field side wall whereas the B-port faces carbon. Impurities variations over an experimental phase scan of I-port antenna hints that Mo might come from the high field side wall facing the I-port and be the results of the so-called far-field effects. This intuition will indeed be supported by modelling results from EVE code. In WEST, evidences of far-field effects were also collected on the divertor by visible spectroscopy along a scan of the isotopic ration from 3 up to 11%, where the ICRF absorption efficiency is expected to improve based on modeling from TOMCAT code. These results will be presented in the next section.

In the next subsection, we will look more in details at the divertor region and show that W originating from the EAST divertor region seems to react equally to ICRH and LH power. We show that the RF rectification on divertor targets plays a minor role on impurity productions. Launched ICRH power can either be lost at the edge, or absorbed by the plasma and increase fluxes on divertor. A discussion on ICRF waves' absorption efficiency is therefore added and a correlation with total injected power is found. In EAST and WEST, thermal analysis made on the divertor with infrared cameras show that in high power discharges, ICRH can cause such an increase of impurity sources (last section) that the radiated fraction can increase beyond 100% of the ICRF power (Fig.6.2b), indicating that some fraction of the LH power is also lost, resulting in a cooling effect on the plasma, and a mitigating effect on the divertor heat fluxes (Fig.A30).

Finally, the last subsection discusses near-fields effects on surfaces magnetically connected to active antennas.

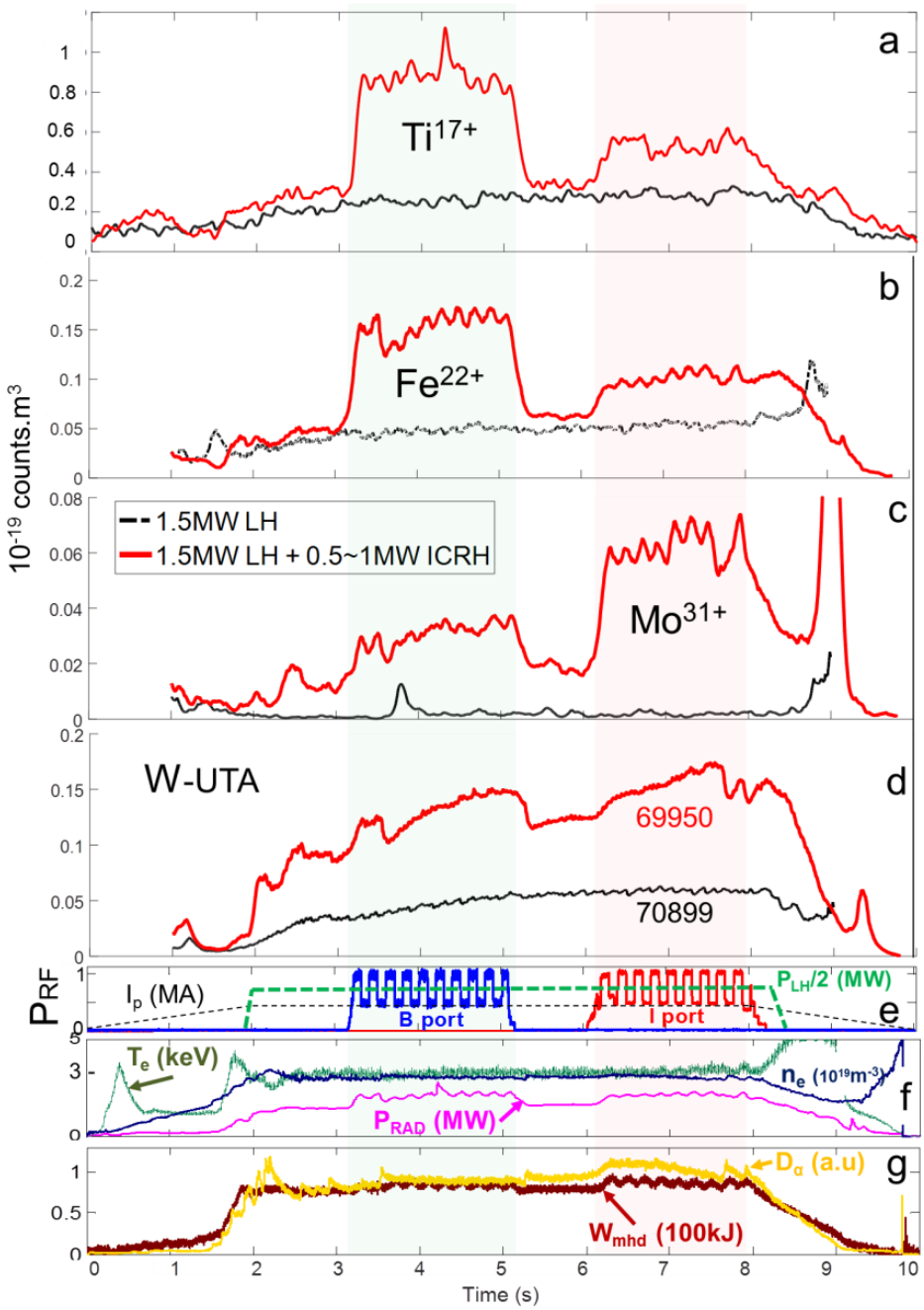

Figure 6.1: High-Z spectral lines brightness from EUV spectrometer normalized by line-integrated density of; titanium XVIII (a), iron XXIII (b), molybdenum XXXII (c), tungsten continuum (W-UTA) (d), ICRH, LH powers and plasma current (e), radiated power from bolometry, electrons temperature from ECE and density from interferometry (f), plasma energy (W_{mhd}) and Dα (g), for EAST #70899 and ICRH heated #69950 pulses

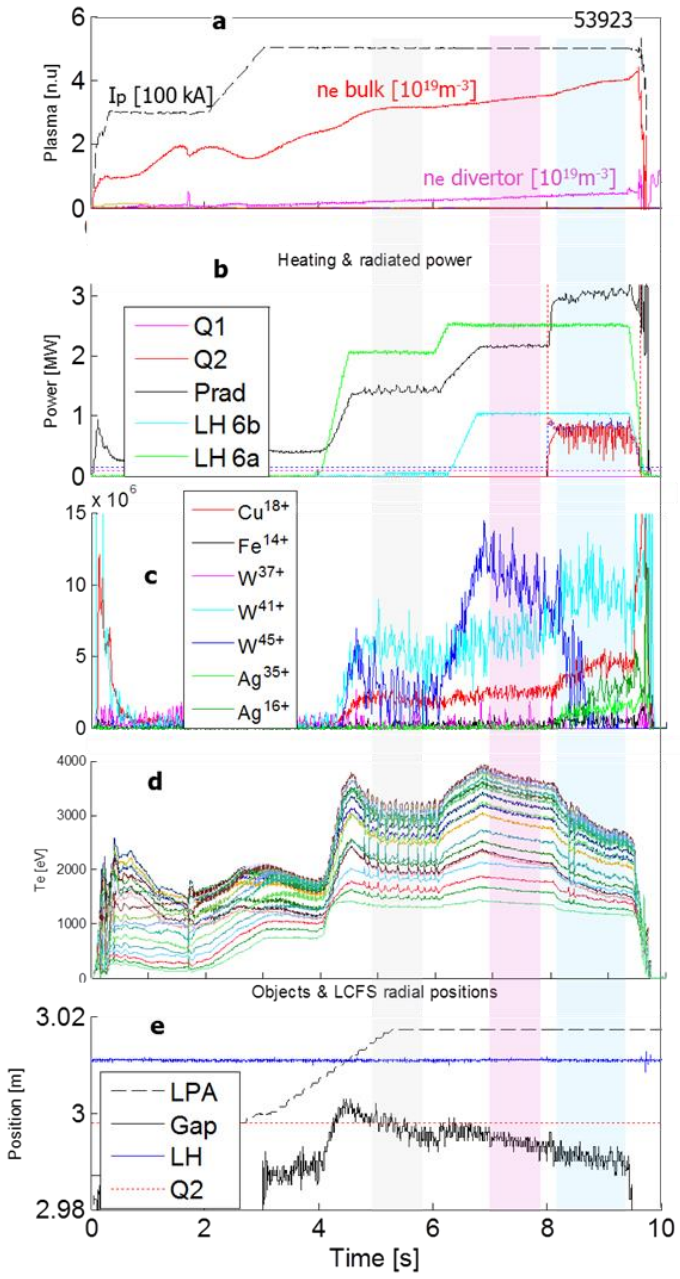

Figure 6.2: Overview of WEST 53923 discharge with (a) plasma current Ip and densities integrated along interferometry lines respectively watching central plasma and edge (divertor) regions, (b) different heating power and total radiation from bolometry (c) high-Z spectral lines brightness from UV spectrometers (d) temperature from ECE and (e) radial positions at mid-plane of separatrix (Gap) and main objects in the vessel. Grey, pink and blue areas enlighten flat-tops with different heating conditions

From Fig 6.1, we know that the total ICRH power in EAST ($P_{ICRH} = P_I + P_B$) is

not itself a fully relevant parameter to estimate impurity levels as power from I (P_I) and B ports (P_B) have different influence on different impurities. It consequently matters to have a relatively constant ratio P_I/P_B over power scan, which is kept close to unity ($P_I \approx P_B$). Note yet that since both antennas still excite RF sheath differently such that non-linear processes detailed in Fig.2.9 happen in different fashion, this hypothesis is still not fully satisfying. Since plasma shape did not change much, EUV spectral line intensities were systematically normalized to line-integrated density from interferometer and averaged over small periods of time (between 0.02 and 0.1s) and noted *Imp*. For each species and shot, ICRH-related impurity production Y_{shot} is calculated as

$$Y_{shot} = (Imp_{withIC} - Imp_{withoutIC}) / \max(Imp_{withIC} - Imp_{withoutIC})_{over.all.shots} \quad (6.1)$$

6.2.1 Far-field effects

6.2.1.1 EAST high field side wall facing an ICRF antenna

The high field side wall is a surface almost never magnetically connected to active ICRH antennas at the low field side. Interactions at the high field side are therefore in principle not correlated to what happens at the low field side as seen on Mo behavior in Fig.6.3. A way ICRH may have an impact on the inner wall is through the far-field, often resulting from a poor absorption efficiency leading to residual ICRH power crossing the plasma. By changing the phase difference between RF currents on toroidally adjacent straps of an IRCH antenna, the launched spectrum changes together with wave propagation and absorption properties. This allows discussing ICRH far-fields effects on the inner wall. In EAST, only phases of the I-port antenna were changed whereas the B-port antenna always operated in presumably dipole phasing. A series of shots with similar power and loadings on both antennas and different phases on the I-port antenna were studied and results shown in Fig.6.3. Ti, Fe and W remained relatively insensitive to the phase variation, which is surprising as both modelling (see appendix) and results from other devices respectively predict higher fields and an increase in impurity production as phasing tends towards monopole [J.H.Zhang 2017], [Bobkov 2017], [Lerche 2009 AIP]. On the one hand the absence of real time feedback control of EAST ICRH port phasing [Z.Chen 2018] can be blamed, but on the other hand Mo content varied in agreement

with what is expected from observations in other devices, namely an increase in Mo production going from dipole to monopole. This peculiar observation suggests high field side wall is a likely source of Mo correlated with the I-port antenna settings.

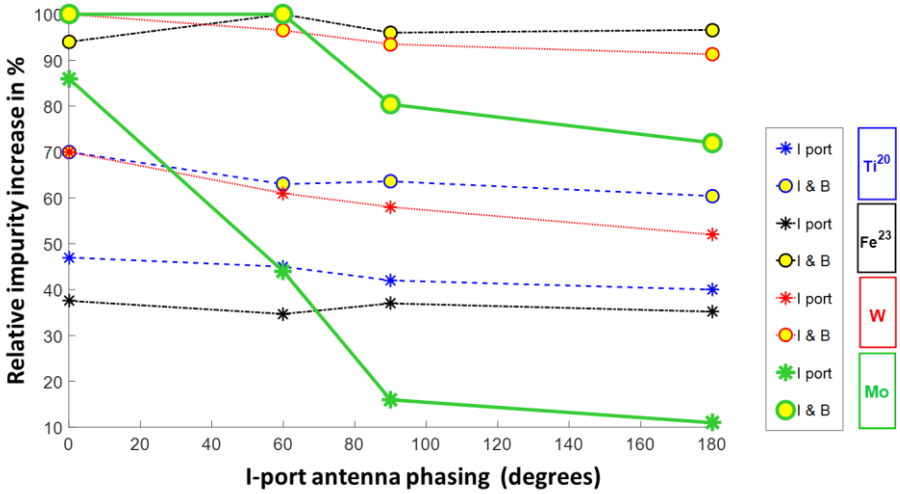

Figure 6.3: ICRH-related impurity production increase (Y_{shot}) versus I-port antenna phases. Cf detailed shot list in Table 6.1.

Note the B-port antenna still remains the principal cause of impurity production, which can be partially understood considering its size, twice smaller than the I-port antenna, leading to much higher power densities for similar generator power and loadings. This is particularly visible for the Fe characteristic of near-field interactions, whose level is quite low all over the I-port phase scan and increases by 150% when the B-port is activated.

Knowing this, and that Mo cover all low field side walls, if it were to come from the low field side, it would behave like Fe. Mo is however sensitive to I-port phasing, suggesting that it may come from the high field side wall facing I-port. Since dedicated experiments to answer on the origin of Mo are too challenging due to the lack of appropriate diagnostic, wave propagation and absorption were respectively simulated with EVE 3D [Dumont 2009] and TOMCAT 1D [Van Eester & Lerche 2013] codes (Annex 1.4). Both codes' results indeed point towards probable Mo source at the high field side. TOMCAT predicts a degradation of the single pass absorption from 50% in dipole phasing down to 15% in monopole phasing. On the real part of the iso-contours of the left-handed polarized electric field (Fig. 6.4), mode conversion can also be seen at the center with increasing residual power reaching the

inner wall as phasing decreases to zero. When this residual power is reflected on the inner wall, part of the fast wave mode can be converted into slow wave and excite RF sheath. In order to better enlighten wave properties in EAST, Fig.5.5 represents E field polarizations in different regions and for different phasing computed by EVE [Dumont 2009] showing mode conversion and increasing field amplitudes as phasing decreases and close to high field side. Where RF sheath excitation and the resulting plasma surface interactions are concerned, the parallel component of the electric field ($E_{||}$) is the most directly-related parameter to look at. Fig.6.5a shows the amplitude $|E_{||}|$ which dramatically increases at the high field side as phasing gets closer to monopole (φ=0°). These simulations suggest that as phasing shrinks to zero, absorption efficiency declines and mode conversion occurs. These fields on the inner wall are likely responsible for enhancing plasma surface interaction on the Mo surfaces at the high field side. So-called positive and negative field polarizations are also available in Fig.6.5b and Fig.6.5c, to better exhibit mode conversion nearby resonance layer (R=1.7m). It can also be seen on loaded spectra in Fig.6.6 that less than 60° phasing leads to the excitation of low $\boldsymbol{k}_{||}$ modes which are poorly absorbed and can results in proper modes in the plasma. These modes propagate in plasma edge and can lead to power losses and further enhance plasma surface interactions.

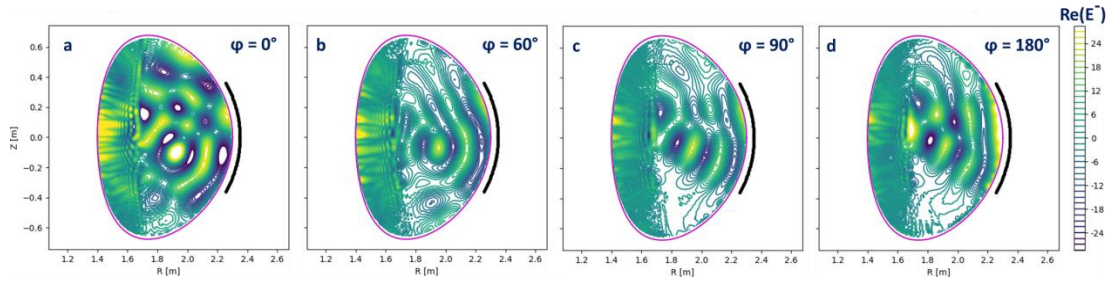

Figure 6.4: Iso-contours of the left-handed polarized electric field (real part), in kV/m, assuming 4.6MW of total absorbed RF power for various phasing of the I-port ICRH antenna; (a) φ=0°, (b) φ=60°,(c) φ=90°,(d) φ=180°.

Fig.6.6 also shows $\boldsymbol{k}_{||}$ spectra in vacuum and loaded by EAST plasma. It can be clearly seen on the loaded spectrum that a low $k_{||}$ mode is excited bellow 60° phasing. Low $\boldsymbol{k}_{||}$ mode absorption might be poor, potentially leading to proper modes in the plasma and power dissipation into the SOL with deleterious impact on plasma surface interaction.

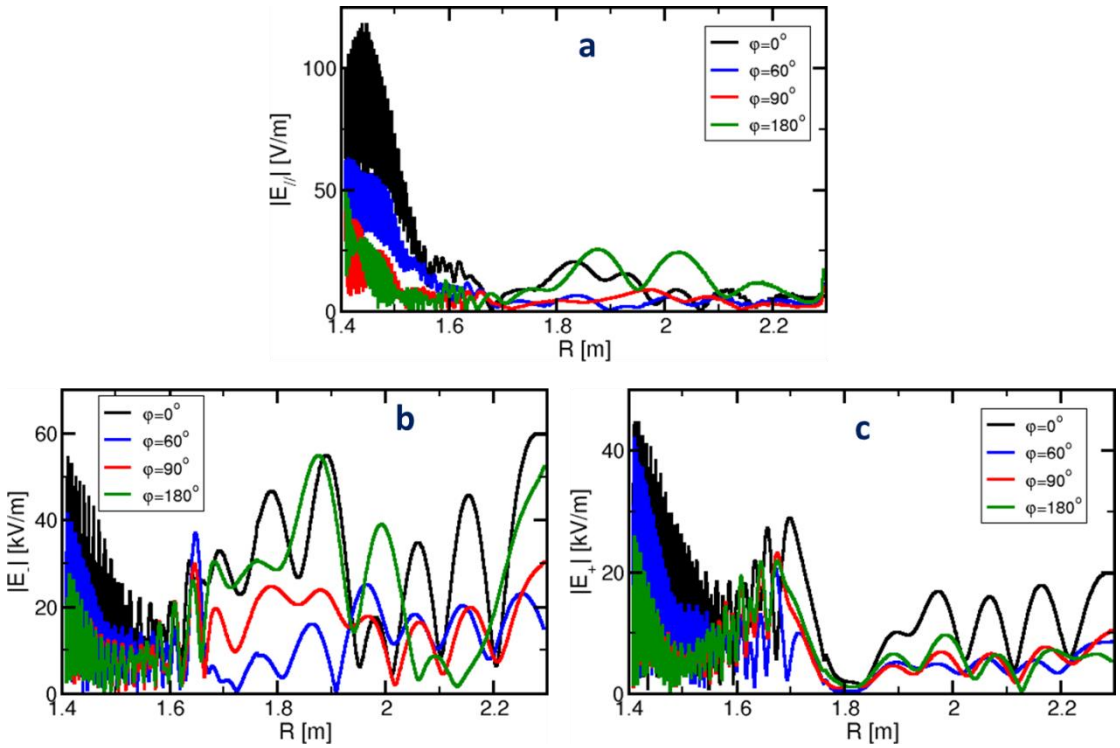

Figure 6.5: (a) Parallel (b) negative (left) and (c) positive (right) components of the electric field (in V/m) radial evolution in the equatorial plane, for the same conditions as in Fig.6.4 (from low field side to the right up to high field side to the left)

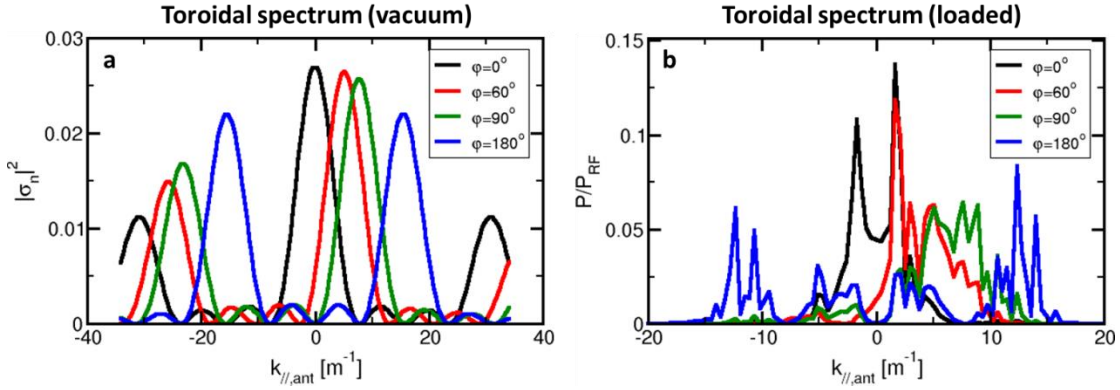

Figure 6.6: Antenna toroidal spectrums for different strap phasing (0°, 60°, 90°, 180°), in (a) vacuum and (b) in front of EAST plasma load (reference shot 69950).

We can also look how Mo behaves while changing ICRH power and keeping phasing as close as possible to dipole on both antennas. Three series of shots with scan of P_{ICRH} at generator in different conditions were analyzed. Y_{shot} as defined in

eq.6.1 is represented in Fig.6.5 for Mo. In the blue series only P_{ICRH} increased, while in the black series P_{ICRH} increased together with P_{LH}. In the red series, power balance on the B-port antenna straps is changed over the scan: one of the four radiating straps is typically switched off as the power is increased on the other straps. Through black and blue series in Fig.6.7, Mo seems to have no obvious correlation with the ICRH power. The red series confirms the negligible impact of B-port antenna on Mo, consistent with a source at the inner wall facing I-port.

Note decreasing phasing closer to zero not only has consequences on far-fields but also on near-fields as shown in Fig.6.7. Near-fields effects will be discussed in further details in section 6.3.3.

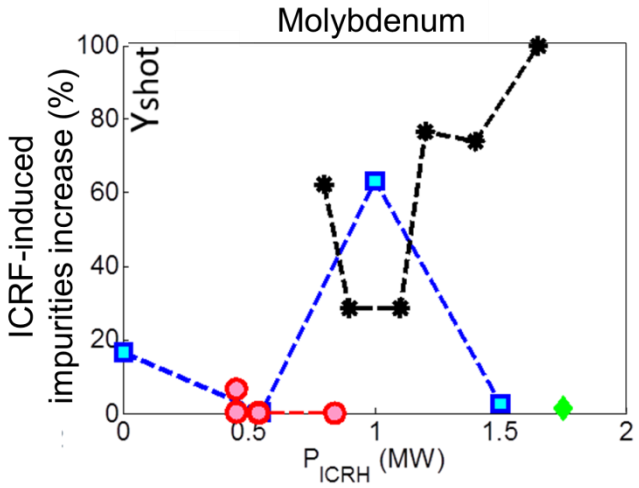

Figure 6.7: ICRH-related Mo production (Y_{shot}) as a function of ICRH power. In the blue series, LH power remained constant while it changed in the black series. Power balance on straps was changed in the red series. Green dot corresponds to a discharge only heated with ICRH power (balanced on all straps).
Cf detailed shot list in Table 6.2.

6.2.1.2 WEST divertor during H concentration scan

In WEST, simulations with TOMCAT [Van Eester & Lerche 2013] (Annex 1.4) predict that a hydrogen concentration of 7% is optimal for ICRF wave absorption (as shown by the green region in Fig.6.8a). However the H concentration was in practice very hard to control and was often too low during C3 campaign (as shown by the red region in Fig.6.8a). This is mainly due to the fact that the link between the voltage

applied to the piezo valve (V21) and its flow rate is not linear for small values. In addition a threshold value is necessary to trigger the opening of the valve, but this value is already too high compared to the flow rate which would be necessary to reach an optimal H concentration of 7%. It was still possible to explore different H concentration in discharges only heated with ICRH. After injecting large amount during the first shot (15% H during 53700 in Table 6.3), we could wait for the H concentration to naturally decrease by about two after each other shot. Observations made on the inner divertor target with visible spectroscopy are represented in Fig.6.8b. Each point is the result of several Lines Of Sight (LOS) averages on a time interval of interest. D and W atom fluxes are estimated from calibrated brightness of DI_{δ} and WI respectively pondered by S/XB coefficients taken for SOL temperatures of about 20eV measured by divertor Langmuir probes as detailed in section 4.3.2.2. Γ_W / Γ_D is again interpreted as a proxy of the effective sputtering yield Y_{eff}.

As the H concentration increases, we see that it does not have much impact on W sputtering yield in ohmic case as seen on the blue series. However in presence of ICRH, we see that both the sputtering and the tungsten outflux decrease as if ICRF absorption improves consistently with H concentration, and less power reaches the divertor target and excites RF sheath. This is another example of far field excitation on WEST divertor. Note far field effects could for instance be totally suppressed if 100% single pass absorption can be fulfilled, which rarely happens, but is expected to improve as the size of the device increases. In addition to this effect, if the ICRF power is absorbed by a small population of thermal H ions which are not well confined (Fig.6.9), these might receive such a kick that they would leave the plasma with high energy (above 2keV) and induce ion ripple losses. In Fig.6.9 representing the positions of the ICRF resonance (magenta curves) and regions of good confinement, we see that these do not intersect such that particles absorbing the ICRF power might very well leave the plasma rapidly down to the lower divertor. This phenomenon is yet not expected to play a major role in impurity production as can be seen in Fig.2.9 showing that the sputtering yield on a W target (lower divertor) of high energy H ions is much lower than the one of D ions in the range of energies due to RF sheath. Note that the gyrofrequency of D is half the one of H ions, such that heating D ions at its 2^{nd} harmonic should in principle be possible. We see however on TOMCAT modeling (Fig.6.8a) that D ions almost do not absorb power at all. This is likely because this type of heating would require having at least a small population of fast D

ions to ignite the absorption. This can for instance be done by directly injecting a neutral beam of ions at high energy, which is not available in WEST.

Break-In-Slope (BIS) analysis on the electron temperature [Lerche 2008] can also be used to get an estimation of the heating efficiency at the beginning or the end of an ICRF pulse. This method provided satisfying results moreover consistent with isotopic ratio estimations from the interpolation of highly resolved Dα spectra on the lower divertor and on the inner bumper (HFS wall). Not while doing these experiments, we only coupled about 200kW per antenna, however impurity sources increase already rapidly due to RF sheath excitation and tend to rapidly cool down the discharge in about 200ms after powering the antennas, sometimes even leading to radiation collapse and plasma disruption (Annex 7). In better cases, we have evidence of ephemeral plasma heating but the effect is rapidly balanced by impurity contamination. This effect has even begun stronger during the last campaign with the third antenna Q4 freshly coated with silver (Z=47) (Annex 8 and 9). The discharge presented in Annex 8 is interesting and will be further discussed in section 6.3.2.2 about the divertor region, because the positions of antennas and separatrix were reduced to bring the well-confined regions (blue areas in Fig.6.9) closer to the resonance. A consequence is that field lines passing in front of the antennas were then connected to the outer divertor (Fig.6.15) target and therefore enhanced impurity production.

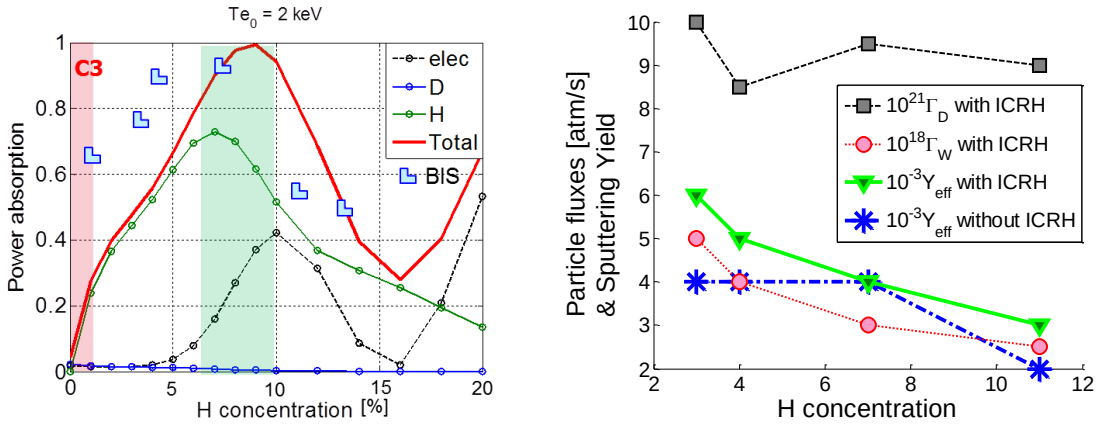

(a) (b)

Figure 6.8: Evolution along H concentration scan of (a) the ICRF power absorption efficiency computed with TOMCAT code and (b) the deuterium and tungsten atom fluxes on inner divertor target measured by visible spectroscopy; the ratio of tungsten over deuterium fluxes is used as a proxy of the effective sputtering yield and plotted with and without ICRH in WEST.

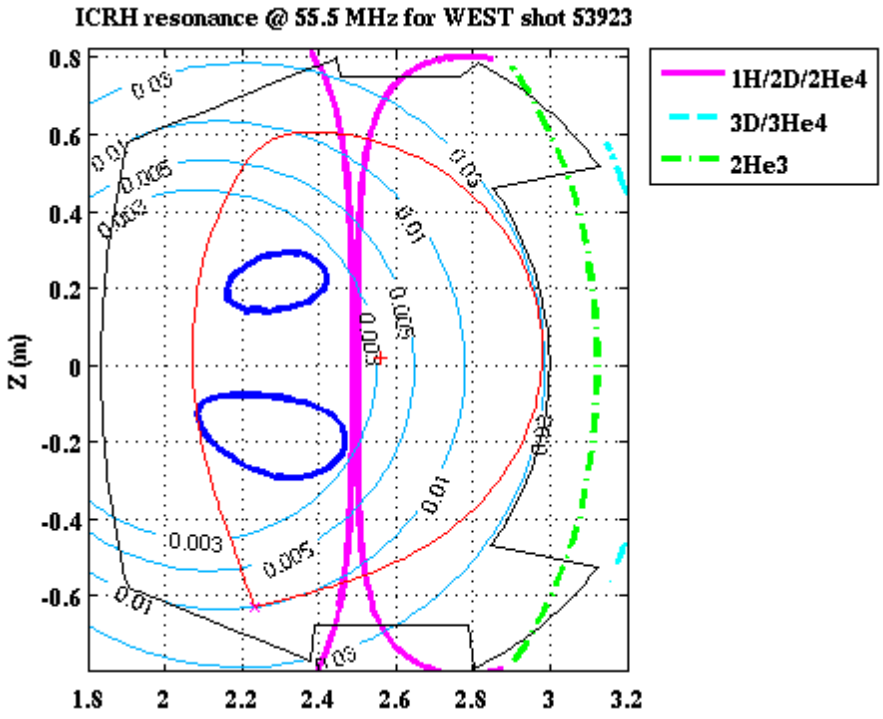

Figure 6.9: ICRH resonance location in WEST for a frequency of 55.5MHz and a magnetic field of 3.7T (shot 53923 which overview in given in Fig.6.2).
Blues circles represent regions where particles are well confined.

In EAST though, even if the absorption is not very good such that far fields certainly somehow have some impact in the divertor region, most observations are correlated with magnetic connections to active antenna and therefore attributed to near field effects [Perkins 2019] [Urbanczyk 2018].

6.2.2 Divertor region, a combination of all effects

6.2.2.1 EAST divertor

In this section will only be discussed cases before 2018, when W could only be found in the upper divertor. We will therefore interpret W continuum from the EUV spectrometer as a modification of W source assuming transport does not have a strong impact on core W content. Y_{shot} as defined in eq.6.1 is represented in Fig.6.10a for W.

For constant ICRH power, we observe similar W content when the power is unbalanced (red series) than when it is well balanced (blue series). This suggests that

the divertor region is insensitive to the antenna settings and only depends on the power injected. Furthermore, looking at the cases when ICRH increases together with LH power (black series), W content increases strongly hinting that the divertor region is sensitive to the total power injected rather than ICRH power alone. This can be confirmed by tracing impurity increase as function of P_{TOT} for all shots (Fig.6.10b). The impurity increase is defined as $|Imp_{\ during\ IC} - Imp_{\ before\ IC}|$ with ICRH (red series) otherwise $|Imp_{\ during\ LH} - Imp_{\ before\ LH}|$ (black series). Note the linear trend of both black and red dots, meaning that W production increases similarly with LH and ICRH.

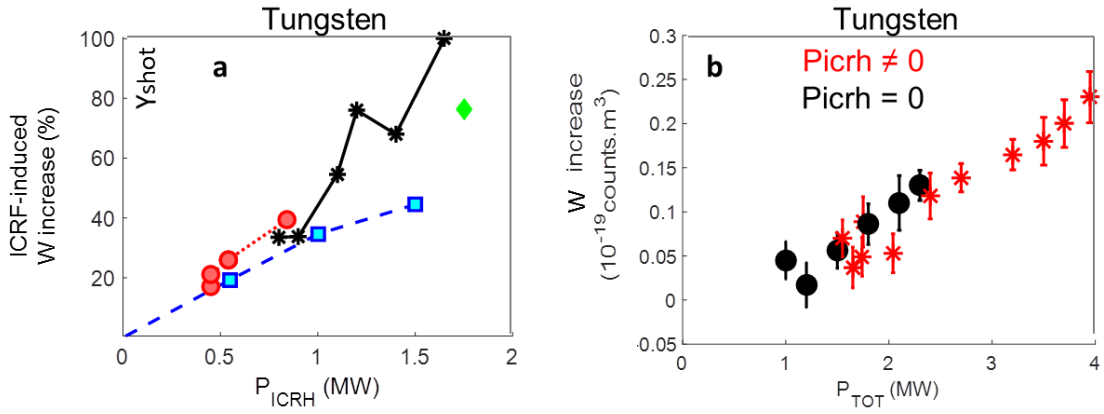

Figure 6.10: W production (Y_{shot}) as a function of (a) ICRH power and (b) total power. Blue, red and black series in graph **a** correspond to the same shots as in Fig.5.5. Graph **b** also represents to the same shots but points without ICRH (black series) were added as well. Cf detailed shot list in Table 6.2.

Considering how linear the red and blue trends are here above, we should now look after footprints of non-linear RF sheath through potential rectification in the divertor region. This is provided in Fig.6.11, representing floating potential and electron density profiles along upper divertor targets measured by Langmuir probes along the black series power scan. In the case without ICRH (black curve), potential and density rectifications are weak, but when ICRH is activated (colored curves) rectification is significantly stronger and increases together with ICRH power. Along the power scan, the inner strike point shifted from a probe onto another, explaining differences in some inner probes signals. This stands as a footprint of the effect of ICRH in the divertor region, and its localization is furthermore consistent with another dedicated study [Perkins 2018]. However we know from the red and blue series in Fig.5.8 that such rectification did not cause significant core W content

increase.

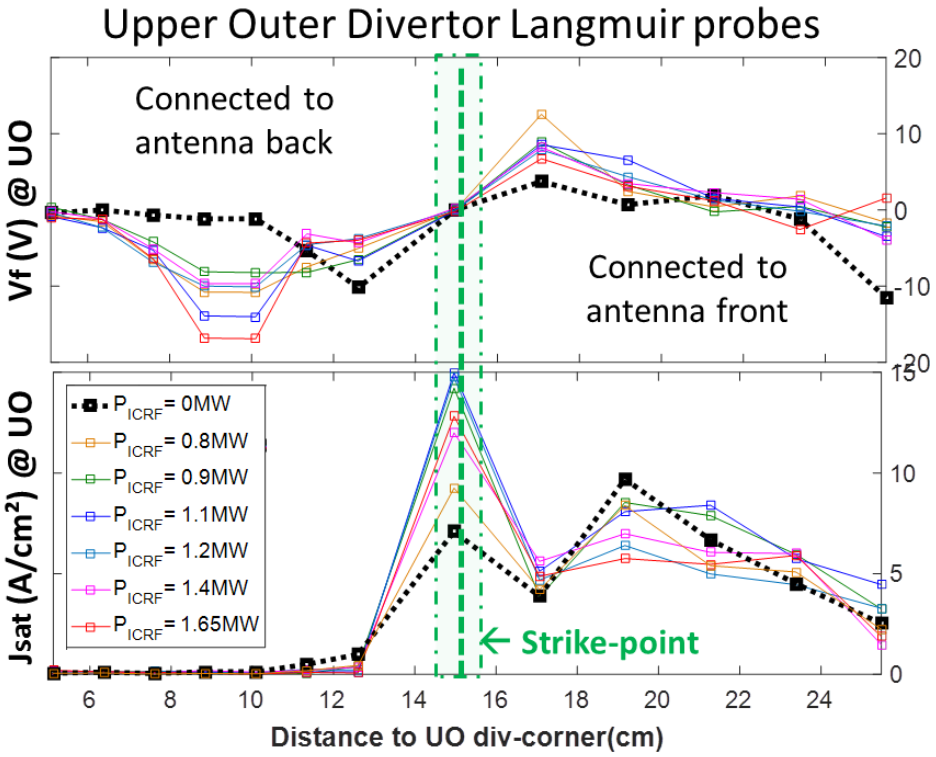

Figure 6.11: Floating potential V_f and ion saturation currents J_{sat} profiles from outer target of the upper divertor for different ICRH power.
Cf detailed shot list in Table 6.2 (black series).

If we assume that the energy absorbed by the plasma ends up on the divertor targets, this can be interpreted in terms of difficulties either to couple waves to the plasma or to have them absorbed efficiently. Since coupling efficiency remained fairly stable along the experiment, observation made in the divertor region might show some correlation with ICRF absorption efficiency, estimated based on the Break-In-Slope method [Lerche 2008]. This method consists in fitting plasma energy W_{ENG} increase when applying ICRH by an exponential, providing the confinement time τ_e:

$$W_{ENG}(t) = W_{ENG}^{beforeICRF} - \left(W_{ENG}^{beforeICRF} - W_{ENG}^{afterICRF}\right)\left(1-\exp(-t/\tau_e)\right) \qquad (6.2)$$

W_{ENG} is measured by diamagnetic probes and its variations are often slightly delayed compared to the ICRH power application, which was taken into account for each fit.

The absorption efficiency is finally calculated as follows:

$$\eta_{ICRH}^{Abs} = \left(\frac{\Delta W_{ENG}}{\tau_e} - \frac{\Delta V_{loop}}{I_p} + \Delta P_{RAD} \right) / \left(\alpha P_{ICRH}^{in} - \frac{P_{ICRH}^{refl}}{\alpha} - \Delta P_{RAD} \right) \qquad (6.3)$$

With Δ meaning the difference between times with and without ICRH, and α the ratio of ICRH power lost in the transmission lines between the antennas and the voltage probes providing incident and reflected powers. The denominator basically represents the effective power step when applying ICRH. Beyond the fact that these estimations are based on single power steps – not optimal for absorption efficiency estimations – their main weakness comes from large uncertainties in power losses in transmission line, such that the coefficient α may vary between 50 and 90%. For our calculations in L-mode, we assume the most optimistic case of only 10% losses (α=0.9). We will not discuss quantitative results but rather look at qualitative trends. This exercise was made for each shot of the three series introduced in the previous section. Ratios of absorbed power against total power injected P_{TOT} were plotted as function of P_{TOT} in Fig.6.12. The result shows that ICRF wave absorption improves with total power injected. In the present regime of operation, since relatively little power is injected, ICRF absorption efficiency is often poor compared to those of lower hybrid. In addition, larger power fraction is radiated during ICRH than during LH. As a conclusion, (i) the divertor target is mostly sensitive to the conducted power, and (ii) the power conducted by LH is often much higher than the one conducted by ICRH, therefore (iii) divertor region is well-correlated to total injected power (mostly LH) rather than ICRH. If the total injected power could be significantly increased, we would expect better ICRF absorption efficiency, more conducted power and therefore an increase of W production in the divertor region. Note for different heating conditions represented by each series in Fig.6.12, absorption does not seem to improve at the same rate, yet the lack of statistics does not allow drawing any strong conclusion.

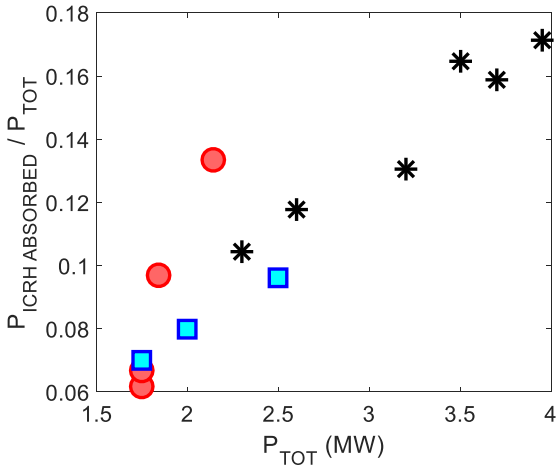

Figure 6.12: ICRF waves' absorption efficiency normalized by total power injected as a function of total power injected. Cf detailed shot list in Table 6.2.

To finally confirm that the divertor region is only sensitive to the amount of power injected regardless of how it may have been launched, we propose to compare rectified potential changes observed by divertor Langmuir probes [J.C.Xu 2016] (Fig.6.13) and W sources from one visible spectroscopy line of sight (Fig.6.14) in both USN and LSN configurations. Fig.5.11 shows time evolutions of floating potential profiles along outer targets of both upper (W) and lower (C) divertors during a LSN discharge partially heated with ICRH. We see that ICRH-related potential rectification occurs in very similar fashion at the upper and lower targets. Furthermore noticing potential rectifications obtained at the lower divertor are comparable to those obtained at the upper divertor (Fig.6.13), RF rectification in divertor targets does not seem to depend on the magnetic configuration but rather on magnetic connections to antenna front face [Perkins 2018]. Based on this observation, if RF rectification played a key role in EAST divertors erosion, at least for ICRH dominated discharges, we would expect to get comparable erosion rates in both configurations. However, as shown by WI line brightness (neutral W visible spectroscopy) for two discharges in similar conditions but different configurations (Fig.6.14), upper divertor erosion rate is much higher in USN than LSN configuration.

As far as EAST and relatively low ICRH power are concerned, these observations allow concluding that RF rectification does not play a strong role in the erosion region of the divertor which is more sensitive to total conducted power and of course magnetic configuration [Perkins 2018].

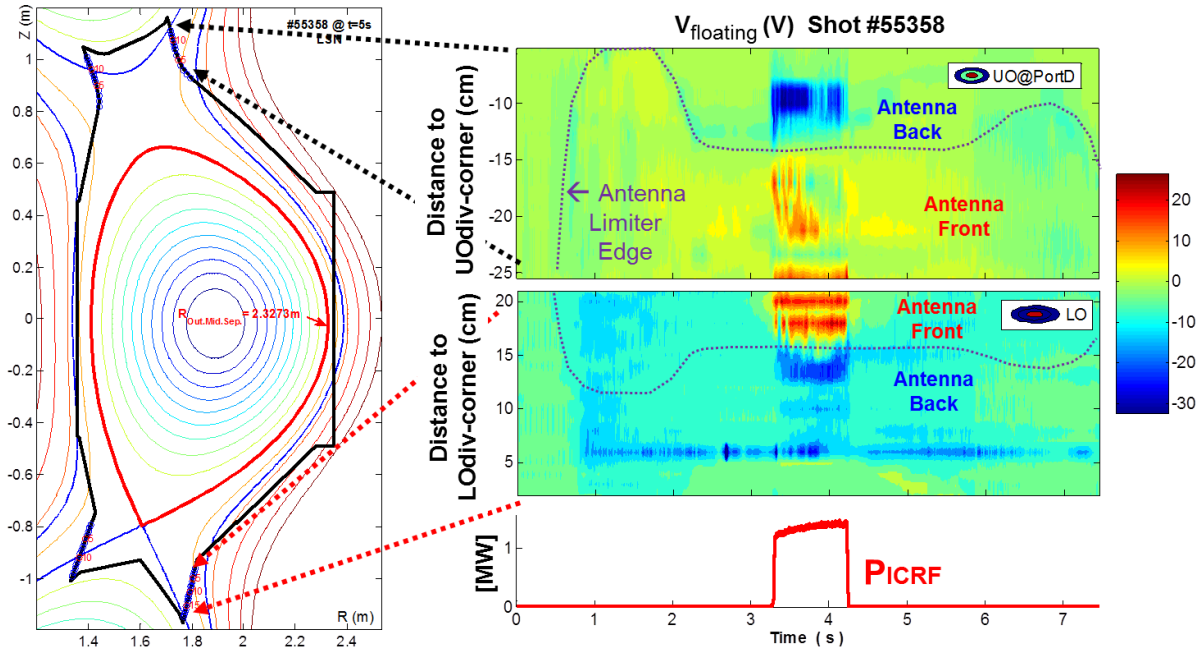

Figure 6.13: Time evolution of Langmuir probes floating potential V_f profiles of both upper and lower divertors outer targets during a LSN discharge. Regions magnetically connected to the front and the back of the antenna limiter edge are separated by the dotted purple curve.

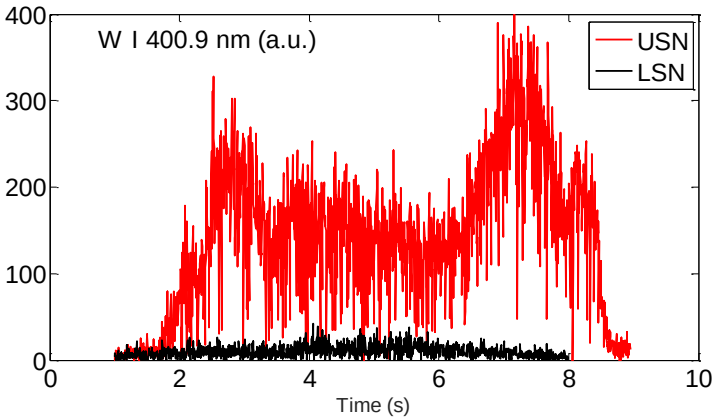

Figure 6.14: Time evolution of W^+ emission (at 400.9nm) measured by visible spectrometer at upper outer divertor target in both LSN (#55358) and USN (#69671) magnetic configurations

6.2.2.2 WEST divertor

WEST divertor can be monitored with visible spectroscopy lines of sight which settings were optimized to look at the same time at the whole divertor target and the right limiter of Q2 ICRF antenna to allow quantitative comparison of each source. Discharge 54633 was made with two float-tops with and without ICRH (Annex 8). The poloidal profiles of deuterium and tungsten ion fluxes were then estimated from DIγ and WI radiance with different visible spectroscopy LOS. Their ratio can also serve as a proxy for the effective sputtering yield (eq.4.19). The outer target is known for being the main source of impurity in several devices [Dux 2009] which can also be particularly enhanced in presence of ICRH [Wukitch 2007 and 2009] [Bobkov 2013]. In Fig6.16a, a sharp increase is observed at the outer target consistent with observations in other devices [Dux 2009] [Wukitch 2007 and 2009] and the fact that antennas were magnetically connected to the divertor outer target (visible in Fig.6.15a) because the positions of antennas and separatrix were reduced by 7cm with others shots. If we consider that W sources in the divertor are homogenous toroidally and dominated by the outer strike point region between R_{in}=2.25m and R_{out}=2.35m with average W fluxes of the order of Γw=5.10^{16}atm/s, we can get an estimation of the *W sources in the divertor (as a number of tungsten atoms released per second) when active ICRF antennas are magnetically connected*:

$$\Gamma w_{divertor}^{total} \approx \Gamma w_{divertor}^{average} \times \pi \times (R_{out}^2 - R_{in}^2) = 7,2.10^{16}\, w/s \qquad (6.4)$$

As far as sources on limiters are concerned, we can look at the right limiter of Q2 antenna and estimate the same quantities to estimate the contribution of each source to core contamination in impurities (Fig.6.16b). In discharge 54633 though, only Q1 and Q4 antennas were powered (Fig.A24), such that effects observed on Q2 right limiter are most likely the result of magnetic connections to the Q1 antenna. For this type of discharge, if we assume from W flux profile in Fig.6.16b that a limiter magnetically connected to an active ICRF antenna contributes on average to about Γw=3.10^{16}atm/s over a 50cm poloidal range roughly around mid-plane location, we can get an estimation of

W sources from a limiter magnetically connected to an active ICRF antenna:

$$\Gamma w_{\lim iter} \approx \Gamma w_{\lim iter}^{average} \times Z_{\lim} \times Y_{\lim} = 3.10^{16} \times 0,1 \times 0,5 = 1,5.10^{15}\, w/s/\lim iter \qquad (6.5)$$

If we now assume that the ten limiters of the chamber (APL retracted during shots) have roughly the same contribution, we can estimate the total contribution limiters to W sources:

$$\Gamma w_{\lim iters}^{total} \approx \Gamma w_{\lim iter} \times N_{\lim} = 1,5.10^{16}\, w/s \qquad (6.6)$$

With these rough estimations, we find mid-plane sources 5 times smaller than divertor ones. Divertor sources might be in general smaller not only because the outer target is usually not magnetically connected to antennas, but also because we are looking at the first ionization state of tungsten (WI) and that impurity are in principle quite well-screened in divertor region. Looking at the second ionization state would for instance have been better for core contamination estimation. However the baffle is always connected to antennas and impurity are badly screened, such that sources close to the leading edge of the baffle (close to the separatrix) could in some cases play a non-negligible role. On the contrary, we will see in section 6.3.3.2 that eq.6.6 is underestimating the contribution of sources on limiters which are not only much higher in limiters of active antennas, but also impurities are badly screened and easily penetrate in the plasma such that WI on limiters is actually a better proxy of the tungsten outflux than in the divertor region.

In terms of heat loads, since ICRF tends to enhance impurity production and radiation losses, heat fluxes usually decrease in the divertor target as for instance during the discharge 53923 which overview is given in Fig.6.2 and λ_q profiles from infrared data inversion along the lower divertor target represented in Annex 9 (Fig.A30).

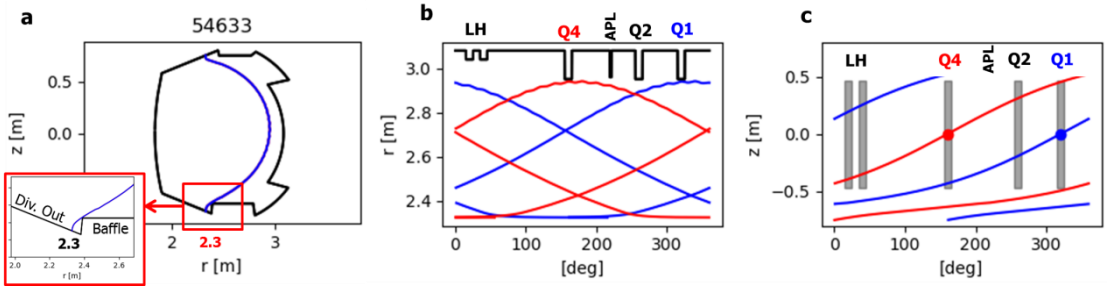

Figure 6.15: Field lines traces from Q1 and Q4 antennas showing (a) a poloidal cut, (b) toroidal-radial map and (c) toroidal-poloidal map

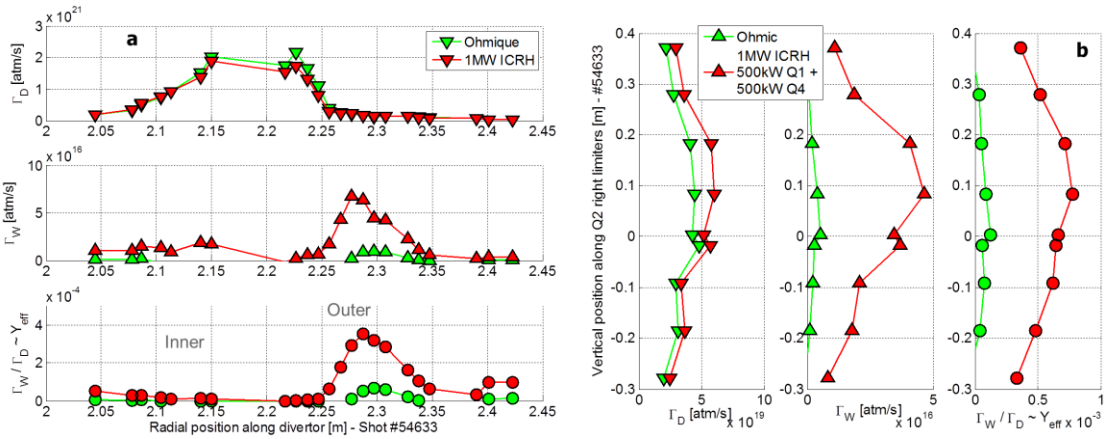

Figure 6.16: Same quantities as in the previous figure plotted along (a) divertor target and (b) Q2 right side limiter, while only Q1 and Q4 antennas were powered (54633)

6.2.3 Near-field effects

6.2.3.1 EAST B-port antenna Faraday screen and magnetically connected Ti plates

Surfaces close and magnetically connected to active ICRH antennas are often subject to much stronger interactions with plasma due to RF sheath excitation. When the incidence angle of the connection is high (almost normal), effects can be particularly deleterious as shown in this section. Fig.6.17 represents Ti (magnetically connected to B-port) and Fe (present in antennas Faraday screens) as functions of both P_{ICRH} and P_{TOT} such as in Fig.6.10.

As expected from graphs **a** and **b** in Fig.6.1, magnetically connected species are well correlated to P_{ICRH}. Fig.6.17a shows that Ti is very sensitive to discharge conditions as each series behaves differently, whereas Fe has different behaviours but globally increases with P_{ICRH} (Fig. 6.17b). At constant LH power and same ICRH power on each strap (blue series), Ti and Fe both follow linearly P_{ICRH}. For constant ICRH power, we observe much higher Ti content when the power is unbalanced (red series) than when it is well balanced (blue series). When ICRH increases together with LH power (black series), Ti remains constant, showing that interactions in regions closely connected to the B-port antenna may not only depend on ICRH power

but also on how it is launched (antenna design, power balance on straps). Fe from antenna Faraday screens always increases with ICRH power in a similar fashion in all cases showing a generally good correlation. Fe sensitivity to one single antenna's settings is however less obvious than for Ti since Fe can come from both antenna Faraday screens.

In Fig. 6.17 **c** and **d** representing Ti and Fe increase as function of P_{TOT} a group of red dots corresponding to the red series in Fig.6.1 **a** and **b** with unbalanced power on straps, is significantly above the others, whereas these cases are not different than others from the divertor's perspective (Fig. 6.10b). For magnetically connected species, in the absence of ICRH, the impurity concentration seems independent of the LH power, at least in the 1-2.5MW power range. This confirms Ti and Fe closely connected to antennas are mostly sensitive to ICRH settings and near-field effects.

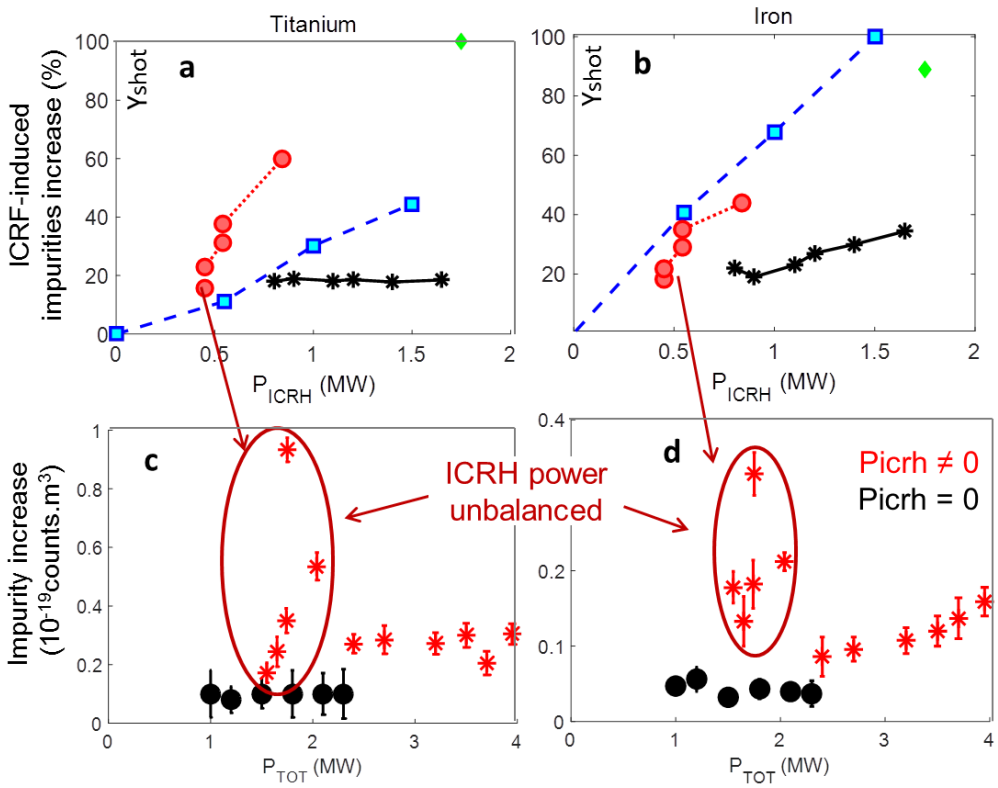

Figure 6.17: Ti and Fe production (Y_{shot}) as a function of (a & b) ICRH power and (c & d) total power. Blue, red and black series in graph **a** correspond to the same shots as in Fig 6.7. Graph b also represents to the same shots but points without ICRH (black series) were added as well. Cf detailed shot list in Table 6.2.

6.2.3.2 WEST antenna limiter and Faraday screen, and magnetically connected APL

WEST ICRF antennas being coated with a layer of silver, UV spectroscopy can be used to look at Ag lines such as Ag^{35+} on the SIR (159.9nm). In the discharge shown in Fig.6.18, we typically see that at the beginning of the ICRF pulse (8s), the coupling efficiency is low, such that voltages measured by probes on transmission lines – also representative of voltages in front of the antenna – are high. The consequence is most likely the excitation of RF sheath on the Faraday screen resulting in the increase of Ag^{35+} brightness in the core plasma. Note similar effect is observed with tungsten which might come from antenna limiters; however we cannot guarantee the origin of tungsten which can also be found everywhere in the vessel. In addition, the phasing of Q1 antenna was badly controlled and deviated from the ideal dipole (180°) down to 140°.

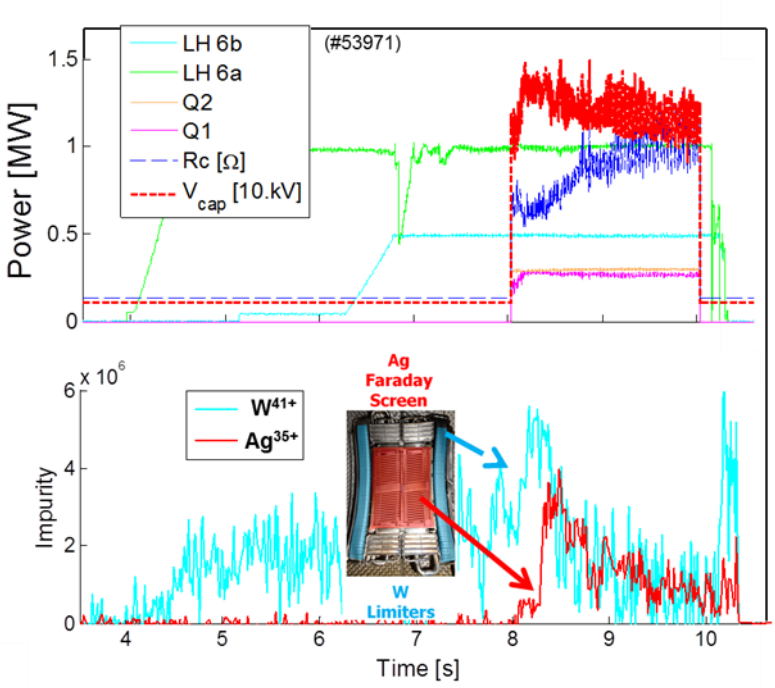

Figure 6.18: Ag^{35+} from antennas Faraday screens and W^{41+} likely mostly from antenna limiters, measured by SIR UV spectrometer. The evolution of species is consistent with the variation of the average antenna loading and voltages. (#53971)

To avoid the difficulty to disentangle the origin of different impurities in the plasma core, it is therefore much more reliable to directly look at neutrals and low

ionized states radiating very close to where they were produced. Like in Fig.6.16, profiles were plotted in different plasma heating conditions along Q2 antenna right side limiter and the magnetically connected APL (Fig.6.19). The scales of particle fluxes and effective sputtering are the same to allow easy comparisons between objects and heating scenarios. In spite of their proximity (Fig.4.6b), it can clearly be seen that W sources on the APL are much smaller than on Q2 limiter. This is most likely because the APL is retracted during the discharge 2cm behind Q2 limiter (Fig.6.2e), such that the deuterium fluxes falling on both limiters is very different in both cases. This illustrates the benefit of retracting objects to lower density region. However in the case of ICRF (and LH) antennas, we have seen that this is constrained by a trade-off with the coupling efficiency and RF sheath excitation. Looking more specifically at Fig.6.19c, profiles were plotted along Q2 limiter by averaging each LOS signals on different time intervals represented by areas of corresponding colors in Fig.6.2. We see that the deuterium flux increases slightly with the LH power (consistent with the correlation between ICRF coupling and LH power found in the previous chapter (Fig.5.6)), resulting in a linear increase of the W sources without any change in the sputtering yield. When turning on ICRH however, despite no further change in the deuterium flux, W sources increase a lot due to a brutal increase in the effective sputtering yield here likely resulting from RF sheath excitation with the famous double hump structure nearby antenna corners (Fig.3.3). In Fig.6.19d, cases with increasing LH and ICRH power are shown, with grey and blue profiles from graph **c** reproduced to enlighten the influence of increasing mostly the ICRF power. We see that sputtering increases mostly with the ICRH power while the deuterium flux increases mostly with the LH power. As a consequence, W sources tend to increase with the combination of both mechanisms. However in a situation with only one type of the heating, LH would behave relatively gently and linearly in comparison with ICRH which RF sheath potential can increase brutally resulting in very deleterious impurity production, as was probably the case with 1MW ICRH (red curve for W flux on Q2 limiter).

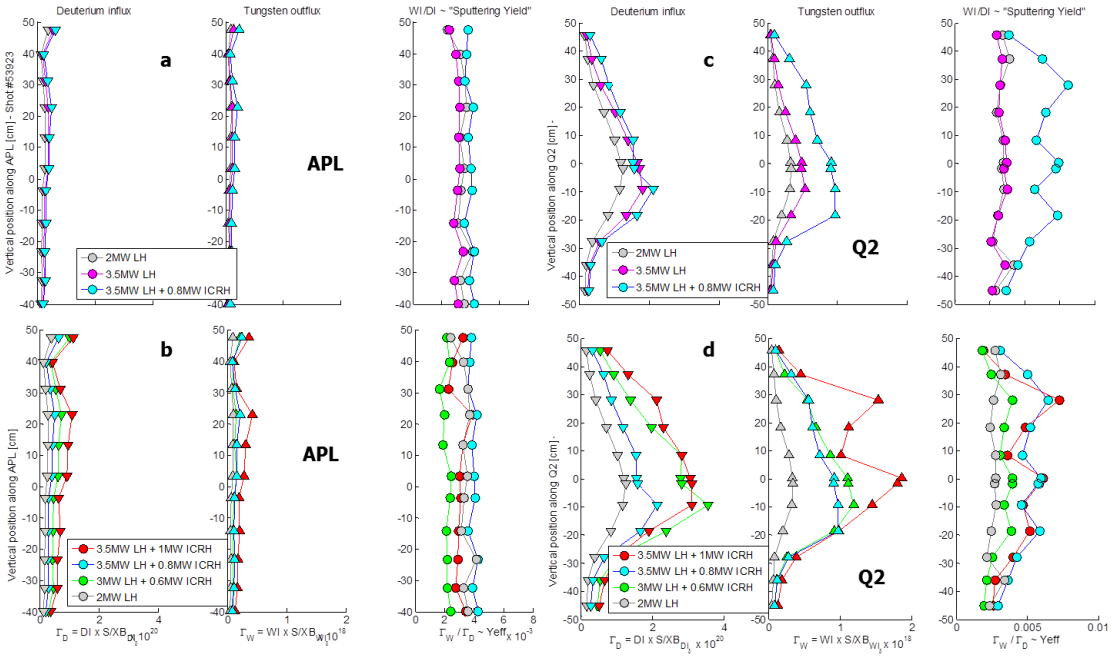

Figure 6.19: Deuterium and tungsten fluxes estimated from DI_δ and WI calibrated data (Ph/m²/s/sr) poloidal profiles along WEST APL and Q2 antenna right limiter with S/XB coefficients determined in section 4.3.2.2. Different profiles are superposed for different heating schemes and ICRH power on Q2. An effective sputtering yield is estimated from the ratio of both species fluxes (eq. 4.19) (#53921, 53923 ,53934)

Note unlike in Fig.6.16b were effects observed on Q2 right limiter were most likely the result of magnetic connections to the Q1 antenna, here (Fig.6.19) Q2 was powered such that dominant effects were most likely Q2-induced near fields on its own limiters. Note also that tungsten fluxes along Q2 limiter are at least 20 times more intense when Q2 antenna is powered (Fig.6.19d) than when others antennas are powered (Fig.6.16b). It is here understandable that sources from limiters were a priori underestimated in eq.6.6. To give a slightly more realistic estimation of these sources by taking into account higher sputtering yields on active ICRF antenna limiters, we can assume the sputtering yield on each ICRF antenna limiter is of similar order as in Fig.6.19d, which is 5 times higher than in Fig.6.16b. Considering a discharge with the three ICRF antennas powered together and the LH launchers protections magnetically connected, we get the following more realistic estimation of limiter W sources contribution:

$$\Gamma w_{\lim iters}^{total} \approx \Gamma w_{\lim iter} \times N_{\lim}^{LH} + 5 \times \Gamma w_{\lim iter} \times N_{\lim}^{ICRH} = 4,8.10^{16} w/s \qquad (6.7)$$

We find that limiter sources are slightly smaller than divertor sources, however remember that sources in the divertor region are in principle better screened than these on limiters, such that mid-plane sources contribution to W contamination of core plasma may be even more serious than the divertor region.

It is important to stress that these behaviors are a priori very sensitive to slight changes since we are not only dealing with the combination of highly non-linear effects (namely RF sheath and physical sputtering as shown in Fig.2.9), but also since the RF power nor the loading of antennas suffice to give a full picture of how things are correlated together. Many others parameters could also be important to understand the way things are changing. For instance, the voltages on the transmission lines can sometimes be a good proxy of electric fields on the antenna structure. Taking now in consideration all discharges during the same experimental session as shot 53923 represented with different power levels explored, we can for instance represent in Fig.6.20 how both tungsten sources (a) and the effective sputtering yield (b) qualitatively changed on Q2 limiter as a function of the voltage measured on the transmission line. It is however important to mention that voltage measurements on Q2 antenna were at that time a priori overestimated due to probes calibration issues that were corrected at the very end of this PhD, bringing Q2 coupling efficiency to the same level as others antennas. Still the relative variations presented were a priori correct, only their absolute value was wrong, such that abnormally high voltages were measured on the transmission lines and triggered the security system to prevent arcs (cf. shad system [Helou 2019]). It appears that ICRH (red dots) has a much stronger impact than LH (blue dots). This is again most likely due to RF sheaths which we suspect based on literature (Fig.3.3) that they occur principally nearby antenna corners, with patterns shifted from squared antenna mouth due to magnetic field pitch angle. In WEST though, since the safety factor is rather low ($q_{95} \approx 4$) meaning the magnetic pitch angle is rather small (<7°), we expect the electric field patterns to be fairly close to the expected square. To get an indication of how corners behave in comparison with the center of the antenna, we can for instance plot the ratio of top and bottom LOSs over central LOS as a function of the total power and see how it behaves with and without ICRH (Fig.6.21). We see that values increase in presence of ICRH compared to cases with only LH which I would tend to interpret as the presence of RF sheaths. We acknowledge that this ratio is however still smaller than 1, meaning

that we are still dominated by plasma surface interactions at the mid-plane. I however expect these effects would decrease if (i) the ICRH power could be increased further and (ii) if the poloidal curvature of the plasma was not larger than the one of the antenna limiters. These fine details are however tricky to predict such that we acknowledge this type of speculation would gain being benchmarked by dedicated experiments and modelling.

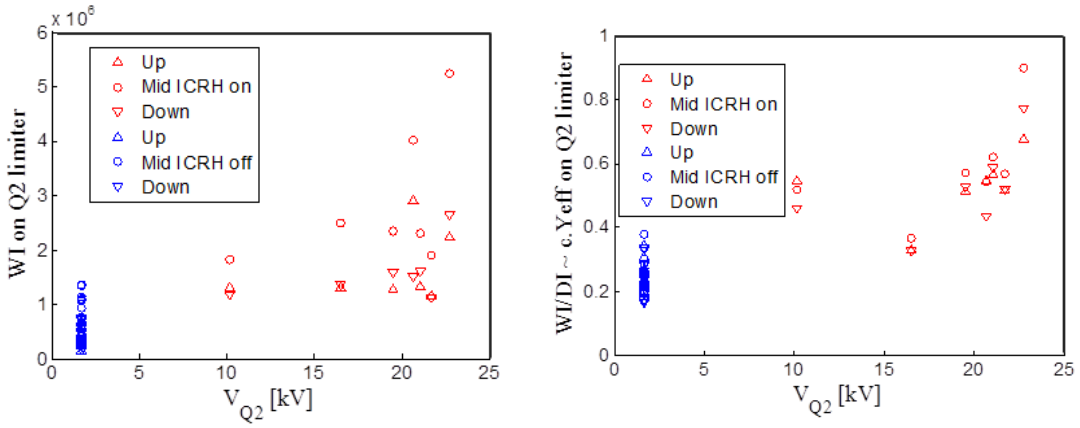

(a) (b)

Figure 6.20: (a) Tungsten sources and (b) proxy of the effective sputtering yield on Q2 limiter variation with the voltage measured on the transmission lines

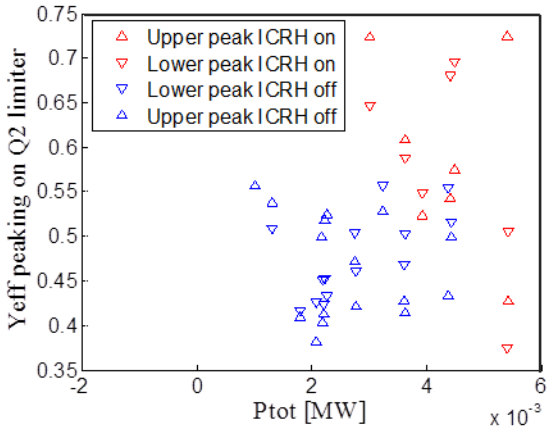

Figure 6.21: Ratio of top and bottom LOSs over central LOS as a function of the total power. We interpret this quantity and the peaking of the sputtering yield at Q2 antenna corners, which happens to increase with ICRH.

Beyond characterizing impurities with visible spectroscopy in plasma edge and furthermore taking into account even more parameters, we can now look at how these

impurities influence radiation losses and how this scales with key parameters. For roughly the same series of shots, Fig.6.22a represents the difference of power radiated with and without ICRH as a function of the scaling law introduced in Fig.2.9 provided by [Basiuk 2004]. We see that the radiated power increases with the ICRH power, in particular for the discharges of interest (Table 6.4). Note also that the discharge 53703 during which the H concentration was below 3% (Table 6.3) also get close to the other group of shots, consistent with large ion ripple losses mentioned in section 6.3.1.2.

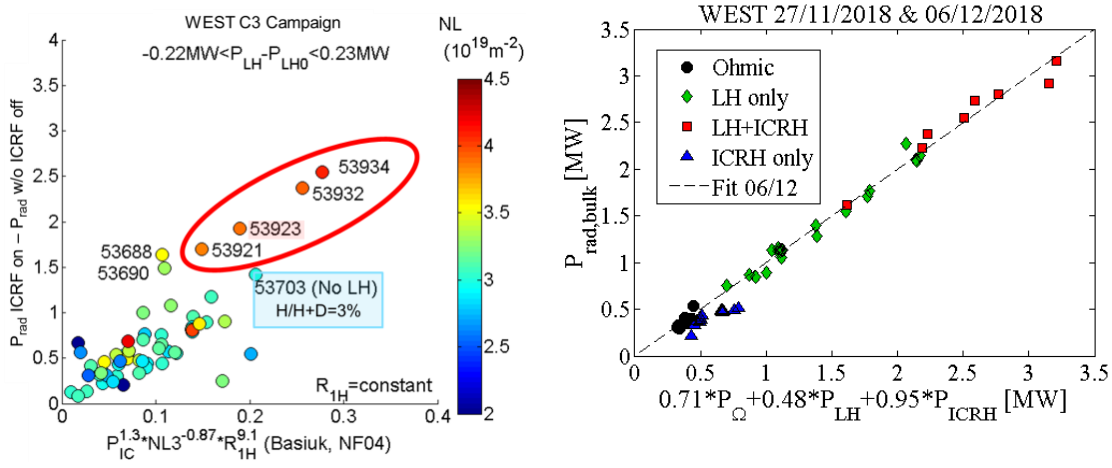

(a) (b)

Figure 6.22: (a) Scaling of the difference of power radiated with and without ICRH as a function of the non-linear scaling law introduced in Fig.2.9 provided by [Basiuk 2004] and (b) linear scaling of the power radiated in the bulk as a function of the additional powers

Fig.6.22b represents another scaling of the power radiated in the bulk as a linear combination of the additional power. This shows basically that the level of radiation increases twice faster with ICRH than with LH and that maximum levels of radiation were reached in discharges with a combination of ICRH and LH consistent with spectroscopic observations. Note the level radiated remains indeed very low in discharges only heated with ICRH, but this is probably a little biased by the fact that when ICRH was powered alone, its low coupling did not allow increasing the power above 200kW per antenna.

Finally, probes magnetically connected to the antenna (Fig.4.6b) can also collect very interesting information such as local density (Fig.5.14b) and floating potential profiles (Fig.6.23). At some point in WEST experiments, despite both ICRF antennas were supposed to sit at the exact same position, Q2 antenna always had a lower

coupling than Q1 antenna (Fig.5.9), therefore Q2 was moved first 7mm forwards and then 8mm again in order to reach the same level of coupling as the other antenna. We still do not know if this coupling difference is real or just the result of voltage probes calibration issues which will be investigated in the future. So far, during this operation, Pecker probe was used to benchmark the position of the Q2 antenna limiter by measuring the profiles on which as potential hump characteristic of the limiter leading edge could be observed clearly and moved consistently with the antenna. Note this potential hump occurs over a very tiny radial range of about 5mm, which will result in high electric fields a priori again characteristics of RF sheaths.

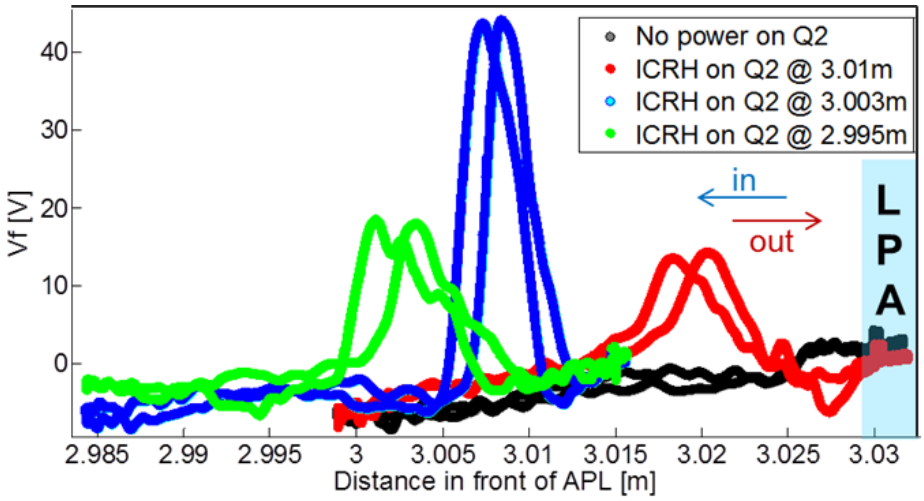

Figure 6.23: Floating potential radial profiles for three different positions of the Q2 antenna to which the upper pecker probe on the APL is magnetically connected

6.2.3.3 EAST I-port antenna limiters surrounding

In EAST as well, reciprocating probes can be inserted through J and K ports mid-plane, both magnetically connected to the I-port antenna. A series of discharges consisted in measuring RF sheath effect with triple reciprocating probes at proximity of I-port antenna and faraway of the B-port antenna. Different power levels were tested for each antenna and probe inserted twice per discharge until the separatrix (Fig.6.24). Floating potentials radial profiles are displayed in Fig.6.25. B-port antenna appeared not to have much influence (blue curves) since it was not only launching relatively low power but also was not magnetically connected and too far from the

J-port. I-port (red curves) however launched higher power and as the probe is very close and connected, it observed the same potential hump as in WEST while passing nearby the antenna limiter edge subject to rather high potential gradients. Note the amplitude of oscillations also increases with the power, indicating good correlation with RF sheath-induced mechanism [Urbanczyk 2017].

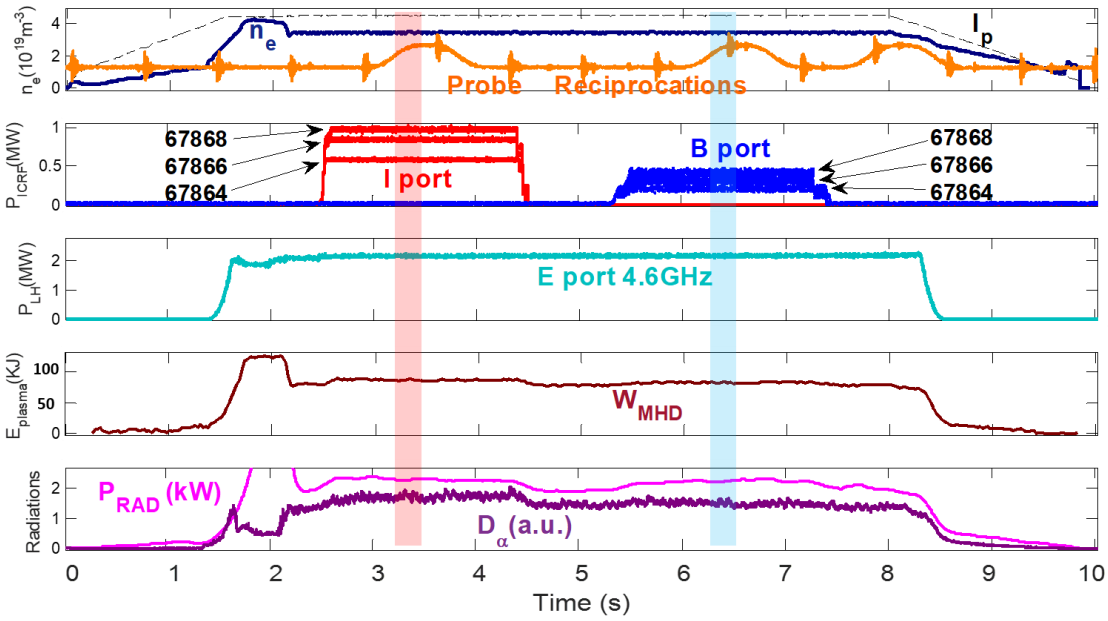

Figure 6.24: Overview of the shots N°67864 / 6 / 8 with respectively three level of ICRF power. To the top are represented the line integrated density in blue, plasma current in dashed black and probe reciprocations in orange. Underneath we find each ICRF antenna power, then each LH grill power. Plasma energy is represented in in brown. Plasma oscillations Dα and radiations are the purple and magenta curves.

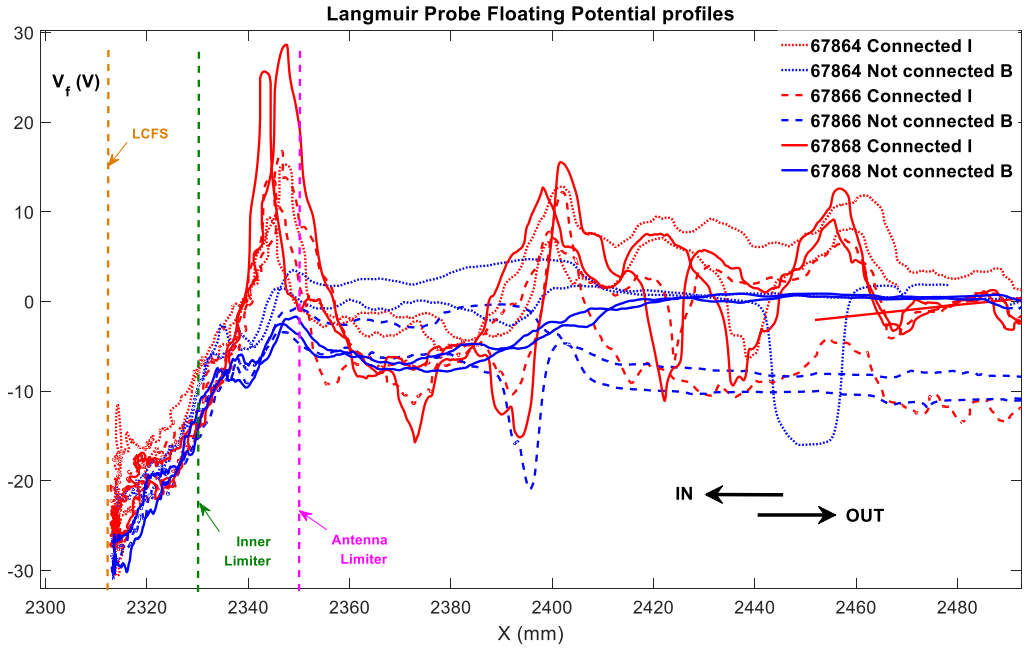

Figure 6.25: Floating potential radial profiles measured by reciprocating Langmuir probe during shots N°67864 (dotted), 67866 (dashed) and 67868 (full). Red curves (respectively blue) correspond to I-port ICRF antenna active (B-port).

Following similar philosophy as for the Ti plate fixed near E-port, two other stainless steel plates were coated with a 5µm layer of Ag (silver) and fixed in 2018 on one limiter of the I-port antenna (the one on the H-port side). This region was chosen as it is very well connected to the I-port and pretty much nothing else. The limiter between G and H ports being radially 1cm closer to the plasma than the antenna limiters, no fast electron accelerated by the LH launcher in E-port can either reach this region. The idea of using Ag as an impurity trace of plasma surface interactions resulting from I-port near-field effects did not work out since no line corresponding to Ag was found in the spectra. However, the plates melted at each corner over about 4cm poloidally, precisely where HFSS model predicts peaks of RF potential due to sheath excitation [C.M.Qin 2015]. As furthermore shown in Fig.6.27, the part that melted on each plate (represented by the stars) is distinct from the one that was the closest to the plasma (represented by the circles). This is therefore an example of the consequences near-fields excited RF sheath may have on plasma surface interactions.

Knowing all the characteristics of the plate and that stainless steel would start melting roughly above 1300°C, a thermal analysis made with ANSYS provides an estimation of the minimal heat flux that may have induced plates melting and which

details are provided in Annex 2.1. Dynamic simulations where made for five different values of maximal heat fluxes at tile corner from 1 up to 10MW/m², and plate maximal temperature evolution is represented in Fig.6.26. Note values estimated in Tore Supra and JET would typically be of the order of 2 to 7MW/m² [Colas 2009]. In EAST, these simulations predict that plate would have started melting after 30s for a maximal heat flux of 3MW/m², after 15s for 5MW/m², and only after 2s for maximal heat flux of 7MW/m².

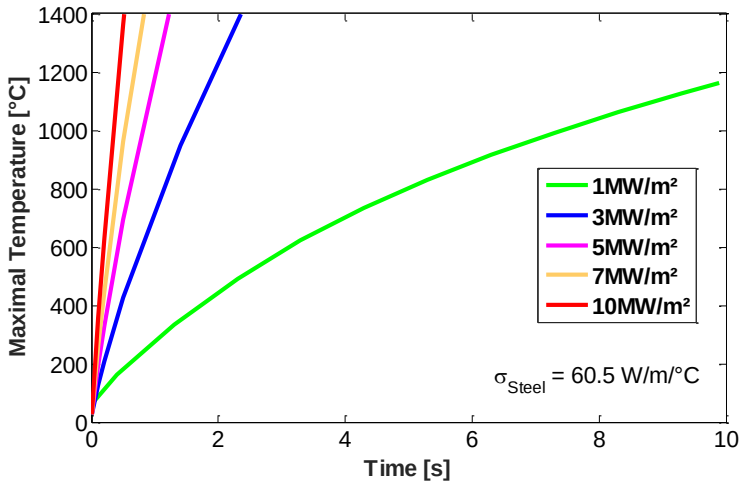

Figure 6.26: Evolution of the maximal temperature of the plate for different parallel heat fluxes

Assuming the heat fluxes were mostly parallel, a parallel flux above 5MW/m² would suffice to induce partial melting of the plate in less than a second. Identifying #78578 as one of the most likely shot of 2018 campaign during which such conditions might have been reached (1.7MW on I-port with 60° phasing and power unbalanced on the straps), we can estimate SOL electron temperature ($T_e \approx 20eV$) and density ($n_e \approx 3.10^{17} m^{-3}$) with nearby Langmuir probes. Following the simplest models in the literature [Perkins 1989] and assuming that parallel heat fluxes are entirely due to DC potential drop across the sheath [Colas 2009], it is finally possible to estimate the DC potentials that would have been necessary to reach such heat fluxes through the parametric scaling

$$V_{DCsheath} = \frac{Q_{\parallel}}{\Gamma_{Bohm} e} \approx \frac{Q_{\parallel}}{n_e \sqrt{T_e + T_i}} \approx \frac{Q_{\parallel}}{n_e \sqrt{3T_e}} = \frac{5.10^6}{3.10^{22} \times 1.6.10^{-19}} = 600V \qquad (6.8)$$

600V happens to be a value pretty consistent with typical potentials measured by Langmuir probes (several hundred volts) not specifically connected

to the region of the maximum.

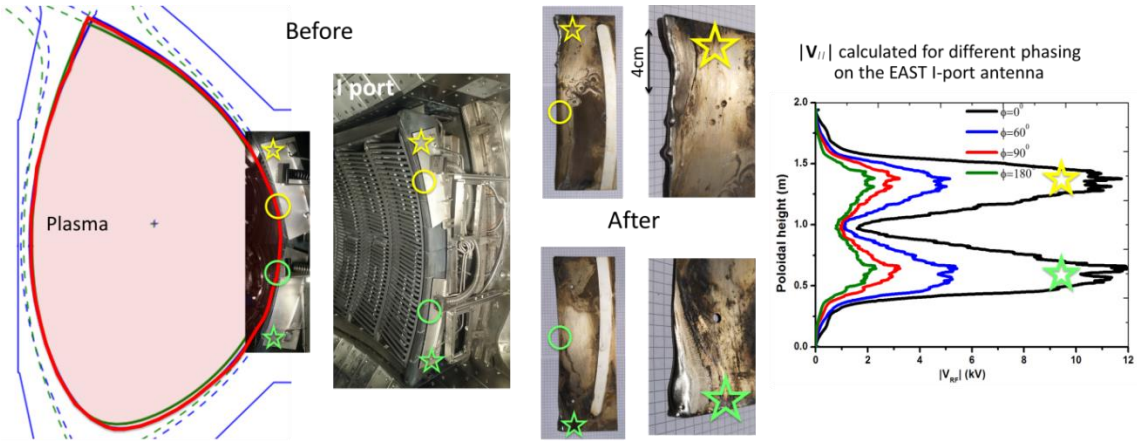

Figure 6.27: Pictures of the plates fixed on I-port antenna limiter, before and after 2018 campaign. Green and yellow circles represent respectively the part of the lower and upper plate that is the closest radially, while the stars represent the region that melted. The graph to the right shows that maximum of sheath potential computed with HFSS are precisely expected in the region where plates melted. On pictures taken after the experiment, plates are superposed on a grill of 5mm squares to give an idea of the dimensions.

Despite no infrared camera was looking at the metallic plates shown above, a camera was fixed and added in K-port in 2019, allowing good resolution infrared measurements on the I-port antenna (Fig.6.28). During discharge 83746 made in 2019, the power was far from balanced on the straps with power changing between 50kW up to 350kW from one strap to its neighbor. Already suspecting from past year that the plate most likely melted due to this type of setting unfavorable for RF sheath excitation, we analyzed the apparent temperature on the antenna bottom corner symmetric to where the plate melted. The temperature remained fairly low along the discharge and saturated at about 300°C in about 20ms as the antenna was powered. Visible on the video, spectacular graphite dusts were also emitted from the hot spot with surprisingly deep penetration before getting ionized and starting following magnetic flux tubes. This peculiar observation is not yet understood and will be the object of future investigation. In order to get an estimation of which heat flux would have been necessary to induce such apparent temperature increase on the infrared

camera, we used TEDDY (Thermography Estimate of Deposited heat DYnamics), a code recently developed in CEA (Annex 1.6 and [Fedorczak 2019]) which is inspired of THEODOR [Herrmann 2001] and basically takes into account further non-linear processes. By prescribing a 10MW heat flux on the target with similar pattern as the one shown in Fig.A6, we see that we recover the same temperature increase as the one observed by the IR camera. Note finally this heat flux is twice larger than the one that would have been necessary to melt the plates based on ANSYS estimations.

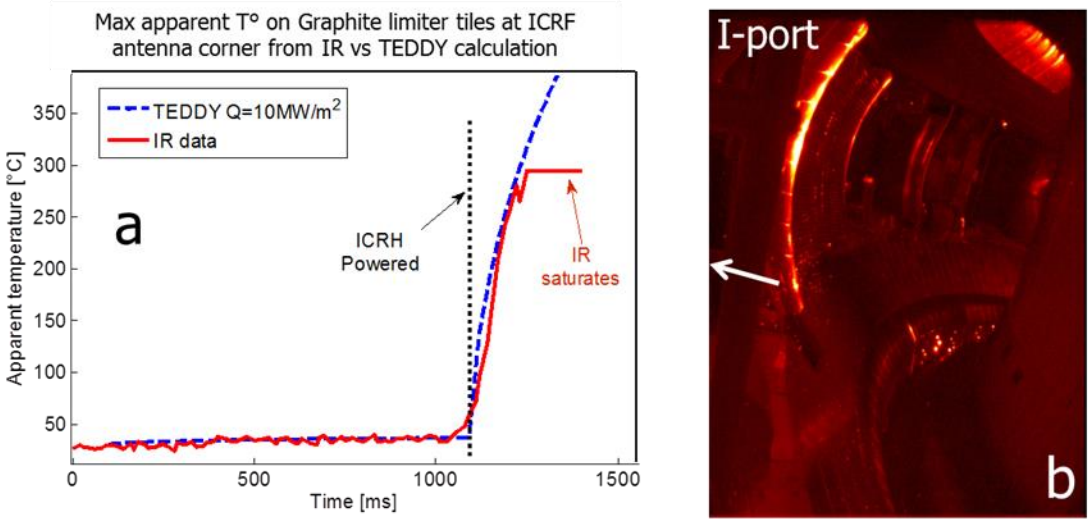

Figure 6.28: EAST I-port ICRF graphite limiter corner maximal apparent temperature estimation from infrared camera (red curve) superposed onto temperature increase induced by 10MW/m² heat fluxes and estimated with TEDDY code.

In view of providing an idea about how potentials induced around the antenna structure vary over a phasing scan, DC rectified potentials were computed for each phasing case of Fig.6.3 with SSWICH-SW code [Jacquot 2014]. All details and 2D maps (Fig.A23) are given in Annex 6 and are consistent with results presented above.

In order to better represent the impurity correlation with P_{ICRH}, we focus on the black series based on maximum number of points and for which each species shows significantly different behaviors. For those shots, ICRH-related impurity production is now represented relatively to the species with the highest ratio P – representative of how likely a given species is to contaminate core plasma when turning ICRH on – which happens to be Fe amongst Ti and W (Fig.6.29).

$$P = (Imp_{withIC} - Imp_{withoutIC}) / \mathrm{mean}(Imp_{withIC} - Imp_{withoutIC})_{over.black.shots} \quad (6.9)$$

The indicator of correlation is now noted $Y_{species}$ and is calculated as

$$Y_{species} = (Imp_{withIC} - Imp_{withoutIC}) / \max(\mathrm{P})_{over.all.species.and.shots} \quad (6.10)$$

Error bars correspond to the root mean square of $Y_{species}$ for the time periods during which Imp_s are assessed. This quantity is basically representative of each species' correlation with P_{ICRH}. Fig.6.29 typically shows that Fe is the species that best correlates with P_{ICRH} which is consistent with the fact that it mostly comes from antenna Faraday screens where the strongest near-fields are expected. Ti farther away from antennas and magnetically connected to the B-port undeniably depends on P_{ICRH}, but mechanisms other than just RF sheath excitation seem to play a role, as simply increasing P_{ICRH} does not necessarily enhance Ti production. W, an element that used to be found only in components in the divertor region, appeared weakly correlated to ICRH power compared to Fe. But this situation changed in 2018 when both LH launchers guard limiters were changed into tungsten. Comparing both situations now allows in the last section to quantify these limiters contribution to core W content.

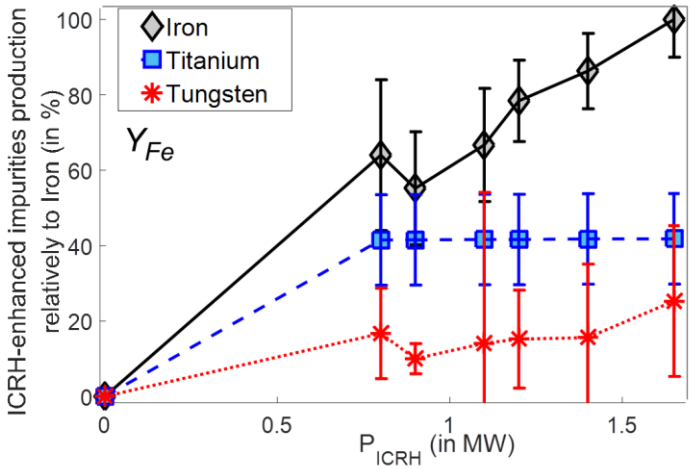

Figure 6.29: ICRH impurities production increase relatively to Fe (Y_{Fe}) as a function of ICRH power. Cf detailed shot list in Table 6.2.

6.3 Estimate the contribution of LH grill limiters to core W contamination in EAST from LSN/USN comparisons.

In 2018, one of the main upgrades made in EAST concerned both LH launchers' lateral protections which used to be composed of graphite tiles and were fully replaced by tungsten tiles with different designs on each grill (Fig 6.30b). Like in other devices like ASDEX Upgrade [Bobkov 2010], having W at the mid-plane substantially changes the impurity production picture we got in the previous sections, and this will now be compared to complement the discussion before concluding. As shown in Fig.6.14 by visible spectroscopy data providing a rather direct estimation of W emission at the divertor, much stronger erosion occurs in USN rather than LSN. This is consistent with core W content whose ratio in USN against LSN are plotted in Fig.6.30a. The black dotted curve represents the core W content ratio between similar discharges in USN versus LSN when W was still characteristic of divertor region, typically showing that erosion rate in USN was about 8 times higher than in LSN. The red solid curve represents the same quantity after the 2018 upgrade for discharges without ICRH (#77724 over #77722). Having W at the mid-plane led to homogenization of W core contents in different configurations, suggesting that the contamination efficiency by divertor sources is negligible compared to mid-plane one.

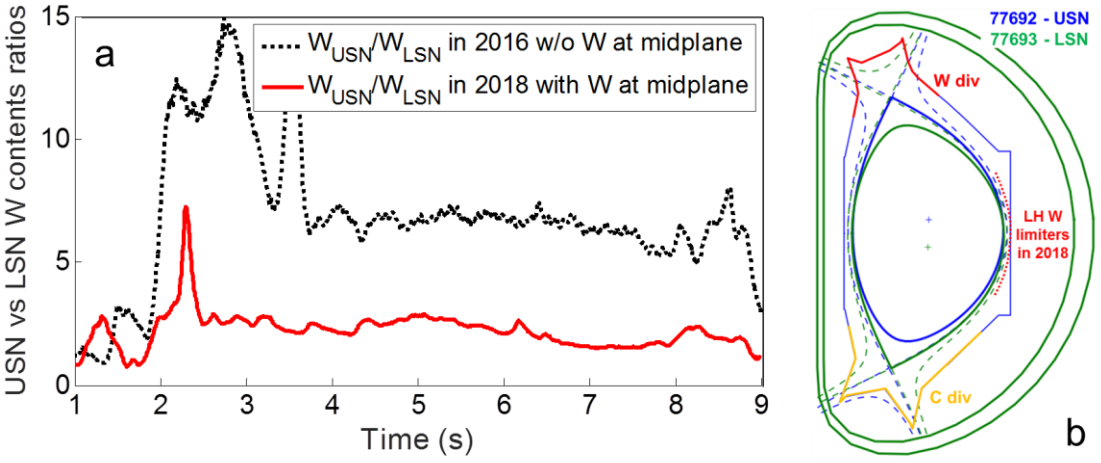

Figure 6.30: (a) Comparison of W contents ratios between similar shots without ICRH in USN and LSN configurations, with (2018 red solid curve) and without (2016 black dashed curve) W present at mid-plane. (b) USN vs LSN EFIT magnetic equilibriums

In order to quantify the contribution of LH limiters to core contamination by W,

we will make the following assumptions:

- A1) The core W content on EAST can be decomposed into 3 contributions:
  - W1 from W upper divertor
  - W2 from LH limiters
  - W3 from "elsewhere" in the main chamber (unknown…)

With these notations, we basically want to estimate the relative contribution of LH limiters to the core contamination, *i.e.* the ratio W2/(W1+W2+W3).

- A2) W2=0 before the tungstenisation of LH limiters.
- A3) W2 and W3 remain the same in USN and LSN configurations.
- A4) W1=0 in LSN configuration.
- A5) W3/W1 is the same before and after tungstenisation of LH limiters.

Assumptions A3 and A4 are used to discriminate the location of the sources. They imply that there is no W source (*e.g.* specific from the lower divertor) that would appear only in LSN configuration. A2 is necessary to discriminate LH limiter contribution from the rest. A5 means that LH limiters tungstenization is the main change in the machine, ideally the only one.

Under the above assumptions USN *vs* LSN comparison before tungstenization of the LH limiters estimates W3/W1:

$$\left(\frac{LSN}{USN}\right)_{before} = \frac{1}{1+W1/W3} \tag{6.11}$$

USN *vs* LSN comparison after tungstenization estimates (W3+W2)/W1.

$$\left(\frac{LSN}{USN}\right)_{after} = \frac{1}{1+W1/(W2+W3)} \tag{6.12}$$

Whence the estimated ratio W2/(W1+W2+W3) without ICRH leads to

$$\frac{W2}{W1+W2+W3} = \frac{\left(\frac{LSN}{USN}\right)_{after} - \left(\frac{LSN}{USN}\right)_{before}}{1-\left(\frac{LSN}{USN}\right)_{before}} = \frac{\frac{1}{3}-\frac{1}{8}}{1-\frac{1}{8}} = 25\% \tag{6.13}$$

While in presence of ICRH, this might tend towards much more as for instance 70% in ASDEX Upgrade's [Bobkov 2015]. This unfortunately could not be done in

EAST campaign problems on the lower carbon divertor.

Note the actual ratio probably depends on the level of ICRH power compared to the total additional power, on the fraction of ICRH power emitted by each ICRF antenna, on the strap phasing, Li conditioning …

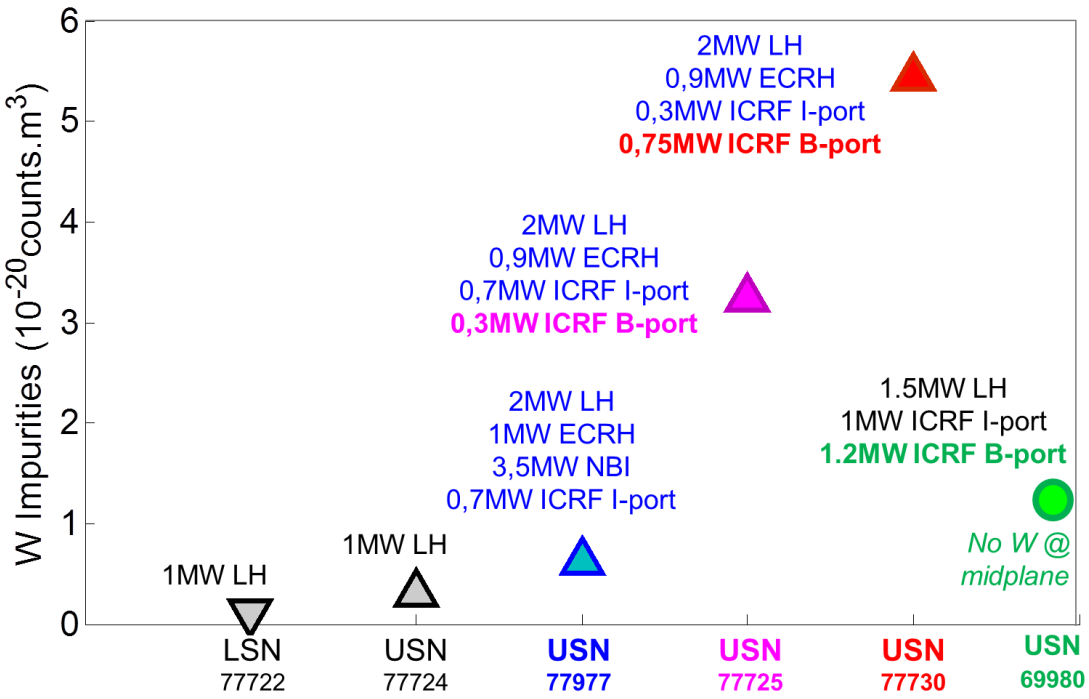

Figure 6.31: With W present at mid-plane, comparison of W contents in one LSN and four USN discharges with different heating scenarios all with I_p=400kA and n_e~4.10^{19}m^{-3}. The large difference when B-port ICRH antenna is powered suggests that main sources are magnetically connected LH launchers limiters.

W content in the core for the two same discharges heated with 1MW LH power during the 2018 campaign were represented by black triangles in Fig 6.31. The small difference between these similar discharges in different configuration (W_{USN} < 2.W_{LSN}) suggests principal W sources are now located at mid-plane. Other USN discharges with different heating scenarios were displayed on the same graph. The blue triangle stands for a discharge heated with all heating systems except the B-port ICRH antenna and we see, despite the relatively high amount of power injected (7.2MW in total with about half from NBI), that the W level remained relatively low. In another shot however (magenta triangle), the 3.5MW from NBI were replaced by 0.3MW ICRH from B-port, and the W content rose more than fivefold. Finally,

another discharge followed with similar total power injected but having 350kW ICRH injected from the B-port rather than from the I-port (red triangle), which led to another sharp increase of the W content. These results are consistent with magnetic connections existing between ICRH antennas and LH launchers limiters. As can be seen on Fig.4.2, the I-port antenna only connects to the upper part of the N-port LH grill and does not connect to the E-port grill shadowed by the limiter between the G and H ports. The B-port antenna is however well-connected to both LH launchers, therefore enhancing interactions with W limiters. These results together show that W sources in a mid-plane region magnetically connected to an active ICRH antenna can lead to severe core contamination by W. To put it differently, this experiment proves that the ICRH antennas should have no magnetic connection with a normal incidence to objects into the vacuum chamber.

Summary of impurity studies

In this section the different ICRF-related impurity sources were presented and their correlation with near and far field effects explained.

During ICRH, impurities contaminate the plasma to a level detrimental for long pulse operation mandatory for EAST, WEST and mostly future devices. Tungsten (W) production is measured mostly by visible spectroscopy lines of sights in WEST and core contamination assessed by extreme ultraviolet spectroscopy. We find that W production increases significantly when an ICRH antenna magnetically connected to W surfaces is powered, compared to a reference phase without ICRH. On some components such as antenna side limiters, the rise is much larger than with a similar power from LH, NBI or ECRH. The relative contribution of each object to core contamination yet remains poorly known due to the regrettable absence of dedicated experiment but only piggy back observations.

In both devices we basically find that since divertor surface is larger and exposed to higher particle fluxes than mid-plane sources, they account for the majority of

impurity in the core. However, impurity coming from the divertor are in principle better screened than these coming from guard limiters where the SOL width is shorter. In addition, when an ICRF antenna is powered, the increase in ions sputtering yield due to RF sheath-induced potential rectification on its limiters and connected object can lead to W production level incompatible with high power long pulse operation.

For instance, since 2018 in EAST the LH guard limiter tiles were W-coated. For a similar surface, their contribution to the core W content appears more important than divertor sources, particularly when the magnetically connected ICRH antenna is powered. Comparing antenna limiters with W-coating *vs* graphite helped roughly quantifying the role of these components in ohmic discharges, yet their contribution in presence of ICRH power remains to be assessed.

When ICRH is powered in WEST, we generally observe an overshoot on the electron temperature, footprint of efficient plasma heating, however this effect is ephemeral and rapidly (~200ms) compensated by a cooling effect due to impurity contamination.

We also found in EAST that the core W content in presence of divertor sources only is correlated with the total injected power, either from ICRH or LH.

As a summary, when 2-strap ICRH antenna magnetically connected to W components at the mid-plane is powered, the W contamination is clearly compromising high performance operations such that major upgrades of WEST and EAST B-port antennas are required in order make them compatible with high power long pulse operations. We already know low-Z material coating of antenna limiters would help mitigating high-Z impurity production, but this solution is not sustainable for future devices. Many discussions and preliminary work aiming at assessing the feasibility of the active limiters concept consisting in insulating and polarizing limiters to actively compensate RF sheath effects, lead to unpractical solutions that will not be discussed. The most promising way to go seems to be the conception of an antenna that would allow coupling significant amount of power from a radially retracted location were sputtering is greatly reduced. Ideally suppressing limiters would also solve many problems. All these ideas have been combined around the Travelling Wave Antenna concept which is undergoing fast progress and may be tested in WEST over the next few years.

7. Conclusion

Among all the challenges that ICRF is facing, the two biggest ones are respectively to efficiently couple the waves to the plasma and mitigate the impurity production. As far as wave coupling is concerned, it can be optimized by order of importance, by increasing the plasma density, the wave frequency and the RF power. Unfortunately these parameters are usually dictated by the scenario or have already been optimized as much as possible. Another powerful actuator still subject to optimization is the way to fuel the plasma and in particular the use of local valves nearby ICRF antennas. The idea is basically to minimize the distance from the strap to the fast wave cutoff layer which is what matters the most for the coupling. Series of experiments were made in L-mode both in EAST and WEST to investigate this effect and determine optimal fueling scheme for each device. Along these experiments, antennas loadings, SOL parameters modification and heat loads on divertor target were studied and discussed [Urbanczyk 2019].

First series of experiments consisted in increasing the quantity of deuterium injected in feed-forward from one or different valves, however this often resulted in a constant increase of the plasma density making hard to disentangle edge from core effects. While it was never possible in WEST to keep the density constant all along discharges with local injection due to poor pumping capacity, we managed to do it in EAST and compared the influence of different valves on antennas' loading.

Unfortunately in WEST no significant benefit was obtained with any valve but they all behave pretty much similarly. This is maybe because only small quantities of gas were injected and that the cutoff layer was in the confined region, therefore more difficult to move towards the straps than if it were in the SOL where most of the neutral gas is ionized.

On the contrary in EAST, the better pumping capacity allowed exploring larger quantity of gas injected by keeping the density globally constant, and since the cutoff layer is in the SOL, significant coupling increase were observed when using local valves compared to routine fueling with top valves and SMBI for feedback control. Despite the poor magnetic connections between both antennas and their respective valves, in all cases, all antennas loadings increased with local injection with respect to routine fueling.

Mid-plane injection maximizes nearby antenna loading, which is common to machines where similar experiments where conducted (AUG, JET, DIII-D).

Specific to EAST is the fact that this effect is observed at least in two opposite toroidal locations, which may be related to the toroidally homogeneous repartition of LH launchers with respect to ICRF antennas. For constant plasma density and the same quantity of gas injected (9.1 10^{20}e/s), highest loading was obtained simultaneously on both antennas by fueling from a single nozzle valve located at mid-plane and radially retracted ~20cm behind the antenna leading edge, emphasizing the importance to let the neutral gas diffuse before being ionized. Putting the valve too close to the plasma ($R_{valve} - R_{LCFS} < 10$cm) presents the risk of having neutrals ionized near plasma facing components, resulting in a very local and strong increase of the deuterium flux and sometimes the creation of a source of impurity, as observed on WEST APL after 2018 campaign.

Using an array of valves poloidally distributed along antenna limiters also did not help as much as single nozzle at mid-plane, most likely because the gas injected from very top and bottom points only weakly contributes to increasing the density in front of the antenna but is rapidly transported away towards divertor regions.

Doing these experiments in L-mode was undeniably a handicap due to the too good fueling efficiency. In H-mode instead, the lower fueling efficiency due to the presence of pedestal allows injecting much more gas that benefits more to SOL density and therefore ICRF coupling as observed in JET and ASDEX-U [Jacquet 2016]. In order to mitigate the fueling efficiency in L-mode and enlarge the margin of the quantity of gas that could be injected to improve edge density, the outer gap was once increased in EAST (plasma moved 2cm away from antennas), which as expected, allowed observing different levels of antenna loading with respect to different amounts of gas injected: 1.5Ω for the injection of 7.9 10^{20}e/s and 1.7Ω for the injection of 9.1 10^{20}e/s for the B-port antenna. In the case of stronger puff though (11.4 10^{20}e/s), the antenna started arcing. Higher puffing levels resulted in prompt disruptions. Similar observation were made in WEST when leaving valves in feedback and requesting different density flat-tops from 6 up to 9 $10^{19}m^{-3}$ which almost systematically ended with disruption.

The modelling tool for antenna loading calculations based on finite element methods (RAPLICASOL) and taking reflectometer density profiles as input, was able to reproduce key experimental trends. Further modelling for instance with

EMC3-Eirene [W.Zhang 2017, 2018] or/and Soledge-2D Eirene [Bufferand 2019] codes would also be suitable to have a better picture of how gas is ionized and transported in EAST and WEST. These results were already extrapolated to larger devices like ITER and DEMO. Despite much larger scales in ITER, engineering and operational constraints ($q_{95} \approx 3$ [Sips 2018]), mid-plane valves are envisaged toroidally adjacent to antennas and radially remote enough to let the gas cloud spread over the antenna surface [W.Zhang 2018]. As for DEMO, another concept of ICRF antennas so called TWA (Travelling Wave Antenna) [Ragona & Messiaen 2016] is also envisaged as an option to couple wave from radially retracted position, which may be distributed through 360° toroidally, and poloidally located in the outer top of the vessel. With such design, modelling suggests that the use of local valves distributed all along the antenna is the best to improve wave coupling [Z.Zhang 2018], however trying to maximize the coupling of such antenna is a priori not suitable since its efficiency relies on a strong mutual coupling between straps.
It is however important to point out that these extrapolations rely on diffusion coefficient that are essentially assumed similar for the different devices, which is actually a rather strong assumption, it may therefore be useful to apply additional models such as k - ε [Baschetti 2018] to self-consistently determine these coefficients.

Coupling waves to the plasma is only the first step and is not sufficient to guarantee successful operation with ICRH. Wave power not only needs to be absorbed by the plasma, but most importantly, it needs to be launched in a way that mitigates the impurity production that often prevents from reaching a steady state at high power. Evidences of efficient wave absorption were collected on each device with break in slope analysis on the electron temperature and energy content. Absorption efficiency changes with the isotopic ratio consistently with modelling predictions in WEST, and was found to increase with the total power injected in EAST. While this effect usually lasts all along the ICRH pulse in EAST thanks to daily lithium coating, it is in WEST rapidly (~200ms) hampered by a cooling effect due to core contamination by high-Z impurities, because the benefits of weekly boron coating only last about four discharges. In discharges without ICRH, we find that divertor sources are largely dominant because both the surface and the particle influx on divertor target are larger than these of outboard antenna limiters for a priori equivalent sputtering yields everywhere. Powering an ICRF antenna however leads to the excitation of RF sheath

and the rectification of potentials enhancing particles' sputtering yield locally on active antenna limiters and also magnetically connected objects. While this effect was directly studied with appropriate visible spectroscopy lines of sight in WEST, VUV spectroscopy was directly used to monitor the presence of impurity in EAST plasma core. The key results from each side are that:

- In EAST, while only divertor and LH launchers limiters are in tungsten, the level of core contamination basically increases by an order of magnitude when 3.5MW from NBI are replaced by 750kW from the B-port antenna (2-strap array magnetically connected to LH launchers W limiters).

  For a given power level on the B-port antenna, we also find many times more tungsten in the discharges after having changed LH limiters from carbon to tungsten
- In WEST, heating effect is rather ephemeral due to impurity contamination. We find that sources on limiters and divertor can sometimes be of similar order, however since an impurity emitted from a source located at the mid-plane has much more chances to penetrate inside the plasma than an impurity emitted from the divertor target (more likely to be screened), we believe no source is negligible, but this can only be confirmed either by looking at higher ionization states (like WII less likely to redeposit at a close location from where it was emitted), or by simulating high-Z impurity transport.

Since the effective sputtering yield varies non-linearly with incident particles energy (Fig.2.9), which itself varies non-linearly with the ICRH power (eq.2.48 and 2.50) and the coupling efficiency, I insist that it is almost impossible either in EAST or WEST to reach a regime where too general conclusion stands for all parameters range. Out of all observations historically made in Tore Supra [Colas 2007] [Kubic 2013], Alcator C-Mod [Ochoukov 2014], LAPD [Martin 2017], ASDEX-U [Bobkov 2017], JET [Colas 2018] and now EAST [Urbanczyk 2018] and WEST [Urbanczyk 2019 RFPPC], the most important conclusion I would make related to near-field, is that ICRF antennas with toroidal array of less than 3-strap magnetically connected to high-Z plasma facing components at the mid-plane is incompatible with operation at high power (more than 1MW) in steady state (more than 10s).

As far as far-field effects are concerned, they exist as soon as the whole power of the wave is not absorbed in a single pass. In this case, a fraction of the power carried by the fast wave can be converted into slow wave and deposited through RF sheath excitation on PFCs not necessarily magnetically connected to active antennas. For instance, we have seen that

- In EAST, changing the phasing of an antenna from dipole ($\varphi=180°$ and $\boldsymbol{k}_{||}=14m^{-1}$) down to monopole ($\varphi=0°$ and $\boldsymbol{k}_{||}=3m^{-1}$) will indeed improve the coupling (cf. eq.1.10), but degrade the absorption efficiency (from 50% down to 15% single pass), resulting in an increase of the power that reaches the high field side wall, higher amplitude of the parallel component of the electric field (characteristic of the SW), and consistent with the apparition of an impurity source. Note exciting asymmetric spectra will in addition cause more near field problems since image currents induced by each strap on adjacent limiters cannot cancel each other but on the contrary add up.
- In WEST, changing the isotopic ratio influences the absorption efficiency, such that when the H concentration was not optimal, non-negligible amount of power presumably reached divertor region magnetically disconnected and induced plasma surface interaction consistent with modelling predictions.

Despite the intensity of far-fields is smaller than that of near-fields, the fact that far-fields can affect all PFCs of the vacuum vessel can also be worrying in cases of poor absorption efficiency. It is still hard to disentangle effects related to far and near fields, in particular in WEST lower divertor where ion ripple losses can also play their role. We can yet be confident that in future devices with higher aspect ratio, fast ion population will be better confined and the absorption will get closer to 100% single pass, such that far fields should become negligible in well-optimized scenarios which a figure of merit should at least include the following aspects:

- Minimal voltage
- Symmetric spectra
- Maximal $\boldsymbol{k}_{||}$
- Optimal plasma composition for chosen heating scheme (ex. Isotopic ratio for H minority heating)
- Resonance centered and as close as possible to the well-confined regions

I sincerely hope this thesis will shed some light on ICRH from the plasma physics perspective. This is yet but only one perspective that is certainly essential, but still insufficient for designing a successful ICRF system for future devices like ITER or CFTER. The RF engineer perspective is also essential which the thesis of Walid Helou constitutes an excellent example complementary to the present one. Unlike other auxiliary heating systems, ICRH really requires taking into account multiple aspects involving very different actors, such that all aspects are almost never self-consistently discussed (at least in France nor in China). I personally believe the success of ICRH no longer relies more on scientific than human challenges, and the capacity of identifying and uniting key actors around a common objective.

Annex

1 Modeling needs and tools for ICRF applications

In the view of improving our understanding of physical processes related to ICRH and experimental observation, modeling can be used and a variety of codes implemented to solve different sets of equations and calculate parameters of interest starting from given inputs. In general, a code almost never simultaneously allows taking all types of physics into account, but rather focuses on one specific mechanism, only relevant in a limited range of parameters, where relevant ordering are necessary to simplify the equations and make their resolution manageable by available computer resources. As far as ICRF-related physics are concerned, it can be necessary to solve different problems relying on sets of equations detailed in chapter 2; for instance wave coupling, propagation and absorption.

1.1 COMSOL Finite Element Software

COMSOL multiphysics is a commercial software [Pryor 2011] using Finite Element Method [Strang & Fix 1973] to model a wide range of physics affecting relatively complex geometries. It offers an efficient mean to investigate the physics without heavy code development. COMSOL was first chosen for its user-friendly graphical interface, the possibility to couple several physics with ready to use natively equations and to define medium with full tensor properties (like plasma). A set of boundary conditions is also available, however COMSOL remaining a commercial software, its tools somehow answer user needs, and since our interest is quite peculiar, we will see that we have reached the limits of COMSOL while trying to implement SBCs in a 3D model. A COMSOL license is available at CEA on high performances computer only due to the excessive cost of the cluster license for several nodes. Since the numerical resources are thus limited, in 3D only gross estimations of the electric field with only PEC boundary conditions is feasible (RAPLICASOL), while only 2D applications are presently possible for modelling with SBCs (SSWICH).

1.2 Wave coupling modeling with TOPICA and RAPLICASOL

Coupling calculations are first necessary to assess the amount of power that a given antenna would be capable of radiating inside given plasma. To do so, the key ingredients are therefore the antenna geometry, and the properties of the plasma immediately facing the antenna (usually cold magnetized plasma with a density profile). The input can then be the power or voltage on antenna ports or directly the current on the straps. The wave equation 2.2 is then solved to calculate how the wave electric field evolves around the antenna. In order to solve this type of problem, TOPICA [Lancellotti 2006] which was written in the beginning of the 3rd millennium is probably one of the best reference capable of taking into account very thin details of the antenna geometry in 3D. TOPICA in itself however does not contain the right physics to model the plasma, it is therefore coupled to another code containing hot plasma physics (FELICE [Brambilla 1989]) and both are resolved self-consistently with the method of moments. This approach has proven to lead to results very consistent with experimental observations and benefits from a large amount of validation that have lead the community to trust this tool enough to now use it for predictive purposes. The main inconvenient of this code is that it requires large resources, whereas other codes like HFSS [Hillairet 2015], ANTITER II [Messiaen 2010 & 2011] or RAPLICASOL [Jacquot 2015] can be numerically much cheaper and faster by relying on others assumptions (cold plasma or dielectric), Finite Element Method and different solvers (Fig.A1). On the one side, these approaches can typically be more powerful strictly for coupling calculations [Messiaen 2011], but they are on the other side limiting as the typically cannot be used for studying RF sheaths that require accurate resolution of the parallel component of the electric field (millimetric wavelength) which plays the main role. Although RAPLICASOL requires considerably fewer computational resources than TOPICA, it appears to be a very attracting compromise since we find that the predicted quantities of experimental interest (including reflection coefficients, coupling resistances, S- and Z -matrix entries, optimal matching settings, and even radiofrequency electric fields) are in good agreement provided we are careful to use the same geometry in both codes [Tierens 2019 NF]. Wave electric field is then calculated over the whole 3D domain

with Perfect Electric Conductor (PEC) boundary conditions on all surfaces, and Perfectly Matched Layers (PMLs) to emulate radiations at infinity analog to 100% single-pass absorption (Fig.2.11) [Becache 2003]. Afterwards, electric field 2D maps can for instance be extracted at the antenna mouth and serve as input for other codes aiming at modelling other effects, like SSWICH code to model RF sheath.

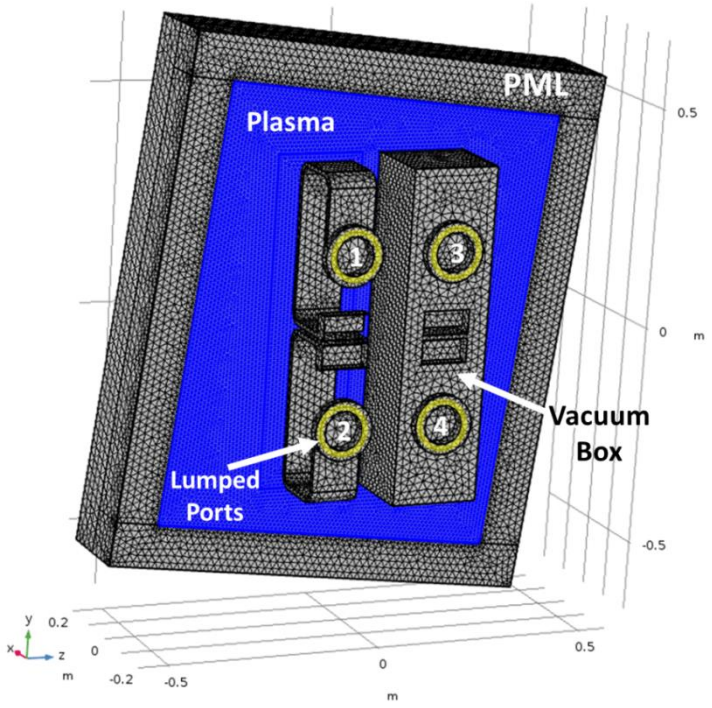

Figure A1: Example of a RAPLICASOL model of a flat antenna with four straps in vacuum seen from the back and radiating into a plasma surrounded by PMLs.

1.3 RF sheath modeling in SOL plasma with SSWICH

As mentioned in annex 1.1, none of the boundary conditions available in a 3D COMSOL model is compatible with the physics of RF sheaths (B_n=D_n=0 [Myra & D'Ippolito 2009]). Many tests and attempts were done using both weak contributions or/and weak constraints, however these did not work out, not only because simulation results were in disagreement with analytic ones in some simple cases, but also because trickily enforcing such boundary conditions can add degrees of freedom to an already complex problem. While no iterative solver can handle this type of boundary conditions, direct solvers such as MUMPS or PARDISO would sometimes fail and

sometimes lead to strange solutions which patterns look very sensitive to the mesh.

So far, best results were obtained with the SSWICH-SW version described under [Colas 2013]. As detailed in section 2.4 (eq 2.49), RF sheath which form on antenna's metal surfaces in contact with the plasma are taken into account; the numerical scheme of code is detailed in Fig.A2. RAPLICASOL provides 2D maps (toroidal-poloidal) of respectively the parallel (Fig.A3a) and perpendicular (Fig.A3b) components of the electric field. These maps are then extracted as 2D matrices, shear transformed to align on the magnetic field lines, tilted with respect to the antenna geometry. E-field 1D profiles are then extracted for several poloidal heights and used as inputs for SSWICH implemented in 2D with the so called "Sheath Boundary Conditions" (SBCs) [Colas 2013]. SSWICH **S**elf consistently calculates the **ICRH** **W**ave propagation in the SOL and RF **S**heath physics (section 2.4) leading to the DC potential rectification along the limiter structure (cf. radial-poloidal maps in Fig. A3c and d).

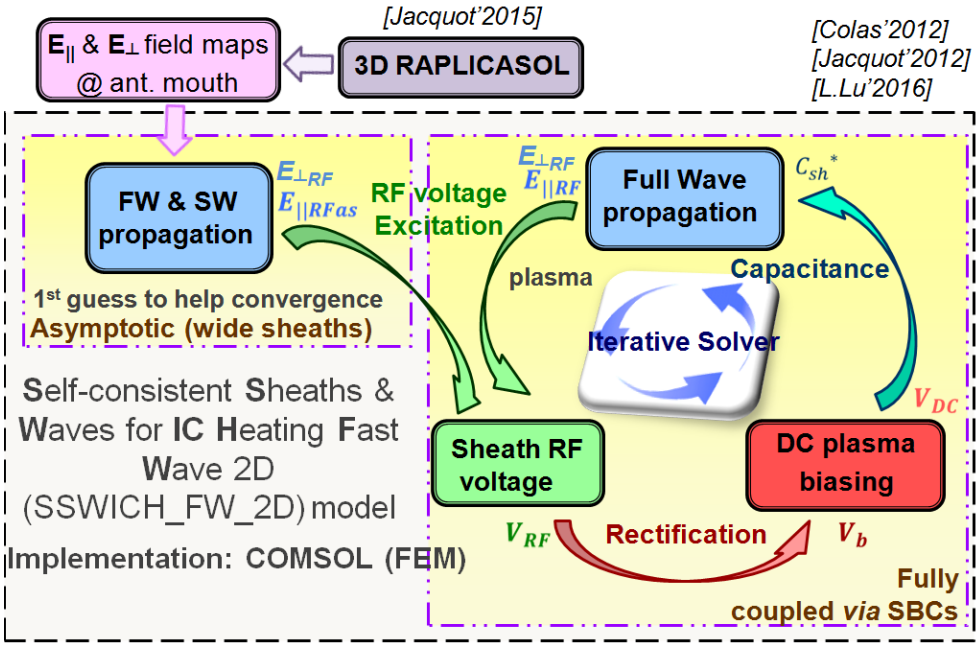

Figure A2: Iterative Process in 2D SSWICH-FW code [L. Lu 2016]

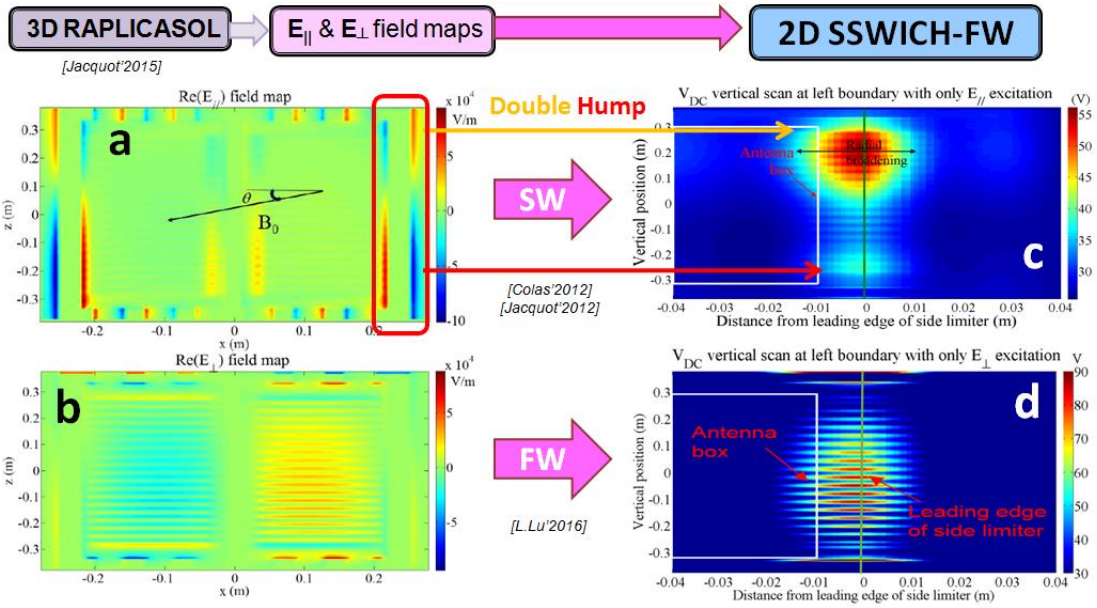

Figure A3: 3D RAPLICASOL (a, b) & 2D SSWICH-FW 2D (c, d) mapping results, respectively for components parallel (SW mode) and normal (FW mode) to magnetic field direction [L. Lu 2016]

In the first version, SSWICH-SW [Colas 2013] only took into account the Slow Wave (SW) propagation [J. Jacquot 2013]. Yet few modifications observed experimentally – in locations that cannot be reached by the evanescent SW – could not be reproduced, so that the FW had to be taken into account [L.F. Lu 2016]. An illustration of the iterative process of the last version is provided on Fig.A2. Multi-2D simulations at different poloidal locations, allow from toroidal distribution to deduce radial one, doing some approximations on 3D effects [L.F.Lu 2016]. This multi-2D/3D approximation constitutes the weakest point of the code, specifically for FW simulations. It is shown in LU LingFeng's thesis that the approximation underestimates FW radial evanescence. As a result, DC potential map A3d generated by the full-wave version of SSWICH from perpendicular electric field distribution of map A3b (extracted from RAPLICASOL), is probably overestimated. Besides SW simulations should provide more realistic results. Indeed, the double hump structure observed on maps A3a and A3c is consistent with experimental results discussed in the previous part (maps d, e and g on Fig.3.3). At this point, we know that SOL modifications are largely dominated by SW mode, yet because of mode conversions at geometry transitions, FW plays a key role in far field sheath excitation. Improvements

of the code could concern in priority the impact of the omitted poloidal direction and the 3D curved geometry of modeled antenna with Sheath Boundary Conditions. As mentioned previously, having SBCs implemented in 3D is however very challenging. Very large amount of time (about one year) during the thesis has actually been spent on this topic without success, many options were explored but COMSOL environment turns out to be too limiting to make any significant progress. Despite any psatisfying solution found so far, the time spent on this topic still allowed sharpening our understanding of how wave equation could be solved in 3D to allow taking into account sheath physics directly [Tierens 2019 PoP]. Numerical problems met are actually likely to be related to the fact that SSWICH so far relies on COMSOL FEM solver, but the work is still un-going with the hope of solving this issue using another more versatile and open source solver of Maxwell's equations, ERMES [Otin 2013].

As was briefly mentioned, the codes should in principle be usable for predictions and used for scenarios development. However before reaching this level of confidence, each code must first be validated by comparing calculations from theory with measurements from experiments. This comparison is crucial in order to adapt model outputs to data measurable with existing diagnostics (cf. SSWICH and ITPA IOS 5.1 task experiments (Fig.3.3)), or reciprocally develop new diagnostics to allow measuring parameters of interest for the physics (SSWICH and stark spectroscopy [Kostic 2018]). Modelling is therefore nothing but a tool which value rises as it can accurately benchmark experimental observations which an overview of topics of interest for the thesis is proposed in chapter 3.

1.4 RF wave propagation and absorption in core plasma with EVE and TOMCAT codes

Beyond cold plasma and interactions with the edge, it is also interesting to assess how ICRF waves propagate in hot plasma up to the resonance layer in the core (Table 2.1) and gets absorbed. Propagation can typically be solved in 3D with EVE [Dumont 2009] or CYRANO codes [Lerche 2009 PPCF] and local RF electric field structure obtained by the full-wave computations consisting in calculating the wave field by a direct solution of the Maxwell's equations (eq.2.2) in the Fokker–Planck description.

The EVE code is a full-wave solver based on the variational formulation described in [Dumont 2009]. It is based on the quasilocal plasma functional obtained

in terms of adiabatic invariants, in which an expansion of the particle Hamiltonian is performed to yield a tractable second-order finite Larmor radius version of this functional that was implemented. Simplistic antenna straps geometry can then be prescribed with key parameters settings (ex: phasing) from which a spectrum discretized in harmonics for each toroidal number is deduced before being loaded with given target plasma defined by its composition (Z_{eff}), aspect ratio (a, R_0), magnetic equilibrium, electron temperature and density profiles ($T_e(r)$ and $n_e(r)$).

EVE code was used in this thesis to assess how electric field amplitude evolve in EAST plasma along an ICRF antenna phase scan, allowing to benchmark spectroscopic observations correlated with impurity sources on the high field side wall facing the antenna inside the vessel. These 3D codes are however complex and take lots of computer resources to run.

Others 1D codes can however be much faster to run and constitute more flexible tools to rapidly explore wide parameter ranges, typically in interest for scenario development [Lerche 2019]. TOMCAT code [Van Eester & Lerche 2013] is typically one of these tools that can efficiently assess waves single pass absorption efficiency (or double pass, single and double transit depending on the absorption efficiency and cutoff layers location, cf. Fig.A4) on each species of the defined plasma. TOMCAT guarantees that a positive definite power transfer from waves to particles ensured for any of the wave modes in plasma with all species following analytical Maxwellian distributions, as is expected from first principles. Rather than relying on a truncated Taylor series expansion of the dielectric response, an integrodifferential approach that retains all finite Larmor radius effects is proposed. To keep the required computation time for this generalized description reasonable, tabulation of integrals is intensively used. TOMCAT was used to assess how wave absorption efficiency varied with antenna phasing in EAST and H concentration in WEST (Fig.6.8) which results are presented in chapter 6.

As a summary, EVE and TOMCAT codes are both interesting tools that calculate the same quantities but relying on different approximations. In practice, TOMCAT is a very powerful tool to rapidly explore wide ranges of parameters that would take unreasonable amount of time with EVE. However not only several effects are not taken into account in TOMCAT, but mostly a Fokker–Planck solver should be added in order to get an estimation of how the energy deposited on each species is redistributed. This is where EVE powerful 3D description comes into play (cf. Fig.10

and 11 in [Bourdelle 2015]).

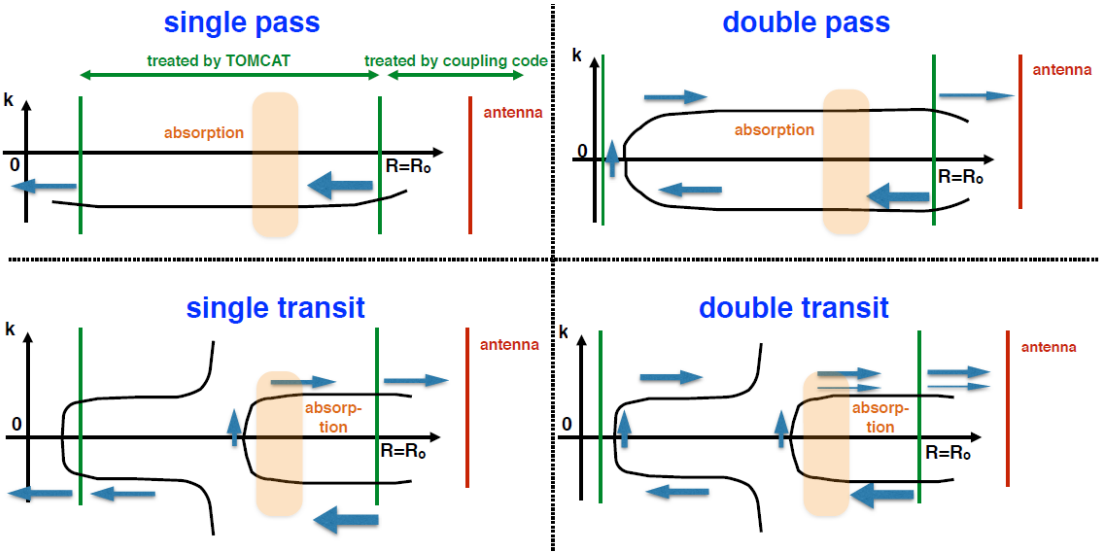

Figure A4: Single and double pass absorption defined as in TOMCAT code
Courtesy of Dirk Van Eester

2 Modeling tools for power exhaust estimations

In the view of improving our understanding of physical processes related to ICRH and experimental observation, modeling can be used and a variety of codes implemented to solve different sets of equations and calculate parameters of interest starting from given inputs. In general, a code almost never simultaneously allows taking all types of physics into account, but rather focuses on one specific mechanism, only relevant in a limited range of parameters, where relevant ordering are necessary to simplify the equations and make their resolution manageable by available computer resources. As far as ICRF-related physics are concerned, it can be necessary to solve different problems relying on sets of equations detailed in chapter 2; for instance wave coupling, propagation and absorption.

2.1 Temperature from dynamic simulations with ANSYS

ANSYS is a software based on Finite Element Method and is used to simulate engineering design. One starts by defining the dimensions of the object, then material

properties are prescribe (geometry (ex: Fig.A5), density, thermal conductivity σ, initial temperature …) and incident heat flux pattern and values (ex: Fig.A6). Finally, the ANSYS software simulates and analyzes temperature distribution evolution along time. In our case, we typically consider an inertial stainless steel plate of 30cm (poloidally) x 10cm (radially) x 1mm (toroidally).The heat flux is assumed parallel (toroidal) and its maximum is found at the closest edge to the plasma, 3cm away from a corner of the plate (Fig.A5 & A6). From this maximum, heat fluxes decrease exponentially in both radial and poloidal directions, as per focusing mostly on RF sheath induced heat flux. Dynamic simulations where made for five different values of maximal heat fluxes from 1 up to 10MW/m², and plate maximal temperature evolution represented in Fig.A7. These simulations basically predict that plate would have started melting after 30s for a maximal heat flux of 3MW/m², after 15s for 5MW/m², and only after 2s for maximal heat flux of 7MW/m².

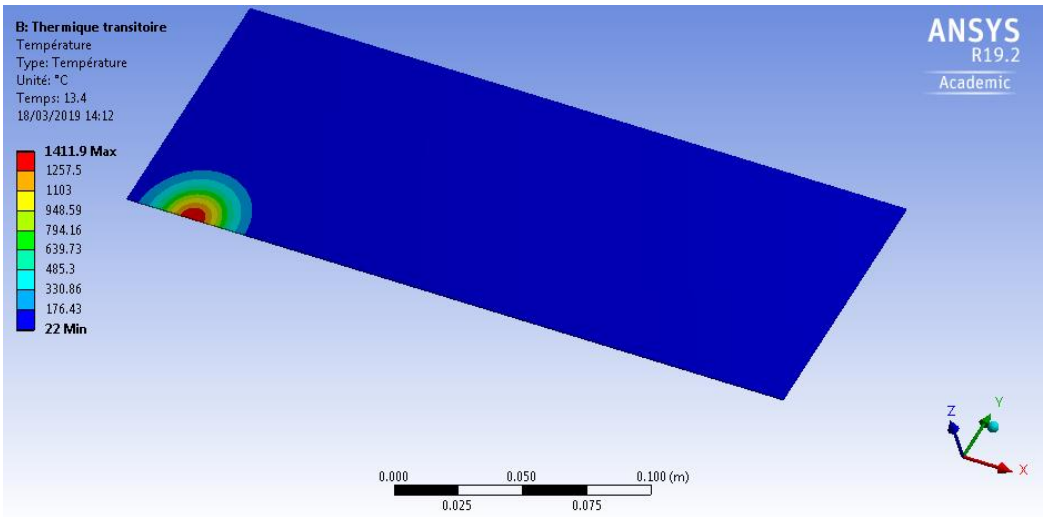

Figure A5: View of the ANSYS model of the plate

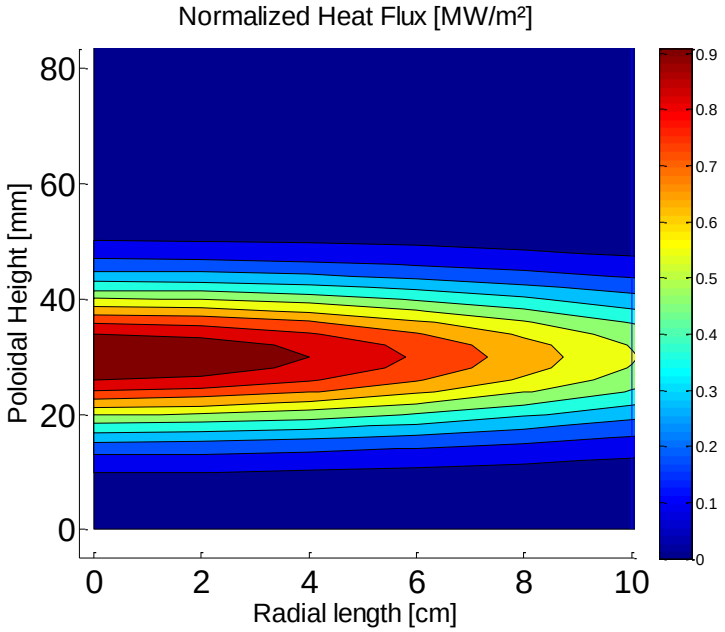

Figure A6: Normalized heat flux structure applied on the plate

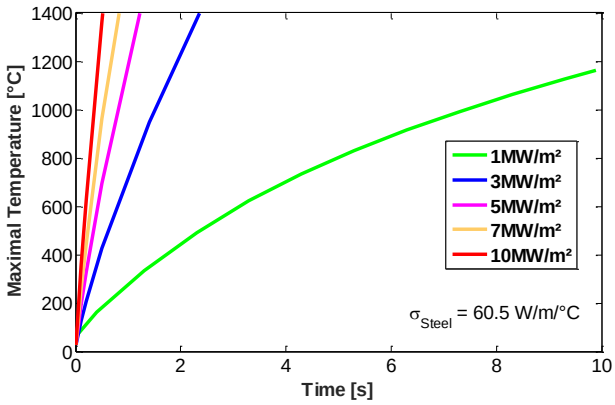

Figure A7: Evolution of the maximal temperature of the plate for different parallel heat fluxes

2.2 Heat loads from infra-red inversion with TEDDY

In view of helping analysis of power exhaust experiments and in general IR data providing apparent temperature of observed objects, the 2D non-linear code TEDDY (Thermography Estimate of Deposited heat DYnamics) [Fedorczak 2019] was used in this thesis to perform inversion of surface heat loads from infra-red thermography of graphite tiles in EAST I-port antenna. This code takes into account the 2D geometry

of a graphite tile assuming heat will mostly diffuse through the tile (radially) and in the poloidal direction with possible anisotropy in material structure such as for carbon fiber composite. We assume the material is uniform in the toroidal direction which is reasonable because most of the heat flux is parallel to the toroidal direction and deposited at the side of the tile with almost normal incidence. Parallel heat load profile ($q_{||}(y)$) is then applied on the tile, with similar pattern to the one shown in Fig.A6. Temperature is then calculated dynamically for each time step δ_t small enough to respect the stability criterion of the Fourier equations as follow:

$$T(t+\delta_t) = T(t) + \delta_t \left(L(t)\Lambda(t) + K(t)q_{||}(t) \right) \quad \text{(A1)}$$

With L, Λ and K matrices depending non linearly on the local temperature as well as the thermal conductivity λ (in W/m/K) and the product of the volumetric mass ρ (in kg/m^3) by the heat capacity of the material C_p (in J/kg/K) as represented in Fig.A8. The surface temperature which should be compared to IR data is finally estimated as follow:

$$T_{surf}(y,t+\delta_t) = T_{Ny}(y,t+\delta_t) + \alpha_s q_{||}(y,t+\delta_t) \quad \text{(A2)}$$

With α_s the thermal resistance of the surface layer (in $K.m^2/W$).

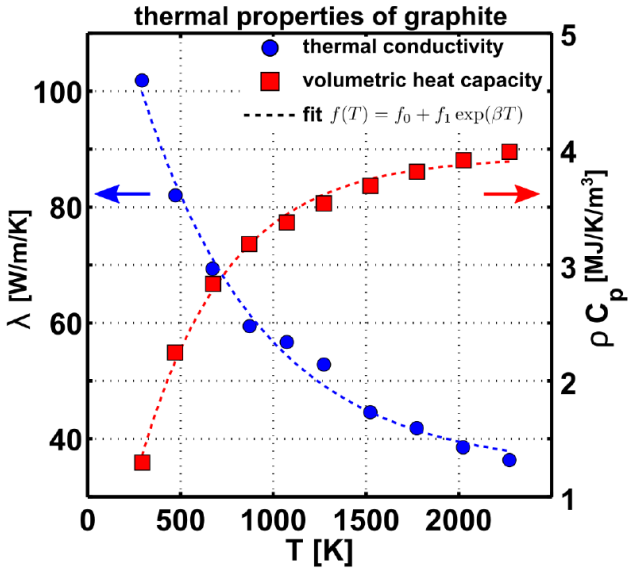

Figure A8: Temperature dependence of thermal properties of graphite.
Courtesy from [Fedorczak 2019]

A reverse version of the code deducing heat loads out of IR surface temperature also exists but was not used in the present thesis.

3. S/XB coefficients function of energy to estimate different particle fluxes from visible spectroscopy

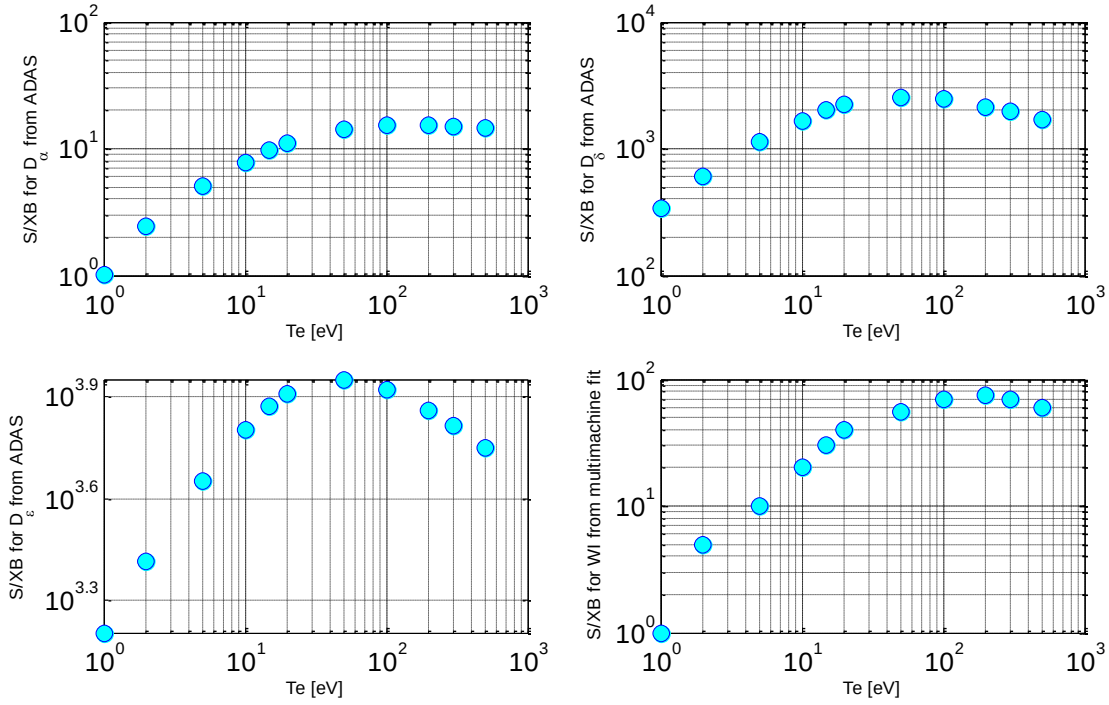

Figure A9: S/XB for different deuterium lines from Balmer series (α, δ and ε) and tungsten

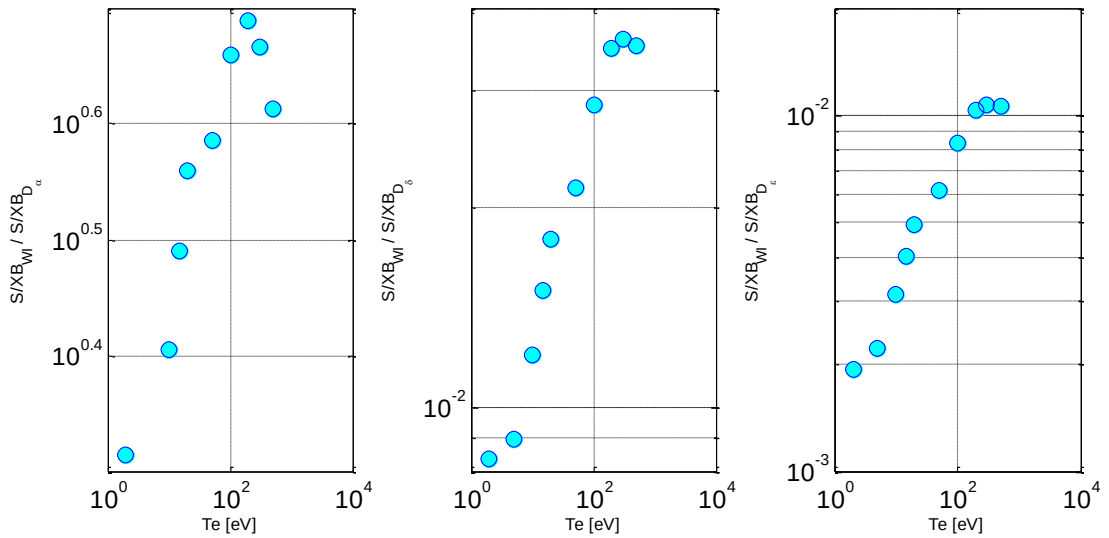

Figure A10: Ratio of S/XB deuterium over tungsten for α, δ and ε from Balmer series

S/XB coefficient allow estimating particle flows out of spectroscopic brightness, however it is important to keep in mind that the S/XB only takes into account atomistic physics and does not include molecular contribution to plasma contamination by impurities. This can however play a role as important as atoms in a carbon environment. Hopefully WEST is an almost full-tungsten environment and as can be seen in the figure bellow, a contribution of maximum 20% in expected from molecules in a tungsten environment.

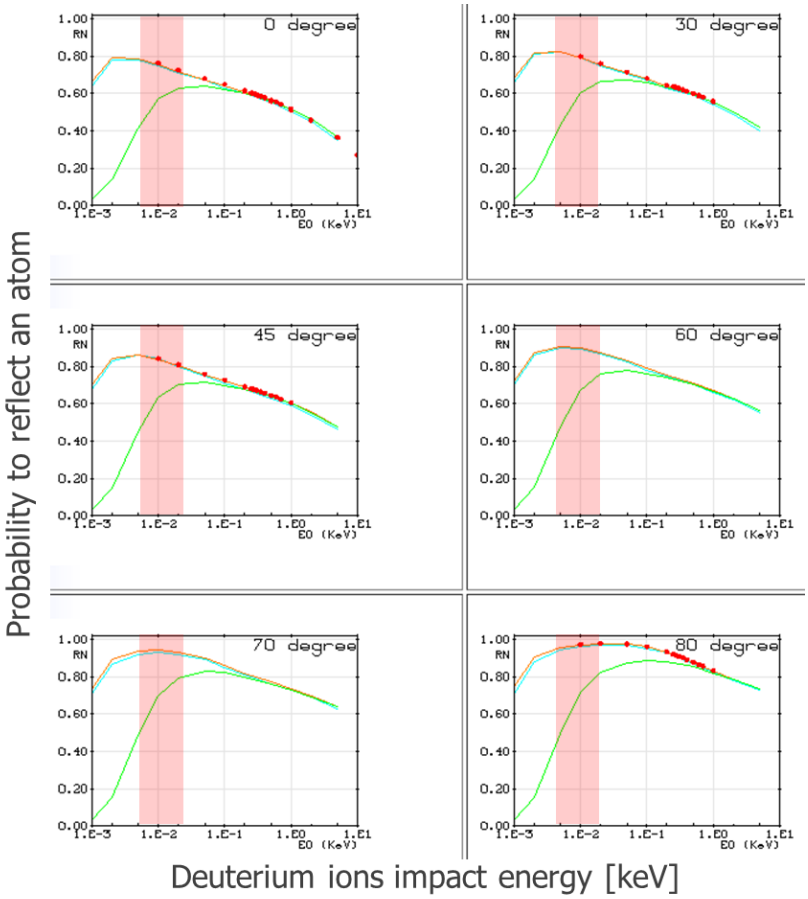

Figure A11: Probability for a deuterium ion falling onto a tungsten surface to sputter an atom as a function of its impact energy and for six different incidence cases from 0° up to 80°. These data were extracted from the Eirene database. The red region represents the range of energies corresponding to typical WEST SOL temperatures.

4. Overview of discharge 54528 discussed in chapter 5

In this discharge, the top valve V11 was in feedback mode and three different densities were requested (5.6, 6.6 and over $7.10^{19}m^{-2}$) such that three different flat-tops are obtained. As expected, the ICRF coupling (blue on graph b) improves with the density (red on graph a) while the temperature decrease (graphs d and f). On the third flat-top though, the density is so large that lower hybrid shuts down, this combined with an increase of the density immediately results in a sharp decrease of the temperature in the divertor (graph f) that is consistent with spectroscopic observation in Fig.5.18b. It is however important to stress at this point that the red profiles are overestimated because we did not take S/XB coefficients dependence on temperature into account (Fig.A9). Ideally one should at each time deduce radial profiles of S/XB along divertor target based on temperature profiles. This could not be done yet due to lack of time.

We also observe an increase of impurity contamination while increasing the density the first time consistent with visible spectroscopy observation in the divertor region. At the third flat-top though, core contamination decreases likely because of the loss of LH power resulting in a decrease of the electron temperature.

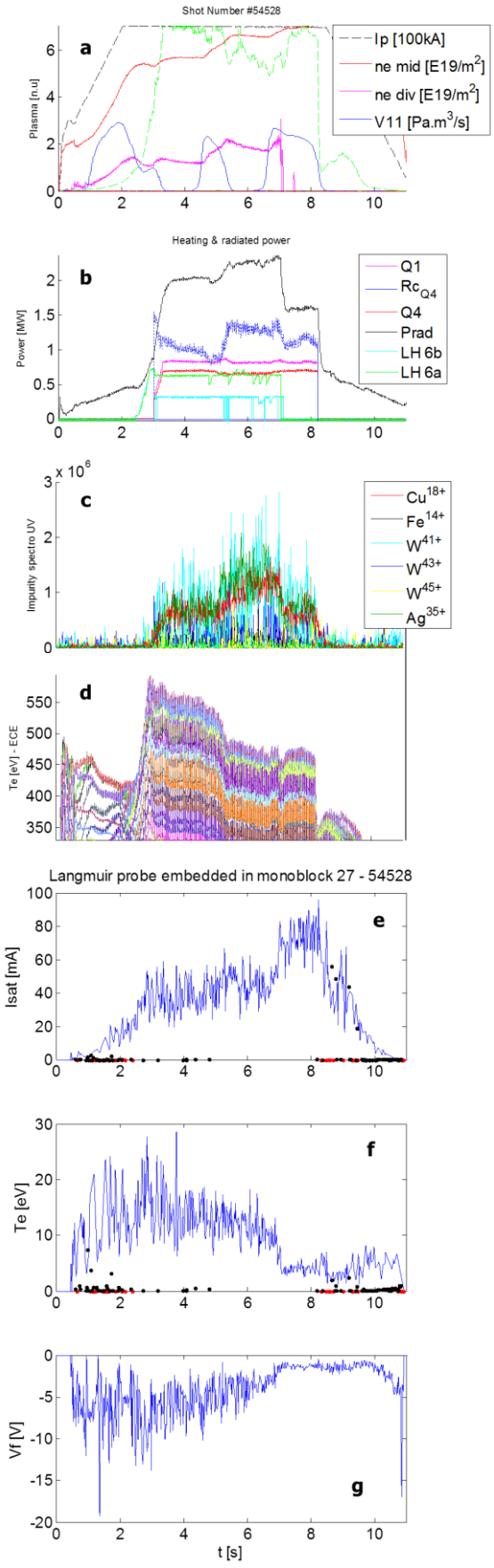
Shot Number #54528
a
Ip [100kA]
ne mid [E19/m2]
ne div [E19/m2]
V11 [Pa.m3/s]
Plasma [n.u]
Heating & radiated power
b
Q1
RcQ4
Q4
Prad
LH 6b
LH 6a
Power [MW]
x 10^6
c
Cu18+
Fe14+
W41+
W43+
W45+
Ag35+
Impurity spectro UV
d
Te [eV] - ECE
Langmuir probe embedded in monoblock 27 - 54528
e
Isat [mA]
f
Te [eV]
g
Vf [V]
t [s]

Figure A12: Overview of the discharge 54528 with three different density flat-tops

5. Coupling simulations with RAPLICASOL

Simulations were made in order to test whether or not the experimental trends are reproducible with an antenna code using experimentally measured 1D density profiles (Fig.5.15) as the main input – which can be inaccurate in one case that will be discussed in details –. RAPLICASOL [Jacquot 2015] is a 3D code detailed in Annex 1.2 and based on finite element method allowing calculations of RF wave coupling for Ion Cyclotron Antenna in the SOL by solving Maxwell's equations in the cold plasma approximation without sheath or any non-linear phenomenon. Its results are in principle comparable with other antenna codes based on different numerical methods like TOPICA [Lancellotti 2006] or HFSS [ANSYS HFSS]. In our case, RAPLICASOL takes as input the 3D antenna geometry flattened to simply delimitate vacuum from plasma regions by a plane. The antenna is then put in vacuum and radiates into the plasma whose properties can be tuned by playing on dielectric tensor components (cf. Fig.A1).

Two cases are hereby presented, calculations respectively for the EAST B-port ICRF antenna without Faraday Screen (31.5MHz) [Urbanczyk 2019 NF] and a WEST ICRF antenna (55MHz) [Tierens 2019]. In both cases, antennas radiate on a 10 cm wide cold deuterium plasma with hydrogen minority (7% in EAST 5% in WEST), magnetic field lines tilted at 7° with respect to the toroidal direction and radial density profiles from reflectometry data (Fig. 5.15). Perfectly Matched Layers (PMLs) [Berenger 1994] are further used behind the plasma to emulate radiation at infinity. Finally, perfect electric conductor conditions are enforced on all the boundaries, except the four coaxial ports of characteristic impedance Z_0 of 50Ω in EAST and 44Ω in WEST, each lumped excited by 1A in dipole phasing. The absence of a Faraday Screen in the imported CAD model could lead to slight overestimations of the coupling, but this simplification allows significant mesh reduction and therefore reduces the time of resolution and memory consumption which was already close from the limits of available workstations. Meshing the domain with tetrahedral whose size is at most a few millimeters leads to about 6 million degrees of freedom. In such conditions, a 4 × 4 Z-matrix calculation requires about 20 h and 80 Gb of memory. As we only discuss the relative impact on antenna loading, such simplification is

therefore acceptable. The impedances Z_i are taken as $Z_i = V_i/I_i$ where the voltage vector $V = [V_1, V_2, V_3, V_4]^T$ is equal to ZI where $Z = R + jX$ is the 4×4 Z-matrix computed by each code. Real (proxy of the coupling efficiency cf. eq.5.4) and imaginary parts of Z_i are calculated, together with the modulus and the argument of the reflection coefficient $\Gamma_i=(Z_i-Zo)/(Z_i+Zo)$. We will also assume ideal inductive dipole excitation of both antennas ($I = [1A, -1A, -1A, 1A]^T$) which can be questionable, in particular in the case of EAST where phases are not controlled in real-time, so that the real situation might be slightly different. With these approximations, $R_i/2$ is interpreted as a proxy of the coupling resistances.

5.1. Calculations for EAST B-port antenna

First it is important to stress that reality may be different from exact dipole phasing case as phases on straps were not feedback controlled [Berenger 1994]. In the first case of density controlled by the SMBI (Fig.5.15), density is rather small at the edge. Total power transmitted to the PML can be assessed by integrating the Pointing vector at the plasma/PML interface and equals 580kW for total power over 600kW on ports. In the red series of Fig.A13, beware that the excitation is not ideal anymore but a little bit more realistic with at least the same power input on straps as during the experiment.

Most reliable density profiles are given by J-port reflectometer and were used as inputs for modelling the B-port antenna loading. The absence of magnetic connections between B and J ports raises the question rather if the reflectometer measured densities consistent with those in front B-port antenna. Since no strong difference was observed in terms of coupling from antennas at opposite toroidal positions (Fig.5.5c), we assume the density profiles at one location relatively homogeneous toroidally. When gas was injected from the B-port, density increased in the SOL but the position of the cutoff layer remained the same as with routine injection as shown on Fig.5.15. The impact on wave coupling appeared limited in the modeling whereas improvements were experimentally observed.

When gas was injected from the J-port mid-plane though, density clearly increased in the SOL, significantly shortening the distance of the strap-to-cutoff layer. Wave coupling was indeed much better with an increase in coupling resistances of each line (J-port mid-plane in Fig.A13), and a 23% increase of power to the PMLs.

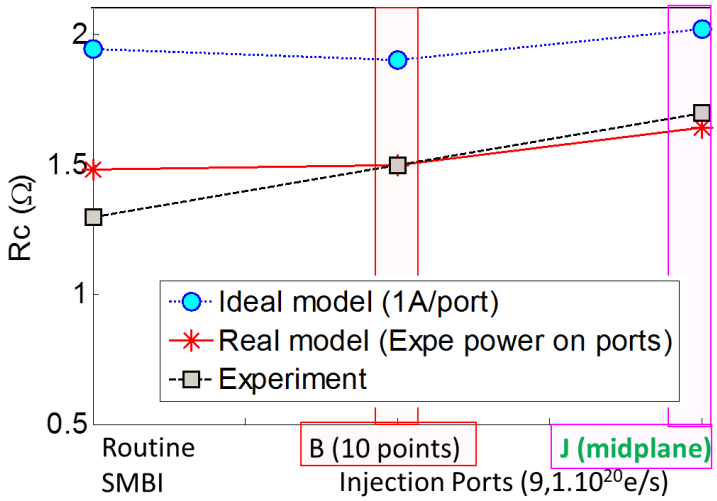

Figure A13: Comparison of experimentally measured (black series) and simulated coupling resistances of B-port antenna in three different gas injection cases; routine fueling with SMBI for feedback control, injection on B-port from 10 different points (Fig.4.12c), and injection on J-port from a single valve located at mid-plane. Cf detailed shot list in Table 4.1.

Those cases nevertheless stand for ideal inductive excitation of each port by 1A of current. In reality, power was not balanced on the straps, so it's worth looking at slightly more realistic cases with the correct input power on each port as shown below. Since incertitude persists on phases, we will run those simulations assuming dipole phasing at the antenna.

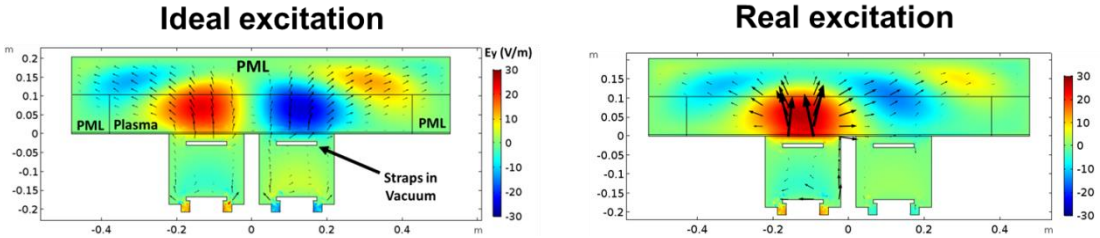

Figure A14: Ey fields (y component of the electric field) with arrows representing power flow extracted at the toroidal-radial plane at poloidal height Z = - 0.2m (straps #2 and #4) with ideal and experimental power inputs.

From previous results we know that the J-port reflectometer was not able to catch the beneficial influence of the B-port gas puffing on the antenna coupling since despite slight changes in the shape of the profile (5.15), cutoff density position was not moved closer enough to make any significant difference. We finally made

simulations slightly more realistic by basing them on experimental power inputs on each port and represent them by the red series in Fig.A13.

The total power from all the ports is now fixed to 600kW and unequally balanced on 3 ports as it was during the experiment. The beneficial impact of gas injection on the J-port still appears on coupling resistances as for previous cases, and it can furthermore be seen looking at current values on ports that are lowered due to improved wave coupling. In practice, it means power can be increased further at the generator without arcing.

From an RF study point of view, we can briefly comment on the 2D field maps extracted on the toroidal-radial plane at poloidal height Z= - 20cm intercepting straps #2 and #4 (Fig.A14) in the two different routine fueling cases respectively. Experimental unbalanced power inputs lead to much higher electric fields in some regions where currents are badly compensated, and where one can expect RF sheath formation and stronger interactions [Bobkov 2017]. Both poloidal and toroidal asymmetries might also cause further scenario problems like bad wave absorption and larger impact of far-fields.

5.2. Calculations for WEST antennas

In this section, calculations for a 4-strap antenna – similar to the ICRF antennas of the WEST tokamak (Fig.4.7) – were made both with RAPLICASOL and TOPICA codes and compared [Tierens 2019]. A vacuum layer of width D_{vac} separates the antenna aperture from the magnetized plasma (Fig.A15). Five calculations are made for D_{vac} increasing from 0 up to 42mm. As D_{vac} increases, the cutoff layer basically moves away from the antenna front face and we therefore expect a decrease of the antenna loading.

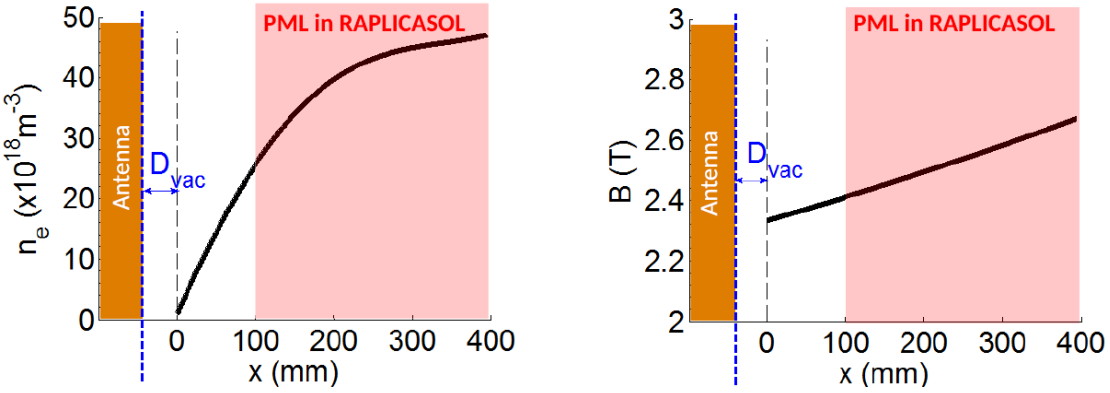

Figure A15: Density and magnetic field profiles in front of the test-case antenna.

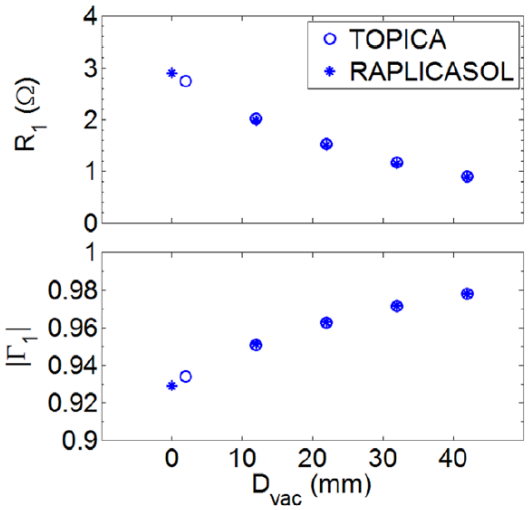

Figure A16: R_i and $|\Gamma_i|$ as function of D_{vac} for i = 1 and I = ID = $[+1A,-1A,-1A,+1A]^T$. Similar results are obtained for the other straps.

Very similar results are obtained with both codes, showing a good agreement between RAPLICASOL and TOPICA. The discrepancy between the codes is around or below ±5%, ±2% for R_i and $|\Gamma_i|$ respectively (Fig.A16). As one would expect, R_i decreases with D_{vac} since as D_{vac} increases the waves radiated by the antenna have to tunnel through a larger evanescent region. It should be noted that while TOPICA's formulation allows handling D_{vac} as small as 2 mm, doing the same in RAPLICASOL is too costly in terms of meshing. Hence, for the case of the smallest D_{vac}, the vacuum layer has been eliminated in RAPLICASOL (D_{vac} = 0 mm instead of D_{vac} = 2 mm). Thus, strictly speaking, comparisons between RAPLICASOL and TOPICA for the smallest considered D_{vac} is not valid. As mentioned earlier, these aspects do not matter

while discussing coupling only, but they would for instance have much more dramatic impact on electric fields patterns in front of ICRF antenna. We can for instance compare toroidal-poloidal maps of each component of the electric field extracted 5 mm behind the plane of the leading edge of the limiters for 1MW coupled power (Fig.A17,A18,A19). We see that the electric fields as calculated by RAPLICASOL are in good agreement with those calculated by TOPICA for this case of D_{vac}=12mm. Without vacuum layer in TOPICA or for D_{vac}=2mm in RAPLICASOL (Fig.5.28), the density gradient at the interface induces mode conversion and excitation of waves propagating on the surface. These field patterns could be related to low $k_{\parallel}$ (or coaxial) modes excitation and can be mitigated by smoothening the transition nearby metallic structure. In this case, we observe clear discrepancy between the codes, with RAPLICASOL which exhibits very different behavior.

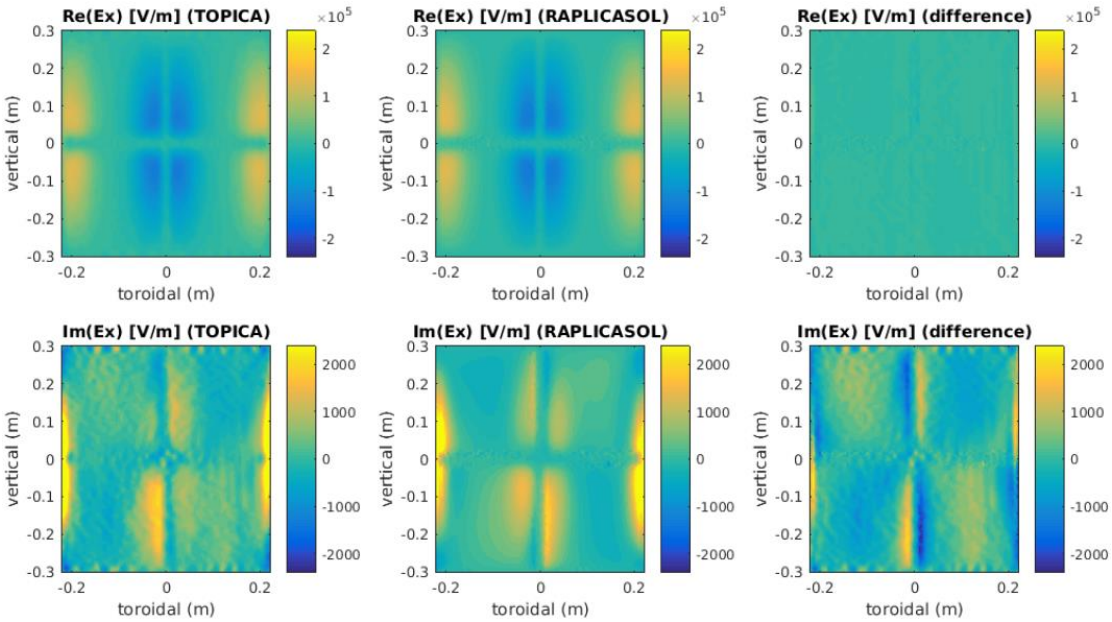

Figure A17: Real and imaginary part of Ex at the aperture of the 4-strap WEST-like antenna, with dipole excitation (1 MW total coupled power), calculated by RAPLICASOL and TOPICA. D_{vac} > 10mm

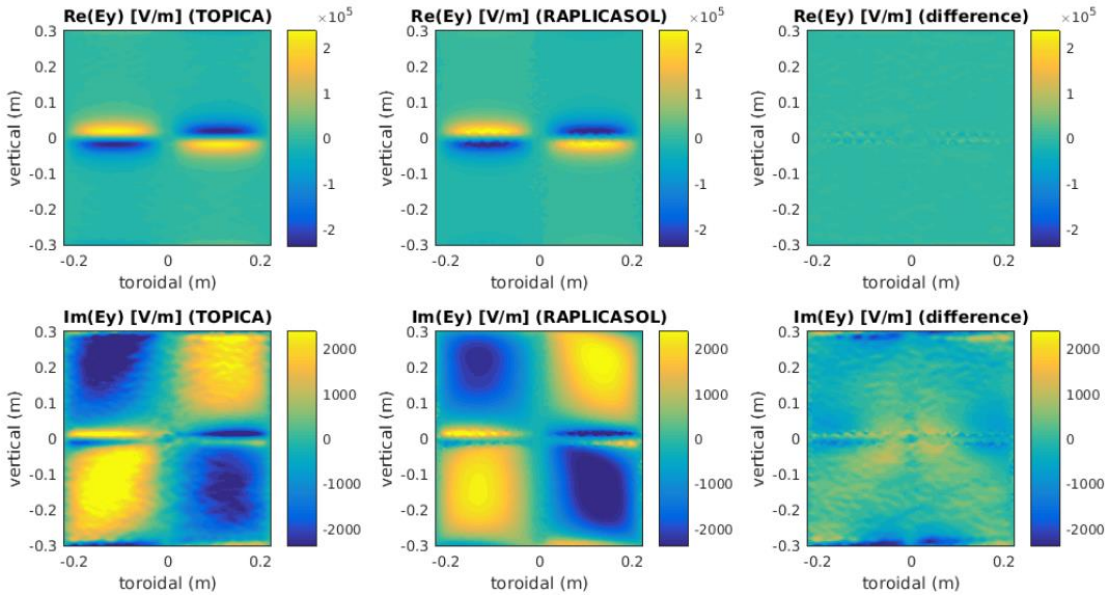

Figure A18: Real and imaginary part of Ey at the aperture of the 4-strap WEST-like antenna, with dipole excitation (1 MW total coupled power), calculated by RAPLICASOL and TOPICA. D_{vac} > 10mm

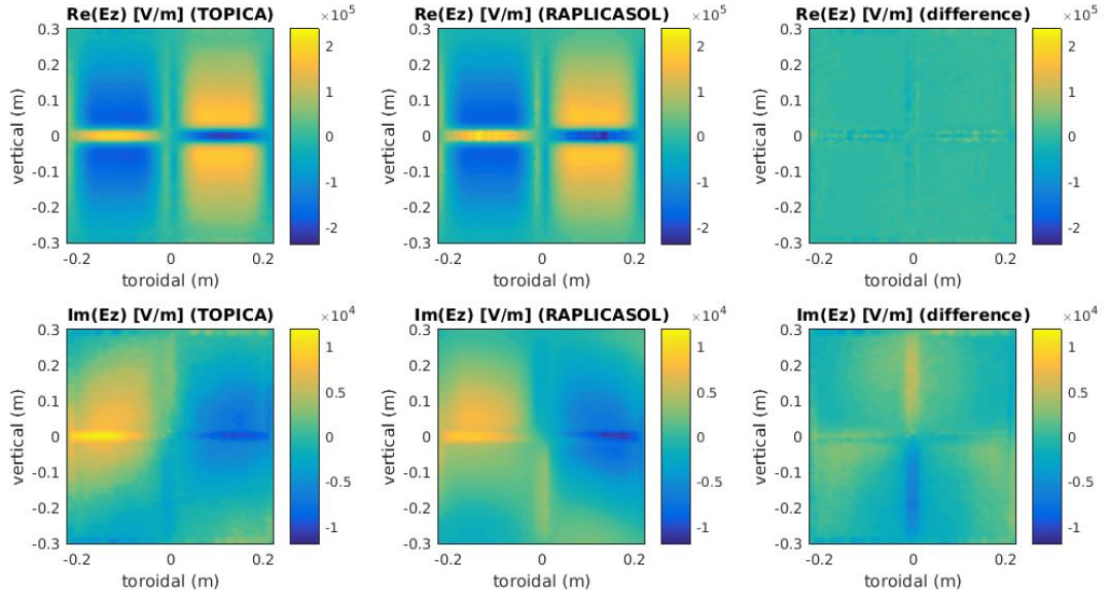

Figure A19: Real and imaginary part of Ez at the aperture of the 4-strap WEST-like antenna, with dipole excitation (1 MW total coupled power), calculated by RAPLICASOL and TOPICA. D_{vac} > 10mm

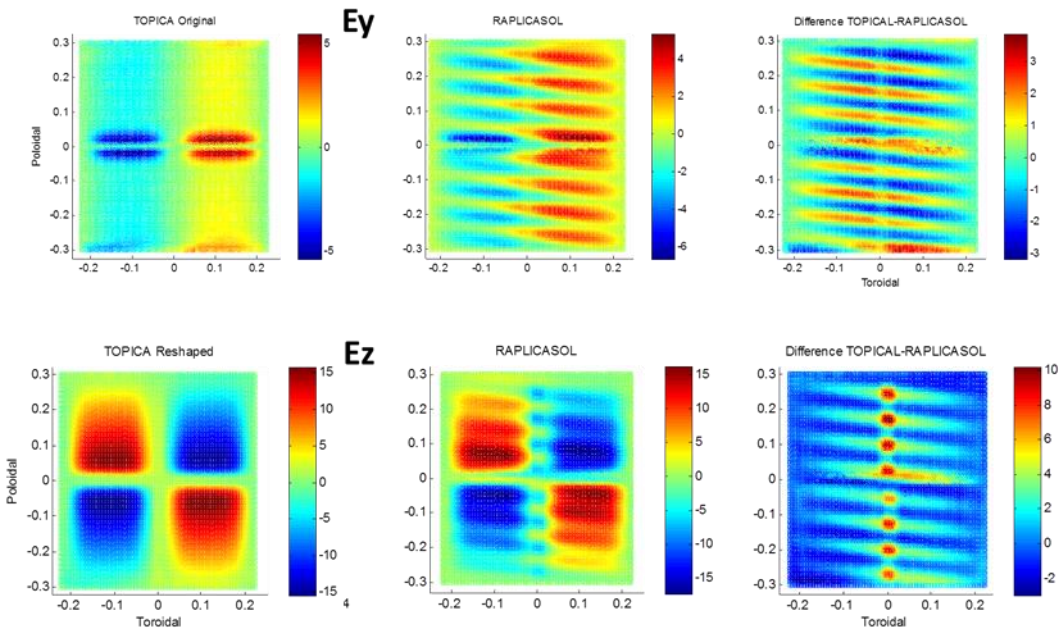

Figure A20: Ey and Ez at the aperture of the 4-strap WEST-like antenna, with dipole excitation (1A on each strap), calculated by RAPLICASOL and TOPICA. $D_{vac} < 2mm$!

During gas puff experiments, the profiles from the reflectometry almost do not change along the valve and injection rate scans. We consequently did not make any simulation since no significant displacement of the cutoff layer was observed on any profile (Fig. A21a and c). Only during the scan of the distance strap-cutoff by moving the plasma away from the antenna did we observe a slight movement of the cutoff layer, even if the effect on density of plasma moving away from the antenna is mitigated by a constant increase in the density similar as during gas puff experiments.

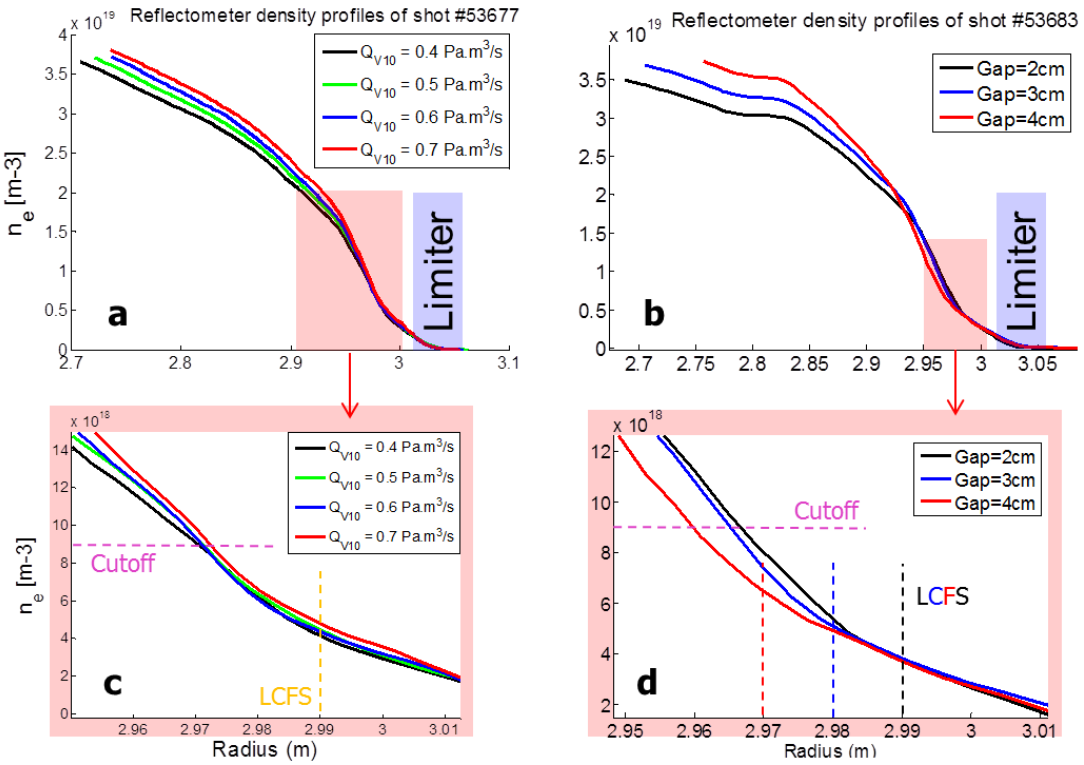

Figure A21: Density profiles from reflectometry are superposed for different cases: (a) different fueling rates on V10 and (b) different distances strap to separatrix (gap), and respective zooms in the edge region that matters the most for the ICRF coupling (c) and (d).

6. Calculations with SSWICH

In view of providing an idea about how potentials induced around the antenna structure vary over a phasing scan, DC rectified potentials were computed for each phasing case of Fig.6.3 with SSWICH-SW code [Jacquot 2014], and 2D maps represented on Fig.6.30 were extracted along the limiters' poloidal extent and over a 6cm radial range. Since no 3D model of the EAST I-port antenna exists, calculations were done based on the JET-A2 antenna geometry which is very similar yet about twice bigger as shown in Fig.A22. We acknowledge the different aspect ratio of both antennas that prevents from extrapolating quantitative results with one antenna to the other, yet the qualitative changes along phase scan can be considered as fairly acceptable and common to a wide variety of ICRH antennas.

Fig.A23 shows how DC potential induced in front of an antenna limiter increases over a phase scan going from dipole to monopole. This can be understood thinking in terms of proximity effect [Colas 2017] and compensation of currents induced on limiters [Bobkov 2017]. In the dipole case (180° phasing), currents from adjacent straps both induce currents in opposite directions on limiters which tend to compensate each other. However on the monopole case (0° phasing), current on all straps are in the same direction such that they all contribute to increase induced-currents, therefore leading to stronger potential rectification and impurity production.

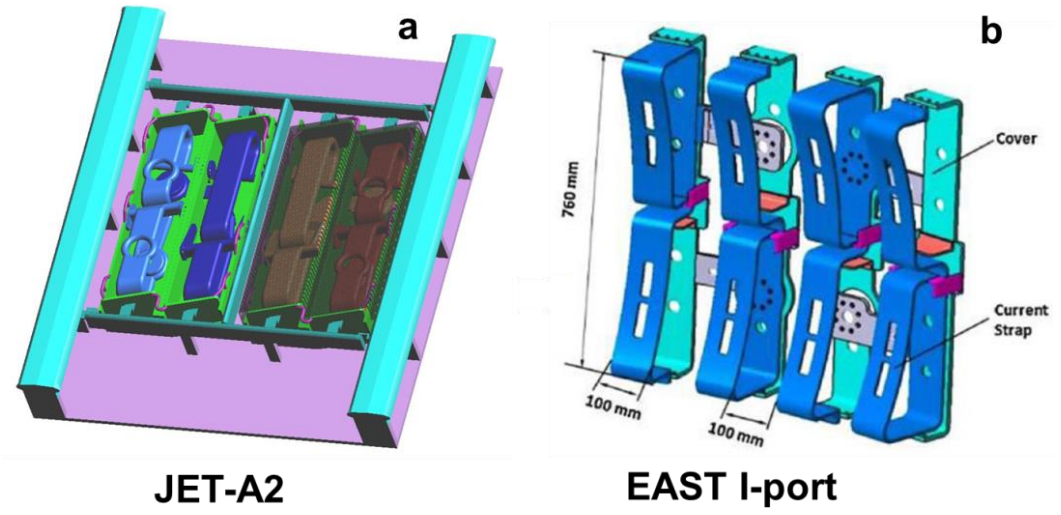

Figure A22: Similar 3D geometries of (a) JET-A2 and (b) EAST I-port antennas

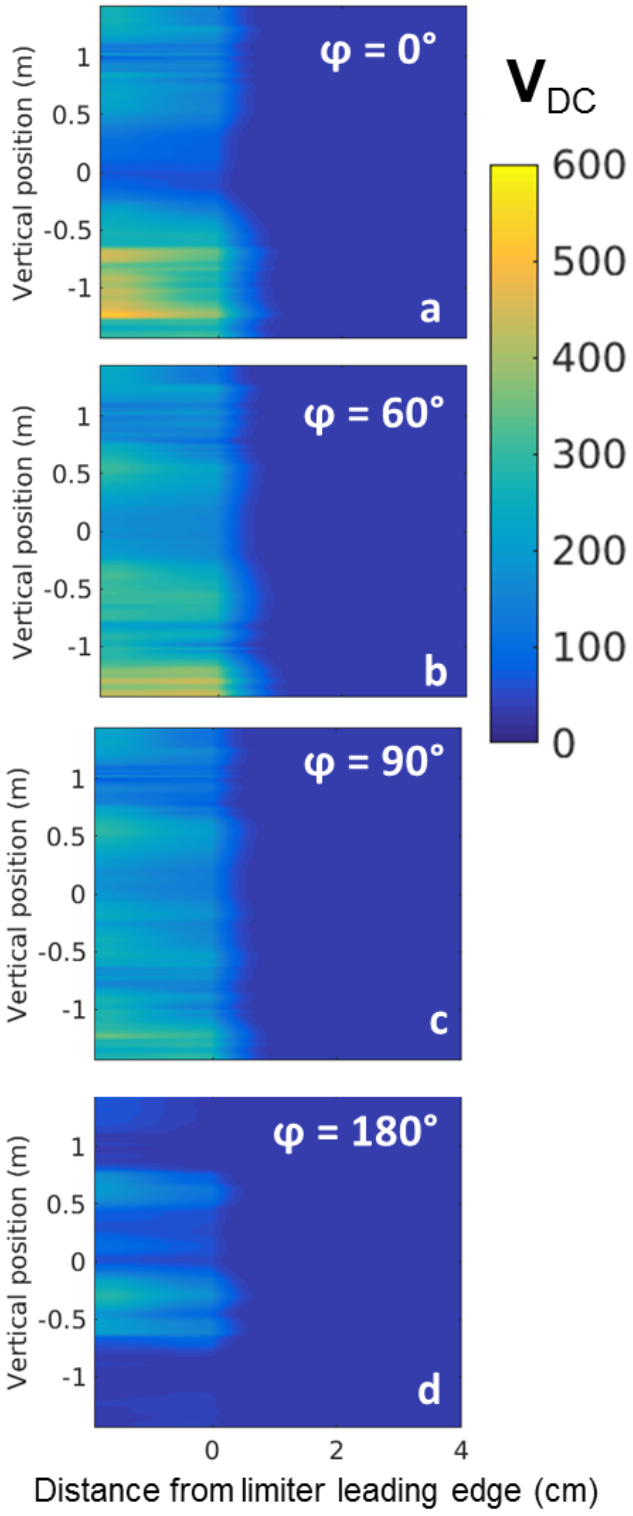

Figure A23: DC rectified potentials were computed along limiter poloidal height and over a 6cm radial range with SSWICH code [Jacquot 2014] for each phasing case of Fig. 6.4, namely (a) monopole (0, 0, 0, 0), (b) (0, π/3, 2π/3, π),

(c) current drive (0, π/2, π, 3π/2) and (d) dipole (0, π, 0, π)

7. Example of disruption caused by ICRF-induced core contamination with tungsten

In this discharge, as soon as ICRF is powered (b), the electron temperature increases (c) sign of efficient plasma heating. Unfortunately, this effect here only lasts about 50ms, then impurity production results in a radiative collapse of the plasma and a sharp increase of the tungsten and silver contents (d) leading to the disruption (a).

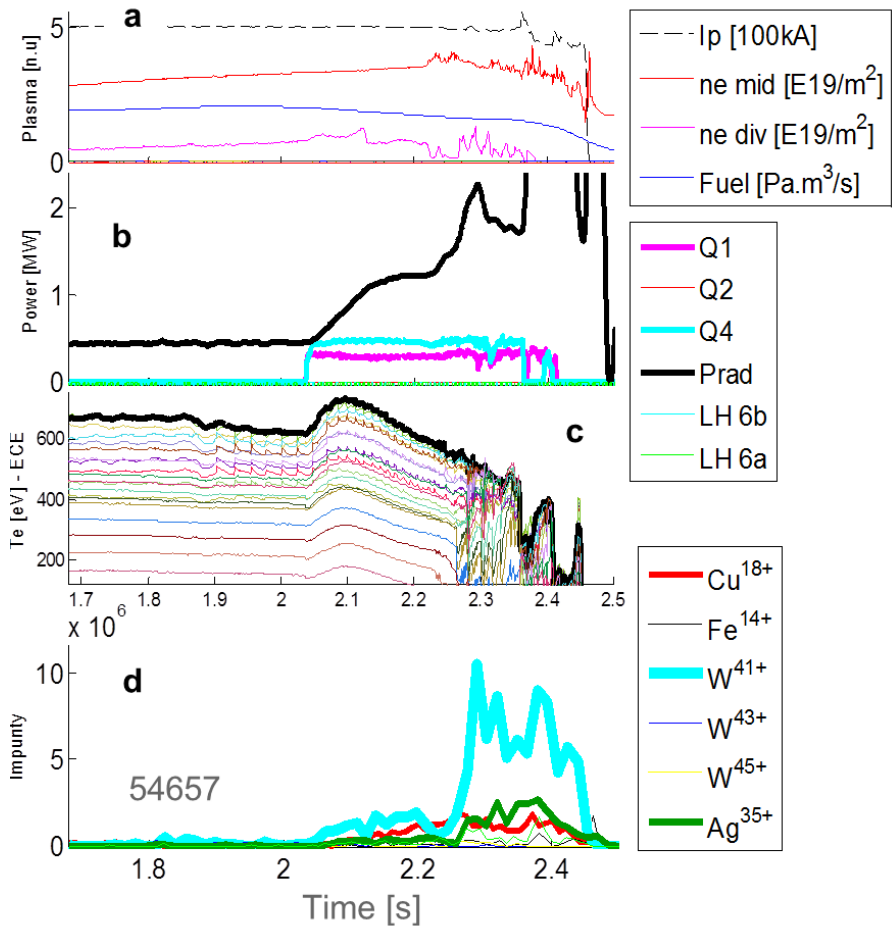

Figure A.24: Example of plasma disruption caused by core contamination with tungsten 200ms after powering ICRH

8. Overview of discharge 54633

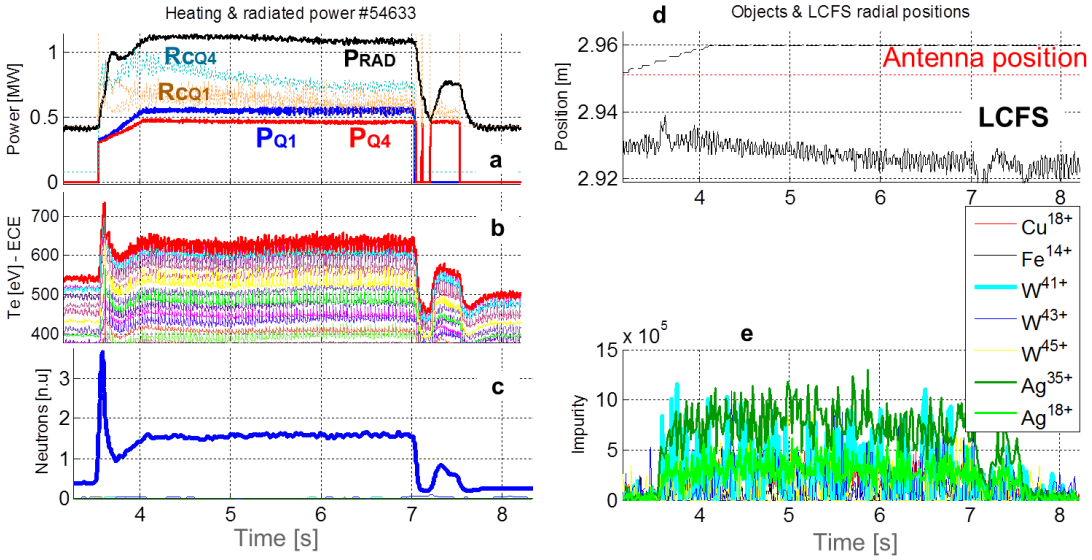

Figure A.25: Overview of discharge 54633

In this discharge, as the plasma moves away from the antenna (d), the coupling efficiency decreases for both antennas (a). Most importantly, we clearly observe the effect of ICRH (a) on the plasma temperature (b) and the neutron rate (c). Unfortunately the effect only last about 200ms, impurities (principally W, Ag and Cu) rapidly penetrate in and cool down the plasma. Note both antennas tripped at 7s resulting in a sharp decrease of Ag production and increase of the temperature. Q4 rapidly recovers and is powered again. During this short phase around 7.5s without Q1, we see that the level of silver almost recovers its previous level, meaning that silver source are mainly related to Q4 antenna which is the last one to have been put in the vessel with a fresh Ag coating. This is rather consistent with Fig.A26 and was further confirmed by a dedicated discharge (Fig.A27).

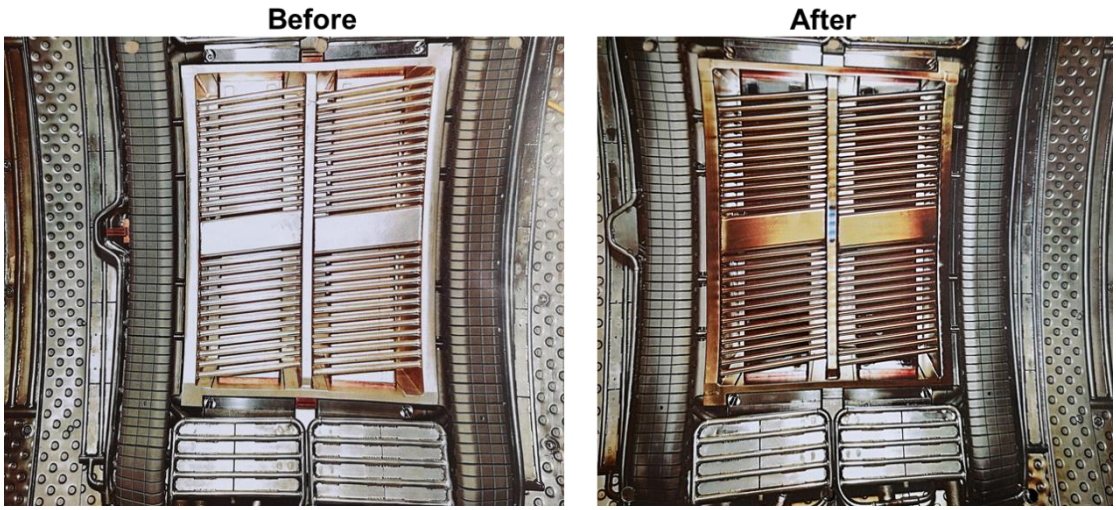

Figure A26: Q1 ICRF antenna before and after the WEST C3b campaign

The silver coated Faraday screen has obviously collected impurity from the plasma. The color can most likely be attributed to copper deposition, but it could also be the result of different oxidation states of tungsten. Antenna structure being at roughly 20°C makes them particularly efficient at trapping impurities, such that the Ag coating of Q1 and Q2 antennas has been slowly covered by other elements, which could explain why during the C4 campaign, presence of Ag in the discharge was most often correlated to the third freshly coated antenna Q4 (Fig.A27).

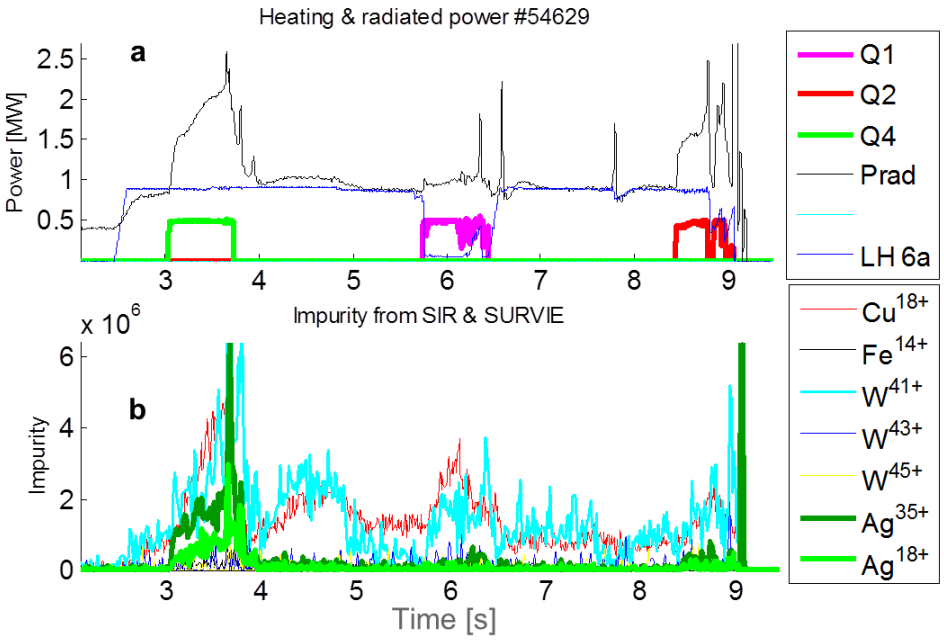

Figure A27: Ag correlation with Q4 antenna during WEST C4 campaign

9. Link between heat fluxes and sputtering in presence of ICRH

Both heat flux and sputtering are phenomena based on a particle flux to a solid surface Γ, but what distinguishes them is mainly the type of particles reaching material surface. Sputtering is entirely due to ions whereas both ions and electrons contribute to heat fluxes. Due to much better transport of electrons than ions in the parallel direction, electrons flow to surface faster than ions, so that the negatively biased material surface repulses electrons and attracts ions. By definition of the Debye length λ_{De}, this effect spreads as far as particles can feel their neighbors-induced electrostatic forces, resulting in the formation of a thin layer (mm) on top of all PFCs across which grow intense electric field; the *thermal sheath*. The effect of the sheath electric field is to slow down electrons, with a net transfer of their energy to ions that are accelerated. Energy balance analysis across the sheath allows deriving heat transmission ratio of each particle, and for a tokamak SOL one can typically expect to have $2/7^{th}$ of heat fluxes carried by electrons and the remaining $5/7^{th}$ by ions [Stangeby 2000]. Such scaling accounts for rather general case since it is based on average result from several models giving different ion distribution functions. One should consequently remain critical using this law which does not hold in any case; electron-dominated regime were for instance observed in Tore Supra [Gunn 2013] and COMPASS [Dejarnac 2018], whereas we now want to prove ICRF can on the contrary lead to ion-dominated regime. In such regime, notions of heat flux and sputtering get correlated, which typically justifies experimentally using infrared camera data to localize impurity sources.

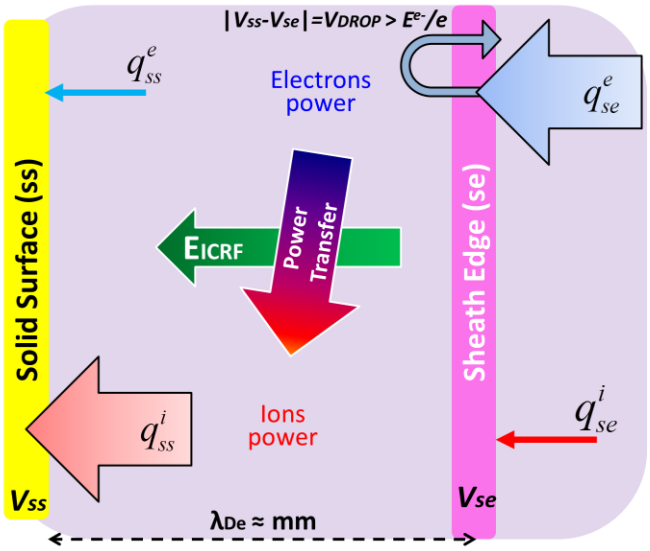

Figure A28: Illustration of energy transfer from electrons to ions across the sheath enhanced by ICRF-induced electric field

For particle species following Maxwellian distribution, heat q induced by a flux Γ are linked by $q = 2kT.\Gamma$ with k the Boltzmann constant and T the species temperature [Stangeby 2000]. Electrons in plasma typically following Maxwellian distribution, they inherently carry $q^e = 2kT_e.\Gamma$. Now considering some electrons flowing towards a solid surface, only those with energies above sheath potential drop V_{DROP} can penetrate and reach the wall, otherwise are reflected. Electrons heat flux at the sheath edge consequently writes $q^e_{se} = \left(2kT_e + \left|eV_{DROP}\right|\right)\Gamma$. For deuterium plasma with hydrogen minority, e.V_{DROP} typically scales as $3kT_e$, such that $q^e_{se} \approx 5kT_e.\Gamma$ (neglecting pre-sheath influence). For ions, Bohm criterion must be fulfilled to penetrate inside sheath region, which sets the minimal Bohm speed bellow which ions are reflected. Simple kinetic approach leads to a Maxwellian drifting at Bohm speed as suitable ions distribution, while more complex models were compared and their results averaged to determine an optimal value of heat power factor leading to $q^i_{se} \approx 2kT_e.\Gamma$ [Stangeby 1986] doing cold plasma approximation. Across the sheath, potential drop accelerates ions and slows down electrons by |e.V_{DROP}| such that at solid surface, ions theoretically end up carrying larger proportion of power heat loads than electrons with respectively $q^i_{ss} = \left(2kT_e + \left|eV_{DROP}\right|\right)\Gamma \approx 5kT_e.\Gamma$ and $q^e_{ss} = q^e_{se} - \left|eV_{DROP}\right|\Gamma \approx 2kT_e.\Gamma$. At this point it is worth

remembering this scaling does not systematically holds true and that big efforts are required to experimentally assess them [Gunn 2013] which are not made in most tokamaks.

Under classic conditions, V_{DROP} is knows under the name of floating potential ϕ_f which perpetually adapts to preserve ambipolarity of charged particles fluxes to the wall:

$$V_{DROP} = \phi_f = \frac{k_B T_e}{2e}.\ln\left(2\pi \frac{m_e}{m_i}\left(1+\frac{T_i}{T_e}\right)\right) \quad \text{(A3)}$$

In presence of ICRH, so called slow waves mode is parasitically excited and the non-null parallel component of their electric field induces the so called RF potential rectification. This effect is specific to the ions frequency waves as ions themselves react to the average field over an RF period, but electrons which gyrofrequency is much higher – above hundreds GHz – react to the instantaneous field. The consequence is an enhancement of charges separation at the edge, basically leading to even higher potential drop in the sheath. This can be shown through calculation of net currents to a solid surface which can be expressed as follow:

$$\tilde{I}(t) = I_{sat}^{+}\left(1-\exp\left(\frac{e}{k_B T_e}\left(\phi_f - \tilde{V}(t)\right)\right)\right) \quad \text{(A4)}$$

Without ICRF $\tilde{V}(t) = V_{DC}$, but with ICRF $\tilde{V}(t) = V_{DC} + V_{RF}\cos(\Omega_{ci}.t)$ with Ω_{ci} and V_{RF} respectively the pulsation (2π.frequency) and amplitude of the waves. Do to non-linearity of the expression, averaging current to the wall over an RF period leads to the appearance of an extra potential term:

$$\bar{I} = I_{sat}^{+}\left[1-\exp\left(\frac{e}{k_B T_e}\left(\phi_f + V_b - V_{DC}\right)\right)\right] \quad \text{(A5)}$$

With

$$V_b = \frac{k_B T_e}{e}\ln\left(I_0\left(\frac{eV_{RF}}{k_B T_e}\right)\right) \quad \text{(A6)}$$

And I_0 Bessel function of order zero. Everything happens as if the wall already biased at the floating potential, additionally receives the influence of ICRF such that $V_{DROP} = \phi_f + V_b$. For stable antenna loading, V_b increases with RF power. It has been shown that beyond some critical values of power and density, potential can be

enhanced of several hundreds of volts, way above thermal sheath induced floating potential $\phi_f \approx 3kT_e \leq 30V$ [Ochoukov 2014]. Thinking back in terms of heat fluxes, since electrons deceleration and ions acceleration across the sheath will be much stronger with increasing ICRF power, heat power transmission will dramatically tend to ion-dominated regime:

$$q_{ss}^{Tot} \xrightarrow{V_{RF}\uparrow} q_{ss}^{i} \tag{A7}$$

Based on empirical observations mostly with infrared cameras in several tokamaks like Tore Supra and JET, efforts were made to determine how RF-induced heat loads may scale with RF and SOL plasma parameters [Colas 2003] [Colas 2009]. Linear dependence with voltages on straps and local density at limiter was also established in another study in Tore Supra $q^{RF}(MW/m^2) = 9.10^{-4}.n_e^{\lim}(10^{19}m^{-3}).V_{strap}^2(kV)$ [Corre 2012]. Due to inherent non-linearity of potential rectification and existence of several parameters threshold, it is important not to take those scaling for granted as none can yet pretend to hold universally over any parameters ranges, which is also the case of physical sputtering changing non-linearly with ions impact energy (Fig.2.9).

Taking the most widespread example of tungsten erosion Γ_W by deuterium ions Γ_D, the sputtering yield Y_{eff} represents the probability that a deuterium ion frees a tungsten atom from the surface, such that $\Gamma_W = \Gamma_D . Y_{eff}$. Sputtering yields depend on which ions bombard which target with which impact energy and angle of incidence. Existence of energy threshold bellow which no sputtering can occur and above which yields increase dramatically is probably what make impurity sources characterization so complex. Around this threshold energy, very little changes in plasma conditions – typically sheath potential drop – can locally result in very sharp increase in impurity production as shown on Fig.1 of [Wukitch 2013] and Fig.2.9. In discharges with ICRH, this behavior is very likely to affect regions magnetically connected to active antenna, where intense potential rectification across the sheath may suddenly allow incoming ions to sputter atoms. This critical regime can be roughly predicted by scaling laws as the one provided by [Myra & D'Ippolito 2008 PRL] and experimentally applied in [Ochoukov 2014], but estimating such parameter requires to know precisely local plasma potential and density, which is therefore not practical for "blind" determination of impurities sources. Furthermore considering the highly

non-linear behavior of sputtering, itself function of fluctuating quantities, one can even wonder rather if visible spectroscopy temporal resolution is systematically appropriated to impurity sources characterization. This question among others was addressed and partially answered under [Reiser 2017] in view of comparing simulation results with optical spectroscopy.

In Fig.A29 and A30, the analogy between infrared data and visible spectroscopy is illustrated respectively nearby antenna limiters and in the divertor region. We acknowledge that these comparison are far from straightforward and would like to stress their lack of appropriate proof that could only be provided if experiment could have actually been dedicated to this topic which was not retained as a priority for WEST objectives. Maybe in the future stronger proofs will be collected and make the object of a publication in a journal. So far these observations are consistent with theoretical expectations and will hopefully motivate dedicated experiments. We show that on ICRF antennas similar patterns are indeed observed on infrared (Fig.A29a) and visible spectroscopy (Fig.A29b) data. Beyond RF sheath, we are so far not able to tell exactly which physical phenomenon is dominating the interactions in different regions of the antenna. We however observe that both for Q2 and Q4 antennas, most observations are usually made on the right limiter in similar poloidal locations. While RF sheaths are known for exciting mainly corners of antennas, the enhanced interaction at the mid-plane is more peculiar. We think it could be the result of a stronger curvature of the plasma than the antennas (Fig.A29c), or the result of large septum at the mid-plane.

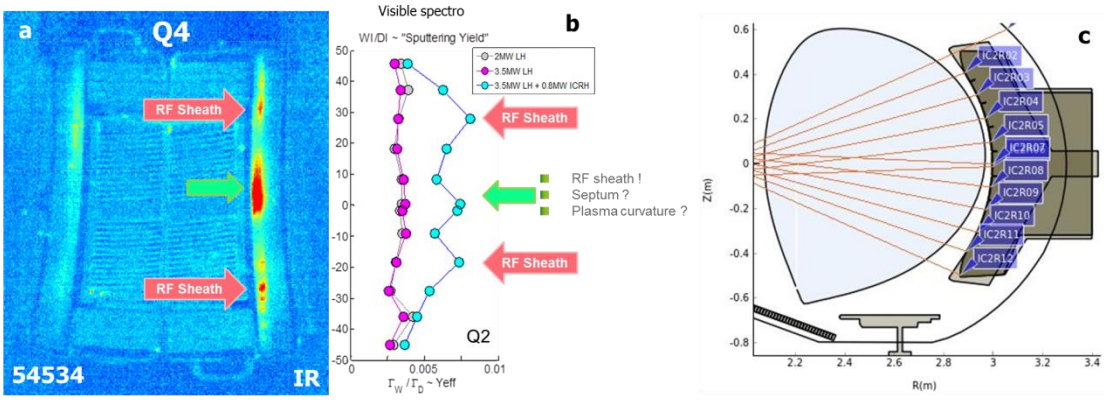

Figure A29: Analogy between poloidal patterns observed on an active ICRF antenna by infrared camera (T° proxy of heat loads) and visible spectroscopy (effective sputtering yield from Fig.6.19b and shot 53923).

As far as the divertor region is concerned, the setting of visible spectroscopy unfortunately was not monitoring the outer target of the divertor which is the one of interest to make analogy with infrared data because it generally receives stronger fluxes. We can still plot profiles along both outer and inner targets of respectively the perpendicular heat fluxes from infrared data inversion (Fig.A30a) and tungsten fluxes deduced from visible spectroscopy data (Fig.A30b), with (blue) and without (red) ICRH during the discharge 53923. Despite these profiles do not correspond to the same divertor targets, they behave similarly with when applying ICRH (in this discharge ICRF antenna were not connected to the divertor). This was most likely the result of large power losses in radiation during the ICRF pulse (over 100% ICRF power radiated, cf. Fig.6.2b). Even if the bolometer is perturbed by Q2, there are several evidence that impurity production during Q2 pulses increases almost always consistently with the radiated power. An alternative could be to also look at the Soft X-Ray signals and find that these also agree fairly well.

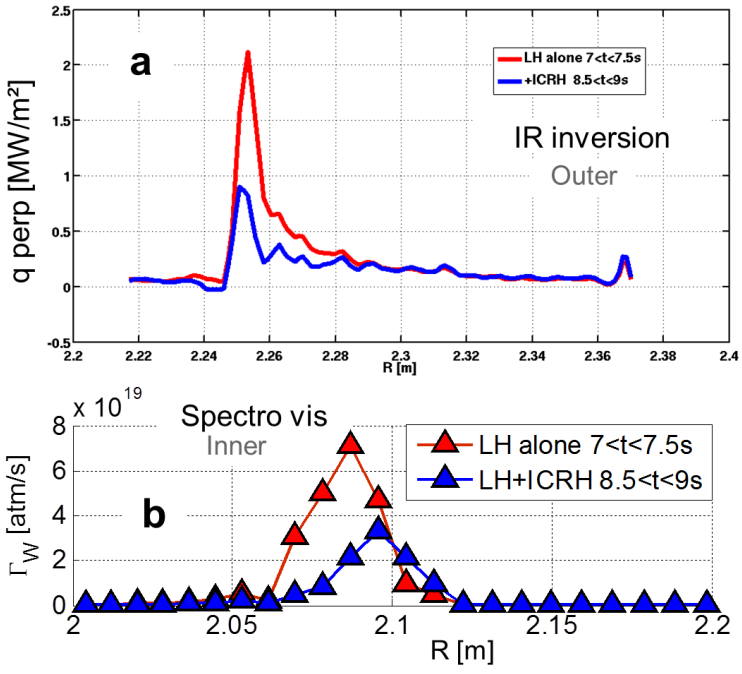

Figure A30: Perpendicular heat flux estimated with IR along the lower divertor outer target (courtesy of N. Fedorczak) and (b) W sources on the inner target with (blue) and without (red) ICRH during the discharge 53923 which overview is given in Fig.6.2.

10. Isotopic ratio measurement in the edge with Hα and Dα lines fitting

The isotopic ratio (H/H+D) indicates the ratio of hydrogen compared to deuterium in a discharge. It can be either assessed by mass spectroscopy (which temporal resolution is usually low) or with visible spectroscopy which is the approach explained here. In WEST, lines of sights can point at different objects (Fig.A.31) as explained in section 4.3.2.2, and different spectroscopes (of essentially different wavelength resolution) can be used to look through the different lines depending on experimental needs. Instead of looking at a wide wavelength range to see many different species by modest resolution (1Å), measuring the isotopic ratio requires focusing on the Hα (6562,1 Å) and Dα (6561 Å) line with large spectral resolution (0.05Å) in order to capture the Zeeman effect (https://en.wikipedia.org/wiki/Zeeman_effect) leading to a splitting of the Dα and Hα lines into several components in the presence of the static magnetic field. A triplet is then observed for both cold and hot populations for each species and fitted by combining several Gaussians together (Fig.A32). Despite the time resolution of the spectroscope if pretty low (0.5s), the fitting algorythm takes time such that this treatment is only applied to two or three lines of sights as shown typically on Fig.A31 and A32.

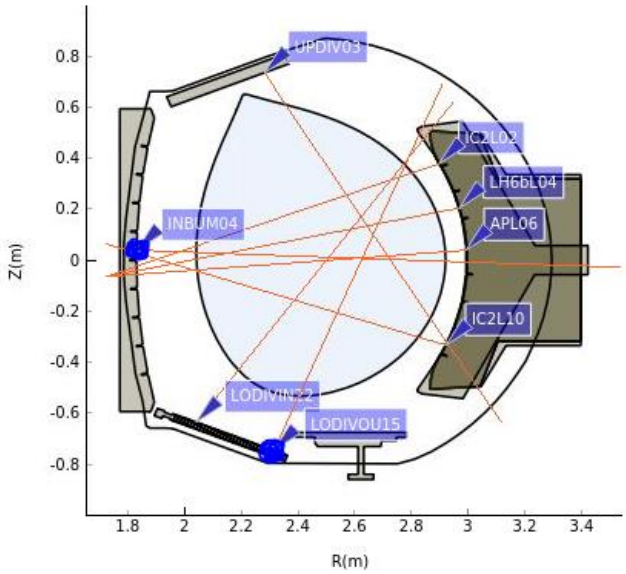

Figure A31: Some of the 240 visible spectroscopy lines of sights of WEST, with the two lines used by default for isotopic ratio measurement enlightened with blue dots

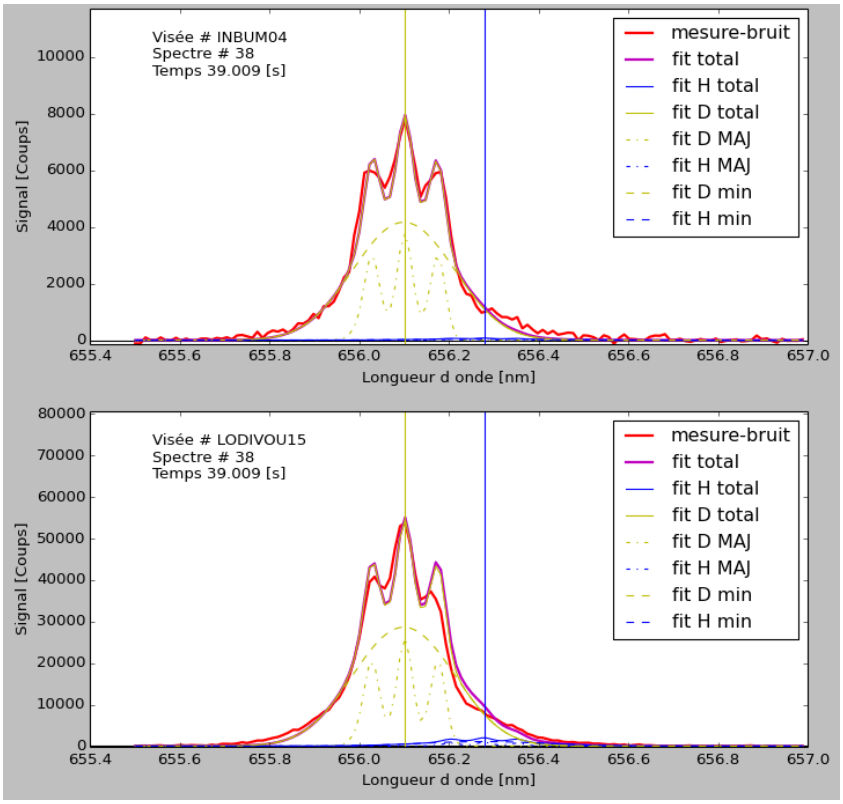

Figure A32: Spectra fitted respectively on the inner bumper at the high field side wall (INBUM04) and on the lower divertor target (LODIVOU15) (#53458)

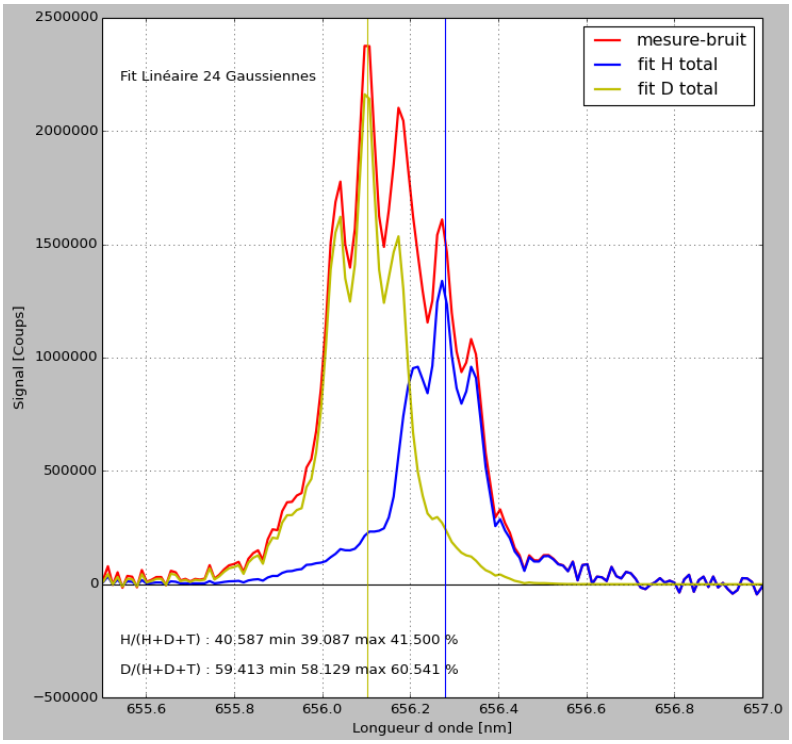

Figure A33: Spectra fitted respectively on the inner bumper at the high field side wall (INBUM04) and on the lower divertor target (LODIVOU15).

The isotopic ratio is then assessed by taking the ratio between the integral of the hydrogen over the deuterium triplets. In Fig.A32, note that the hydrogen (blue curve centered on 656.21 Å) was really low compared to the deuterium, which was in the case of very small hydrogen concentration. Fig.A33 provides another example of a discharge with over 40% hydrogen, such that the triplet on the right (blue) becomes comparable to the one on the left (red). Note in Fig.A32 that the signal on the lower divertor target (LODIVOU15) was higher than on the inner bumper at the high field side wall (INBUM04), which may lead to CCD camera saturation (~2.2 10^5 counts) if the time resolution is too low. This effect was first observed in some discharges when the application of ICRH induced the saturation of the camera. In practice this saturation effect looks like an increase of the right part of the line as shown in spectra b, c, d and e in Fig.A34. Of course in these cases, any attempt to post process the spectra in order to estimate the isotopic ratio would lead to wrong results. Despite the absence of meaning behind these spectra shapes, the fact that this occurs in different region of the vessel for different plasma currents (magnetic connections) is an interesting information. Such observation is likely to be the result of a change in particle fluxes on the PFCs, but the physical cause is still not clearly understood and could either be related to transport, confinement, ripple losses and so on. Without understanding this peculiar observation, it is so far hard to predict what its application

could be, but it clearly gives ununderstood information that worth beign further investigated.

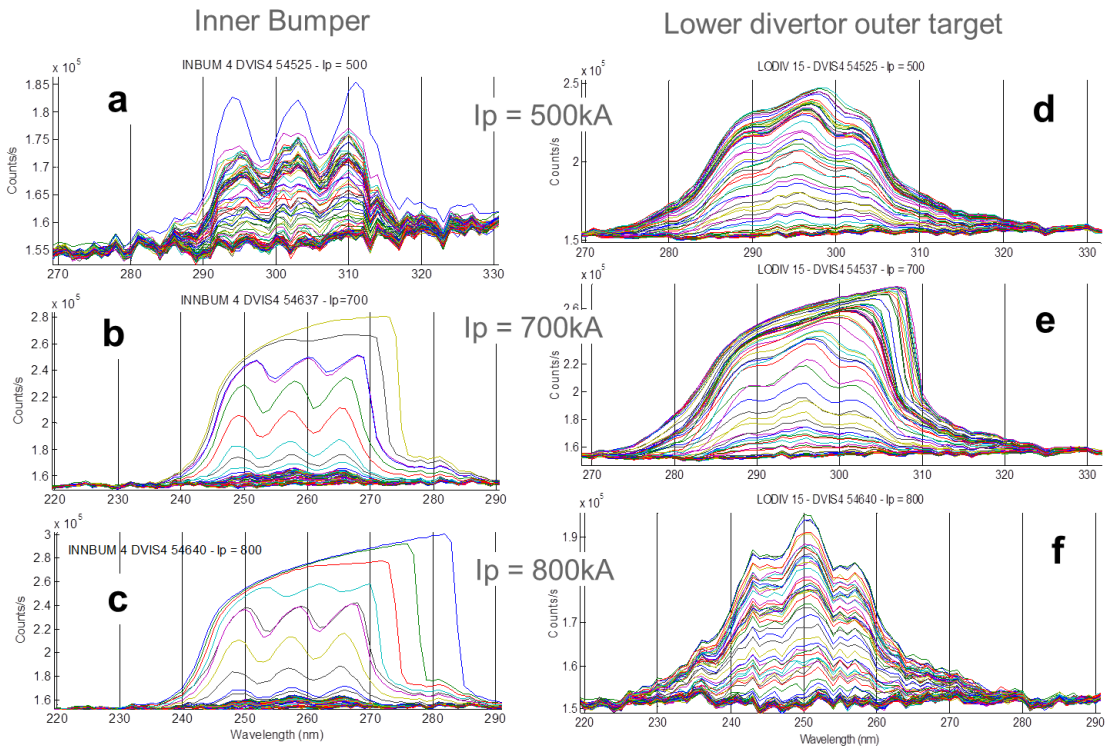

Figure A34: Spectra showing Hα and Dα lines on both (a,b,c) the inner bumper and (d,e,f) the lower divertor outer target, for different times of three ICRF-heated discharges with different plasma currents

11. ICRF wave properties in EAST and WEST

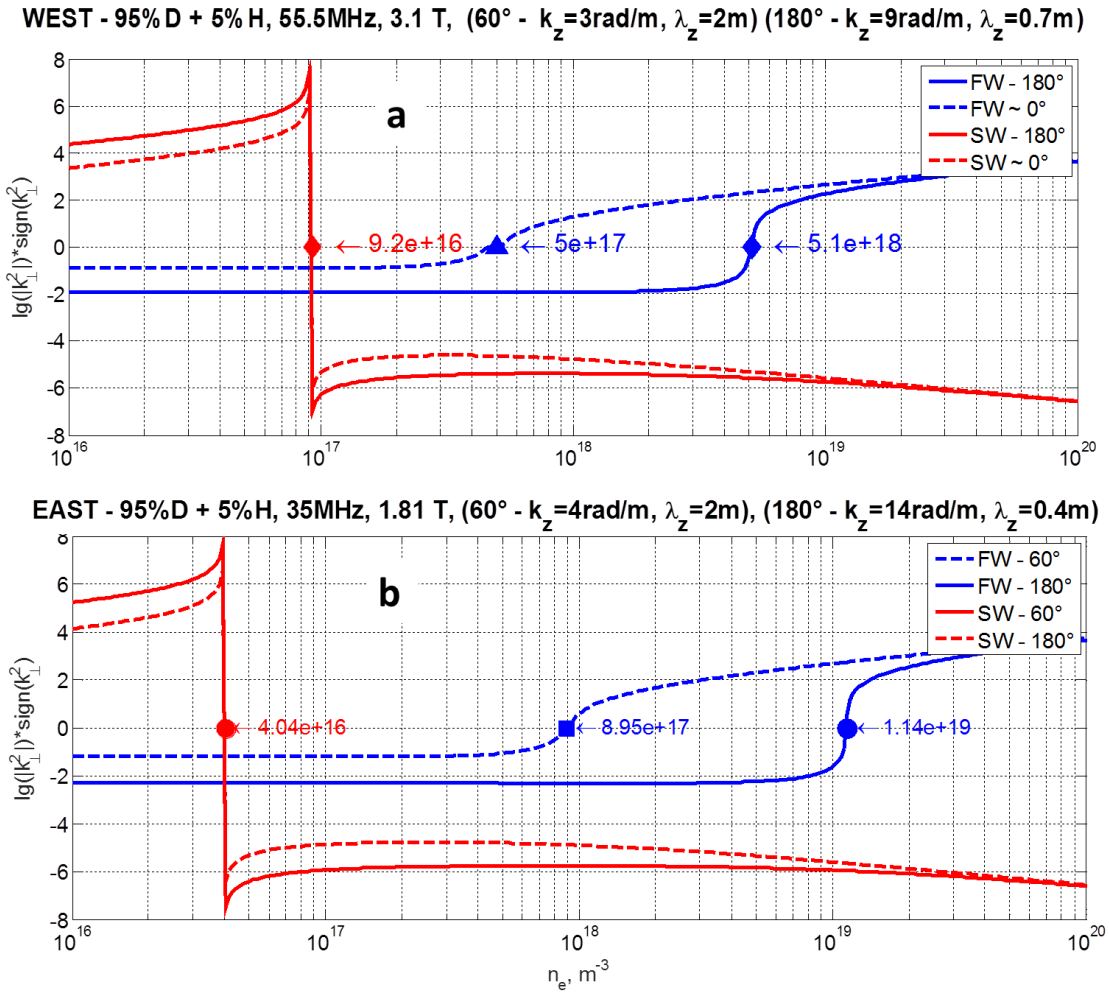

Figure A35: ICRF waves properties in EAST (a, b, c) and WEST (d, e, f).

We see that SW is not propagative anymore above $10^{17}m^{-3}$. Also, from the coupling perspective, we clearly see the interest of working at low $\boldsymbol{k}_{\parallel}$ (or phasing closer to monopole 0° than dipole 180°) since the FW cutoff generally drops of an order of magnitude. However we have shown that this trick is not a good thing in terms of impurity production. While phasing control is known to be inaccurate in EAST since no feedback of measurement made close to the antenna are used to control generator phasing [C. Zhao 2018], we believe we are generally close to the 60° phasing case. It is therefore clear that a real dipole phasing would induce a significant drop in the coupling efficiency. In WEST, most efforts have been put in priority to optimize the matching of the antennas to the cost of accurate phasing control. Recently (September 2019), improvements in phase measurements have been made,

such that the power fraction radiated in L-mode decreased from about 80% in the past down to about 50% now. This is likely an indication that phasing might have deviated from dipole in the past, leading to abnormally high levels of impurity and radiation [Bobkov 2019]. When changing phasing from dipole to monopole (for instance of Q2 antenna), we observe a large increase of local W sources on limiters, while divertor sources only slightly increase (Fig.A36). Still, despite progress made on Q2 and Q4 antennas, Q1 phasing control is still inaccurate, such that the importance of working with accurate phasing can be illustrated by looking at the stronger influence that Q1 antenna has on impurity production compared to others antennas (Fig.A37). The excessive influence of Q1 on Cu is also due to their proximity and tight magnetic connection. This will be further documented in the future, but already clearly constitutes a key step in making ICRF compatible with high power long pulse operations in H mode.

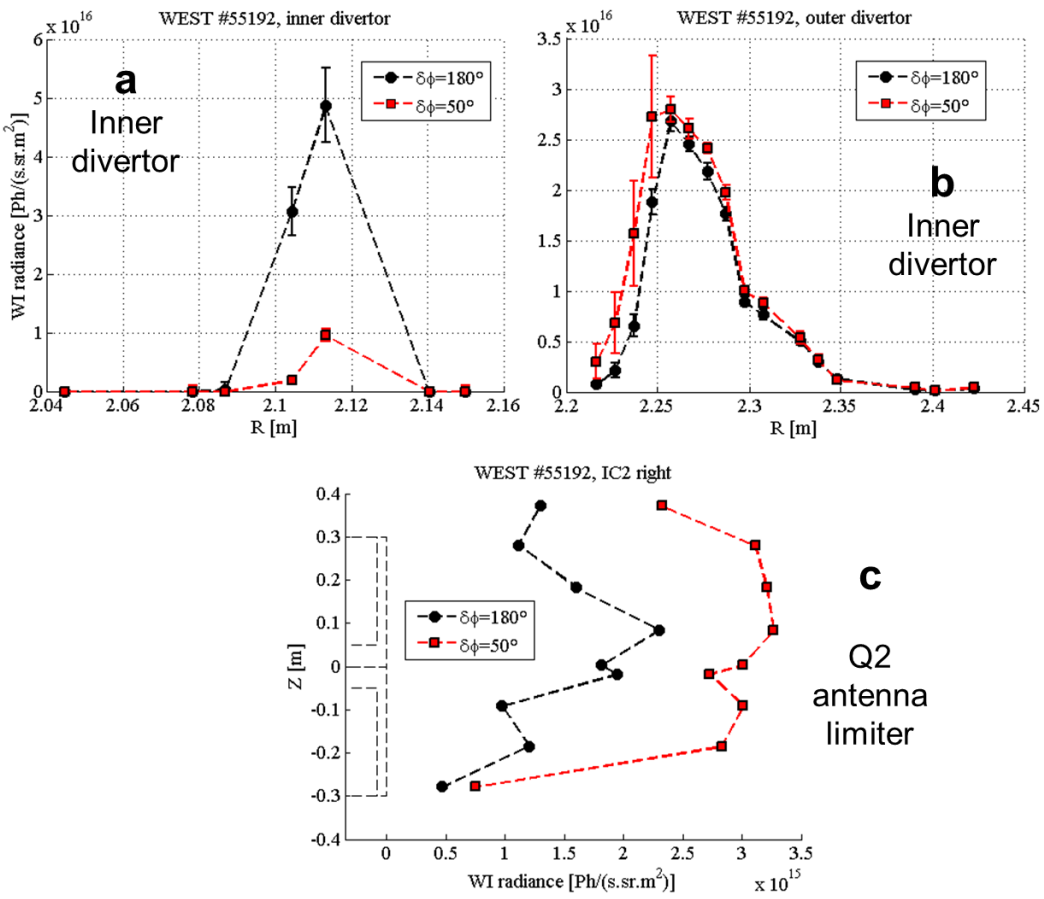

Figure A36: W sources profiles along divertor (a) inner and (b) outer targets and (c) Q2 limiter when changing Q2 phasing from dipole (180°) down to 50° phasing.

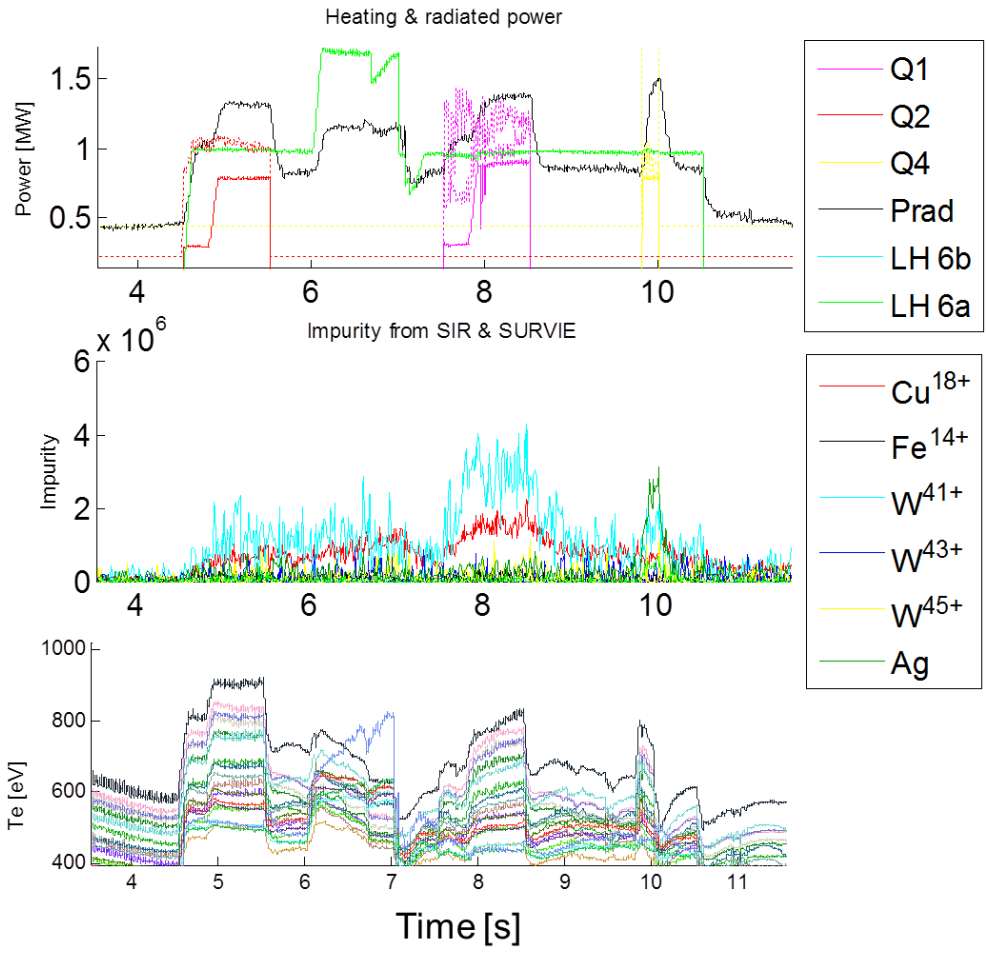

Figure A37: Overview of WEST discharge 55216 showing the both the largest influence of Q1 on impurity productions due to poor phasing control, and the large influence of Q4 antenna on Ag content as discussed in Annex 8.

Bibliography

[ANSYS HFSS] Ansoft, ANSYS HFSS, 3D Full-wave Electromagnetic Field Simulation (2014-2015), U4L http://www.ansoft.com/products/hf/hfss/

[Antar 2001] G.Y. Antar et al., Phys. Rev. Lett. 87, 065001 (2001).

[Baschetti 2018] S. Baschetti – Journal of Physics Conference Series 1125(1):012001

[Basiuk 2004] V. Basiuk et al. Nucl. Fusion 44 (2004) 181–192

[Becache 2003] E. Becache et al. Stability of perfectly matched layers, group velocities and anisotropic waves. J. Computational Physics, 188, 399-433, July 2003.

[Bécoulet 2002] M. Bécoulet et al. Physics of Plasmas, 2619 (2002)

[Berenger 1994] J. Berenger, Journal of computational physics 114,185 (1994)

[Bibet 1995] P Bibet et al. 1995 Nucl. Fusion 35 1213–23

[Bilato 2004] R. Bilato et al. 31st EPS Conference on Plasma Phys. London, 28 June - 2 July 2004 ECA Vol.28G, P-5.164 (2004)

[Bobkov 2010] V. Bobkov et al. 2010 Nucl. Fusion 50 035004

[Bobkov 2013 NF] V. Bobkov et al. Nucl. Fusion 53 (2013) 093018

[Bobkov 2013 JNM] V. Bobkov et al. Jour. of Nucl. Materials 438 (2013) S160–S165

[Bobkov 2015] V. Bobkov et al. AIP Conference Proceedings 1689, 030004 (2015);

[Bobkov 2017 RFPPC] V. Bobkov et al. EPJ Web of Conferences 157, 03005 (2017)

[Bobkov 2017 NME] V. Bobkov et al. Nucl. Mat. and Energy 12 (2017) 1194–1198

[Bobkov 2017 PPCF] V. Bobkov et al. Plas. Phys. Control. Fusion 59 (2017) 014022

[Bobkov 2019] V. Bobkov et al. Nucl. Mat. and Energy 18 (2019) 131–140

[Bourdelle 2015] C Bourdelle et al, Nuclear Fusion 55 (2015) 063017

[Brambilla 1989] M. Brambilla et, Plasma Phys. Control. Fusion 31(723) 1989

[Brambilla 1999] M. Brambilla, Nucl. Fusion 38 (1998) 1805

[Brezinsek 2011] S. Brezinsek Phys. Scr. T145 (2011) 014016

[Brezinsek 2017] S. Brezinsek et al 2017 Phys. Scr. 2017 014052

[Brezinsek 2019] S. Brezinsek et al 2019 Nucl. Fusion 59 096035

[Bufferand 2019] H. Bufferand et al. Nucl. Mat. Ener, 2019

[Bures 1988] M. Bures 1988 Plasma Phys. Control. Fusion 30 149

[Bures 1992] M. Bures 1992 Nucl. Fusion 32 539

[Butler & Kino 1963] H. S. Butler & G. S. Kino The Physics of Fluids 6, 1346 (1963)

[C.M.Qin 2015] Qin Chengming et al. Plas. Sc. and Tech., Vol.17, No.2, Feb. 2015
[Chabert 1969] Physics of Radio-Frequency Plasmas - Pascal Chabert, Nicholas Braithwaite ISBN 978-0-521-76300-4
[Chodura 1982] R. Chodura. The Physics of Fluids 25, 1628 (1982)
[Clairet 2004] F. Clairet et al. Plasma Phys. Control. Fusion 46 (2004) 1567–1580
[Colas 2003] L. Colas et al. Nucl. Fusion 43 (2003) 1–15
[Colas 2007] L Colas et al. Plasma Phys. Control. Fusion 49 (2007) B35–B45
[Colas 2007] L. Colas et al Journal of Nuclear Materials 363–365 (2007) 555–559
[Colas 2009] L Colas et al. AIP Conference Proceedings 1187, 133 (2009)
[Colas 2013] L. Colas et al. Journal of Nuclear Materials (2013) 438:S330–S333
[Colas 2014] L. Colas et al. AIP Conference Proceedings 1580, 259 (2014)
[Colas 2017] L Colas et al. Plasma Phys. Control. Fusion 59 (2017) 025014
[Colas 2018] L. Colas et al. EPS 2018 proceedings
[Colas 2019] L. Colas et al, "First application of ICRF waves on WEST plasma scenario", AIP Conference Proceedings RFPPC 2019
[Corre 2012] Y. Corre et al. Nucl. Fusion 52 (2012) 103010
[Cziegler 2012] I. Cziegler et al 2012 Plasma Phys. Control. Fusion 54 105019
[Cziegler 2012] I. Cziegler et al, Plasma Phys. Control. Fusion 54 (2012) 105019
[Decker 2011] J. Decker 2011 Nucl. Fusion 51 073025
[Dejarnac 2018] R. Dejarnac et al 2018 Nucl. Fusion 58 066003
[DEMO] http://fusionforenergy.europa.eu/
[Dumont 2009] R. Dumont, Nuclear Fusion 49, 075033 (2009)
[Dumortier 2015] P. Dumortier and A.M. Messiaen, "ICRH Antenna Design and Matching", Carolus magnus 2015 proceedings
http://juser.fz-juelich.de/record/283582/files/Energie_Umwelt_298.pdf
[Dux 2007] R. Dux et al. Journal of Nuclear Materials 363–365 (2007) 112–116
[Dux 2007] R. Dux et al. Journal of Nuclear Materials 363–365 (2007) 112–116
[Dux 2009] R. Dux et al. Journal of Nuclear Materials 390–391 (2009) 858–863
[Dux 2009] R. Dux Journal of Nuclear Materials 390–391 (2009) 858
[E.H.Kong 2013] E. H. Kong et al 2013 Plasma Phys. Control. Fusion 55 065007
[E.H.Kong 2013] E. H. Kong et al 2013 Plasma Phys. Control. Fusion 55 065008
[Ekedahl 2009] A Ekedahl et al 2009 Plasma Phys. Control. Fusion 51 044001
[Ekedahl 2015] A Ekedahl et al. Proc. 21st Topical Conf. on RF Power in Plasmas, CA (2015)

[Escarguel 2002] A. Escarguel et al. Contrib. Plasma Phys. 42 (2002) 6-7, 622−629

[Fedorczak 2015] N. Fedorczak et al. Journal of Nuclear Materials 463 (2015) 85–90

[Fedorczak 2015] N. Fedorczak et al. Journal of Nuclear Materials 463 (2015) 85–90

[Fedorczak 2019] N. Fedorczak et al. PFMC 2019 "Infra-red thermography estimate of deposited heat load dynamics on the lower tungsten divertor of WEST"

[Felici 2011] Federico Felici PhD Thesis on Real-time control of tokamak plasmas http://dx.doi.org/10.5075/epfl-thesis-5203

[Feng 2004] Y. Feng et al. Contributions to Plasma Physics 10.1002/ctpp.200410009

[FusionWiki] http://fusionwiki.ciemat.es/wiki

[G.Z.Zuo 2013] Zuo.G. Z et al. Journal of Nuclear Materials, 438, p. S90-S95 (2013)

[Guilhem 2011] D Guilhem et al. Fusion Eng. Design 86 (2011) 279

[Gunn & Pascal 2011] Gunn J P and Pascal J-Y 2011 Rev. Sci. Instr. 82 123505

[Gunn 2013] J.P. Gunn et al Journal of Nuclear Materials 438 (2013) S184–S188

[Gunn 2016] J. P. Gunn et al J. Phys. Conf. Ser. 700, 012018 (2016)

[H.Mao 2017] H. Mao et al. Nuclear Materials and Energy 12 (2017) 447–452

[Hartmann 2008] D.A. Hartmann. Stellerators. Fusion Science and Technology, 53 (2T), 44-55, Feb 2008. http://www.ans.org/pubs/journals/fst/a_1690

[Helou 2015] W Helou et al. Fusion Eng. Design 96-97 (2015) 473

[Helou 2019] W. Helou et al, "Pre-characterization tests and commissioning of the WEST MW-level load-resilient ICRF launchers" RFPPC 2019

[Helou PhD] Walid Helou PhD Thesis on the "Design and operation of antennas at the ion cyclotron and lower hybrid range of frequencies for nuclear fusion reactors" 2018

[Herrmann 2001] A. Herrmann et ASDEX U Team. ECA, 25A:2109{2112}, 2001

[Hillairet 2015] J. Hillairet et.al, AIP Conf. Proc, 1689, 070005 (2015)

[Hong 2017] R. Hong et al. Plasma Phys. Control. Fusion 59 (2017) 105008

[Ignat 1981] Ignat D.W. 1981 Toroidal effects on propagation, damping, and linear mode conversion of lower hybrid waves Phys. Fluids 24 1110

[ITER] https://www.iter.org/proj/inafewlines/

[J.C.Xu 2016] J.C. Xu et al, Review of Scientific Instruments 87, 083504 (2016)

[J.H.Wang 2017] J.H. Wang et al. Fus. Eng. and Design 122 (2017) 196–203

[J.H.Wang 2018] Jianhua WANG et al 2018 Plasma Sci. Technol. 20 045603

[J.H.Zhang 2017] J.H. Zhang et al. Nucl. Fusion 57 (2017) 066030 (10pp)

[Jacquet 2016] P. Jacquet et al. Nucl. Fusion 56 (2016) 046001

[Jacquinot 1991] J. Jacquinot 1991 Plasma Phys. Control. Fusion 33 1657

[Jacquot 2013] J. Jacquot et.al, PPCF 55 115004 (2013)
[Jacquot 2014] J. Jacquot et al, Phys. Plasmas 21 061509 (2014)
[Jacquot 2015] J. Jacquot et.al, AIP Conf. Proc, 1689, 050008 (2015)
[Kazakov 2015] Yevgen Kazakov, Dirk Van Eester, and Jef Ongena, "Plasma Heating in Present-day and future devices fusion machines", Carolus magnus 2015 proceedings http://juser.fz-juelich.de/record/283582/files/Energie_Umwelt_298.pdf
[Kazakov 2017] Y. Kazakov et al. 2017 Nature Physics
[Kirov 2009] K. K. Kirov - Plasma Phys. Control. Fusion 51 (2009) 04400
[Kočan 2008] M. Kočan et al. Rev. Sci. Instrum. 79, 073502 2008
[Kočan 2009] Martin KOČAN PhD Thesis – "Ion temperature measurements in the scrape-off layer of the Tore Supra tokamak"
[Koch 2008] R. Koch. Fast Particle Heating. Fusion Science and Technology, 53 (2T), 184-193, Feb 2008. http://www.ans.org/pubs/journals/fst/a_1703.
[Koch 2015] R. Koch, "The ion cyclotron, lower hybrid and Alfvén wave heating methods", Carolus magnus 2015 proceedings
[Kong 2013] E H Kong et al 2013 Plasma Phys. Control. Fusion 55 065007
[Kostic 2018] A. Kostic et al. Rev Sci Instrum. 2018 Oct;89(10):10D115.
[Krasheninnikov 2001] S. I. Krasheninnikov, Phys. Lett. A 283, 368 (2001).
[Kubic 2013] M. Kubic et al. Journal of Nuclear Materials 438 (2013) S509–S512
[Kubic 2013] M. Kubic et al. Journal of Nuclear Materials 438 (2013) S509–S512
[L.F.Lu 2017] L. Lu et al, Plasma Phys. Control. Fusion 60 (2018) 035003
[L.Zhang 2015] L. Zhang et al 2015 Rev Science Instruments, 123509
[Lancellotti 2006] V. Lancellotti et Nucl. Fusion 46(2006) S476-S499
[Lawson 1957] J.D. Lawson. Some Criteria for a Power Producing Thermonuclear Reactor. Proc. Royal Physical Society B, 70, 6-10, 1957.
[Lerche 2008] E. Lerche et al. Plasma Phys. Control. Fusion 50 (2008) 035003
[Lerche 2009 AIP] E. Lerche et al AIP Conference Proceedings 1187, 93 (2009)
[Lerche 2009 PPCF] E. Lerche et al. 2009 Plasma Phys. Control. Fusion 51 044006
[Lerche 2015] E. Lerche et al, Journal of Nuclear Materials 463 (2015) 634–639
[Lerche 2016] E. Lerche et al 2016 Nucl. Fusion 56 036022
[Lerche 2019] E. Lerche et al. 2019 RF topical conference – «ICRH options for JET-ILW DTE2 operation »
[Lipshultz 2001] B. Lipschultz, D.A. Pappas, et al, Nucl. Fusion 41, p.585 2001
[Louche & Koch 2015] F. Louche and R. Koch, "The Coupling of Electromagnetic

Power to Plasmas", Carolus magnus 2015 proceedings

[Lu 2016] L. F. Lu et al Plasma Phys. Control. Fusion 58 (2016) 055001 (13pp)

[M.H Li 2016] M. H. Li et al. Physics of Plasmas 23, 102512 (2016)

[Martin 2017] M.J. Martin et al. PRL 119, 205002 (2017)

[Mayberry 1990] M.J. Mayberry et al. 1990 Nucl. Fusion 30 579

[Messiaen 2010] A. Messiaen et al, Nucl. Fusion, 50(2) 2010

[Messiaen 2011] A. Messiaen et al, Fus. Engineering and Design 86 (2011) 855–859

[Messian & Weynants 2011] A Messiaen and R Weynants 2011 Plasma Phys. Control. Fusion 53 085020]

[Meyer 2016] O. Meyer et al. Rev. Sci. Instrum. 87, 11E309 (2016)

[Meyer 2018] O. Meyer et al. Rev. Sci. Instrum. 89, 10D105 (2018)

[Milanesio 2009] D. Milanesio et al 2009 Nucl. Fusion 49 115019

[Miyamoto 2005] K. Miyamoto, Plasma Physics and Controlled Nuclear Fusion, Springer-Verlag (2005) ISBN 3540242171

[Mück 2005] A. Mück et al . Sawtooth control experiments on ASDEX Upgrade. Plasma Physics and Controlled Fusion, 47, 1633-1655, Oct. 2005.

[Myra & D'Ippolito 2008 PRL] Myra & D'Ippolito PRL 101, 195004 (2008)

[Myra & D'Ippolito 2008 PoP] D.A. D'Ippolito, J.R. Myra, Physics of Plasmas 15, 102501 (2008)

[Myra & D'Ippolito 2009] Myra & D'Ippolito, AIP Conf. Proc. 1580 (2014) 326

[Myra & D'Ippolito 2010] J. R. Myra and D. A. D'Ippolito. Plasma Physics and Controlled Fusion, 52:015003¨C15, 2010.

[Nieuwenhove 1990] R. Van Nieuwenhove et al - Fusion Engineering and Design 12 (1990) 203-207

[Ochoukov 2013] R Ochoukov PhD Thesis "Investigation of Plasma Potential Enhancement in the Scrape-Off Layer of Ion Cyclotron Range of Frequencies Heated Discharges on Alcator C-Mod"

[Ochoukov 2014] R Ochoukov et al Plasma Phys. Control. Fusion 56 (2014) 015004

[Ochoukov 2017] R. Ochoukov EPJ Web of Conferences 157, 03038 (2017)

[Otin 2013] Otin R. 2013 "ERMES: a nodal-based finite element code for electromagnetic simulations in frequency domain" Comput. Phys. Commun. 184 2588–95

[Palkina 1971] L.A. Palkina et al. Zh. Eksp. Teor. Fii. 61, 2319-2325 (December, 1971)

[Parisot 2004] A. Parisot et al. Plasma Phys. Control. Fusion 46 (2004) 1781–1792
[Perkins 1989] F. W. Perkins 1989 Nucl. Fusion 29 004
[Perkins 2012] R. Perkins et al Physical Review Letters 109(4) · July 2012
[Perkins 2017] R. Perkins et al EPJ Web of Conferences 157, 03039 (2017)
[Perkins 2018] R. Perkins et al. 2018 Plasma Phys. Control. Fusion - Accepted
[Pfalzner 2006] Susanne Pfalzner. "An introduction to inertial confinement fusion" (http://kfe.fjfi.cvut.cz/~limpouch/plazma/Pfalzner_Introduction_ICF.pdf)
[Pinsker 2011] R. I. Pinsker et al, AIP Conference Proceedings 1406, 313 (2011)
[Pitts 2013] R. Pitts, ITER full W divertor Final Design Review, June 2013
[Pryor 2011] R.W. Pryor. Multiphysics modeling using COMSOL: a first principles approach. Jones and Bartlett Publishers, 2011.
[Q.P.Yuan 2009] Q. P. Yuan et al 2009 Plasma Sci. Technol. 11 231
[Ragona & Messiaen 2016] R. Ragona and A. Messiaen 2016 Nucl. Fusion 56 076009
[Reiser 2017] D Reiser et al. Phys. Scr. T170 (2017) 014039
[S.Zhang 2014] S. Zhang et al 2014 Plasma Sci. and Technol. 16 311
[Schmitz 2008] O. Schmitz et al 2008 Plasma Phys. Control. Fusion 50 115004
[Scwhob 1987] J.L. Scwhob et al., Rev. Sci. Instr, 1987.
[Sertoli 2017] Sertoli et al. Phys. Plasmas 24, 112503 (2017)
[Sips 2018] A.C.C. Sips et al 2018 Nucl. Fusion 58 126010
[Sorensen 1996] J. Sorensen 1996 Nucl. Fusion 36 173
[Stangeby 1986] Stangeby P C 1986 Physics of Plasma–Wall Interactions in Controlled Fusion ed
[Stangeby 2000] P.C. Stangeby 2000 The Plasma Boundary of Magnetic Fusion Devices - Institute of Physics Publishing Bristol and Philadelph (2000)
[Stangeby 2012] P.C. Stangeby 2012 Nucl. Fusion 52 083012
[Stober 2012] J. Stober – The European Physical Journal Conferences 32:02011
[Stoler 2010] D.P. Stoler, ARIES Meeting May 2010
[Strang & Fix 1973] G. Strang and G. Fix. An Analysis of the Finite Element Method. Prentice Hall, 1973.
[L. Zhang 2015] Zhang et al. Rev. Sci. Instrum. 86, 123509 (2015)
[Tanaka 1996] T. Tanaka 1996 Nucl. Fusion 36 1609
[Thomas 1996] C. E. Thomas 1996 Fusion Technology Vol. 30
[Urbanczyk 2017] G. Urbanczyk et al EPJ Web of Conferences 157, 03057 (2017)
[Urbanczyk 2018] G. Urbanczyk et al. Nuc. Materials and Energy 17 (2018) 274–278

[Urbanczyk 2019] G. Urbanczyk et al 2019 Nucl. Fusion 59 066023

[Van Eester & Lerche 2013] D. Van Eester and E. Lerche. Plasma Phys. Control. Fusion 55 (2013) 055008

[Van Oost 2008] G. Van Oost and E. Rebhan, Fusion Science and Technology, 53 (2T), 16-26, Feb 2008 http://www.ans.org/pubs/journals/fst/a_1687

[Van Wiessener 2011] Van Wiessener et al. Europhysics conference abstracts, Vol. 35G, P5.098, http://ocs.ciemat.es/EPS2011PAP/pdf/P5.098.pdf

[Vdovin 1973] V. Vdovin et al. JETP Letter. 17 (1973) 2

[W.Zhang 2010] W. Zhang et al Rev. Sci. Instrum. 81, 113501 (2010)

[W.Zhang 2016] W. Zhang et al Nucl. Fusion 56 (2016) 036007

[W.Zhang 2017] W. Zhang et al Nucl. Fusion 57 (2017) 056042

[W.Zhang 2018] W. Zhang et al Nucl. Fusion 58 (2018) 126005

[Westerhof 2008] E. Westerhof. Electron Cyclotron Waves. Fusion Science and Technology, 53 (2T), 202-209, Feb 2008 http://www.ans.org/pubs/journals/fst/a_1694

[Weynants 2008] R.R. Weynants. Fusion Machines. Fusion Science and Technology, 53 (2T), 37-43, Feb 2008. http://www.ans.org/pubs/journals/fst/a_1689.

[Wukitch 2004] S. Wukitch et al. Plasma Phys. Control. Fusion 46 (2004) 1479–1491

[Wukitch 2007] S.J. Wukitch et al. Journal of Nuc. Material 363–365 (2007) 491–497

[Wukitch 2009] S. Wukitch et al Journal of Nucl. Materials 390–391 (2009) 951–954

[Wukitch 2012] S. J. Wukitch et al 2012 PSFC/JA-12-45

[Wukitch 2013] Wukitch et al. Phys. Plasmas 20, 056117 (2013)

[Wukitch 2014] S. Wukitch et al APS Division of Plasma Physics Meeting 2014 DPPUO3012W

[X.J.Zhang 2011] X. J. Zhang et al. 2011 Plasma Sci. Technol. 13 172

[X.W.Zheng 2013] X. W. Zheng et al 2013 Plasma Phys. Control. Fusion 55 115010

[X.Zong 2018] Z. Xu et al 2018 Nucl. Fusion 58 016001

[Y.Q.Yang 2017] Y. Q. Yang et al. Plasma Phys. Control. Fusion 59 (2017) 095001

[Z.Chen 2018] Z. Chen et al. Nucl. Sci. Tech. (2018) 29 19

[Z.Xu 2018] Z. Xu et al 2018 Nucl. Fusion 58 016001

[Zhang 2017] W. Zhang et al 2017 Nucl. Fusion 57 116048

.

Acknowledgements

Laurent Colas is by far the person who with I have interact the most all along the thesis, even when I was in China for several months we kept a close contact and he always took time to reply several times per week to the mails I sent him several times per day. When I was in Cadarache, we talked to each other on a daily basis, especially at the beginning and during the period when I spent lots of time on COMSOL trying to get a 3D version of SSWICH which is a great challenge, still on-going. He was very patient with me and several times explained me the same things until I really understood. It was also a great pleasure to be able to freely share opinion and even speculate on original solutions, though he's the kind hard to convince otherwise but with equations, and since I am honestly not the best person at writing them, we made a wonderful team.

This also applies to Wouter Tierens who has become a good friend, our approaches are very complementary, out of the two times I visited him in Garching came two nice papers and quite many ideas to be explored along on-going works. His passion for science and culture in general make any idea subject to discussion while his additional motivation and competence makes most of them come true. A man of high theoretical abilities who I'm always very grateful to work with.

Olivier Meyer is the spectroscopist who has developed the most important diagnostic of my thesis and taught me more than expected about the diagnostic and its data analysis. Despite Olivier left CEA the last year of my thesis, he took time during his last campaign to show me how to operate the visible spectroscopy and change the settings of the lines of sight, which has been very useful during the last campaign, while nobody was personally in charge of operating the diagnostic.

This got me the chance to get involve quite intensely into the maintenance choices on the diagnostic, and assisting mainly Jean-Yves Pascal who was habilitated and in charge of doing modifications. Jean-Yves also does a lot of work for the maintenance and operation of the different probes systems, he explained me many details on the probes systems together with Jamie Gunn, which was very useful for the thesis.

I met Jamie a year before starting my thesis in CEA, at that time asked him the first of a long series of precious advices he gave me since I know him. His first advices helped optimizing the design of the probes I developed in EAST, while he later taught me and proposed to operate the Pecker probes of WEST which has been a

very nice experience and allowed me collecting many interesting sets of data. In the future, I may do a post-doc that would imply keeping working in relatively close collaboration with Jamie; I sincerely hope I will get such a chance.

Corinne Desgranges is Jamie's physical neighbor in WEST control room, and the lady in charge of VUV spectroscopy. Corinne is like Olivier a person who taught me a lot. We even started working all three together for the construction of a spectroscopic database for all discharges. Later with Corinne we developed other tools for UV spectroscopy data treatment and diffusion of data to all WEST user's, facilitating systematic analysis and by then helping the validation of new lines correspondence to an identified species.

Nicolas Fedorczak is the octopus on the middle of all, without any diagnostic out of reach to his tentacles, he undeniably one of the persons to do the most important contributions for WEST, why working with him to analyze several data has been so rewarding. Beyond his exemplary implication in the WEST project, his interests extend to many other topics on which we shared many interesting discussions. I wish to get the chance to keep interacting with Nicolas as much as possible in the future, which might be easy considering the number of topics he's involved in !

Julien Hillairet is somebody … somebody who I had the chance to spend very nice moments with, both in France and China. Julien has been for me like a mentor, who helped me a lot on modelling first, then progressively more and more involved in WEST ICRH system operation, we performed several complementary analysis that together helped understanding better the situation of the ICRF in WEST. Rare is the question that remains unanswered when asked to Julien, great virtue for a researcher.

Giles & Patrick, ion cyclotron waves' masters, active from the tetrodes up to the control room, we owe them the magnificent excitation of RF sheath which motivated this thesis, and now I personally owe them a lot for all their taught me and their positive and steady behaviors in spite of myriads of difficulties.

Jean-Michel has also always been very kind to me, he contributed a lot in making me part of the ICRF team on the middle of which I spent most of my time. Our relation was also strengthened by our common participation in many projects. He gave me many precious advice that help me managing lots of things during my thesis.

Walid Helou sadly jumped across the fence up to ITER in the last year of my thesis, hopefully I had the chance to work with him first on different modelling aspects, and later shared the first three experimental campaigns, during which we interacted daily for getting the best we could out of a busy planning that lead us to work late many times allowing to perform several important advances. Walid has given me numerous advices, his competences are as wide as France, Lebanon and Russia together, may I one day be to his side again in a larger control room …

Yves Peysson has become a very nice friend who with I almost did my PhD,

unfortunately my competences at the time seemed to me miles away from the exigence of the subjects he proposed. Despites this choice, I had the chance to keep interacting with him a lot and even work together on various modelling for EAST.

Marc Goniche has also been a very active colleague both on EAST and WEST experiments analysis, which lead us to interact in different contexts.

Mostly in the last months of the thesis did I interact particularly intensely with Bernard Pégourié who with we made surprising spectroscopic observations which the potential analysis extents may allow monitoring the influence of ICRF on particles transport (cf. Annex 10). Bernard has also taught me a lot about spectroscopy and it will be a pleasure to keep working with him in the future.

Stéphane Heuraux, a professor who deserves his title, rare seems to be the fields that remain mysterious to him. Advices he has for all, and we all listen carefully. Pity Nancy is so far from Cadarache, but I hope we will get to work together again in many on-going collaborations.

Li Jiangang has been my supervisor since I arrived in China for my Master, he invited me in the institute in Hefei for the first time, he received the Chinese title of Yuanshi laoshi during my PhD, as if people doubted how good he is. Professor Li has always been extremelly kind to me, and I reciprocally have always been loyal to him. I completely owe him what I did and where I am now. After the work I did in EAST, people in the best European labs would now be glad to have me as a post-doc, however if Professor Li wishes to continue the adventure we started, I will not doubt for a second and keep working with him as his post-doc to hopefully find a good solution to heat CFETR plasmas. And if this is another success, who knows what can happen next …

People from the ICRH group, Wang Jianhua, Zhang Xinjun, Zhang JiaHui, Qin Chengming, LiuluNan, Zhao Yanpin, Chen Zhao, YuanShuai, who with I interacted for about four years on a daily basis. Diagnostician friends, Yang XiuDa, Zhang Ling, Zhang Heng, Xu JiChen …

I am also deeply grateful to many other colleagues such as Remi Dumont, Alex Grosjean who helped me with modelling and who became a good friend as we shared common experience in China both being part of the same EU-CN collaboration, Remi Guirlet, Yann Core who taught me a lot on spectroscopy analysis and sputtering yield estimations,

Rory Perkins sadly left the field on the middle of my PhD together with his brilliant mentor Joel, fortunately we had several chances to meet and share delighting discussions. Too bad he and his supervisor both left the field so early, while significant improvements have been done by Wouter, Wei Zhang and John Myra in understanding phenomena observed Rory's and Joel's past observations on NSTX.

Riccardo Ragona also had the chance to learn from one of the best pioneer of ICFR, André Messiaen, and fortunately both remain in the field ! I very much like working with Riccardo whose practical approach is somehow similar to mine. I wish we keep interacting as we do and that I can do my best to help him succeeding in undeniably the most promising and ambitious project that may one day shaken the ICRF community by providing with an engineering concept solving the two biggest problems of ICRF addressed in this thesis. May you win that silly trade-off game!

Mariia Usoltceva and her Rrrussian temper not less tough than mine, working in different labs but sharing the same supervisor, I'm very glad we had the chance to build a frrructful connection and keep exchanging, debating, and fighting for the best.

Ernesto Lerche, undeniably one of the best researchers of the field, which implication in everything he touches is a gift. Same with Dirk who I hope have more chances to interact with in the future. They taught me how to use TOMCAT, the code they developed together, and had many more chances to interact with Ernesto who came several times in WEST to perform some of the most interesting experiments on which relies this thesis.

Volodimir Bobkov is also one of the most brilliant RF physicists who came up with one of the best antenna design ever achieved. Having been several times to Garching and even envisaged the possibility of doing a post-doc there, Vladimir has given me very useful advices each time we had a chance to talk. For many personal reasons, I changed my mind about doing a post doc with him, but I sincerely hope our relation will not change because of this choice and that we will keep exchanging for the best of present and future ICRF systems.

Annika,

I owe her this very thesis. She is the first person I met from CEA who gave me consideration and invited me in Cadarache for three interviews including the one with Laurent. We met in China while I only started working in EAST and was not yet very clear about the topic I would later focus on. She later helped me with Laurent to find solutions to get funded by EUROfusion as part of the EU-CN successful collaboration. Annika has always given me excellent advices and helped me all along my PhD. Her strong implication in both EAST and WEST experiments got us to also interact on scientific aspects on each side, in particular about the successful LHCD system of WEST, actually making her and Lena the most powerful ladies of the IRFM so far!
I hope she is proud of having initiating the wonderful experience of my thesis, I will anyways always be very grateful.

I want to thank my mother and sister for always being here for me even when I was not there with them during my long stays in China.
Finally, I naturally dedicate this thesis to my dad who I know must be proud.

Guillaume

Publications and oral

Published as first author：

[Urbanczyk 2019 RFPPC] G. Urbanczyk et al, EPJ Web of Conferences (2019)

[Urbanczyk 2019 NF] G. Urbanczyk et al 2019 Nucl. Fusion 59 066023

[Urbanczyk 2018] G. Urbanczyk 2018 – Nucl. Mat. and Energy 17 (2018) 274–278

[Urbanczyk 2017] G. Urbanczyk et al, EPJ Web of Conferences 157, 03005 (2017)

Published as co-author：

[Tierens 2019 NF] W. Tierens et al 2019 Nucl. Fusion 59 046001.

[Tierens 2019 PoP] W. Tierens et al 2019 Physics of Plasma.

[Wang 2017] J.H. Wang et al. Fusion Engineering and Design 122 (2017) 196–203

[Wang 2018] Jianhua WANG et al 2018 Plasma Sci. Technol. 20 045603

[Colas 2019] L. Colas et al. EPJ Web of Conferences (2019)

[Helou 2019] W. Helou et al. EPJ Web of Conferences (2019)

[Tierens 2019 RFPPC] W. Tierens et al. EPJ Web of Conferences (2019)

[Colas 2019] L. Colas et al. Journal of Computational Physics (2019)

[Krivska 2019] A. Krivska 2019 - Nuclear Materials and Energy 17 (2019) 274–278

[Bourdelle 2019] C. Bourdelle et al. EPS 2019

[Y. Q. Yang 2017] Y. Q. Yang et al. Plasma Phys. Control. Fusion 59 (2017) 095001

[Gallo 2019] A. Gallo et al. PET 2019 – “Application of SolEdge2D-EIRENE with Zhdanov multi-fluid collisional closure to the interpretation of VUV spectroscopic measurements of oxygen in WEST ”

Oral : One invited talk at the 2019 RF topical conference

Résumé en Français

Cette thèse vise à étudier les interactions entre le plasma et les parois de tokamaks liées aux ondes à la fréquence cyclotronique ionique (FCI), les interactions plasma-métaux étant à éviter absolument car elles sont synonymes de dégradations matérielles de l'enceinte et la libération d'impuretés métalliques dans le plasma dont les performances s'en trouvent grandement réduites. Cette problématique affecte concrètement toute machine visant à chauffer les ions via des ondes à la fréquence FCI, ce qui sera notamment le cas d'ITER. Cette thèse pleinement financée par EUROfusion dans le cadre d'une collaboration entre l'Europe et la Chine a été effectuée à l'Institut de Recherche pour la Fusion Magnétique au CEA Cadarache en ainsi qu'à l'Institut de Physique des Plasma à Hefei. Divers **travaux expérimentaux** ont alors été effectués incluant **sur** le tokamak **EAST** (Chine) :

- Conception (design), fabrication et installation de réseaux de sondes de Langmuir sur un limiteur d'une antenne ICRH afin d'y mesurer les effets de rectification de gaine causés par l'onde RF.

- Conception et installation de l'électronique associée (électronique des sondes, isolation optique et carte d'acquisition)

- Développement des outils associés permettant l'analyse des données par tout utilisateurs intéressé (Traitement des données en Matlab)

- Installation dans la machine de matériaux traces permettant l'étude de sources d'impuretés via le suivi spectroscopique de ces espèces et la caractérisation de leur présence dans le cœur des plasmas

Et sur le tokamak **WEST** (France) :

- Le développement et mise à disposition d'outils de traitement et d'analyse de données spectroscopiques visible et ultraviolet.

- Construction d'une base de données spectroscopique UV remplie choc à choc permettant un suivi global au cours de toutes les campagnes.

Pour compléter les observations expérimentales, des simulations ont été faites avec de nombreux codes. Côté France, les aléas de WEST ont en particulier forcé à revoir l'aspect expérimental de la thèse au profit de la modélisation de gaines RF à l'aide du code SSWICH développé à l'IRFM avant le début de la thèse. Beaucoup de temps aura été passé à améliorer le code SSWICH pour en faire une version 3D qui

permettrait de solutionner les principaux problèmes soulevés par mes prédécesseurs Jonathan JACQUOT et LU LingFeng dont les thèses étaient entièrement dédiées à la modélisation. Malheureusement cet ambitieux projet n'a pas encore aboutit, mais mes efforts ont permis l'avancée de ces travaux en étroite collaboration avec Wouter TIERENS qui est désormais le principal utilisateur du code. Après de multiples efforts et trois papiers sur le sujet, nous en sommes arrivés à la conclusion que cette tâche n'est pas possible tant que le code reposera sur l'outil commercial COMSOL dont le manque de flexibilité est devenu un réel obstacle empêchant d'atteindre nos objectifs. Un nouvel outil plus prometteur et open source est alors en cours d'investigation et peut être permettra de réussir en faisant l'objet d'une autre thèse.

Le présent ouvrage comporte :

1) une introduction sur la fusion et le chauffage des plasmas de tokamaks,
en particulier à l'aide d'ondes à la fréquence cyclotronique ionique (FCI)
2) le bagage physique requis à la compréhension des principaux mécanismes à l'œuvre lors de l'application de ce type de chauffage dont la caractérisation à l'aide de
3) différent diagnostiques, complémentaires et utiles dans diverses circonstances, utilisés à la fois dans les tokamaks EAST et WEST.
4) Les expériences s'organisent alors autour des deux principaux challenges du chauffage FCI qui sont le couplage de l'onde au plasma et la minimisation de la production d'impuretés reposant essentiellement sur l'excitation de gaines RF.
5) Les diverses méthodes pour maximiser l'efficacité avec laquelle l'onde est peut être couplée sont alors établies via des expériences sur EAST et WEST et validées par des simulations détaillées en Annexe.
6) Les divers mécanismes menant à la production d'impuretés liés au chauffage FCI sont enfin détaillés, permettant d'identifier un certain nombre de critères qui seront utiles voire nécessaires pour optimiser cet aspect crucial dans la perspective de plasmas stables, performants et pertinents pour la fusion pas seulement en tant qu'expérience scientifique mais en tant que nouvelle source d'énergie.

Un plasma est un gaz ionisé, ou bien un nuage de particules chargées positivement (ions) et négativement (électrons). Par exemple dans un tube de néon, le tube de verre est rempli de gaz (néon), et lors que l'on appuie sur l'interrupteur, une différence de potentiel est créée entre les électrodes à chaque extrémité du tube, le gaz est alors ionisé et passe à l'état de plasma. Ce type de plasma

est en revanche utile pour émettre de la lumière mais est relativement froid et donc inapproprié à la réaction de fusion nucléaire. La réaction de fusion nucléaire requiert de vaincre la répulsion coulombienne entre des ions de même charge qui naturellement tendent à se repousser, afin qu'ils fusionnent ensembles et libèrent de l'énergie sous forme de neutrons (lesquels peuvent être utilisés pour chauffer de l'eau et faire tourner une turbine pour faire de l'électricité). La réaction envisagée pour les futures machines pour avoir la plus haute section efficace est la fusion du deutérium et du tritium (D-T) : ${}^{2}_{1}D + {}^{3}_{1}T \rightarrow {}^{4}_{2}H_e(3.56MeV) + {}^{1}_{0}n(14.03MeV)$. Pour ce faire, il s'agit ni plus ni moins d'imiter le soleil ! Et tout le challenge réside dans la conception d'une machine qui ne fonde pas, la technique la plus prometteuse s'appelant le tokamak.
Les tokamaks sont des chambres toroidales plus ou moins grandes (de 50cm à plus de 20 mètres de diamètre) autour desquelles des aimants permettent de confiner le plasma. Le plasma lévite donc dans la chambre autour duquel une couche de vide ($\sim 10^{-5}$ Pa) le sépare des parois métalliques qui autant que faire se peut ne doivent pas être en contact direct avec le plasma dont les températures périphériques peuvent atteindre la centaine de milliers de degrés alors que les plus hautes au cœur sont de l'ordre de plusieurs centaines de millions de degrés. Pour atteindre ces températures, il faut donc chauffer le plasma ;
- chauffage ohmique en utilisant le courant généré par le plasma et sa résistivité, ce qui est efficace jusqu'à environ 30 millions de degrés, au-delà de quoi la résistivité du plasma devient trop faible pour cette approche, des chauffages auxiliaires peuvent sont alors utilisés pour atteindre des températures encore supérieures
- chauffage par injection de particules neutres (pour qu'elles ne soit pas déviées par le champs magnétique et pénètrent le plasma) à haute énergie, qui par collisions transfèrent leur énergie aux autres particules
- chauffage par ondes ; à haute fréquence pour chauffer les électrons légers et rapides (FCE), à basse fréquence pour chauffer les ions plus lourds et plus lents (FCI), et à fréquence intermédiaire (hybride) pour accélérer des électrons et générer du courant de manière non inductive.

La problématique de couplage des ondes à un plasma de tokamak repose sur le fait que les ondes ne se propagent correctement que lorsque la densité du plasma est supérieure à une certaine valeur appelée densité de coupure, en deca de laquelle

l'onde est dite « évanescente » (la puissance est réfléchie et l'amplitude de son champ électromagnétique décroit exponentiellement à mesure qu'elle avance dans le plasma). La propriété propagatrice ou évanescente de l'onde dépend alors de sa fréquence ou de sa longueur d'onde, de son nombre d'onde, et de la densité du milieu dans lequel elle est excitée. Idéalement nous aimerions donc pouvoir directement exciter l'onde dans une région du plasma ou la densité est déjà élevée, malheureusement cela impliquerait de plonger les antennes dans un plasma déjà trop dense et trop chaud, de sorte que les matériaux ne résisteraient pas longtemps à de tels flux de chaleur. Les antennes sont donc placées en périphérie des tokamaks à quelques centimètres du plasma confiné, et les ondes émises doivent généralement traversée une fine couche où elles sont évanescentes avant d'atteindre une région plus dense où elles deviennent propagatrices. Dans le cas particulier de l'onde FCI, il existe deux modes d'onde ; l'un dit « rapide » et l'autre « lent » en référence à leurs vitesses de phase. Le mode rapide est celui que nous cherchons donc à exciter majoritairement car il permet de chauffer les ions au cœur du plasma, puisque sa polarization est dans la même direction que la rotation des particules autour des lignes de champ magnétique. Cette onde doit alors traverser une fine couche d'évanescence devant les antennes (quelques centimètres), et optimiser le couplage de l'onde FCI consiste alors à minimiser l'épaisseur de cette couche, pour minimiser la quantité de puissance réfléchie et par là maximiser la quantité de puissance qui peut être injectée dans le plasma (1cm d'évanescence représentant une réflexion d'environ 20% de la puissance) sans abîmer le système (à cause d'arc électriques par exemple). Nous avons alors démontré via des expériences sur les tokamaks EAST et WEST, qu'il est possible pour une position donnée des antennes, d'**optimiser** cette **efficacité de couplage** en jouant sur plusieurs paramètres par ordre d'importance :

- **augmenter** la **densité** globale du plasma (et donc celle devant les antennes)
- **augmenter** la **fréquence** de l'onde
- **diminuer** les **nombres d'onde** excités par les antennes, ce qui en pratique peut être accompli en diminuant le phasage entre les courant circulant dans les straps
- **augmenter** la **puissance** additionnelle d'ondes à la fréquence **hybride** basse, permettant une meilleure ionisation des particules dans le plasma de bord et donc une augmentation de la densité devant les antennes
- agir sur le **fueling** du plasma en injectant du gaz par des vannes **à proximité des antennes** FCI (idéalement localisées au plan médian et radialement rétractées

d'environ 20cm derrière la face avant des antennes), permettant une augmentation locale de la densité devant les antennes

Une fois le couplage optimisé (excitation de l'onde rapide maximale), l'autre fléau du chauffage FCI est le phénomène de gaines RF qui donne lieu à des problèmes d'interaction plasma parois, l'érosion accélérée des matériaux, et la pollution du plasma par des impuretés métalliques (W, Fe, Cu, Mo, Ag …) qui non seulement ne présentent aucun intérêt pour la réaction de fusion D-T, mais ont surtout de nombreux effets délétères sur le plasma (rayonnement de puissance, refroidissement du cœur, apparition d'instabilités magnétohydrodynamiques …). Le mécanisme de gaine électrostatique est naturel et réside dans le fait que lorsque le plasma est en contact avec un élément métallique, les électrons qui sont bien plus légers et rapides que les ions s'accumulent sur la surface du matériau, repoussant les autres électrons et attirant des ions sur une couche d'épaisseur millimétrique. Il résulte de cette séparation des charges un champ électrique qui ralentie les électrons et accélère les ions en direction du matériau, de sorte que leur énergie augmente et éventuellement dépasse un seuil au-delà duquel la pulvérisation d'atomes métalliques devient possible et de plus en plus efficace. En plus de cette gaine que l'on pourrait qualifier de naturelle puisqu'inévitable, peut s'ajouter la gaine radiofréquence (RF) propre à FCI. Cette gaine RF repose sur l'excitation parasite de l'onde « lente », laquelle est généralement évanescente presque partout et propagatrice en deca d'une très faible densité ($<10^{17}m^{-3}$) appelée résonance hybride basse que l'on rencontre souvent plusieurs centimètres derrière les limiteurs d'antennes FCI. La polarisation de cette onde lente étant parallèle aux lignes de champ magnétique, elle contribue à augmenter la différence de potentiel entre le métal et le plasma, ou bien à élargir l'épaisseur de la gaine qui oscille à la fréquence FCI (dizaines de MHz). Sur une période RF ($\sim10^{-7}s$), les électrons légers et rapides réagissent au champ instantané de l'onde tandis que les ions lourds et lents ne sont sensibles qu'à une valeur moyenne et non nulle du fait de la non linéarité du processus. Le résultat de l'augmentation des champs électriques parallèles est alors l'augmentation du potentiel de la gaine, soit l'augmentation de l'énergie d'impact des ions, et donc l'augmentation de leur efficacité de pulvérisation du métal. Le présent ouvrage apporte diverses caractérisations expérimentales de ces effets de gaine RF en combinant un maximum de diagnostics afin de s'affranchir des défauts, limitations et hypothèses simplificatrices de chacun ;

- **sondes de Langmuir** sensibles aux radiofréquences

- **sondes émissives** fragiles et pas pratiques en environnement tokamak
- **spectroscopie** de bord (domaine **visible**) et dépendance des coefficients S/XB avec la température locale
- **spectroscopie** de cœur (domaine **ultraviolet**) souvent nécessite de s'affranchir d'effets de transports et requiert une certaine stabilité de la température électronique.

Les observations expérimentales sont regroupées autour des deux principaux mécanismes par lesquels FCI est susceptible d'exciter la gaine RF dans différentes régions, à savoir :

- les effets de **champ proche** qui sont le fruit d'une excitation parasite directe de l'onde lente par l'antenne, lesquels sont en général maximums au voisinage direct des antennes FCI (puisque l'onde lente est en général évanescente) et peuvent affecter d'autres régions connectées par des lignes de champ magnétique (limiteurs d'antennes, divertor …)
- les effets de **champ lointain** qui résultent souvent d'une mauvaise absorption de l'onde rapide qui est alors réfléchie, et dont une partie de la puissance est convertie en onde lente, laquelle peut alors exciter des gaines RF même dans des régions éloignées et non connectées magnétiquement (mur côté fort champ, divertor …)

Les effets de champ lointain ne semblent jouer un rôle majeur que dans des cas où l'absorption est franchement médiocre, or il est a priori aisé d'éviter ce genre de cas. De surcroit l'absorption sera à priori bien meilleure sur les tokamaks futurs à mesure que leur taille augmentera.

Les effets de champ proche semblent en revanche beaucoup plus complexes à éradiquer, en particulier dans le cas d'antennes avec seulement deux strapes de courant dans la direction toroidale, ce qui est le cas de toutes les antennes de WEST et d'une antenne d'EAST. Avec plus de deux strapes et un bon contrôle des phases, il a été en revanche démontré à plusieurs reprises (sur les tokamaks ASDEX, JET et Alcator C-Mod) qu'il est possible en appliquant environs deux fois plus de puissance sur les strapes centrales que sur les strapes extérieures, de compenser les courants induits sur les structures passives comme les limiteurs et par là de réduire grandement l'excitation parasite de l'onde lente et les sources d'impureté. En l'absence de cet outil sur EAST et WEST, il est observé qu'**opérer des antennes à deux strapes toroidales connectées à des objets en tungstène** (matériau envisagé pour les machines futures avec un grand nombre Z) **situés au voisinage du plan médian**, est quasiment **incompatible avec les principaux objectifs de performances** qui

consistent à faire de longues décharges (plus de 10s) à haute puissance (plus de 2MW FCI). Cette incompatibilité vient du fait que les sources d'impuretés augmentent trop en regard du volume de plasma disponible, faisant émerger nombreux effets néfastes tels que l'augmentation de la puissance rayonnée, le refroidissement du plasma, l'apparition d'instabilités magnétohydrodynamiques souvent la cause de disruption (extinction du plasma). Il est vrai qu'à mesure que la taille du tokamak augmentera, les sources d'impuretés n'augmenteront que de manière quadratique alors que leur concentration dans le plasma diminuera de manière cubique. Il est également vrai qu'en déposant un certain niveau de puissance au cœur du plasma, FCI peut permettre d'éviter l'accumulation d'impuretés lourdes, ce qui est observé à JET dans des décharges à haute puissance totale et au moins 4MW FCI. Il semble néanmoins capital de tenir compte des problèmes de peut causer le champ proche lors du design d'antennes FCI pour les futures machines.

Glossary

APL: Antenna Protection Limiter

ASDEX: (German device)

DC: Direct Current

ECRH: Electron Cyclotron Resonant Heating

HFS: High Field Side

FDTD: Finite Difference Time Domain

FEM: Finite Element Method

ICRH: Ion Cyclotron Resonant Heating

ITER: International Thermonuclear Experimental Reactor

FS: Faraday Screen

JET: Joint European Tokamak (British device)

LAPD: LineAr Plasma Device (Los Angeles)

LH: Lower Hybrid

LCFS: Last Closed Flux Surface

LFS: Low Field Side

L / H modes: Low / High confinement modes

MHD: Magnetohydrodynamic

NBI: Neutral Beam Injection

PEC: Perfect Electric Conductor

PMC: Perfect Magnetic Conductor

PFC: Plasma Facing Components

PSI: Plasma Surface Interaction

PML: Perfectly Matched Layer

RDL: Resonant Double Loop

RF: Radio-Frequency

SW / FW: Slow Wave / Fast Wave

SOL: Scrape Off Layer

SSWICH: Self-consistent Sheaths & Waves for Ion Cyclotron Heating

TOPICA: TOrino Polytechnic Ion Cyclotron Antenna

EAST: Experimental Advanced Superconducting Tokamak (Chinese device)

WEST: W Environment in Steady-state Tokamak (French device)

Notations

$e \approx 1.6\ 10^{-19}$C : Elementary charge

$k_B = 1.3806503\ 10^{23}$ m².kg/s²/K : Boltzmann's constant

$c = 2.997\ 10^{8}$ m/s : Speed of light

$\varepsilon_0 = 8.85\ 10^{-12}$ $m^{-3}.kg^{-1}.s^4.A^2$: Vacuum permittivity

$\mu_0 = 1.25\ 10^{-6}$ $m.kg.s^{-2}.A^{-2}$: Vacuum permeability

δ : Width of something detailed in the context [m]

τ_e : Energy confinement time [s]

B_p, B_t and B or B_0 : poloidal, toroidal components and total magnetic field [T]

θ : Pitch-angle (angle between B_0 and B_t) → $\theta \sim 7°$ in EAST and WEST (Note Faraday Screen bars are in principle tilted of the same angle)

θ' : Incidence angle of a magnetic field line on a PFC

m_s : Mass of specie s [kg]

$\Omega_{cs} = q_s B_0 / m_s$: Cyclotron frequency of a given specie s in the plasma [rad/s]

$\omega_{ps} = \sqrt{q_s^2 n_s / \varepsilon_0 m_s}$: Specie plasma frequency [rad/s]

f_0 : Wave frequency (simply noted f in general cases) → $35_{EAST} \leq ICRF \leq 57_{WEST}$ MHz

$\omega_0 = 2\pi.f_0$: Wave pulsation (simply noted ω in general cases) [rad/s]

$\lambda_{De} = \sqrt{\varepsilon_0 k_B T_e / n_e e^2}$: Debye length (order of millimeter)

$\boldsymbol{\lambda}$: Wavelength (ex: ICRF wavelengths are about 2m in EAST and 70cm in WEST)

$\boldsymbol{k}$: Wave-vector (ex: ICRF parallel wave-vectors are about 4rad/m in EAST and 9rad/m in WEST)

φ : phasing

ϕ_f : floating potential (usually several volts but can reach several hundreds of volts in regions with RF sheath)

ϕ_p : plasma potential (several volts)

I^+_{sat} and I^-_{sat} : respectively ion and electron saturation currents

V_{DC} : DC plasma potential V_{sh} : Voltage across the sheath

V_{RF} : Amplitude of an ICRF wave (typically hundreds of volts)

V_{TL} : Maximum voltage in transmission lines (several kV, typically ~25kV in WEST)

V_0 : quantity of voltage carried by SW that is penetrating the sheath ($V_0 \approx P_{ICRF}^{1/2}$)

Résumé

Cette thèse vise à étudier les interactions entre le plasma et les parois de tokamaks liées aux ondes à la fréquence cyclotronique ionique (FCI), les interactions plasma-métaux étant à éviter absolument car elles sont synonymes de dégradations matérielles de l'enceinte et la libération d'impuretés métalliques dans le plasma dont les performances s'en trouvent grandement réduites. Cette problématique affecte concrètement toute machine visant à chauffer les ions via des ondes à la fréquence FCI, ce qui sera notamment le cas d'ITER. Cette thèse s'inscrit dans une collaboration entre le CEA Cadarache (France) et l'Institut de Physique des Plasmas à Hefei (Chine). Divers travaux expérimentaux ont été effectués sur les tokamaks EAST (Chine) et WEST (France) afin d'identifier les paramètres pertinents pour d'une part optimiser l'efficacité par laquelle les ondes FCI utilisées pour chauffer le plasma doivent être excitées afin de maximiser la quantité de puissance couplée au plasma tout en minimisant les interactions du plasma avec les parois dues à ce type d'ondes et souvent attribuées au concept de gaine radiofréquence au cœur de cette thèse.

Summary

This thesis aims at studying phenomena by which Ion Cyclotron Resonance Heating (ICRH) induces interactions between the plasma and the walls of tokamaks, the plasma-metal interactions being deleterious not only to prevent vessel materials degradation but also not to affect plasma performance due to the presence of heavy metallic impurity compared to foreseen fuel (namely deuterium and tritium). This problematic basically affects any machine aiming at heating the ions with waves at the ion cyclotron frequency, which in particular will be the case of ITER. This thesis is the result of a collaboration between CEA Cadarache (France) and the Institute of Plasma Physics in Hefei (China). Various experimental work have been carried out on the EAST (China) and WEST (France) tokamaks in order to identify the relevant parameters allowing to optimize the efficiency by which the ICRF waves – used to heat the plasma – must be excited in order to maximize the amount of power coupled, while simultaneously minimizing the plasma interactions with the walls due to this type of waves and the so called radiofrequency sheath excitation.